DEFENCE S&T TECHNICAL BULLETIN

VOL. 12 NUM. 1 YEAR 2019 ISSN 1985-6571

CONTENTS

Discriminating Closely Spaced Aircrafts Using Time Difference of Arrival (TDOA) Based Association Algorithm 1 - 15
Abdulmalik Shehu Yaro, Ahmad Zuri Sha'ameri & Sa'id Musa Yarima

A Review of Copter Drone Detection Using Radar Systems 16 - 38
Surajo Alhaji Musa, Raja Syamsul Azmir Raja Abdullah, Aduwati Sali, Alyani Ismail, Nur Emileen Abdul Rashid, Idnin Pasya Ibrahim & Asem Ahmad Salah

Spaceborne Synthetic Aperture Radar (SAR) Sensors in Low Earth Orbit (LEO) for Real-Time Detection and Monitoring of Floods 39 - 50
Arun Kumar Verma, Ranbir Nandan & Aditi Verma

Development of HF Modelling in Peninsular Malaysia During the Rise of Solar Cycle 24 51 - 60
Rafidah Abd Malik, Mardina Abdullah, Sabirin Abdullah, Yokoyama Tatsuhiro & Clara Y. Yatini

Review of Machine Learning Based Hardware Trojan Detection Methods 61 - 78
Chee Hoo Kok, Chia Yee Ooi, Michiko Inoue, Nordinah Ismail, Mehrdad Moghbel & Hau Sim Choo

A Message Cryptography Technique Using DNA Based Hybrid Approach 79 - 90
Vaibhav Godbole

Investigation of Vehicle Occupant Response Subjected to Under-Vehicle Explosion 91 - 100
Khalis Suhaimi, Risby Mohd Sohaimi, Muhammad Fahmi Md. Isa, Muhd Azhar Abu Bakar, Norazman Mohamad Nor, Ariffin Ismail & Victor Feisal Knight

Optimisation of Hybrid Composite Reinforced Carbon and Glass Using AHP Method 101 - 112
Nur Aizatul 'Ain Md Zahir, Ahmad Fuad Ab Ghani, Mohd Ahadlin Mohd Daud, Sivakumar Dhar Malingam & Ridzuan Mansur

The Influence of Fibre Stacking Configurations on the Indentation Behaviour of Pineapple Leaf / Glass Fibre Reinforced Hybrid Composites 113 - 123
Ng Lin Feng , Sivakumar Dhar Malingam, Kathiravan Subramaniam, Mohd Zulkefli Selamat, Mohd Basri Ali & Omar Bapokutty

Mechanical Properties of Cross-Ply Banana-Glass Fibre Reinforced Polypropylene Composites 124 - 135
Norizzati Zulkafli, Sivakumar Dhar Maligam, Siti Hajar Sheikh Md Fadzullah, Zaleha Mustafa, Kamarul Ariffin Zakaria & Sivarao Subramonian

Sound Insulation Performance of Kenaf Fibre as A Noise Control Treatment in Car Using Statistical Energy Analysis 136 - 149
Norzailan Azahari, Azma Putra, Reduan Mat Dan & Muhammad Nur Othman

Properties of Electrodeposited Nickel Cobalt Coated Mild Steel Developed from Alkaline Bath 150 - 160
Nik Hassanuddin Nik Yusoff, Othman Mamat & Mahdi Che Isa

Wear Behaviour of a-C:H Helical Gear Through Particle Generation 161 - 175
Abdul Hakim Abdul Hamid, Reduan Mat Dan, Azma Putra, Mohd Nizam Sudin & Rozdman Khaidir Mazlan

Ministry of Defence
Malaysia

SCIENCE & TECHNOLOGY RESEARCH INSTITUTE FOR DEFENCE (STRIDE)

AIMS AND SCOPE

The Defence S&T Technical Bulletin is the official technical bulletin of the Science & Technology Research Institute for Defence (STRIDE). The bulletin, which is indexed in, among others, Scopus, Index Corpenicus, ProQuest and EBSCO, contains manuscripts on research findings in various fields of defence science & technology. The primary purpose of this bulletin is to act as a channel for the publication of defence-based research work undertaken by researchers both within and outside the country.

WRITING FOR THE DEFENCE S&T TECHNICAL BULLETIN

Contributions to the bulletin should be based on original research in areas related to defence science & technology. All contributions should be in English.

PUBLICATION

The editors' decision with regard to publication of any item is final. A manuscript is accepted on the understanding that it is an original piece of work that has not been accepted for publication elsewhere.

PRESENTATION OF MANUSCRIPTS

The format of the manuscript is as follows:

a) Page size A4
b) MS Word format
c) Single space
d) Justified
e) In Times New Roman, 11-point font
f) Should not exceed 20 pages, including references
g) Texts in charts and tables should be in 10-point font.

Please e-mail the manuscript to:

1) Gs. Dr. Dinesh Sathyamoorthy (dinesh.sathyamoorthy@stride.gov.my)
2) Dr. Mahdi bin Che Isa (mahdi.cheisa@stride.gov.my)

The next edition of the bulletin (Vol. 12, Num. 2) is expected to be published in November 2019. The due date for submissions is 21 August 2019. **It is strongly iterated that authors are solely responsible for taking the necessary steps to ensure that the submitted manuscripts do not contain confidential or sensitive material.**

The template of the manuscript is as follows:

TITLE OF MANUSCRIPT

Name(s) of author(s)

Affiliation(s)

Email:

ABSTRACT

Contents of abstract.

Keywords: *Keyword 1; keyword 2; keyword 3; keyword 4; keyword 5.*

1. TOPIC 1

Paragraph 1.

Paragraph 2.

1.1 Sub Topic 1

Paragraph 1.

Paragraph 2.

2. TOPIC 2

Paragraph 1.

Paragraph 2.

Figure 1: Title of figure.

Table 1: Title of table.

Content	**Content**	**Content**
Content	Content	Content
Content	Content	Content
Content	Content	Content

Equation 1 (1)
Equation 2 (2)

REFERENCES

Long lists of notes of bibliographical references are generally not required. The method of citing references in the text is 'name date' style, e.g. 'Hanis (1993) claimed that...', or '…including the lack of interoperability (Bohara *et al.*, 2003)'. End references should be in alphabetical order. The following reference style is to be adhered to:

Books

Serra, J. (1982). *Image Analysis and Mathematical Morphology*. Academic Press, London.

Book Chapters

Goodchild, M.F. & Quattrochi, D.A. (1997). Scale, multiscaling, remote sensing and GIS. *In* Quattrochi, D.A. & Goodchild, M.F. (Eds.), *Scale in Remote Sensing and GIS*. Lewis Publishers, Boca Raton, Florida, pp. 1-11.

Journals / Serials

Jang, B.K. & Chin, R.T. (1990). Analysis of thinning algorithms using mathematical morphology. *IEEE T. Pattern Anal.*, **12**: 541-550.

Online Sources

GTOPO30 (1996). *GTOPO30: Global 30 Arc Second Elevation Data Set*. Available online at: http://edcwww.cr.usgs.gov/landdaac/gtopo30/gtopo30.html (Last access date: 1 June 2009).

Unpublished Materials (e.g. theses, reports and documents)

Wood, J. (1996). *The Geomorphological Characterization of Digital Elevation Models*. PhD Thesis, Department of Geography, University of Leicester, Leicester.

DISCRIMINATING CLOSELY SPACED AIRCRAFTS USING TIME DIFFERENCE OF ARRIVAL (TDOA) BASED ASSOCIATION ALGORITHM

Abdulmalik Shehu Yaro[1,2], Ahmad Zuri Sha'ameri[1*] & Sa'id Musa Yarima[1,3]

[1]Division of Electronic and Electrical Engineering, School of Electrical Engineering, Universiti Teknologi Malaysia (UTM), Malaysia
[2]Department of Communications Engineering, Faculty of Engineering, Ahmadu Bello University (ABU), Nigeria
[3]Department of Electrical and Electronics Engineering, Faculty of Engineering, Abubakar Tafawa Balewa University (ATBU), Nigeria

[*]Email: zuri@fke.utm.my

ABSTRACT

A time difference of arrival (TDOA) based locating system determines the location of an aircraft by measuring the time difference between transponder emissions received at ground station antenna (GSA) pairs. To locate multiple aircrafts, the TDOAs are first grouped according to each aircraft using an association algorithm prior to the individual aircraft locating process. The ability to correctly associate the TDOAs to the right aircraft depends on the received signal to noise ratio (SNR) and the separation between the aircraft. For a given horizontal range, azimuth and altitude separation between an aircraft pair, a technique is developed to evaluate an association algorithm capability to group the measured TDOAs to the correct aircraft. The performance of the association algorithm considers three different military flying formations using emissions from the onboard weapon control radar (WCR) and replies to a secondary surveillance radar (SSR) interrogator. The simulation results show that with the technique, it is possible to determine the probability of correct association of the estimated TDOAs to the right aircraft by the association algorithm. Furthermore, based on a horizontal range and azimuth separations of 50 m and an altitude separation of 1,000 ft, the TDOA based locating system coupled with the association algorithm has the best locating performance using TDOAs obtained from emissions through the main lobe of the WCR antenna.

Keywords: *Military flying formation; time difference of arrival (TDOA); weapon control radar; association probability; air defense radar.*

1. INTRODUCTION

The demand for air travel for transportation of goods and in support of the tourism industry has resulted in high air traffic density. An average growth in air traffic density of greater than 4% has been forecasted in Latin America, Africa, Asia-Pacific and Middle East, in addition to the already packed air traffic density in North America and Europe (IATA, 2017). Among the measures implemented by the International Civil Aviation Organization (ICAO) to meet this challenge are the implementation of the reduced vertical separation minimum (RVSM) initiative, reduction in the horizontal lateral separation between aircraft at the enroute flight levels (FLs), and the introduction of satellite based locating systems (FAA, 2014; CANSO, 2016; ICAO, 2016). Prior to the implementation of the RVSM initiative, enroute FLs within the 29,000 ft and 41,000 ft were at an interval of 2,000 ft (600 m), resulting in a total of seven FLs. With the implementation of this initiative, the FL interval is reduced to 1,000 ft (300 m), which brings about six new FLs, resulting in a total of 13 FLs (ICAO, 2016). The horizontal lateral separation between aircraft at any of the enroute FLs is 5 NM (~9 km). However, at areas with high traffic demand, such as the terminal

maneuvering area (TMA), the lateral separation can be reduced to a minimum of 3 NM (~5 km) by the appropriate air traffic services (ATS) authority (ICAO, 2016). Through the next generation (NextGen) program initiated by the Federal Aviation Administration (FAA), a satellite-based locating system referred to as automatic dependent surveillance broadcast (ADS-B) has been introduced to revolutionize ATS surveillance in the civil aviation industry. This initiative is expected to meet up with global traffic demands with full global deployment by the year 2025 (ICAO, 2014; Strohmeier *et al*., 2014; CANSO, 2016). Compared to the conventional systems for ATS, which are surveillance radar and time difference of arrival (TDOA) based systems, ADS-B has the highest update rate and is the cheapest in terms of installation and maintenance cost (CANSO, 2016).

Military aircrafts ranging from fighter aircraft to transport aircraft utilizes the same airspace used by the civil air aviation. However, these aircraft follow a different flight profile, such as formation flying, depending on the operational requirements, including training, aerial refueling, attack and interception. Whenever military aircrafts fly in formations, they do not follow the conventional separation standard set for the civil aviation, but rather the military authority assumes responsibility for separation of aircraft (MARSA) (Ray, 2015). This means that the pilots use visual inspection to maintain separation. Therefore, the ATS systems used in civil aviation, such as primary radar, secondary radar and radio based locating systems, are not expected to detect military targets correctly. The flight profiles of military aircrafts are considered in the design of air defense radars (ADRs) (Martin, 2018). In general, the ADR should be able to detect aircrafts used in both civil and military aviation, and in some instances used to perform ATS in the event of surveillance radar failure (UPI Archives, 1992). Compared to radars used in civil aviation, the ADR performs aircraft position estimation (PE) in 2-dimensional (2-D) or 3-dimensional (3-D). It has a range resolution accuracy of about 50 m, azimuth resolution accuracy of about 0.22^0, with an elevation resolution accuracy of about 0.3^0 (Martin, 2018). The reason for such high range resolution accuracy is due to the use of pulse compression as compared to the civil aviation radars, which normally are based on simple pulse modulation, where the range resolution is determined by the pulse width (a pulse width of 1 μs provides a range resolution of about 300 m) (Christian, 2018).

As mentioned earlier, ADS-B may be the main component in the NextGen surveillance system. However, it suffers security vulnerability, such as the lack of authentication of aircraft transponder emissions used in the location process and it is also possible to fake the location of an aircraft (Strohmeier *et al*., 2014; CANSO, 2016). The TDOA-based locating system, also known as multilateration (MLAT), has been recommended to complement ADS-B (CANSO, 2016). Besides verifying the integrity of aircraft locations estimated from ADS-B, MLAT could serve as a back-up in the event of satellite failure. Both military and civilian aircrafts are equipped with airborne radar – whether as weather radar or weapons control radar (WCR) – operating in the X-band (8 to 12 GHz) and / or transponders that transmit signals as response to an interrogator by the secondary surveillance radar (SSR) or independently periodically transmit signals to the ground-based system (ADS-B) (Ahmad & Sha'ameri, 2015; Sha'ameri *et al*., 2015). These emissions are detected by the ground station antenna (GSA)s and are used by the TDOA-based locating system to determine the position of the aircraft (Yaro *et al*., 2017). The system first estimates the TDOAs of the emissions detected at GSA pairs and secondly, estimate the position of the aircraft using a lateration algorithm with the TDOAs as input variable. In the case of multiple aircrafts, the TDOAs are grouped according to aircraft in a process called association by an association algorithm prior to the PE with the lateration algorithm (Ni *et al*., 2013; Li & Li, 2014). The multiple aircraft locating capability of the TDOA-based systems depends on how accurate the association algorithm groups the TDOAs to the right aircraft. The major contributing factors to the TDOA association accuracy are the separation between aircraft pair; the effective horizontal range of the aircraft pair from the locating system; and the received signal to noise ratio (SNR) of the aircraft emissions. In this paper, a technique is developed to assist in systematically determining the TDOA association capability given the horizontal range, azimuth and altitude separations of a pair of emitting targets.

The remainder of the paper is organized as follows; Section 2 provides the description of the signals used for the TDOA estimation, while Section 3 presents the development of the technique to

determine the performance of the TDOA-base association algorithm. The simulation results and discussion are presented in Section 4, and the conclusion is presented in Section 5.

2. SIGNALS AND TDOA ESTIMATION METHODOLOGY

In this section, a brief description of the different type of signals used by military and civilian aircrafts for TDOA estimation is first presented. This is followed by the mathematical derivation of multiple aircraft TDOA estimation.

2.1 Military and Civilian Aircraft Signaling Formats

Aircrafts used in civilian or military operations are equipped with different signaling formats, resulting in different emissions (Neven *et al*., 2005; Christian, 2018). In civil aviation, the aircraft emission is either the reply to the interrogator of the SSR (Neven *et al*., 2005) or ADS-B transponder (Ahmad & Sha'ameri, 2015) at 1,090 MHz, and the weather radar in the X-band (8 to 12 GHz). Both downlink emissions in the civilian aircraft are at 1,090 MHz frequency band. Similar bands are also used by military aircrafts, except the WCR, which is similar to the weather radar that also operates in the X-band (Christian, 2018).

The aircraft emission in response to the SSR interrogator contains information about the aircraft and it depends on the mode of operation of the SSR interrogator. There are three SSR interrogator operation modes, namely modes A, C and S (Christian, 2018). In modes A and C, each emission contains a 12-bit message with information about the aircraft identity number and its current altitude respectively. In mode S, the emission could contain either a 56- or 112-bit message with information about both aircraft identity number and its current altitude amongst other information about the aircraft (Christian, 2018). The ADS-B transponder emission is periodic at intervals of either 0.5 or 1μs, and not in response to an interrogator as compared to the SSR. Its emission contains a 112-bit message similar to the SSR mode S, commonly known as extended squitter (Neven *et al*., 2005; Abdulaziz *et al*., 2015).

Using the emissions from civilian (SSR or ADS-B) or military aircrafts received by the GSA pair, the TDOA is then estimated. The TDOA estimation is not the scope of this work, but it is assumed that the TDOAs have already been estimated using the available techniques in literatures (Neven et al., 2005; Marmaroli *et al*., 2012), but they contain errors. All that is left for the association algorithm is to group the TDOAs according to aircraft for subsequent PE using the lateration algorithm of the TDOA based locating system.

2.2 Multiple Aircraft TDOA Estimation

Consider two aircrafts labelled A and B, and their emissions are $x^a(t)$ and $x^b(t)$ respectively. If $x^a(t)$ and $x^b(t)$ are from a WCR, then they both have different carrier frequencies, but if they reply to an SSR interrogator, then both share the same carrier frequency (1,090 MHz). For the reception of weather radar or WCR signals, the actual carrier frequency of each signal is not known, but lies within the X-band and it is assumed that a channelized receiver is used, which operates in the X-band (Lopez-Risueno *et al*., 2005). Within an observation window, the signal received at the GSA labelled 1 and 2 respectively are:

$$x_1(t) = x^a(t - \tau^a_{1,[s]}) + x^b(t - \tau^b_{1,[s]}) \quad (1)$$

$$x_2(t) = x^a(t - \tau^a_{2,[s]}) + x^b(t - \tau^b_{2,[s]}) \quad (2)$$

where $\tau^{a}_{1,[s]}$ and $\tau^{b}_{1,[s]}$ are the time of arrivals (TOAs) in s, indicated by the subscript [s] of the emissions of aircrafts A and B respectively at the GSA labelled 1, while $\tau^{a}_{2,[s]}$ and $\tau^{b}_{2,[s]}$ are the TOAs at GSA labelled 2 of the emissions of aircrafts A and B respectively.

Taking the cross-correlation of $x_1(t)$ and $x_2(t)$, the resulting expression is (Marmaroli *et al*., 2012):

$$\begin{aligned} R_{x_1x_2}(\tau) = {} & R\left(\tau-\left(\tau^{a}_{1,[s]}-\tau^{a}_{2,[s]}\right)\right)+R\left(\tau-\left(\tau^{a}_{1,[s]}-\tau^{b}_{2,[s]}\right)\right) \\ & +R\left(\tau-\left(\tau^{b}_{1,[s]}-\tau^{a}_{2,[s]}\right)\right)+R\left(\tau-\left(\tau^{b}_{1,[s]}-\tau^{b}_{2,[s]}\right)\right) \end{aligned} \tag{3}$$

Due to statistical independency of the emissions from the different aircrafts, then:

$$R\left(\tau-\left(\tau^{a}_{1,[s]}-\tau^{b}_{2,[s]}\right)\right)=0 \tag{4a}$$

$$R\left(\tau-\left(\tau^{b}_{1,[s]}-\tau^{a}_{2,[s]}\right)\right)=0 \tag{4b}$$

Substituting Equation 4 into Equation 3, the resulting expression is:

$$R_{x_1x_2}(\tau)=R\left(\tau-\tau^{a}_{12,[s]}\right)+R\left(\tau-\tau^{b}_{12,[s]}\right) \tag{5}$$

where:

$$\tau^{a}_{12,[s]}=\tau^{a}_{1,[s]}-\tau^{a}_{2,[s]} \tag{6a}$$

$$\tau^{b}_{12,[s]}=\tau^{b}_{1,[s]}-\tau^{b}_{2,[s]} \tag{6b}$$

where $\tau^{a}_{12,[s]}$ and $\tau^{b}_{12,[s]}$ in Equation 5, presented by Equations 6a and 6b respectively, are the TDOAs of the emissions of aircrafts A and B detected at GSA labeled 1 and 2. In a practical scenario, the TDOAs in Equation 6 are obtained with error due to several factors such as quantization error, noise in the emission and ground station clock synchronization error. By modelling the TDOA error as a zero mean Gaussian random variable (Li *et al*., 2016), the estimated TDOAs are:

$$\hat{\tau}^{a}_{12,[s]}=\tau^{a}_{12,[s]}+N\left(0,\sigma^{a}_{12,[s]}\right) \tag{7a}$$

$$\hat{\tau}^{b}_{12,[s]}=\tau^{b}_{12,[s]}+N\left(0,\sigma^{b}_{12,[s]}\right) \tag{7b}$$

where $\sigma^{a}_{12,[s]}$ and $\sigma^{b}_{12,[s]}$ are the TDOA error standard deviations (SDs) in obtaining the TDOAs of the emissions of aircrafts A and B respectively.

3. TDOA-BASE ASSOCIATION PERFORMANCE METHODOLOGY

The ability of a TDOA-based association algorithm to correctly associate estimated TDOAs to the right aircraft depends on the received SNR of the aircraft emissions and the separation between the aircraft. Therefore, the conditions that will result in a wrong association, which is an association error of the estimated TDOAs derived in Equation 7. Secondly, a mathematical expression is established to determine if there is an association error when the conditions for the wrong association are valid. Finally, the probability at which the estimated TDOAs are correctly associated to each aircraft is presented.

3.1 Conditions for Wrong Association of Estimated TDOA

The correct association of the estimated TDOAs in Equation 7 results in the correct PE of the aircraft by the TDOA-based locating system. In this sub-section, the conditions for wrong association of two aircrafts are presented.

For association error to occur in the estimated TDOAs of two aircraft, they must be closely spaced (Reale *et al*., 2013). This leads to their estimated TDOAs to be close together in the TDOA domain to the extent that their TDOA error probability density distributions (PDFs) have an overlapping region (regions A and B), as shown in Figure 1. When the TDOAs are estimated in either of the overlapping regions, there is a likelihood that an association error will occur.

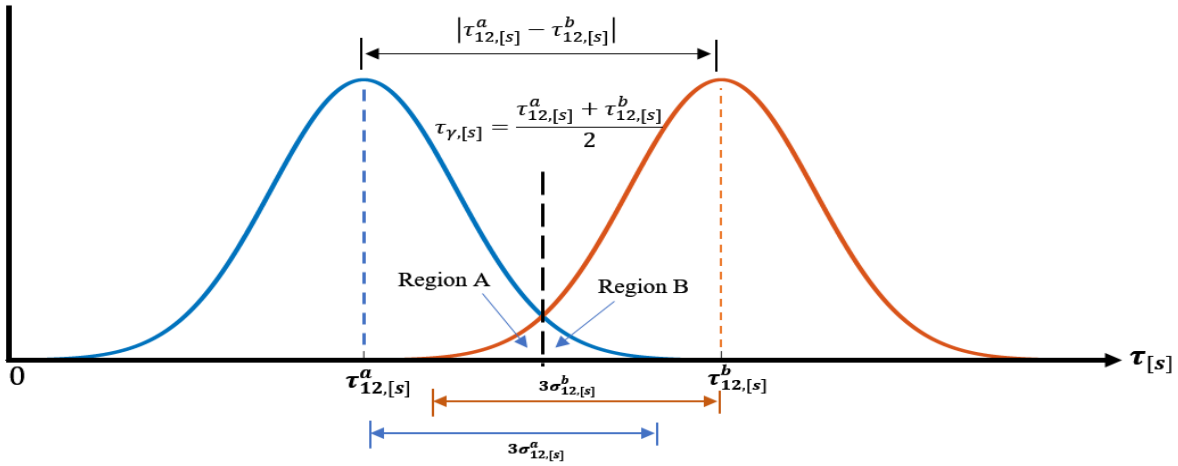

Figure 1: TDOA error conditional probabilities of aircrafts A and B.

There are two conditions that could lead to an association error of the estimated TDOAs. The first condition is when three times the sum of the TDOA error SDs (refer to Figure 1) is greater than the absolute difference between the mean TDOA values ($\tau^a_{12,[s]}$ and $\tau^b_{12,[s]}$) in Equation 6. When this happens, the overlapping region in Figure 1 is created and there is likelihood that the TDOAs are estimated in this region. The mathematical representation of the first condition for an association error to occur is:

$$\left|\tau^a_{12,[s]} - \tau^b_{12,[s]}\right| < 3\left(\sigma^a_{12,[s]} + \sigma^b_{12,[s]}\right) \tag{8}$$

The left-hand side (LHS) of Equation 8 is the distance between the mean TDOAs of aircrafts A and B obtained from Equation 6, whereas the right-hand side (RHS) of the equation is the distance between the TDOA error distribution of aircrafts A and B. The RHS of the equation is used to determine if the overlapping region given as regions A and B in Figure 1 are created and this happens only when it is greater than the LHS.

The second condition is that either $\tau^a_{12,[s]}$ is estimated in region B or $\tau^b_{12,[s]}$ is estimated in region A. When both $\tau^a_{12,[s]}$ and $\tau^b_{12,[s]}$ are estimated in either regions A or B, the association algorithm is not able to decide which TDOA belong to which aircraft. As such, both TDOAs are considered to belong to the same aircraft. This leaves no TDOA assigned to the other aircraft, resulting in an association error.

In the next sub-section, a technique to systematically determine if there is an association error given the effective SNR of the aircraft emissions and the separation between the aircraft pair is presented.

3.2 Association Error Determination Methodology

In this sub-section, a mathematical approach is presented to determine if there is an association error given the locations of the aircraft and the SNR of their emissions detected at the GSA pairs. As earlier presented in Section 3.1, the first condition for an association error to occur is when Equation 8 is valid. Let the RHS of Equation 8 be:

$$\sigma_{\tau,[s]} = 3\left(\sigma^{a}_{12,[s]} + \sigma^{b}_{12,[s]}\right) \tag{9}$$

It can be seen that $\sigma_{\tau,[s]}$ in Equation 9 is a function of the TDOA error SDs. According to Galati *et al*. (2012), the TDOA error SD is a function of the SNR of the received emission and their relationship is mathematically expressed as follows:

$$\sigma^{w}_{12,[s]} = \frac{1}{\sigma_{f,[Hz]}\sqrt{2}} \times \sqrt{\left(\frac{1}{\gamma_1^{w}} + \frac{1}{\gamma_2^{w}}\right)} \qquad \text{for} \qquad w \in [a,b] \tag{10}$$

where $\sigma_{f,[Hz]}$is the bandwidth of the receiver in Hz, and γ_1^w and γ_2^w are the SNR values (in linear scale) of the received emissions at the GSAs labelled 1 and 2 respectively.

The SNR in Equation 10 is obtained from it decibel (dB) value as follows:

$$\gamma_i^{w} = 10^{\left(\frac{\gamma^{w}_{i,[dB]}}{10}\right)} \qquad \text{for} \qquad i \in [1,2] \tag{11}$$

Recall that for an association error to occur, the aircraft must be closely spaced to the extent that:

$$\gamma_1^{a} \approx \gamma_1^{b} = \gamma_1 \tag{12a}$$

$$\gamma_2^{a} \approx \gamma_2^{b} = \gamma_2 \tag{12b}$$

This means that from Equation 9:

$$\sigma^{a}_{12,[s]} \approx \sigma^{b}_{12,[s]} = \sigma_{12,[s]} \tag{13}$$

The revised version of Equation 10 after substituting Equation 10 into Equation 13 is:

$$\sigma_{\tau,[s]} = \frac{3}{\sigma_{f,[Hz]}\sqrt{2}} \times \sqrt{10^{-\left(\frac{\gamma_{1,[dB]}}{10}\right)} + 10^{-\left(\frac{\gamma_{2,[dB]}}{10}\right)}} \tag{14}$$

Furthermore, substituting $\gamma_{1,[dB]}$ and $\gamma_{2,[dB]}$ with the effective SNR value ($\gamma_{eff,[dB]}$) between the GSA pair (Stein, 1981), Equation 14 after further simplification is rewritten as:

$$\sigma_{\tau,[s]} = \frac{3}{\sigma_{f,[Hz]}} \times \sqrt{10^{-\left(\frac{\gamma_{eff,[dB]}}{10}\right)}} \tag{15}$$

where:

$$\gamma_{eff,[dB]} = \min\left(\gamma_{1,[dB]}, \gamma_{2,[dB]}\right) \tag{16}$$

The LHS of Equation 8 is a function of the mean TDOA values in Equation 6. The mean TDOA values have a geometrical relationship to the locations of the aircraft and are expressed as follows:

$$\tau^{a}_{12,[s]} = \frac{\left\|\mathbf{x}_{a,[km]} - \mathbf{s}_{1,[km]}\right\| - \left\|\mathbf{x}_{a,[km]} - \mathbf{s}_{2,[km]}\right\|}{3\times10^{5}} \tag{17a}$$

$$\tau^{b}_{12,[s]} = \frac{\left\|\mathbf{x}_{b,[km]} - \mathbf{s}_{1,[km]}\right\| - \left\|\mathbf{x}_{b,[km]} - \mathbf{s}_{2,[km]}\right\|}{3\times10^{5}} \tag{17b}$$

where $\mathbf{x}_{a,[km]}$ and $\mathbf{x}_{b,[km]}$ in kilometer, as indicated by the subscript [km], are the locations of aircrafts A and B respectively, while $\mathbf{s}_{1,[km]}$ and $\mathbf{s}_{2,[km]}$ are the coordinates of the GSA labelled 1 and 2 respectively.

Therefore, given the locations of the aircraft, Equation 18 is used to determine if there is an association error at a given $\gamma_{eff,[dB]}$ value. This occurs if the numerical value of the RHS is greater than that of the LHS:

$$\left|\tau^{a}_{12,[s]} - \tau^{b}_{12,[s]}\right| < \sigma_{\tau,[s]} \tag{18}$$

where $\sigma_{\tau,[s]}$ a function of $\gamma_{eff,[dB]}$ of the emission as shown in Equation 15.

3.3 Association Error Probability

After it has been determined using Equation 18 that an association error occurs, the next step is to determine the association error probability (P_{error}) which is presented in this sub-section. It can be recalled from Section 3.1 that for association error to occur, either $\tau_{a,[s]}$ is estimated in region B or $\tau_{b,[s]}$ is estimated in region A (Figure 1). The mathematical expression for the PDFs of the estimated TDOAs for aircrafts A and B respectively are:

$$p\left(\tau \middle| \tau^{a}_{12,[s]}\right) = \frac{1}{\sigma_{[s]}\sqrt{2\pi}} \exp\left[-\frac{1}{2}\left(\frac{\tau - \tau^{a}_{12,[s]}}{\sigma_{[s]}}\right)^{2}\right] \tag{19}$$

$$p\left(\tau \middle| \tau^{b}_{12,[s]}\right) = \frac{1}{\sigma_{[s]}\sqrt{2\pi}} \exp\left[-\frac{1}{2}\left(\frac{\tau - \tau^{b}_{12,[s]}}{\sigma_{[s]}}\right)^{2}\right] \tag{20}$$

The probability that $\tau^{a}_{12,[s]}$ is estimated in region B from Figure 1 is mathematically expressed as:

$$P\left(e \middle| \tau^{a}_{12,[s]}\right) = Q\left(\frac{\tau_{\gamma,[s]} - \tau^{a}_{12,[s]}}{\sigma_{[s]}}\right) \tag{21}$$

while the probability that $\tau^{b}_{12,[s]}$ is estimated in region A is:

$$P\left(e\middle|\tau_{12,[s]}^{b}\right)=Q\left(\frac{\tau_{12,[s]}^{b}-\tau_{\gamma,[s]}}{\sigma_{[s]}}\right) \tag{22}$$

where

$$\tau_{\gamma,[s]}=\frac{\tau_{12,[s]}^{a}+\tau_{12,[s]}^{b}}{2} \tag{23}$$

Thus, the association error probability is mathematically obtained as:

$$P_{error}=P\left(e\middle|\tau_{12,[s]}^{a}\right)+P\left(e\middle|\tau_{12,[s]}^{b}\right) \tag{24}$$

where $P\left(e\middle|\tau_{12,[s]}^{a}\right)$ and $P\left(e\middle|\tau_{12,[s]}^{b}\right)$ are obtained from Equations 21 and 22 respectively.

The performance of an association algorithm is evaluated using the probability of correct association $(P_{correct})$ and is obtained from P_{error} in Equation 24 using Equation 25.

$$P_{correct}=1-P_{error} \tag{25}$$

In the next section, the evaluation of the performance of an association algorithm based on $P_{correct}$ is presented considering certain aircraft positions.

4. SIMULATION RESULTS AND DISCUSSION

This section evaluates the capability of a TDOA-based association algorithm using the technique presented in Section 3 to associate estimated TDOAs to the correct aircraft. The performance is quantified by the probability of correct PE of individual aircraft locations by a TDOA-based locating system.

4.1 Simulation Parameters

As mentioned in Section 1, military aircrafts fly in close formation, which contributes to association error. Thus, the analysis considers aircraft locating in various military operating scenarios. The aircraft locating capability of the TDOA-base system coupled with the association algorithm is compared with the ADR since it is designed specifically to locate military aircrafts. Table 1 shows the range, azimuth and elevation accuracies of the ADR based on 90% probability of detection.

Table 1: ADR aircraft locating accuracy (Martin, 2018).

Parameters	Values
Range accuracy	50 m
Azimuth accuracy	0.22°
Elevation accuracy	0.28°

The parameters shown in Table 1 describe how well the ADR accurately estimates the aircraft position. The range accuracy of the ADR indicates the minimum range separation between aircraft on the same FL that it can accurately differentiate and locate. The use of pulse compression technology allows a range of accuracy of about 50 m. This is achieved by the choice of modulation (frequency or phase), sub-pulse duration and bandwidth (Skolnik, 2009). As for the azimuth and elevation accuracy, they are respectively the minimum distance and FL between two aircrafts at the same range that the ADR can distinguish and separate. Both the azimuth and elevation accuracy are functions of the

aircraft range from the ADR system. For instance, at a range of 100 km, the minimum distance and FL between a pair of aircraft that the ADR can distinguish are 383 m and 1,603 m respectively.

The parameters of the aircraft transponder, WCR, and ground-based system considered for the analysis are shown in Table 2. For the aircraft transponder, it is considered to have a downlink frequency of 1,090 MHz connected to an antenna with a gain of 3 dBi (Sha'ameri et al., 2015). A transponder transmit power of 250 W is chosen as it is commonly used onboard aircrafts capable of flying above 15,000 ft (Francis *et al*., 2011). As for the WCR, emissions through the main and side lobes of the antenna are considered with gains of about 35 and -15 dBi respectively (Ahmad & Sha'ameri, 2015). The peak power of a WCR could be within a range of 5 to 20 kW. However, this paper considered a peak power of 10 kW (Ahmad & Sha'ameri, 2015). The system parameters presented in Table 2 are chosen to conform to both civilian and military surveillance purposes. Free space path loss propagation model is used for the SNR calculation. This is because at the operational FLs (above 15,000 ft) of the aircraft, line of slight (LOS) exists between aircraft and GSA (Yaro & Sha'ameri, 2018).

Table 2: Transmitter and receiver parameters (Francis *et al*., 2011; Ahmad & Sha'ameri, 2015).

Parameters				Values
Aircraft	WCR	Antenna gain	main lobe	35 dBi
			side lobe	-15 dBi
		Peak transmit power		10 kW
		Operating frequency		8 to 12 GHz
	transponder	Antenna gain		3 dBi
		Peak transmit power		250 W
		Operating frequency		1090 MHz
Ground system		Antenna gain		12 dBi
		Sensitivity		-95 dBm
		Antenna height		200 m

Three flying formations are considered as shown in Figure 2. In Figure 2a and Figure 2b, both fighters are on the same FLs, but are separated in range by about 50 m as shown in Figure 2a, while are separated as shown in Figure 2b in azimuth (side by side) at the same range by about 50 m (Alcatraz, 2016). As for flying formation C, as indicated in Figure 2c, both fighters are at the same range, but are separated in altitude by about 1,000 ft (300 m) (FAA, 2014). For each of the flying formations in Figure 2, the probability of correct association of the estimated TDOAs obtained from the fighter emission is determined for horizontal ranges within 200 km from the TDOA-based locating system at intervals of 20 km.

4.2 TDOA-Based Association Performance Validation

By varying γ_{eff} from 0 to 70 dB, the relationship between $\sigma_{\tau,[s]}$ and γ_{eff} in Equation 15 is determined and presented in Figure 3. This is to determine the minimum effective SNR (MES) for a given aircraft pair separation at which an association error occurs. The value $\sigma_{\tau,[s]}$ decreases exponentially with γ_{eff} from 0 to 61 dB, with $\sigma_{\tau,[s]}$= 0 nsec at γ_{eff} > 61 dB. At γ_{eff} values of 20, 40 and 65 dB, the numerical values of $\sigma_{\tau,[s]}$ are 30, 3 and 0 nsec respectively. For a given aircraft pair separation in which $\sigma_{\tau,[s]}$ = 30 nsec, the MES for correct TDOA association is γ_{mes}= 20 dB based on the results presented in Figure 3. This means that when γ_{eff} of the fighter emissions received are below 20 dB, an association error will occur as indicated in Equation 18. For the aircraft pairs with $\left|\tau^{a}_{12,[s]} - \tau^{b}_{12,[s]}\right|$ = 3 nsec and $\left|\tau^{a}_{12,[s]} - \tau^{b}_{12,[s]}\right|$ = 0 nsec, the MESs for correct TDOA association are γ_{mes}= 40 dB and γ_{mes} = 65 dB respectively.

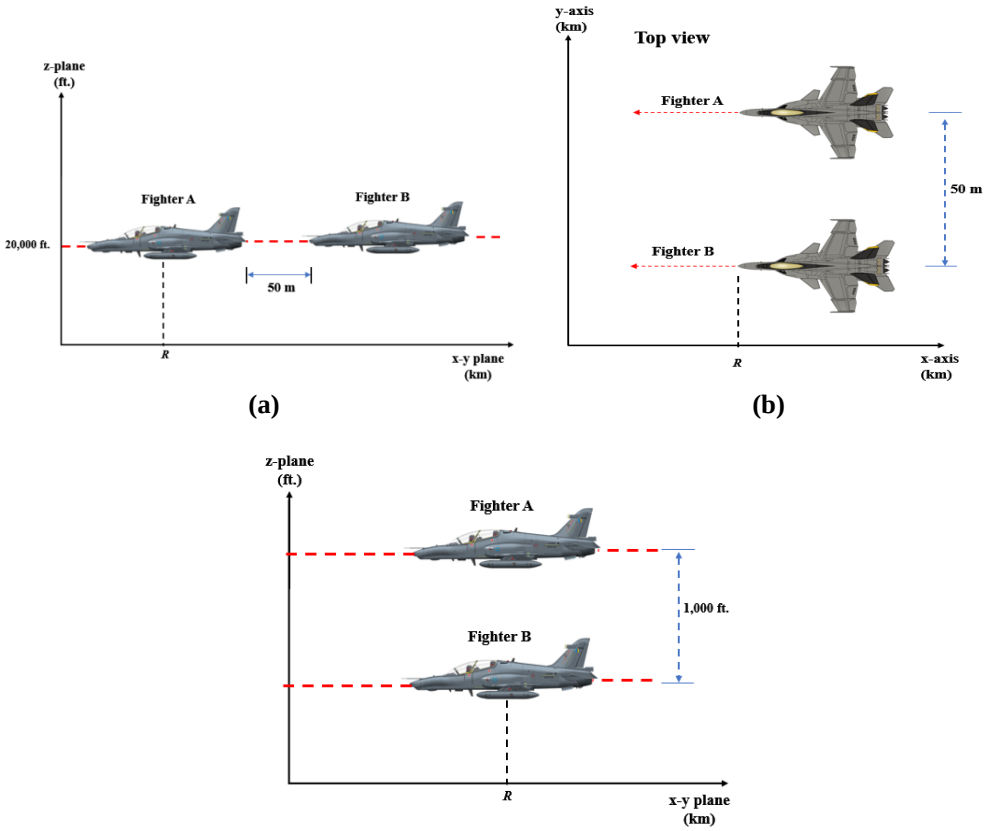

Figure 2: The three military flying formations: (a) Flying formation A (b) Flying formation B (c) Flying formation C.

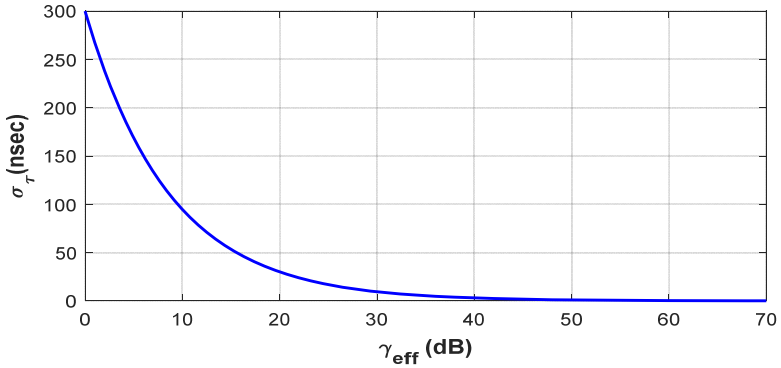

Figure 3: The relationship between $\sigma_{\tau,[s]}$ and SNR.

4.2.1 Probability of Correct Association Based on Flying Formation A

From Figure 2a, the $\sigma_{\tau,[s]}$ = 0 nsec irrespective of horizontal range of the fighters from the locating system. This corresponds to γ_{mes}= 62 dB from Figure 3. To correctly associate the estimated TDOAs to each fighter, $\gamma_{eff} \geq \gamma_{mes}$ = 62 dB while an association error occurs when $\gamma_{eff} < \gamma_{mes}$. Hence, the probability of correct TDOA association is determined based on the approach presented in Section 3.3. Table 3 gives the summary of γ_{mes}, γ_{eff} and $P_{correct}$ based on an SSR transponder reply and WCR emissions for the fighters flying in formation A.

Table 3: TDOA association performance based on flying in formation A.

Target range (km)	γ_{mes} (dB)	SSR based transponder		WCR			
				Main lobe		Side lobe	
		γ_{eff} (dB)	$P_{correct}$ (%)	γ_{eff} (dB)	$P_{correct}$ (%)	γ_{eff} (dB)	$P_{correct}$ (%)
20	62	45	0	≥ 62	100	24	0
40		39	0		100	18	0
60		36	0		100	14	0
80		33	0		100	12	0
100		31	0	60	57	10	0
120		30	0	58	28	8	0
140		28	0	57	16	7	0
160		27	0	56	9	6	0
180		26	0	55	6	5	0
200		25	0	54	4	4	0

The value of γ_{eff} for both the SSR reply and WCR emissions decreases with the horizontal range of the fighters from 20 to 200 km. At horizontal ranges of 40 and 140 km, γ_{eff}= 39 dB and γ_{eff}=38 dB respectively for the SSR reply. As for emissions from the main lobe of the WCR antenna, $\gamma_{eff} \geq 62$ dB and γ_{eff}=57 dB respectively, while γ_{eff}= 18 dB and γ_{eff}=7 dB for emissions from the side lobe of the WCR antenna. Within the 200 km radius of the locating system, $P_{correct}$= 0% for the association algorithm using the emission in response to the SSR interrogator. This means that for fighters flying in formation A and the emissions detected at the GSAs as replies to the SSR interrogator, the algorithm is not able to associate the estimated TDOAs to the correct fighter. Thus, the TDOA based locating system cannot correctly resolve the individual positions of each fighter.

As for WCR emissions, the association algorithm has $P_{correct}$= 100% within 80 km for emissions from the main lobe of the antenna, while within the 200 km, $P_{correct}$= 0% for emissions from the side lobe of the antenna. In summary, the TDOA based locating system accurately estimates the individual locations of the fighters using emissions from the main lobe of the WCR antenna for up to about 80 km horizontal range. This is because beyond the 80 km horizontal range, the γ_{eff} of the received emission is less than the γ_{mes}.

Comparing the locating performance of the TDOA based system with the ADR, the horizontal range accuracy of the ADR is about 50 m at 90% probability of detection. This means that within the 200 km radius, the ADR can individually locate each of the fighters flying in formation A, whereas the TDOA-based system can only locate within 80 km using emissions from the main lobe of the WCR antenna.

4.2.2 Probability of Correct Association Based on Flying Formation B

As the fighter horizontal range increases from 20 km to 200 km, $\sigma_{\tau,[s]}$ decreases. This means that γ_{mes} increases. Table 4 gives the summary of γ_{mes}, γ_{eff} and $P_{correct}$ based on the SSR transponder reply and WCR emissions for the fighters flying in formation B. Using the fighters' SSR interrogator reply transponder emissions, $P_{correct}$= 100% within 120 km. This means that the association algorithm can accurately associate the estimated TDOAs to each fighter flying in formation B within 120 km coverage. As for the estimated TDOAs obtained from the emissions of the WCR, $P_{correct}$= 100% within 200 km for emissions from the main lobe of the antenna, while $P_{correct}$= 100% within 20 km for emissions from the side lobe of the antenna.

Table 4: TDOA association performance based on flying in formation B.

Target range (km)	γ_{mes} (dB)	SSR based transponder		WCR			
				Main lobe		Side lobe	
		γ_{eff} (dB)	$P_{correct}$ (%)	γ_{eff} (dB)	$P_{correct}$ (%)	γ_{eff} (dB)	$P_{correct}$ (%)
20	14	45	100	≥ 62	100	24	100
40	20	39	100		100	18	98
60	24	36	100		100	14	67
80	27	33	100		100	12	44
100	28	31	100	60	100	10	29
120	30	30	100	58	100	8	19
140	31	28	97	57	100	7	15
160	33	27	90	56	100	6	12
180	34	26	81	55	100	5	9
200	35	25	71	54	100	4	7

The azimuth accuracy of the ADR depends on the range of the fighter from the ADR. Table 5 shows the minimum azimuth separation between fighters for different horizontal ranges within 200 km. The azimuth separation increases with the horizontal range. At horizontal ranges of 40, 80 and 160 km, the azimuth separations are 154, 307 and 614 m respectively. This means that at a horizontal range of 40 km with fighter flying in formation B, the ADR can individually determine the positions of each target if they are separated by at least 77 m. As for fighters at 80 and 160 km, the minimum separation that the ADR can individually determine their positions are 307 and 614 m respectively. With a 50 m fighter azimuth separation as shown in Figure 2b, the ADR cannot individually estimate the positions of each fighter as it is less than its minimum azimuth separation.

Table 5: ADR's minimum azimuth separation.

Horizontal range (km)	20	40	60	80	100	120	140	160	180	200
Minimum azimuth separation (m)	77	154	230	307	383	461	537	614	691	767

4.2.3 Probability of Correct Association Based on Flying Formation C

Table 6 gives the summary of γ_{mes}, γ_{eff} and $P_{correct}$ based on the SSR transponder reply and WCR emissions for the fighters flying in formation C. The value of γ_{mes} differs for each fighter horizontal ranges. At horizontal ranges of 80, 140 and 180 km, $P_{correct}$ is 100, 48 and 23% respectively using the emissions in response to the SSR interrogator by the fighters. Within a 80 km coverage, $P_{correct}$ = 100%, which means the association algorithm accurately grouped the estimated TDOAs obtained using the transponder emission in response to the SSR interrogator.

Extending the analysis to the associating estimated TDOAs obtained using the WCR emissions, $P_{correct}$ = 100% within 200 km using the emissions from the main lobe of the WCR antenna. However, using emissions from the side lobe, $P_{correct}$ = 100% only within 20 km. This means that the TDOA-based locating system coupled with the association algorithm can accurately locate each of the fighters up to a range of 200 km using their WCR emissions from the main lobe of the antenna. As for using the emissions from the side lobe only within 20 km, the TDOA-based locating system can accurately estimate each of the fighters.

Table 6: TDOA association performance based on flying in formation C.

Target range (km)	γ_{mes} (dB)	SSR based transponder		WCR			
				Main lobe		Side lobe	
		γ_{eff} (dB)	$P_{correct}$ (%)	γ_{eff} (dB)	$P_{correct}$ (%)	γ_{eff} (dB)	$P_{correct}$ (%)
20	9	45	100	≥ 62	100	24	100
40	19	39	100		100	18	99
60	27	36	100		100	14	54
80	33	33	100		100	12	26
100	36	31	93	60	100	10	13
120	38	30	74	58	100	8	7
140	43	28	48	57	100	7	5
160	49	27	33	56	100	6	3
180	52	26	23	55	100	5	2
200	54	25	17	54	100	4	1

Table 7 shows the relationship between the fighter horizontal range and minimum altitude separation between the fighter pair that the ADR can resolve. The minimum altitude separation increases with horizontal range from 20 to 200 km. At fighter horizontal ranges of 20, 60, 100, 160 and 200 km, the minimum altitude separations of the ADR are 320, 96, 1,603, 2,565 and 3,207 ft respectively. With a fighter altitude pair separation of 1,000 ft based on flying formation C, the ADR accurately estimates each of the fighters up to a range of 60 km.

Table 7: ADR minimum altitude separation variation with horizontal range. The red shade indicates fighter horizontal range with altitude pair separation greater than the minimum altitude separation of the ADR.

Horizontal range (km)	20	40	60	80	100	120	140	160	180	200
Minimum altitude separation (ft)	320	641	961	1,283	1,603	1,924	2,245	2,565	2,886	3,207

5. CONCLUSION

In this paper, a technique to verify the accuracy of a TDOA-based association algorithm measured from the emissions of a pair of fighters flying in close formation is presented. The probability of correct TDOA association is used as the performance measure and is compared with the ADR in terms of aircraft locating. Three fighter formations are considered, in which the horizontal and azimuth separations are about 50 m, while the altitude separation is about 1,000 ft. With regards to the source of emissions for TDOA estimation and association, emissions from the fighter's transponder in respond to the SSR interrogator and that from the WCR onboard the fighters are considered. Based on the range, azimuth and altitude separations considered, the proposed technique shows that the TDOA association algorithm has the best association performance using emissions from the main lobe of the WCR. Using the emissions of the main lobe, the TDOA-based target locating system can accurately locate each fighter flying with a minimum azimuth and altitude separation of 50 m and 1,000 ft respectively for up to a range of 200 km. As for the fighters having a range separation of 50 m, the system accurately estimates the location of each fighter up to a maximum range of 60 km. As compared to the ADR, its best performance is resolving fighters with a 50 m range and 1,000 ft altitude separation up to about 60 km, but cannot resolve fighter pair having 50 m azimuth separation. The results verify that the technique can be used in determining the TDOA association capability of the association algorithm given the locations of the fighter and the received SNR of their emissions.

ACKNOWLEDGMENT

The authors thank Universiti Teknologi Malaysia (UTM) for providing the resources and support for this research.

REFERENCES

Abdulaziz, A., Yaro, A.S., Ahamd, A.A., Tukur, K.M. & Habeeb, S.B. (2015). Optimum receiver for decoding automatic dependent surveillance broadcast (ADS-B) signals. *Am. J. Signal Process.*, **5**: 23–31.

Ahmad, A.A. & Sha'ameri, A. Z. (2015). Classification of airborne radar signals based on pulse feature estimation using time-frequency analysis. *Defence S&T Tech. Bull.*, **8**: 103–120.

Alcatraz, D. (2016). From a *Strategic Point of View, What is the Importance of Different Flying Formations*? Available online at: https://www.quora.com/From-a-strategic-point-of-view-what-is-the-importance-of-different-flying-formations (Last access date: 7 January 2019).

CANSO. (2016). *ANSP Guidelines for Implementing ATS Surveillance Services Using Space-Based ADS-B*. Amsterdam Airport Schiphol, Netherlands. Available online at: https://www.canso.org/sites/default/files/ANSP Guidelines for Implementing ATS Surveillance Services Using Space-Based ADS-B.pdf (Last access date: 7 January 2019).

Christian, W. (2018). Database of Radars. Available online at: http://www.radartutorial.eu/19.kartei/ka01.en.html (Last access date: 24 July 2018).

FAA. (2014). *Advisory Circular AC91-4: Reduced Vertical Separation Minimum (RVSM)*. Available online at: https://www.caa.govt.nz/Advisory_Circulars/AC091_4.pdf (Last access date: 7 January 2019).

Francis, R., Vincent, R., Noël, J.-M., Tremblay, P., Desjardins, D., Cushley, A. & Wallace, M. (2011). The flying laboratory for the observation of ADS-B signals. *Int. J. Nav. Obs.*, **Vol. 2011**: Article ID 973656.

Galati, G., Leonardi, M., Mantilla-Gaviria, I.A. & Tosti, M. (2012). Lower bounds of accuracy for enhanced mode-S distributed sensor networks. *IET Rad. Son. Nav.*, **6**:190-201.

IATA (2017). *2036 Forecast Reveals Air Passengers Will Nearly Double to 7.8 Billion*. Available online at: https://www.iata.org/pressroom/pr/Pages/2017-10-24-01.aspx (Last access date: 23 July 2018).

ICAO (2014). *Guidance Material: Security Issues Associated With ADS-B*. Available online at http://www.atlascorporation.ro/upl/documents/01gd_security_adsb.pdf?time=1520398061 (Last access date: 7 January 2018).

ICAO (2016). *Doc 4444: procedures for air navigation services air traffic management*. Montréal, Quebec, Canada. Retrieved from http://flightservicebureau.org/wp-content/uploads/2017/03/ICAO-Doc4444-Pans-Atm-16thEdition-2016-OPSGROUP.pdf

Li, H. & Li, C. (2014). TDOA based data association and multi-targets passive localization algorithm. *7th Int Cong. on Imag. and Sig. Process,* Dalian, China, pp. 1120-1124.

Li, X., Yao, W., Zhu, L., Wang, X. & Yu, J. (2016). Ground target localization algorithm for semi-active laser terminal correction projectile. *Def. Tech.,* **12**: 234–241.

Lopez-Risueno, G., Grajal, J. & Sanz-Osorio, A. (2005). Digital channelized receiver based on time-frequency analysis for signal interception. *IEEE Trans. Aerosp. Electron. Syst*, **41**: 879–898.

Marmaroli, P., Falourd, X., & Lissek, H. (2012). A comparative study of time delay estimation techniques for road vehicle tracking. In *11th French Cong. of Acoust. & 2012 Annual IOA Meeting* (pp. 136–140). Nantes, France.

Martin, L. (2018). TPS-77 multi-role radar system. Available online at: https://www.lockheedmartin.com/en-us/news/features/2017/rms-completes-production-of-tps-77-mrr-its-first-multi-role-surveillance-radar.html (Last access date: 24 July 2018).

Neven, H.L.W., Quilter, J.T., Weedo, R. & Hogendoorn, R.A. (2005). *Wide Area Multilateration (WAM)*, No. Report on EATMP TRS 131/04 Version 1.1, Eurocontrol, Brussels.

Ni, L., Gao, S., Feng, P. & Zhao, K. (2013). Rough sets probabilistic data association algorithm and

its application in multi-target tracking. *Def. Tech.*, **9**: 208–216.
Ray, E.L. (2015). *Air Traffic Organization policy: Order JO 7110.65W*. Department of Transportation, Federal Aviation Administration, US.
Reale, J. F., Huie, L. M., & Fowler, M. L. (2013). Locating closely spaced coherent emitters using TDOA techniques. *Asilomar Conf. Sig. Sys. Comp*., Pacific Grove, California, pp 2060-2064.
Sha'ameri, A. Z., Yaro, A. S., & Astuti, W. (2015). Performance analysis of a minimum configuration multilateration system for airborne emitter position estimation. *Defence S&T Tech. Bull.*, 8: 27–41.
Skolnik, M. I. (2009). *Introduction to Radar Systems*. McGraw-Hill, New York.
Stein, S. (1981). Algorithms for ambiguity function processing. *IEEE T. Acoustics Speech Signal Proces.*, **29**: 588–599.
Strohmeier, M., Schäfer, M., Lenders, V. & Martinovic, I. (2014). Realities and challenges of nextgen air traffic management: The case of ADS-B. *Int. Conf. Mag.*, **52**: 111–118.
UPI Archives. (1992). Suspicious fire causes $21 million of damage at Malaysian airport. Available online at https://www.upi.com/Archives/1992/10/15/Suspicious-fire-causes-21-million-of-damage-at-Malaysian-airport/4950719121600 (Available online at 31 July 2018).
Yaro, A.S. & Sha'ameri, A.Z. (2018). Effect of path loss propagation model on the position estimation accuracy of a 3-dimensional minimum configuration multilateration system. *Int. J. Integrated Eng.*, **10**: 35–42.
Yaro, A.S., Sha'ameri, A.Z. & Kamel, N. (2017). Ground receiving station reference pair selection technique for a minimum configuration 3D emitter position estimation multilateration system. *Adv. Electr. Electron. Eng.*, **15**: 391–399.

A REVIEW OF COPTER DRONE DETECTION USING RADAR SYSTEMS

Surajo Alhaji Musa[1,3], Raja Syamsul Azmir Raja Abdullah[1*], Aduwati Sali[1], Alyani Ismail[1], Nur Emileen Abdul Rashid[2], Idnin Pasya Ibrahim[2] & Asem Ahmad Salah[1]

[1]Wireless and Photonics Networks (WIPNET) Research Centre, Computer and Communication System Engineering University Putra Malaysia (UPM), Malaysia
[2]Electrical Engineering Department University Tekologi MARA (UiTM), Malaysia
[3]Computer Engineering Department, Institute of Information Technology Kazaure, Nigeria

[*]Email: r_syamsul@upm.edu.my

ABSTRACT

The exponential growth of copter drone usage and the threats posed by drone users, such as unauthorised imaging and filming in restricted areas, illegal surveillance, air collisions, drug smuggling, terrorist attacks, and radio frequency (RF) jamming, have led to many efforts and research projects aimed at drone detection. The attempted methodologies include using acoustics, cameras, cascades (audio-visual) and radio frequency. In addition, there are the nontechnical methods such as shooting and netting. This paper presents radar systems as a method for copter drone detection. It presents the state of the art review of the efforts so far made towards detecting drones given preference to radar systems for micro-Doppler-based analysis. It also introduces passive forward scatter radar (PFSR) as an emerging methodology, presenting its reported achievements for both ground and airborne target detection. In an attempt to improve the detection of low-profile targets, this paper discusses the basic parameters aiding Doppler and micro-Doppler analysis of a copter drone. The paper concludes by proposing digital video broadcasting satellite (DVBS) based PFSR for drone detection due to its improved capabilities, thereby making micro-Doppler analysis for a low-profile target, a feasible endeavour.

Keywords: *Micro-Doppler; passive forward scattering radar (FSR); drone; low-small-slow (LSS); radar cross section (RCS).*

1. INTRODUCTION

Radar, which is an acronym for "Radio Detection And Ranging," is an electronic device designed to detect an object, usually called a target, at a predefined distance (De Luca *et al*., 2015) and is achieved by transmitting radio frequency at the speed of light and echoing a reflection from the referenced target at a distance that a normal eye (unaided) cannot see. At the same time, radar can estimate the distance of the object (Abdullah & Ismail, 2006). The history of radar can be traced as far back as the year 1800 from an experiment conducted by Michael Faraday, who proved that an electric current can produced a magnetic field that returns the energy contained in this field to the circuit even if the current is absent (Willis, 2005). James Maxwell, Christian Hulls Meyer and Gughelmo Marconi formed the vanguard studying this magnetic field and its applications (e.g., radar), leading to the 1922 studies on the observed issues of radar effects by Dr. Albert Taylor of the Naval Research Laboratory (NRL) in Washington D.C. Resulting from an NRL test conducted in 1930, the emergence of the use of co-located transmitters and receivers was a breakthrough for tracking aircraft and ships after the observation that a plane flying through a beam generated by a transmitter distorts the signal. Thus, the finding led to a competitive experimental approach among the USA, UK, Soviet Union, France, Italy, Germany and Japan.

World War II was an avenue of exploration for radar applications, initially as a defensive weapon, but later became an automatic aircraft tracking device (De Luca *et al*., 2015). Despite the low frequency and other attributed limitations of the very-high-frequency (VHF) band, it formed the basic building blocks of radar technology prior to its application for war. Although radar applications were explored

for military uses, progress in radar technology diversified to civil marine and other civilian applications (Willis, 2005). Recently, the popularity of using various illuminators of opportunities (passive) for target detection and classification were explored by many scholars, ranging from monostatic to bistatic approaches, as illustrated in Figure 1. The use of illuminators in a passive bistatic approach (PBR), such as a global navigation satellite system (GNSS) (Golabi *et al*., 2013), long-term evolution (LTE) signal WIFI-based (Hassan & Mazhar, 2016), digital video terrestrial broadcast (Peto & Seller, 2016), digital audio broadcast (DAB) (Weiß, 2014) and FM-based (Rao, 2016) became a boosting tool for radar worldwide, thereby making it a prominent tool for both military and civilian applications. The active radar approach, e.g., forward scatter radar (FSR) approach (see Figure 1c), formed another breakthrough as to how well the effect of the radar cross section (RCS) of the target could be minimised (De Luca *et al*., 2015). Although many implemented applications were achieved via the aforementioned approaches, exploring more advantages is of paramount importance. This exploration may involve enhancing the current radar capability by implementing the passive mode via a forward scattering approach through their bistatic characteristics and simplify target detection and/or classification (Clemente & Soraghan, 2012), hence achieving a passive FSR topology.

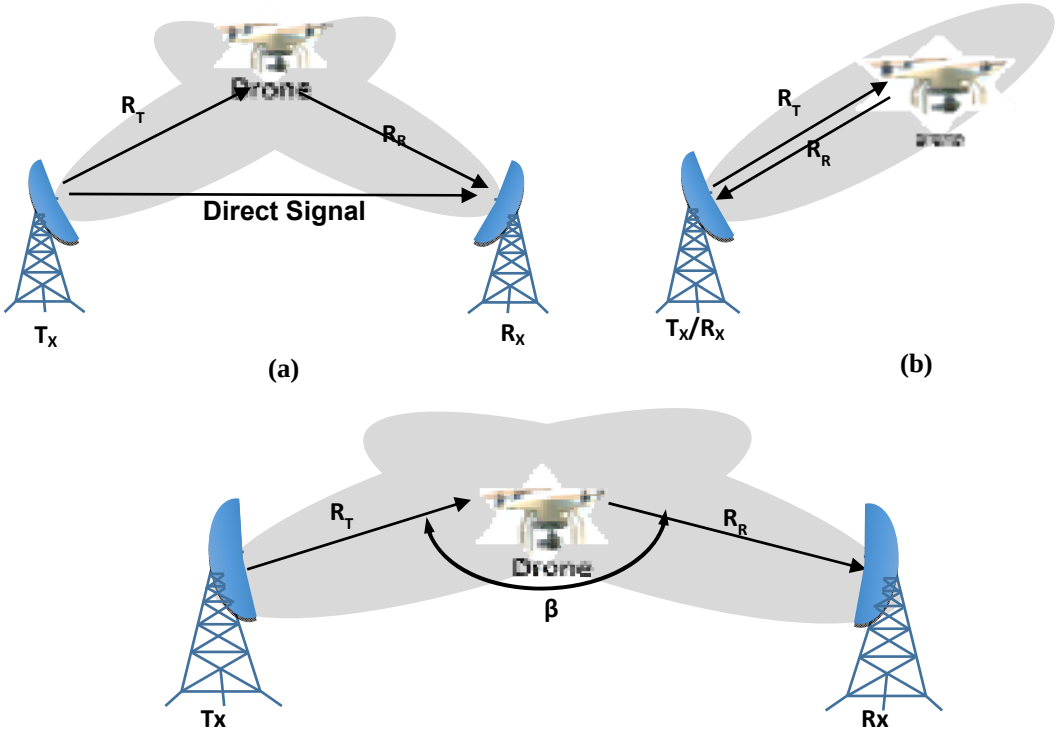

Figure 1: Radar configurations: (a) monostatic (b) bistatic (c) forward scatter.

The need for drone detection can be traced back to the increase in consumer drone usage by civilian society, apart from military applications, as a result of its low cost and operational flexibility (Ganti & Yoohwan, 2016). A drone is an ambiguous term and is synonymously used for an unmanned aerial / aircraft vehicle (UAV) because every drone can be regarded as a UAV, but not every UAV is considered to be a drone. Regulatory agencies, aircraft engineers and other stakeholders, such as the media and general public, each view drones and UAVs in their respective perspectives. The regulatory agencies consider several terms, such as unmanned aircraft systems (UAS) and remotely piloted aircraft systems (RPAS), which is a UAS subcategory. Aircraft engineers view the terms drone and UAV as interchangeable, but normally, UAV is used to differentiate a military drone from a hobbyist drone. The Federal Aviation Administration (FAA) designated UAS to describe remote-

controlled helicopters, and the Department of Defense uses UAV to define a software-controlled aircraft or balloon from a distance (Door, 2017).

Summarily, a drone may mean a non-piloted aircraft autonomously controlled via a remote on the ground or another vehicle, while a UAV is more or less a military term used to identify drone-like remote-controlled (RC) airplanes, remote-controlled piloted (RCP) aircraft and drones that have autonomous flying software (Maartens, 2015). In this paper, a drone is viewed as an UAV, usually regarded as a hobbyist drone or a copter drone, characterised by multiple rotors, such as a quadcopter, hexacopter, and octocopter (unlike a UAV with fixed wings) that is controlled by remote and/or mobile apps, can have a programmable Global Positioning System (GPS) route to follow, usually has a video camera with a live view streamed to mobile phones, and can carry a payload (Osamu, 2017). Figure 2 (a-c) portrays a typical example of copter drones while Figure 2(d) shows an example of a fixed-wing UAV.

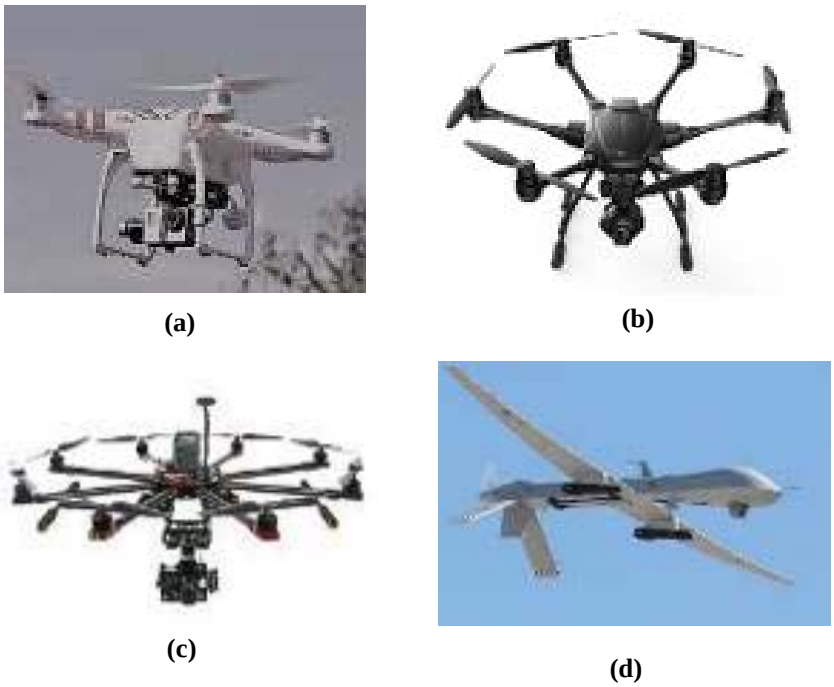

Figure 2: (a) DJI Phantom-3, (b) Yuneec Typhoon, (c) octocopter, (d) fixed-wing UAV (Sources: Dedrone, 2015; Maartens, 2015).

Drones are therefore tagged as an emerging threat for both the military and civilian domains (Ritchie, *et al*., 2015). Despite its applications in areas such as aerial imaging, monitoring, search and rescue, security surveillance, entrepreneurial hobbies (Petrides *et al*., 2017) and precision agriculture (Nguyen *et al*., 2016), drone usage has gone viral because of users' abuse of these devices for nefarious activities, such as drug smuggling, conveyance of contraband materials such as weapons (Osamu, 2017) and other significant vulnerabilities (Sturdivant & Chong, 2017), privacy violations, antisocial activities and other unsafe acts (Wit *et al*., 2012). Drones equipped with RF jammers pose challenges to GPS receivers and cell phones, and at the same time can launch a long-distance attacks while allowing the perpetrators to remain unnoticed (Hoffmann *et al*., 2016). The dangers posed by drones, according to Sziill *et al*., 2017), can crash aircrafts while taking off or landing if there is a collision or by getting sucked into a jet engine. The damage caused may be no different than a collision with birds.

As far back as 2000, a Technical Cooperative Committee (TTCP) led by the US Action Group 6 (AG6) and other countries such as the UK, Canada and Australia with some critically identified goals toward investigating and curtailing the potential dangers posed by small drones (Pham & Srour, 2004) and have

stressed the foreseen threats. The dangerous potentiality of drones was brought forward by a rogue party to Chancellor Merkel in September 2013, and many drones have been spotted near French nuclear plants, posing significant potential threats to those power plants (Busset *et al*., 2015). Figure 3 shows a photo illustration of illegal activities that have misused drones. For example, a drone was used in smuggling a package to a prison cell window (Figure 3a), while Figure 3b shows an unmanned drone that was spotted two miles from a New York airport, which seemed to be an unsafe situation, proving the potential abuse of drones (Diego & Mich, 2017). Figure 3c shows an image of recovered drugs, hacksaw blades and other destructive materials that were carried by a drone.

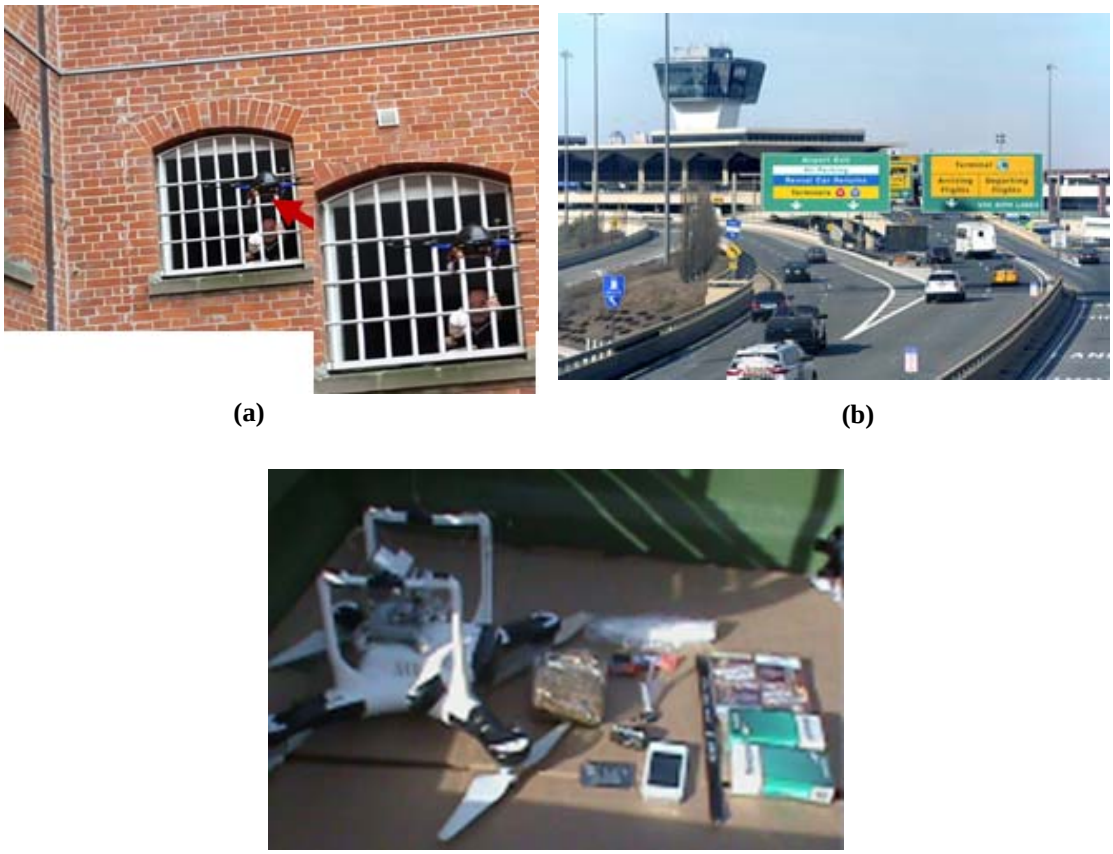

(a) **(b)**

(c)

Figure 3: (a) Drone smuggling a package to a prison (Dedrone, 2015). (b) Drone spotted around the New York Airport (Diego & Mich, 2017). (c) Drone carrying forbidden items crashed (Brandes, 2015).

A drone crashed while carrying illegal objects into Oklahoma prison and five other reported cases, in less than a month between 30 July to 19 August 2017, while 28 lb of heroin were dropped into the border town of Calexico, California. A drone was spotted by a border patrol agent swooping over the border fence. Three people were arrested after a drone dropped a cell phone and drugs into a prison yard (Dedrone, 2015). Recently, a distressful situation was caused by a sighted drone over the Gatwick airport London, causing much chaos that resulted to incoming flight diversions (BBC, 2018). In summary, the exponential increase in drone usage within the past decade poses a security challenge as a result of drone misuse and has become a matter of concern, hence mandating the need for drone detection. Although achievements have been made regarding attempts toward drone detection, some information is missed due to the target's smaller size, high speed, low altitude and disturbance caused by its blade rotation, rendering micro-Doppler analysis difficult (Clemente *et al*., 2015; Nguyen *et al*., 2016; Contu *et al*., 2017; Osamu, 2017).

The aim of this paper is to review the efforts made so far towards drone detection, thus addressing some trending challenges, by proposing an emerging passive FSR approach to improve the performance of the previous methods. Although some aspects of drone classification may yet be reported, a thorough signal processing-based classification of the drone is beyond the scope of this paper. The remainder of this

paper consist of Section 2, presenting attempted non-radar methodologies, while radar-based systems for drone detection is discussed in Section 3. An aspiring passive forward scatter radar (PFSR) methodology is discussed in Section 4, identifying the achievements so far made using this method and proposing how possible it is for use in drone detection and classification. The challenges deemed worthy of further study are presented in Section 5 followed by some recommendations. The paper thus concludes with achievements summary so far made, citing some grey areas for future studies in Section 6.

2. NON-RADAR METHODOLOGIES FOR DRONE DETECTION

This section is aimed at discussing some attempted methodologies toward drone detection, thereby highlighting the achievements made so far and suggesting the need for further studies. The methodologies to be discussed are acoustic, video, and hybrid systems, thermal and radio frequency (RF) techniques and other unclassified systems such as netting.

2.1 Acoustic Method

Acoustic means of detecting aircraft remained popular prior to the proliferation of radar technology and can be traced as far back as World War I (Becker & Güdesen, 2000; Namorato, 2000). After the formation of the Technical Cooperative Team (TTCP) led by the US action Group-6 (uAG6) of the Army Research Laboratory (ARL), the TTCP-AG6 confirmed the feasibility of detecting UAVs using acoustic sensors after collecting experimental data and signal processing of the array signal, and conducting four different experiments (Pham & Srour, 2004). Recent work by Case *et al*. (2004) also proved that commercial off-the-shelf (COTS) hardware can detect and locate the sound source of a drone. The work used a far-field antenna array, and a calibration and beamforming algorithm coupled with a relatively simple software for signal processing. To address this issue, UAV sound detection that considered audio fingerprinting and mathematical solutions via GPS technology (correlation) was adopted by Mezei *et al*. (2015). A sound sample was recorded and stored in the GPS database such that it compared / correlated every value with a newly detected sound, allowing matching based on the source of the original sound. The challenge usually faced by this method was that the stored samples have no noise content in them, unlike the detected sound, thus deforming the result obtained.

Figure 4: Array of microphone and Omni360 cameras (Source: Busset *et al*., 2015).

An array of cameras and speakers to track acoustic sound in real time was made possible by analysing the signal phases using an acoustic imaging algorithm (Figure 4), thereby following the sound source (tracking) using the tracking algorithm in Busset *et al*. (2015). The object type is identified through its sound signature extracted by a beamforming algorithm from all the tracked sounds. The obtained result so far manifested a detection range between 150 to 290 m with a 7 to 26 ha coverage area, depending on the drone type. Mezei & Molnár (2016) later improved the correlation approach in

Mezei *et al*. (2015) by introducing a noise filtering module. Normalised maximum, cross correlation, Pearson, Spearman rank, and Kendall rank correlation were used with each quadcopter, AR-drone and airplane model, thereby selecting the best correlation suitable for the target. Three other sounds compared with were an electric mower, a hairdryer and music.

The Spearman rank seemed to be the most suitable, as it yields the most impressive matching for all cases, but it is not good at identifying similar disturbing sounds, similar to the Kendall rank. The Pearson and the normalised maximum correlations were thus selected as the suitable correlation methods recommended for the selected drone. Research by Nijim & Mantrawadi (2016) was aimed at audio classification of a drone through data mining (algorithm used for pattern extraction), thereby identifying the drones from one another. The Quadcopter FPV-250 model and Quadcopter DJI Phantom-3 were the drone types used in this experiment. A data mining library stored the sounds of multiple UAV platforms. Clustering techniques were adopted for training the data during the processes. The detection is purely dependent on the UAV-generated sound, while the data bank is for classification purposes.

Detecting and thwarting a drone within an airport using a baseline concept for a system of systems (SoS) solution was introduced by Sturdivant & Chong (2017), which simply involved identifying the already existing independent systems within the airport premises and integrating them to work as one through system architecture using ilities (SAI). In Vilimek & Burita (2017), a proposed designed algorithm for UAS detection highlighted some identified opportunities for improving the system based on the evaluated algorithm parameters. The newly developed system recognises sound irrespective of its source hence there is need to improve for sound identification coming from different sources. It claimed that linear predictive coding (LPC) coefficients can be used to identify copter UAS and may be improved by connecting the system database.

2.2 Video (Appearance) Method

An attempt was made based on video imaging to overcome the problem of detecting a small moving object appearing in a complex background with a single moving camera. The method involved the object's appearance and motion cues as illustrated in Figure 5 (Rozantsev *et al*., 2015). An object-centric motion was developed to compensate for the changes in the object and the background appearance. This approach can potentiality be used for collision avoidance in addition to detection and can therefore improve a vision-guided tracking algorithm. Hence, this feature gave the method an upper hand when compared with other state-of-the-art techniques. The advanced version of this method used a single moving camera to film and record the object occupying a small portion of the field view (Rozantsev *et al*., 2017).

(a) **(b)**

Figure 5: Detecting a small drone against a complex moving background: (a) Drone almost invisible to the human eye. (b) Proposed motion clues algorithm make the drone visible (Source: Rozantsev *et al*., 2015).

Three approaches (appearance-, motion- and hybrid-based methods) are the approaches adopted so far. The appearance-based method (which relies on machine learning) is considered when the object is clearly visible and large, whereas the motion-based method relies on background subtraction and optical flow, while the hybrid approach combines both. Background subtraction was found to be best when the camera is static or in slow motion, while the optical flow depends on the quality of the flow vector. The results proved that temporal information from a sequence of frames has a great impact toward detecting and tracking a small, fast-flying moving object. An object-centric learning-based motion was therefore developed to compensate for both object and motion appearance. A Pan-Tilt-Zoom (PTZ) camera based convolutional object detectors was used by Park *et al*. (2017) for real time drone detection. Six convolutional object detectors were compared based on their speed and accuracy. Once a trace of drone presence was detected, a command will be sent to the PTZ camera to track the detected drone, and maintain the horizontal and vertical field of view (FoV) using the calculated zoom action. Faster region-based convolutional neural network (R-CNN) was considered the best in term of accuracy of *F* measures but slowest, while solar system dynamics (SSD) with Mobile-Net is better in term of speed. Aker & Kalkan (2017) further introduced a convolutional neural network (CNN) for drone localisation within a video frame through training the network with artificial dataset of real drone and images of birds.

2.3 Radio Frequency (RF) Method

The lack of an automatic, cost-effective approach for drone detection was addressed in Nguyen *et al*. (2016). The adopted approaches involved continuous transmission of wireless signals and then listening to the reflected component (active) from the detected drone (Figure 6). The second was based on tracking the RF transmission between the drone and its controlled point (passive), which after analysis concluded the detection of a drone via its signature. COTS technologies involving WIFI and software-defined radios (SDR) were implemented in this work, and a subsequent number of conducted experiments addressed the challenges. Both the active and passive approaches presented promising results, with few challenges having to be subsequently addressed. In addition, RF was used to detect and classify a DJI Phantom 4 from other micro-drones (Osamu, 2017).

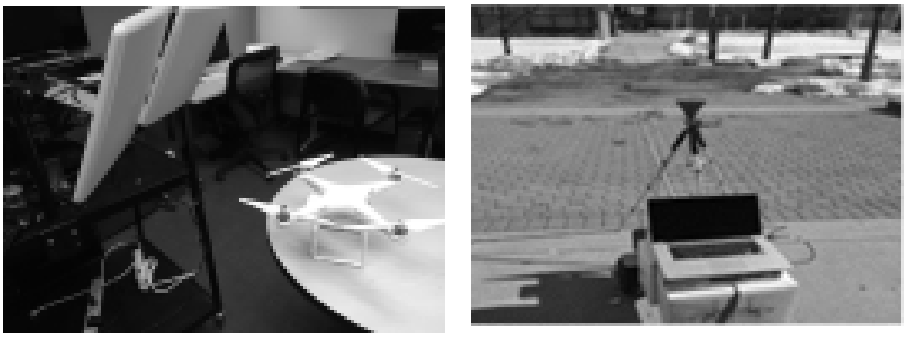

(a) **(b)**

Figure 6: Experimental setup to validate the feasibility of drone detection by using an RF signal in the (a) active and (b) passive approaches (Source: Nguyen *et al*., 2016).

The author adopted three stages, i.e., detection, location and mitigation of the RF communication link. The received signature was matched with the bank of signatures stored, using a banded search software. The result seems to be successful, while some remaining challenges include the fact that new emerging drones face some complications while operating with the 2.4 GHz ISM band, and some drones do not emit RF signals while operating. This setup is considered to be less expensive, with only three sensors to geolocate a drone and isolate the signal via the proposed software. Basak & Scheers (2018) described how a mini-RPAS system can be localised through estimation of its direction of arrival (DoA). This was made possible by passively detecting the position of the drone and that of the operator using spectrum sensing techniques through their two-way radio control

communication. The DoA can be estimated through direction finding algorithm, and thus localisation was achieved via the triangulation method.

2.4 Hybrid Method

An acoustic system plays a vital role towards the detection of a small drone, although a camera was sometimes implemented as well to optimise the detection performance. A hybrid approach of acoustic and camera methods (Nguyen *et al*., 2016) demonstrates a cost-effective method with a kind of robustness in drone detection. As an alternative, a cascaded audio-visual involving image processing and mechanical tracking are the two hybrid methodologies as applied in Ganti & Yoohwan (2016). The proposed system consisted of a camera, microphone, tracking mechanism, software and hardware module, and a single computer for image processing. The parameters under surveillance were the drone motion when the UAS occupies more than the threshold amount of the pixels, sound and colour.

Figure 7: System view of a camera array coupled with microphones mounted on the frame for large-scale surveillance (Source: Liu *et al*., 2017).

The description made Sedunov *et al*. (2016) (which is focused on aircraft detection) is relevant in this review paper due to the concerns regarding the low-flying characteristics of the target and the acoustic nature of the system. Autonomously powered clusters of microphone sensors, a pre-processing system and a camera formed the basic building blocks of the entire system. Acoustic aircraft detection (AAD) was deemed successful in tracking the detected target (a low-flying aircraft) as well as classifying it in real time. Research by Liu *et al*. (2017) demonstrated the ability of a camera array for large-scale airspace surveillance coupled with microphones to serve as a detector for a Phantom 4 drone (Figure 7). This setup was achieved by implementing 30 high-resolution cameras and three microphones mounted on a hemispherical frame, with sets of four cameras integrated into a workstation to provide a complete coverage of the sky. The method was considered to be more accurate than the visual-feature-based method.

2.5 Other Methods

There have been several other methods adopted, among which some involved non-technical approaches, such as shooting down the drone (Schulman *et al*., 2014). Others achieved detection by using a drone machine access code (MAC) address, allowing detection to be possible as described in Peacock & Johnstone (2013). After presenting other approaches, video, acoustic, RF, etc., the net-shooting method was among the reviewed methods in Sathyamoorthy (2015), whereby netting can be implemented at restricted sites such that the drone can be under surveillance and simply brought down

when sighted as described in Figure 8. Schaaf (2014) presented countermeasures for a future missile threat extending to 2040. The countermeasures were made possible by shooting a laser beam to disable the operating drone in addition to specially trained eagles (BBC, 2018). Electronic means can also be used to hack the control mechanism of approaching drones (Pleban *et al*., 2014), and drone localisation can also be deceived by GPS spoofing, as reported in Humphreys (2015). In an attempt to showcase an alternative to radar airspace surveillance implementation, Boddhu *et al*. (2013) used a software-based intelligent smartphone application capable of a capturing drone's attribute, thereby predicting the possible path and direction of a hostile drone.

(a) **(b)**

Figure 8: A Malou Tech MP200 interceptor UAV: (a) A net to intercept the drone. (b) Interceptor catching the intruding drone (Source: Humphreys, 2015).

The advantages of this approach were demonstrated in cities by humans on the ground with personal hand-held smartphones that were preinstalled with UAV-T flight path (Figure 9). Detection was achieved simply by having either the operator sense a UAV or being notified by the software that another person nearby sensed a UAV. Once the UAV was spotted, the apps will be launched and start tracking after inputting the pre-installed general direction vector, a back-facing camera view will then appear, allowing the user to view the flight route, and even snap pictures or record flight activities (Boddhu *et al*., 2013).

(a) **(b)** **(c)** **(d)**

Figure 9: UAV-T flight path app: **(a) Home Screen (b) Dialog Setting (c) Data Record Screen (d) User observational data input Screen (Source: Boddhu *et al*., 2013).**

3. RADAR FOR DRONE DETECTION

The previous section elaborated on drone detection based on acoustic, video imaging, RF, thermal, software-based smartphone and other non-technical (shooting and netting) methodologies and listed some notable achievements. Nevertheless, there could be some unresolved challenges that may need attention towards small drone detection and tracking. For instance, detecting drone-generated audio frequencies (usually approximately 40 kHz) may fail due to a higher noise ratio in urban cities (Ganti & Yoohwan, 2016). Some drones have been identified that follow a predefined GPS path, and as such, there is no link to trace the RF link (Busset *et al*., 2015; Osamu, 2017). While the drone's signatures need a constant update in a referenced database, it also has become a challenging issue for RF-based systems (Osamu, 2017). Noise is another challenge due to many users of unlicensed WIFI

RF bands as described in Nuss *et al*. (2017). A target with a dynamic background suffers from few representative pixels and may be hidden in the case of camera-based detection. These methods may also have difficulty in differentiating a drone from flying birds (Busset *et al*., 2015; Ganti & Yoohwan, 2016). Ganti & Yoohwan (2016) further explained that thermal detection is less efficient because of a drone's plastic frames and minimal heat exhaust. Thus, as an alternative, a radar system is considered important due to its confirmed capability in automotive and military applications, and in dark, noisy and blurred or misty environments (Nuss *et al*., 2017; BBC, 2018). We therefore categorised the detection in terms of main Doppler and micro Doppler (drone and other airborne targets).

3.1 Main Doppler for Drone Detection by using Radar

This section presents a summary of trends of radar base systems targeted at main Doppler analysis for drone detection. Various configurations, signal processing techniques of the echoed signal and other parameters that make detection possible are all involved. For simplicity, a summary in tabular form is presented in Table 1.

Table 1: Main Doppler analysis for drone detection.

Author(s)	Configuration	Analysis
Blyakhman *et al*. (2014)	Ground-based CW-FSR	RCS analysis to improve efficiency for drone detection
Krátký & Fuxa (2015)	X-band pulse (ReVISOR) Military radar	Verified the detectability of mini-drone via RCS comparison
Jahangir & Baker (2016)	L-band holographic radar	To produce an inherent 3D multibeam surveillance sensor from 2D antenna array
Jahangir *et al*. (2017)	L-band holographic radar	To detect the main and micro Doppler of different drones over different clutter background
Drozdowicz *et al*. (2016)	35 GHz FMCW coherent radar	Speed estimation and localisation of target
Sung et al. (2016)	Keysight MXG N5182B measuring instrument	Signal analysis using pseudo-random binary sequence (PRBS) to verify detection possibility
Knoedler *et al*. (2016)	GSM based PCL using BCCH channel	Small UAV detection and localisation
Yang *et al*. (2016)	Passive radar	Processing of (OFDM) echoes of drone for detection
Ochodnický *et al*. (2017)	Ku-band battle field radar	SNR and RCS derivation for detection of multiple drone targets
Shin *et al*. (2017)	K-band FMCW radar	Fiber optics link-based distributed FMCW for drone detection
Nuss *et al*. (2017)	MIMO OFDM	Comparative measures of objects with a known RCS
Sziill *et al*. (2017)	Multistatic passive (WIFI and UHF) coupled with RF-based	Detection base on the time of arrival of the signal
Gaigals *et al*. (2017)	Compress sense passive radar	Signal processing for detection using Monte Carlo simulation
Martelli et al. (2017)	WIFI based passive radar	Drone localisation in 3D adopted from an achieved 2D small aircraft
Nakamura & Hadama (2017)	Ultra wideband (UWB) Radar	Drone features characterization under different trajectories
Fang et al. (2018)	Multistatic (MSDPR) Radar	Detection and localization of the drone
Solomitckii *et al*. (2018)	5G mm wave base stations (BSs) as Radar	For amateur drone detection
Stasiak *et al*. (2018)	Continuous wave radars in C-band	Detection comparison among the three subsystems (analog, digital and noise) radars

Jian *et al*. (2018)	C-band phase-interferometry Doppler radar	RCS estimation for Doppler and micro Doppler detection
Rzewuski *et al*. (2018)	Off-the-shelve equipment for radar application	RCS estimation
Pisa *et al*. (2018)	Monostatic radar	Carrier frequency selection for designing anti-drone radar device through RCS evaluation.

The presented radar system based methods for drone detection as depicted in Table 1 are uniquely related to feasibility of detection, tracking and localisation of the drone, all embedded to the target main Doppler. While portraying the efforts made so far within half a decade, Sung *et al*. (2016), Yang *et al*. (2016) and Gaigals *et al*. (2017) dealt with echoed signal analysis to verify the target presence and establish the detection feasibility. Others such as Blyakhman *et al*. (2014), Krátký & Fuxa (2015), Ochodnický *et al*. (2017) and Rzewuski *et al*. (2018) evaluated the target RCS by verifying the capability of the configuration used. The simulation in Solomitckii *et al*. (2018) explored how 5G mmWave base stations can be adopted for amateur drone detection. Krátký & Fuxa (2015) and Ochodnický *et al*. (2017) addressed the implementation of military radar for civilian applications.

All the presented works, except Jahangir *et al*. (2017), worked with the drone main Doppler analysis in their quest of making drone detection feasible. Although achievements were made, yet some pending challenges rendered micro Doppler analysis difficult due to the target size, speed, altitude and other factors such as the altitude and operating frequency. To serve as our reference point, some micro Doppler analyses of non-drone airborne target (e.g. aircrafts) are therefore presented.

3.2 Micro-Doppler for Drone Detection and other Airborne Targets

Until now, this paper has discussed the capability of a radar system to detect drones without delving into detail about the utilised characteristics of the drone. It focuses on a copter drone, which has a moving propeller that inherently carries Doppler information. Hence, drone detection is possible by analysing the motions and / or micro-motions apart from the main body's silhouette. Therefore, available micro-Doppler-based papers for drone detection are also discussed.

In a situation where different parts of the target produce micro-movements with respect to the main silhouette-generating centre, the resulting additional frequency modulations of the reflected wave is termed as the micro-Doppler effect (Clemente *et al*., 2013; Kamil Ba *et al*., 2015; Xia *et al*., 2016). The signal is determined by a moving or rotating part of the target that is different from the main body's motion (Harmanny *et al*., 2014). The micro-motions may involve rotation and / or vibrations (Chen, 2011; Clemente & Soraghan, 2012) due to multiple combinations of point scatterers (Cammenga *et al*., 2014). Therefore, the micro-Doppler signature forms the basic parameter used for the detection, tracking, classification and RCS analysis of drones and other airborne targets, as seen subsequently. Although there have been various micro-Doppler analyses performed so far for targets other than airborne ones, such as human gait (Zhang *et al*., 2007; Zhang & Andreou, 2008; Seifert *et al*., 2017), remote sensing (Koo *et al*., 2013; Raja Abdullah *et al*., 2017), vital sign detection (Ren *et al*., 2016), and optimised human classification (Francesco *et al*., 2017), this paper is concerned about airborne targets, specifically for the analysis of quadcopter drones. Section 3.2.1 consists of an analysis of non-drone air targets while Section 3.2.2 provides a micro-Doppler analysis attempted for drone detection.

3.2.1 Micro-Doppler Analysis of Non-Drone Air Targets

This part discusses some efforts made towards detecting and classifying airborne targets such as a helicopters via its generated micro-Doppler signals, as this can serve as a reference point when dealing with the intended quadcopter analysis. A helicopter is an airborne target that can be detected and/or classified via its extracted micro-Doppler signals, even though this seems to be less challenging looking at the two important Doppler resolution parameters of the target, i.e., size and

speed (Contu *et al*., 2017). Theoretical radar returns generated due to a rotational part of the airborne target, giving preference to the helicopter blades (Martin, & Mulgrew, 1990), describing how each blade effect changes with its distance from the centre of rotation and with its angular position with respect to time. Wavelet scales was used in Thayaparan *et al*. (2007) describing how the received radar returns were decomposed into multiple components and later reconstructed by applying an inverse wavelet transform for further time-frequency analysis. Different types of battlefield targets were identified via their generated micro-Doppler due to vibrations caused by their movement and engine speed. It was concluded that wavelet transform may be an effective tool for extracting micro-Doppler features. In Barber (2008), used a physical optics approximation to analyse a synthetic radar aperture (SAR) image produced. An analysed X-band SAR structure of an image resulting from flashes generated by a hovering helicopter revealed how the receding and leading blade edges were shifted in opposite directions and clearly portrayed the image structure of the blade rather than the cross section.

A feasibility study by Clemente & Soraghan (2012) extracted a micro-Doppler effect of a helicopter's main and tail rotor for detection and classification. A forward scattering (FS) mode was used to compensate the illuminator's setback of low power produced at the receiver output. Carmine (2014) further used physical optics to simulate an AW-109 Agusta, AH-64 Apache, a UH-60 Black Hawk and an MD 500E Defender, thereby extracting their signature via a generated micro-Doppler and validated in Clemente *et al*. (2015) experimentally using flying helicopters at Cumbernauld Airport in Scotland to analyse the helicopter's rotor blades effect on radar returns. Kamil Ba *et al*. (2015) implemented a digital video broadcast terrestrial DVBT-based method to model a multi-static scenario at the receiving end i.e. single input multiple output (SIMO) to enable a view of the micro-Doppler effect at different bistatic angles of the main and tail rotor, thereby obtaining additional information for classification. An experimental approach of the above scenario revealed that the flashes of the helicopter's main rotor blades and that of the weak tail rotor are all visible, with a time shift between the four receivers due to their different bistatic angles. It was further highlighted that the number of blades and their rotation velocities can be obtained as well through these flashes.

3.2.2 Micro-Doppler Analysis for Drone Detection

For drone micro-Doppler analysis, Park *et al*. (2012) proposed a modified Hilbert Huang transform (HHT) micro-Doppler analysis of a nonlinear, nonstationary rotating target with a small RCS. Effort was made by Wit *et al*. (2012) to provide a reliable basis for classifying different drones by adopting a coherent radar approach. His effort resulted to the ability of detecting micro-motions of a small object and its advantage in scanning a large volume of objects, irrespective of weather conditions. The method can then address some of the challenges due to the target's hidden features resulting from terrain, long buildings and a false alarm caused by flying birds. A simulated spectrogram of two blades (or an even number blades) showed symmetrical flashes, while three blades (or an odd number blades) resulted in an asymmetrical spectrum. In the resulting experiment, the Doppler features of the quadcopter blades could be extracted. However, it is difficult to be certain about the signals due to the plastic nature of the blades as compared to the metal blade of a helicopter.

New robust features could be extracted from the micro-Doppler analysis in Molchanov *et al*. (2013), who used 11 targets with an X-band continuous wave radar with a 9.5 GHz carrier. The new proposed classifier used was successful with a correct classification probability of 95% was reported. The extracted signatures using a spectrogram and cepstrogram for distinguishing flying birds from UAVs based on their generated micro-Doppler effects were described in Harmanny *et al*. (2014). Much emphasis was given to the fast classification of man-made objects, e.g., drones, from that of other targets, such as birds, in an effort to minimise track overload. The man-made object was further classified by its number of rotors, approximate size and the drone type in the second stage. The simulation of the spectrogram and cepstrogram was done for a helicopter with different rotors to confirm its capability to extract key features for visual and automatic recognition from a lifeform and low (altitude), small (RCS) and slow (speed) LSS target. Further experimental validation was then

conducted. Differentiating maneuvered motion from the ground clutter while tracking the drone was described in Hoffmann *et al*. (2016) to curtail transporting suspicious items by extracting the centroid features of the drone. Both simulated and experimental RCS of the small drone were discussed. The UAV was accurately tracked in the second scenario in the transmit-receive beam overlap region. The third scenario showed an accurate tracking following the ground truth.

Simulated and experimental validation was conducted in Ritchie *et al*. (2015) on the RCS of a DJI Phantom Vision 2, who analysed its magnetic scattering feature variation as a function of its polarisation, frequency and azimuthal angle, in addition to its material choice or effect. It confirmed that the micro-Doppler additional signatures that may be good for classification. In Ritchie et al. (2016), signatures of a hooded vulture, a Eurasian eagle owl, a barn owl and a DJI Phantom Vision-2 were compared. The receiving effect between a monostatic horizontal-horizontal (HH) and horizontal-vertical (HV), along with a coherent bistatic HH measurement of different birds and micro-drones were used to evaluate the key differences of their radar returns. The drone RCS was found to be larger than that of the barn owl but was smaller than that of the hooded vulture and the eagle owl, which may be due to the plastic nature of the drone blades that is virtually invisible to radar. A bird's wing was also observed to have a better RCS than its body and hence may be an avenue to differentiate a bird from a drone. In the quest of improving the previous systems despite their acknowledged achievements, passive FSR is worth considering and may be an avenue of taking forward the previous system.

4. PASSIVE FORWARD SCATTERING RADAR (PFSR) TECHNIQUE

This section introduces an improved methodology that involves a passive transmitter (using an illuminator of opportunity) coupled with a forward scattering receiving (FSR) end, cascaded to be a passive FSR. The FSR is a special mode for a bistatic radar arrangement such that the target is near the baseline (Salah *et al*., 2009), as seen in Figure 10. The FSR enhances the radar performance due to some important features, such as a long coherent interval of the received signal, and improves the target RCS regardless of the target's surface shape and relative simple hardware (Abdullah & Ismail, 2006). These and other features of similar robustness to stealth technology (Cherniakov *et al*., 2005; Sizov *et al*., 2007) are the attractive advantages that make the method a good candidate. A beneficial feature of an FSR used in micro-Doppler extraction was further presented in Raja Abdullah *et al*. (2017), to enhance its potential ability for target recognition. Based on the aforementioned features, the PFSR methodology may be able to improve small target detection due to its cascaded nature of concatenating the two independent methodologies, i.e., passive and FSR methodologies, thus complimenting the setbacks of one another. The implemented PFSR-based methodology for both Doppler and micro-Doppler extraction as well as efforts made toward the detection, tracking and classification of both ground and airborne targets are presented. The achievements recorded by the PFSR approach since its emergence to the point of this write up are also presented. Some attempted efforts via PFSR for both ground and air target detection exploiting various illuminators of opportunity are therefore summarised and presented in Table 2.

As seen from the summarised PFSR approaches depicted in Table 2, it is revealed that some of the implemented work was based on a ground moving target, (e.g., Figure 11). Other studies involving airborne targets were Suberviola *et al*. (2012) for the RCS verification of different aircrafts, feasibility of cascading PCL into FS mode in Gashinova *et al*. (2013), an algorithm for aircraft detection (Marra *et al*., 2015), a micro-Doppler analysis of the main and tail rotor for helicopter detection and classification (Clemente *et al*., 2015; Radmard et al., 2016a) aiming at air surveillance of a shuttle orbiter. The recent efforts have been small, light Cessna 172 aircraft detection (Contu *et al*., 2017), SNR verification to detect a target without crossing the baseline (Liu C. *et al*., 2017), SISAR imaging of aircraft (Hu *et al*., 2017), velocity estimation (Arcangeli *et al*., 2017) and a passive bistatic for detecting and tracking a Phantom 4 drone in a cluttered background via its generated micro-Doppler signature described in (Liu Y. *et al*., 2017). Among the airborne-based PFSR methods so far presented, only Clemente *et al*. (2015) and Liu Y. *et al*. (2017) attempted micro-Doppler analyses

using PFSR, with the latter focusing on drone detection in a bistatic case. Recently, Kabakchiev *et al*. (2017) described the feasibility of using pulsars in FSR using high gain radio telescope receiver.

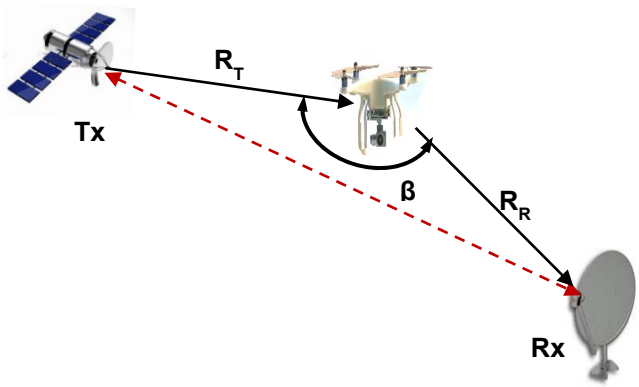

Figure 10: Topology of DVBS-based FSR.

Table 2: PFSR for detection.

Author(s)	Methodology	Aim
Kabakchiev *et al*. (2013)	GNSSL1-based FSR	Ground target detection
Kabakchiev *et al*. (2014)	GPS-based FSR	To detect and differentiate velocity and size of two different moving targets
Kabakchiev *et al*. (2015)	GPS-based FSR	Algorithm for automatic detection of radio shadows ground targets
Kabakchiev *et al*. (2016)	GPS-based FSR	Parameter estimation of different ground target to verify target detected to be based on a bistatic RCS or by FS mode.
Krysik *et al*. (2013)	GSM-based FSR	To detect a ground moving target
Abdullah *et al*., (2016)	LTE-based FSR	Vehicle recognition in LTE-based PFSR
Raja Abdullah *et al*. (2016)	LTE-based (4G) FSR	Ground moving target detection and classification
Martelli *et al*. (2016)	WIFI-Ch6 FSR	Vehicle signature detection
Colone *et al*. (2017)	WIFI-based FSR	Performance comparison between two sensor geometries for transportation monitoring solutions.
Non-drone airborne target		
Suberviola *et al*. (2012)	GPS-based FSR	To determine RCS of different aircraft
Clemente *et al*. (2015)	GNSS-based FSR	Micro-Doppler based detection and classification of a helicopter's main and tail rotor
Garvanov *et al*. (2016)	GPS-based FSR	Feasibility study as to whether the GPS based FSR is achievable in air target detection
Radmard *et al*. (2016b)	Passive FSR	Geostationary for air surveillance of shuttle orbiter
Liu *et al*. (2017)	GNSS-based FSR	Signal to noise ratio (SNR) performance of using omnidirectional and horn antennae to detect airborne targets without crossing the baseline
Hu *et al*. (2017)	GNSS-based FSR	Signal modelling and experimental detection and imaging via designed simplified SAR (SISAR) of aircraft
Marra *et al*. (2015)	DVBT-based FSR	Algorithm for airborne target detection (aircraft)
Arcangeli *et al*. (2017)	DVBS-based FSR	Target velocity estimation (Aircraft)
Gashinova *et al*. (2013a)	Multiple Illuminators FSR	Cascading FSR mode into traditional passive coherent locator (PCL) for RCS enhancement using a 4x4 vehicle and UAV

		simulated models
Gashinova *et al*. (2013b)	Multiple illuminators FSR	Signal characterization PCL in FS mode. Computer simulation technology (CST) simulated targets with inherently low RCS (ground and airborne targets)
Kulpa *et al*. (2015b)	DVB-T & FM FSR	To improve detection sensitivity (comparative studies) for airborne targets
Contu *et al*. (2017)	Multi freq._FSR	To determine the possibilities of airborne detection
Kabakchiev *et al*. (2017)	Pulsars in FSR	Feasibility of air target detection using pulsars in FSR
Drone detection		
Liu *et al*. (2017)	DVB-T passive bistatic radar	Multichannel for detection and tracking of drone under different trajectories

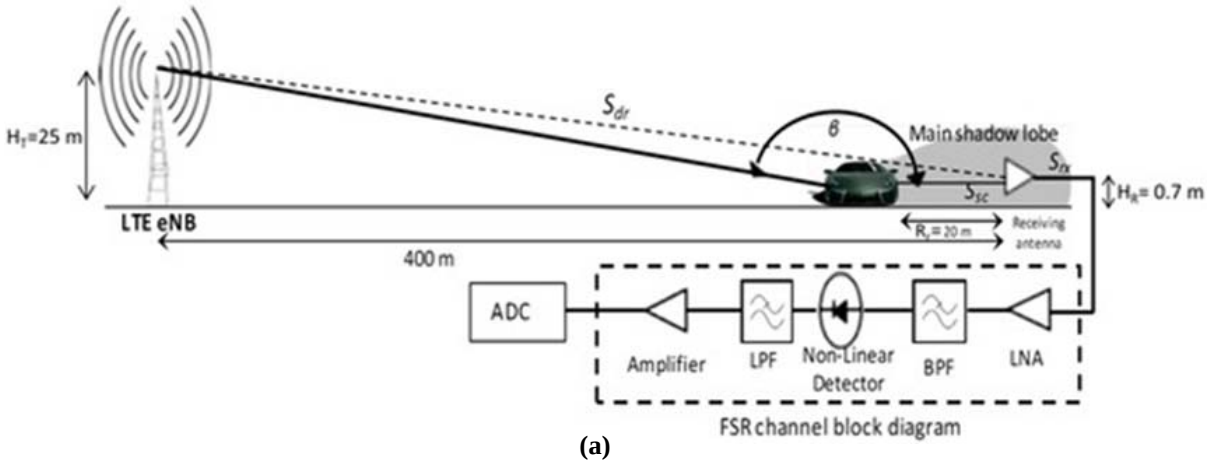

(a)

(b)

Figure 11: (a) LTE-based sensor system. (b) Aerial photo of experimental site (Source: Raja Abdullah *et al*., 2016).

5. CHALLENGES AND FUTURE WORK

Biological targets such as insects and birds exist in the same surveillance volume with drones. The drone's small size leads to a very low RCS, with typical value of 0.0005 m^2 (-33.01 dBsm) for a Phantom-3 drone, an insect of 0.00001 m^2 (-50 dBsm) (Stupples, 2015) and a bird of 0.01 m^2 (-20 dBsm) (Ritchie *et al*., 2015) without reference to aspect angle and the operating frequency. Drone RCS is sometimes confused with a comparable RCS value to that of birds, and also the flying pattern makes it tough to differentiate. This necessitated the need for additional Doppler information from the drone rotating wing to help discriminate it from flapping birds' wings (Jahangir *et al*., 2017). Micro-Doppler analysis of a small sized target with the aforementioned characteristics in addition to disturbances caused by the rotating blade was challenging (Contu *et al*., 2017), making its classification from other airborne target difficult. In addition classification of smaller objects within few cm is difficult, especially when high-precision radar profiles are used (Molchanov *et al*., 2013). Other factors affecting the RCS are the aspect angle during flight and material type, of which most drones are made of either plastic material or carbon fibre (Ritchie *et al*. 2015). A computer simulation technology (CST) simulation is shown in Figure 12 (a-c) describing how aspect angle and material makes, affected the bistatic RCS of a Phantom-3 drone blade model (G'llaume, 2017). Figure 13 (a-c) is the Cartesian and Polar RCS representation based on the three different materials. It is clearly shown how for perfect electrical conductor (PEC) material; the blade was transformed at (0-0-0) with the e-field direction facing the blade face (Figure 13a) yields the highest RSC of 0.736 dBm^2 with a bistatic arrangement. This is indeed expected to improve when the FSR mode was incorporated.

Drone speed leads to a small integration of time of observation. Low altitude usually within a maximum allowable vertical height of 400ft (121.92 m) above sea level, which is outside the range of conventional radars, make detection an issue of concern, in addition to regulation allowing the flying altitude in restricted areas. The cost of getting a new license to transmit new signal may be deterrent to the selection of an illuminator of opportunity with an appropriate sampling rate as a function of the Doppler resolution and their characterised low power received from illuminators is of vital importance. The illuminators explored in Table 2 with each having their pros and cons, the low received power yield of digital video broadcasting satellite (DVBS) can thus be compensated using a high gain receiver coupled with a long integration time to improve the SNR (Hu *et al*., 2017). The DVB-S can be an option due to its spectrum capability, coverage area and position, leading to a larger target RCS and resulting in the reliable detection of a low-profile target such as the drone (Radmard *et al*., 2016a). This can be seen in a feasibility studies of implementing DBS for air surveillance in Shiyou & Zengping (2006), suggesting how targets with small RCS can be addressed despite some highlighted difficulties, especially for a high-altitude targets. Another earlier study, which reported satellite-based passive bistatic radar (PBR) meant to detect a real-life target, demonstrated the detection SNR of three different targets - a truck, a train and an airplane - in relatively close range (Palmer *et al*., 2009). DVBS' potentiality of detecting a target as determined by its ambiguities, described the signal characteristics thus verifying how the detection distance was affected by antenna gain, signal bandwidth and integration time (Yu & Peng, 2015).

Summarily, FSR features of a high power yield capable of the FS mode, appreciable RCS, elimination of multiple receivers, lack of extra cost for deploying a transmitter, robustness ability to compensate the lack of a range resolution in FSR, low environmental impact, and covert operation (De Luca *et al*., 2015). The challenge for stealth technology may further be minimised as the features of the passive FSR region to devise anti-jamming target detection (Raja Abdullah *et al*., 2016) are the benefits to be derived from the cascaded system, which make PFSR a viable option.

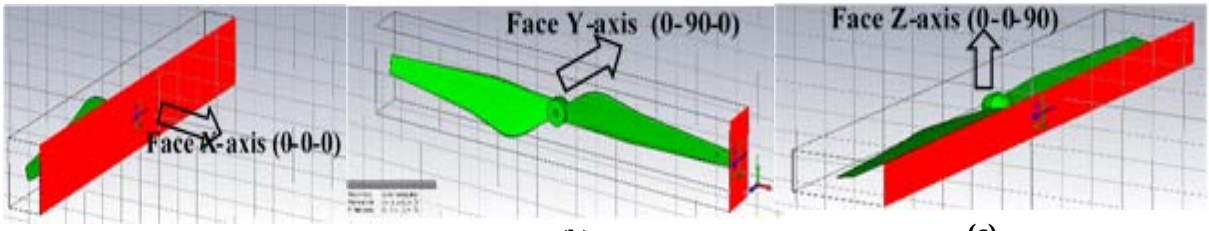

(a) **(b)** **(c)**

Figure 12: Blade transformation: (a) *x*-direction (b) *y*-direction (c) *z*-direction (Source: G'llaume, 2017).

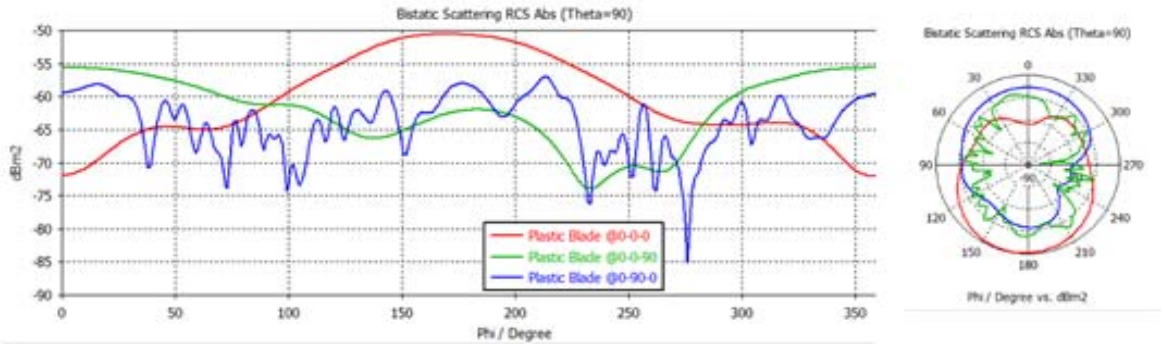

(a)

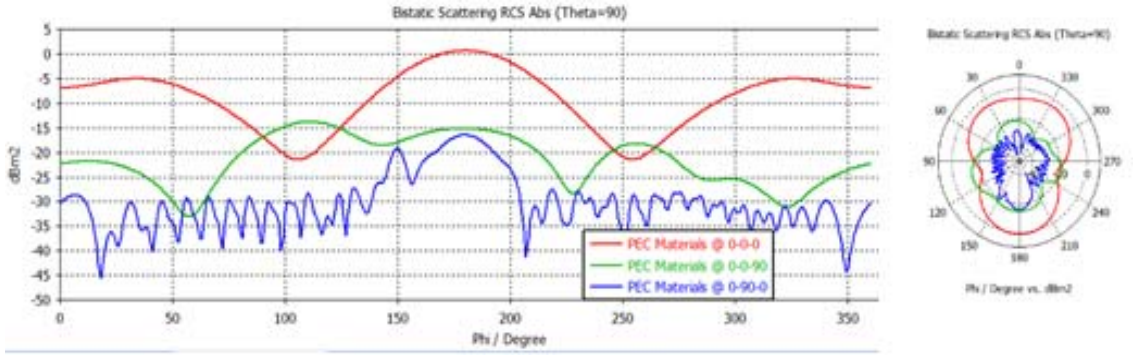

(b)

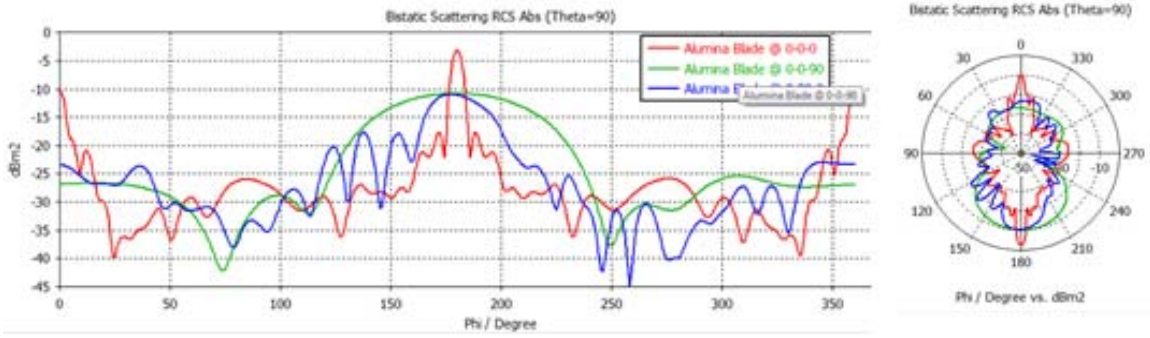

(c)

Figure 13: Blade RCS simulation of: (a) Plastic (b) Alumina (c) PEC materials.

6. CONCLUSION

This paper described radar generation technologies ranging from the early radars as an electronic fence through passive and active approaches (e.g., FSR) to the current passive FSR mode. Drone detection and the trending challenges that are deemed to make its detection necessary were discussed,

thereafter presenting some attempted methodologies ranging from those that are technically related like acoustic, video and hybrid methods through non-technical-based methods, such as netting. It further described the state of the art of drone detection by using radar systems following the trending techniques so far implemented for airborne target detection. A part from a main Doppler detection approach, different implementations of a micro-Doppler analysis for drone detection and other airborne targets were also presented. The highlighted authors' contributions toward ground and airborne target detection with the emergence of a passive FSR is an attempt to improve detection and / or classification of the previous methods, and was evidence to current trend for radar application. The implementation of the cascaded system (PFSR) as seen from Table 2, was an evidence to the lacking reported literatures on drone detection using this methodology despite its highlighted benefits/advantages. The benefits of DVBS into FSR for drone micro-Doppler analysis was also discussed. This work is currently in progress by these authors, with an attempt of designing a model / framework for drone blade micro-Doppler analysis for drone feature extraction. The extracted features can further be used for detection, tracking and classification.

REFERENCES

Abdullah, R. & Ismail, A. (2006). Forward scattering radar: Current and future applications. *Int. J. Eng. Tech.*, **3**: 61–67.

Abdullah, R.S.A.R., Salah, A. A., Abdul-Aziz, N. H. & Abdul Rashid, N. E. (2016). Vehicle recognition analysis in LTE based forward scattering radar. *IEEE 16th Int. Radar Conf.*, pp. 1–5.

Aker, C. & Kalkan, S. (2017). Using deep networks for drone detection. *14th IEEE Int. Conf. Adv. Video Sig. Based Surv. (AVSS) 2017*. pp. 1-6.

Arcangeli, A., Bongioanni, C., Ustalli, N., Pastina, D. & Lombardo, P. (2017). Passive forward scatter radar based on satellite TV broadcast for air target detection: Preliminary experimental results. *IEEE Radar Conf.*, pp. 1592–1596.

Barber, B.C. (2008). Imaging the rotor blades of hovering helicopters with SAR. *IEEE Conf. Pub.*, pp. 1–5.

Basak, S. & Scheers, B. (2018). Passive radio system for real-time drone detection and DoA estimation. *Int. Conf. Military Comm. Infor. Sys. (ICMCIS)*, pp. 1–6.

BBC (2018). *How Countries Counter the Drone Threat*. Available online at: http://www.bbc.com/news/technology-46639099 Last access date: (25, Dec, 2018).

Becker, G. & Güdesen, A. (2000). Passive sensing with acoustics on the battlefield. *Appl. Acoustics*, **59**: 149–178.

Blyakhman A.B., Burov V.N., Myakinkov A.V. & Ryndyk A.G. (2014). Detection of unmanned aerial vehicles via multistatic forward scattering radar with airborne transmit positions. *Int. Radar Conf.*, pp. 1–5.

Boddhu, S. K., McCartney, M., Ceccopieri, O. & Williams, R. L. (2013). A collaborative smartphone sensing platform for detecting and tracking hostile drones. *J. Modern App. Sci.,* **3**: 16-25.

Brandes, H. (2015). *Drone Carrying Drugs, Hacksaw Blades Crashes at Oklahoma Prison*. Available online at: http://www.reuters.com/article/us-oklahoma-prison/drone (Last access date 28 Sep, 2017).

Busset, J., Perrodin, F., Wellig, P., Ott, B., Heutschi, K., Rühl, T. & Nussbaumer, T. (2015). Detection and tracking of drones using advanced acoustic cameras. *SPIE Proc.*, pp. 1–8.

Cammenga, Z. A., Baker, C. J., Smith, G. E. & Ewing, R. (2014). Micro-Doppler target scattering. *IEEE Nat. Radar Conf. Proc.*, pp. 1451–1455.

Case, E. E., Zelnio, A. M. & Rigling, B. D. (2004). Low-cost acoustic array for small UAV detection and tracking. *IEEE Nat. Aeros. Elect. Conf. Proc. 2004.* pp. 24–30.

Chen, V. C. (2011). T*he Micro-Doppler Effect in Radar*. Artech House Radar Series, Artech House Boston, London.

Cherniakov, M., Salous, M., Kostylev, V. & Abdullah, R. (2005). Analysis of forward scattering radar for ground target detection. *IEEE Conf. Pub.*, pp. 145–148.

Clemente, C. & Soraghan, J. J. (2012). Vibrating target micro-Doppler signature in bistatic SAR with a fixed receiver. *IEEE Trans. Geosci. Remote Sensing*, **50**: 3219–3227.

Clemente, C., Balleri, A., Woodbridge, K. & Soraghan, J. J. (2013). Developments in target micro-Doppler signatures analysis: Radar imaging, ultrasound and through-the-wall radar. *EURASIP J. Adv. Sig. Proc.*, **47**: 1–18.

Clemente, C., Parry, T., Galston, G., Hammond, P., Berry, C., Ilioudis, C. & Soraghan, J. J. (2015). GNSS based passive bistatic radar for micro-Doppler based classification of helicopters: experimental validation. *2015 IEEE Radar Conf. Pub.*, pp. 1104–1108.

Clemente, C. & Soraghan, J. J. (2012). Passive bistatic radar for helicopters classification: A feasibility study. *IEEE Nat. Radar Conf. Proc., 2012.* pp. 0946 - 0949.

Clemente, C. & Soraghan, J. J. (2014). GNSS-based passive bistatic radar for micro-Doppler analysis of helicopter rotor blades. *IEEE Trans. Aerospace Elect. Sys.2014.* **50***:* 491-500.

Colone, F., Martelli, T., & Lombardo, P. (2017). Quasi-monostatic versus near forward scatter geometry in WiFi-based passive radar sensors. *J. IEEE Sensors*, **17**: 4757–4772.

Contu, M., De Luca, A., Hristov, S., Daniel, L., Stove, A., Gashinova, M. & Cristallini, D. (2017). Passive multifrequency forward-scatter radar measurements of airborne targets using broadcasting signals. *IEEE Trans. Aerospace Elect. Sys.*, **53**: 1067–1087.

Contu, M., Luca, A. De, Hristov, S., Stove, A. & Gashinova, M. (2017). Passive multi-frequency forward-scatter radar measurements of airborne targets using broadcasting signals. *IEEE Trans. Aerospace Elect. Sys., 2017.* pp. 1–23.

De Luca, A., Daniel, L., Kabakchiev, K., Hoare, E., Gashinova, M. & Cherniakov, M. (2015). Maritime FSR with moving receiver for small target detection. *Int. Radar Symp.*, 2015. pp. 834–839.

Dedrone. (2015). *Drone Smuggling a Package to a Prison Cell Window.* Available online at: http://www.dedrones.com/en/newsroom/overview-drone-news (Last access date: 28 Sep, 2017)

Diego, S. & Mich, I. (2017). *Drones Threats*. Available online at: http://nypost.com/tag/drones/ (Last access date: 28 Sep, 2017).

Door, L. (2017). *Descriptive Analysis and Comparisons.* Available online at: http://www.differencebetween.info/difference-between-drone-and-uav (Last access date: 28 Sep, 2017).

Drozdowicz, J., Wielgo, M., Samczynski, P., Kulpa, K., Jaroslaw, K. & Maj, M. (2016). 35 GHz FMCW drone detection system. *IEEE Conf. Pub.*, pp. 1–4.

Fang, G., Yi, J., Wan, X., Liu, Y. & Ke, H. (2018). Experimental research of multistatic passive radar with a single antenna for drone detection. *IEEE Access*, **6:** 33542–33551.

Francesco, F., Ritchie, M., Sevgi, Z. G. & Griffiths, H. (2017). Feature diversity for optimized human micro-Doppler classification using multistatic radar. *IEEE Trans. Aeros. Elect. Sys.*, **53**: 640–654.

Gaigals, G., Vavilina, E. & Carlo, M. (2017). Simulation of compressed sensing based passive radar for drone detection. *5th IEEE Workshop Adv. Infor. Elect. Elect. Engr. (AIEEE)*, 2017. pp. 1–5.

Ganti, S. R. & Yoohwan, K. (2016). Implementation of detection and tracking mechanism for small UAS. *Int. Conf. Unmanned Aircraft Sys. (ICUAS)*, *2016.* pp. 1254–1260.

Garvanov, I., Kabakchiev, C., Behar, V. & Daskalov, P. (2016). Air target detection with a GPS forward scattering radar. *IEEE 14th Int. Conf. Pub.*, pp. 1–4.

Gashinova, M., Daniel, L., Hoare, E., Kabakchiev, K., Cherniakov, M. & Sizov, V. (2013). Forward scatter radar mode for passive coherent location systems. *Int. Conf. Radar - Beyond Orthodoxy: New Paradigms in Radar, 2013.* pp. 235–239.

Gashinova, M., Daniel, L., Hoare, E., Sizov, V., Kabakchiev, K. & Cherniakov, M. (2013). Signal characterisation and processing in the forward scatter mode of bistatic passive coherent location systems. *EURASIP J. Adv. Sig. Proc.*, **36:** 1–13.

Golabi, M., Sheikhi, A. & Biguesh, M. (2013). A new approach for sea target detection in satellite based passive radar. *2013 21st Iranian Conf. Elect. Engr. (ICEE), IEEE Conf. Pub.*, pp. 1–5.

G'llaume, RBL. (2017). *Drone Propellers*. Available online at: http://www.grabcad.com/library/propellers (Last access date: 14 March, 2017).

Harmanny, R. I. A., De Wit, J. J. M. & Prémel Cabic, G. (2014). Radar micro-Doppler feature extraction using the spectrogram and the cepstrogram. *11th European Microwave Radar Conf. EuMW 2014.* pp. 165–168.

Hassan, S. A. & Mazhar, H. (2016). Analysis of target multipaths in WiFi-based passive radars. *IET*

Radar, Sonar Nav. **10**: 140–145.
Hoffmann, F., Ritchie, M., Fioranelli, F., Charlish, A. & Griffiths, H. (2016). Micro-Doppler based detection and tracking of UAVs with multistatic radar. *IEEE Radar Conf. 2016*. pp. 1-6
Hu, C., Liu, C., Wang, R., Chen, L. & Wang, L. (2017). Detection and SISAR imaging of aircrafts using GNSS forward scatter radar: Signal modeling and experimental validation. *IEEE Trans. Aeros. Elect. Sys.* **53**: 2077–2093.
Humpreys, T. (2015). *Statement on the Security Threat Posed by Unmanned Aerial Systems and Possible Countermeasures*. Statement to the Subcomm. on Oversight and Mgt. Eff. of the House Comm. on Homeland Security, 18 March 2015, Washington D.C.
Jahangir, M., & Baker, C. (2016). Robust detection of micro-UAS drones with L-band 3-D holographic radar TM. *IEEE Conf. Pub.* pp. 3–7.
Jahangir, M., Baker, C. J. & Oswald, G. A. (2017). Doppler characteristics of micro-drones with L-band multibeam staring radar. *2017 IEEE Radar Conf. 2017*. pp. 1052–1057.
Jian, M., Lu, Z. & Chen, V. C. (2018). Drone detection and tracking based on phase-interferometric Doppler radar. *2018 IEEE Radar Conf., 2018*. pp. 1146–1149.
Kabakchiev, C., Behar, V., Garvanov, I., Kabakchieva, D., Kabakchiev, A., Rohling, H. & Fernandes, J. (2017). Air target detection using pulsar FSR. *Int. Radar Sympo. Proc,* pp. 3–9.
Kabakchiev, C., Garvanov, I., Behar, V., Daskalov, P. & Rohling, H. (2014). Study of moving target shadows using passive forward scatter radar systems. *Int. Radar Sympo. Proc.,* pp. 1-4.
Kabakchiev, C., Garvanov, I., Behar, V., Kabakchieva, D., Kabakchiev, K., Rohling, H. & Yarovoy, A. (2015). The study of target shadows using passive FSR systems. *Int. Radar Sympo. Proc.,* pp. 628–633.
Kabakchiev, C., Garvanov, I., Behar, V., Kabakchieva UNWE Sofia, D., Kabakchiev, K., Rohling, H. & Yarovoy, A. (2016). Experimental verification of target shadow parameter estimation in GPS FSR. *17th Int. Radar Sympo. (IRS) IEEE Conf. Pub.,* pp. 1–5.
Kabakchiev, C., Garvanov, I., Behar, V. & Rohling, H. (2013). The experimental study of possibility for radar target detection in FSR using L1-based non-cooperative transmitter. *14th Int. Radar Sympo. (IRS), 2013.* pp. 625–630.
Kamil Ba, M., Samczynki, P., Kulpa, K. & Misiurewicz, J. (2015). Micro-Doppler signatures of helicopters in multistatic passive radars. *IET Radar, Sonar Nav.* J. **9**: 1276-1283.
Knoedler, B., Zemmari, R., & Koch, W. (2016). On the detection of small UAV using a GSM passive coherent location system. *Int Radar Sympo. Proc. 2016.* pp. 4–7.
Koo, Y.S., Ren, L., Wang, Y. & Fathy, A. E. (2013). UWB Micro Doppler radar for human gait analysis of tracking more than one person, and vital sign detection of moving persons. *IEEE Conf. Pub.,* pp. 1–4.
Krátký, M. & Fuxa, L. (2015). Mini UAVs Detection by Radar. *IEEE Conf. Pub.*, pp. 1–5.
Krysik, P., Kulpa, K. & Samczyński, P. (2013). GSM based passive receiver using forward scatter radar geometry. *IEEE Conf. Pub.,* pp. 637–642.
Kulpa, K., Malanowski, M., Baczyk, M. & Krysik, P. (2015). Passive radar detection range enhancement using forward scatter geometry. *16th Int. Radar Sympo. (IRS) IEEE Conf. Pub.,* pp. 54–59.
Liu, C., Hu, C., Wang, R., Nie, X. & Liu, F. (2017). GNSS forward scatter radar detection: Signal processing and experiment. *IEEE Conf. Pub.,* pp. 1–9.
Liu, H., Zhiqiang, W., Yitong, C., Jie, P., Le, L. & Ren, Y. (2017). Drone detection based on an audio-assisted camera array. *IEEE 3rd Int. Conf. Multimedia Big Data*, pp. 1–5.
Liu, Y., Wan, X., Tang, H., Yi, J., Cheng, Y. & Zhang, X. (2017). Digital television based passive bistatic radar system for drone detection. *2017 IEEE Radar Conf. 2017*. pp. 1493–1497.
Maartens, E. (2015). *Drone Versus UAV, What's the Difference.* Retrieved from Available online at: https://www.ezvid.com/drone-vs-uav-whats-the-difference (Last access date: 28 Sep, 2017).
Marra, M., De Luca, A., Hristov, S., Daniel, L., Gashinova, M. & Cherniakov, M. (2015). New algorithm for signal detection in passive FSR. *IEEE Radar Conf.,* pp. 1–6.
Martelli, T., Colone, F. & Lombardo, P. (2016). First experimental results for a WiFi-based passive forward scatter radar. *2016 IEEE Radar Conf. Pub.* pp. 1–5.
Martelli, T., Murgia, F., Colone, F., Bongioanni, C. & Lombardo, P. (2017). Detection and 3D localization of ultralight aircrafts and drones with a WiFi-based passive radar. *Int. Conf. Radar*

Sys. Belfast, UK, pp. 1–6.
Martin, J. & Mulgrew, B. (1990). Analysis of the theoretical radar return signal from aircraft propeller blades. *IEEE Int. Radar Conf.1990.* pp. 569–572.
Mezei, J., Flaska, V. & Molnár, A. (2015). Drone sound detection. *16th IEEE Int. Sympo. Comp. Intelligence Infor.* pp. 333–338.
Mezei, J. & Molnár, A. (2016). Drone sound detection by correlation. *11th IEEE Int. Sympo. App. Comp. Intelligence Infor.*, pp. 509–518.
Molchanov, P., Egiazarian, K., Astola, J., Harmanny, R. I. A. & de Wit, J. J. M. (2013). Classification of small UAVs and birds by micro-Doppler signatures. *Int. J. Microwave Wireless Tech.,* **6**: 435–444.
Nakamura, R. & Hadama, H. (2017). Characteristics of ultra-wideband radar echoes from a drone. *IEICE Comm. Exp.,* **6**: 530–534.
Namorato, M. V. (2000). A concise history of acoustics in warfare. *App. Acoustics*, **59:** 101–135.
Nguyen, P., Ravindranathan, M., Nguyen, A., Han, R. & Vu, T. (2016). Investigating cost-effective RF-based detection of drones. *2nd Workshop Micro Aerial Vehicle Net. Sys. App. Civilian Use, DroNet 2016.* pp. 17–22.
Nijim, M. & Mantrawadi, N. (2016). Drone classification and identification system by phenome analysis using data mining techniques. *IEE Conf. Pub.* pp. 1–5.
Nuss, B., Sit, L., Fennel, M., Mayer, J., Mahler, T. & Zwick, T. (2017). MIMO OFDM radar system for drone detection. *18th Int. Radar Symp. IEEE Conf. Pub.,* pp. 1–9.
Ochodnický, J., Matousek, Z., Babjak, M., & Kurty, J. (2017). Drone detection by Ku-band battlefield radar. *Int. Conf. Military Tech. (ICMT)*, pp. 613–616.
Osamu, T. (2017). RF techniques for detecting and classifying UAV. *5th Smart city (SMC) Eng. UPM workshop proc.,* pp. 1–15.
Palmer, J., Palumbo, S., Summers, A., Merrett, D. & Howard, S. (2009). DSTO's experimental geosynchronous satellite based PBR. *IEEE Int. Radar Conf.,* pp. 1–6.
Park, J., Choi, I. & Myung, N. (2012). Modified HHT analysis of micro-Doppler signatures scattered from rotating flat blades. *Proc. ISAP2012, Nagoya, Japan*. pp. 608–611.
Park, J., Kim, D. H., Shin, Y. S. & Lee, S. H. (2017). A comparison of convolutional object detectors for real-time drone tracking using a PTZ camera. *Int. Conf. Control Auto. Sys. (ICCAS) 2017.* pp. 696–699.
Peacock, M. & Johnstone, M. N. (2013). Towards detection and control of civilian unmanned aerial vehicles. *Australian Infor. Warfare Sec. Conf.,* pp. 1–8.
Peto, T. & Seller, R. (2016). Quad channel DVB-T based passive radar. *17th Int. Radar Sympo. (IRS), IEEE Pub.,* pp.1–4.
Petrides, P., Kyrkou, C., Kolios, P., Theocharides, T. & Panayiotou, C. (2017). Towards a holistic performance evaluation framework for drone-based object detection. *IEEE Int. Conf. Unmanned Aircraft Sys. (ICUAS) Conf. Pub.,* pp. 1785–1793.
Pham, T. & Srour, N. (2004). Acoustic detection and tracking of UAVs. *Unattended/Unmanned Ground, Ocean, Air Sensor Tech. App.,* **5417:** 24–30.
Pisa, S., Piuzzi, E., Pittella, E., Lombardo, P., Ustalli, N., Cao, W. & Zambotti, A. (2018). Evaluating the radar cross section of the commercial IRIS drone for anti-drone passive radar source selection. *22nd Int. Microwave Radar Conf. (MIKON)*, 2018. pp. 699–703.
Pleban, J.-S., Band, R. & Creutzburg, R. (2014). Hacking and securing the AR. drone 2.0 quadcopter: investigations for improving the security of a toy. *SPIE-IS&T Elect. Imaging Proc.,* **9030:** 1–12.
Radmard, M., Bayat, S., Farina, A., Hajsadeghian, S. & Nayebi, M. M. (2016a). Satellite-based forward scatter passive radar. *Int. Radar Sympo. Proc. 2016.* pp. 4–7.
Radmard, M., Bayat, S., Farina, A., Hajsadeghian, S. & Nayebi, M. M. (2016b). Satellite-based forward scatter passive radar. *17th Int.l Radar Sympo. (IRS) IEEE Conf. Pub.* pp. 1–4.
Raja Abdullah, R. S. A., Abdul Aziz, N., Abdul Rashid, N., Ahmad Salah, A. & Hashim, F. (2016). Analysis on target detection and classification in LTE based passive forward scattering radar. *Sensors*, **16**: 1607.
Raja Abdullah, R. S. A., Salah, A. A., Alnaeb, A. A., Sali, A., Abd Rashid, N. E. & Ibrahim, I. P. (2017). Micro-Doppler detection in forward scattering radar: Theoretical analysis and experiment. *Elect. Letters*, **53**: 426–428.

Rao, N. V. K. (2016). A cross-correlation approach to determine target range in passive radar using FM broadcast signals. *IEEE WISPNET Conf.* pp. 524–529.

Ren, L., Tran, N., Wang, H., Fathy, A. E. & Kilic, O. (2016). Analysis of micro-Doppler signatures for vital sign detection using UWB impulse Doppler radar. *IEEE Tropical Conf. Biomedical Wireless Tech. Net. Sensors.* pp. 18–21.

Ritchie, M., Fioranelli, F. & Griffiths, H. (2016). Monostatic and bistatic radar measurements of birds and micro-drone. *IEEE Radar Conf. 2016.* pp. 2–6.

Ritchie, M., Fioranelli, F., Griffiths, H. & Borge, T. (2015). Micro-drone RCS analysis. *IEEE Radar Conf. 2015.* pp. 452–456.

Rozantsev, A., Lepetit, V. & Fua, P. (2015). Flying objects detection from a single moving camera. *IEEE Comp. Society Conf. Proc. Comp. Vision Pattern Recog.*, 2015. pp. 4128–4136.

Rozantsev, A., Lepetit, V. & Fua, P. (2017). Detecting flying objects using a single moving camera. *IEEE Trans. Pattern Analysis Machine Intelligence*, **39**: 879–892.

Rzewuski, S., Kulpa, K., Member, S., Salski, B., Kopyt, P., Borowiec, K. & Member, S. (2018). Drone RCS estimation using simple experimental measurement in the WIFI bands. *22nd Int. Microwave Radar Conf. (MIKON) 2018.* pp. 695–698.

Salah, M., Rasid, M., RSA, &, Abdullah, R. & Cherniakov, M. (2009). Speed estimation in forward scattering radar by using standard deviation method. *Modern App. Sci. J. (CCSE)* **3**: 16 -25.

Sathyamoorthy, D. (2015). A review of security threats of unmanned aerial vehicles and mitigation steps. *J. Def. & Sec.,* **6**: 81–97.

Schaaf, R. Vander. (2014). What technologies or integrating concepts needed for the US military to counter future missile threats looking out to 2040. A Research Reported *Submitted to Air War Col.,* pp. 1-31.

Schulman, B., Affairs, L. & Cornblatt, M. (2014). *How to shoot down a Drone*. Available online at: http://www.popularmechanics.com/flight/drones/how-to/a16756/ how-to-shoot-down-a-drone. (Last access date: 28 Sep, 2017).

Sedunov, A., Sutin, A., Sedunov, N., Salloum, H., Yakubovskiy, A. & Masters, D. (2016). Passive acoustic system for tracking low- flying aircraft. *IET Radar Sonar Nav.,* **10**: 1561–1568.

Seifert, A., Amin, M. G. & Zoubir, A. M. (2017). New analysis of radar micro-Doppler gait signatures for rehabilitation and assisted living. *IEEE Int. Conf. Acoustics, Speech Signal Proc.* pp. 4004–4008.

Shin, D., Jung, D., Kim, D., Ham, J., Park, S. & Member, S. (2017). A distributed FMCW radar system based on fiber-optic links for small drone detection. *IEEE Tran. Instr. Meas.*, **66**: 340–347.

Shiyou, X. & Zengping, C. (2006). Feasibility surveillance air/space surveilance. *IEEE Conf. Pub.,* pp. 6–9.

Sizov, V., Cherniakov, M., & Antoniou, M. (2007). Forward scattering radar power budget analysis for ground targets. *IET Radar Sonar Nav.,* **1**: 437–446.

Solomitckii, D., Gapeyenko, M., Semkin, V., Andreev, S. & Koucheryavy, Y. (2018). Technologies for efficient amateur drone detection in 5G millimeter-wave cellular infrastructure. *IEEE Comm. Mag.*, **56**: 43–50.

Stasiak, K., Ciesielski, M., Kurowska, A. & Przybysz, W. (2018). A study on using different kinds of continuous-wave radars operating in C-Band for drone detection. *22nd Int. Microwave Radar Conf. (MIKON), 2018.* pp. 521–526.

Stupples, D. W. (2015). Future Systems Surveillance Technology. In *Complexity Science Workshop, City University London*. City University London. pp. 1-22.

Sturdivant, R. L. & Chong, E. K. P. (2017). Systems engineering baseline concept of a multispectral drone detection solution for airports. *IEEE J. Magazines*, **5:** 7123–7138.

Suberviola, I., Mayordomo, I. & Mendizabal, J. (2012). Experimental results of air target detection with a GPS forward-scattering radar. *IEEE Geoscience Remote Sensing Letters*, **9:** 47–51.

Sung, J. L., Jae, H. J. & Bonghyuk, P. (2016). Possibility verification of drone detection radar based on pseudo random binary sequence. *IEEE Conf. Pub.,* pp. 291–292.

Sziill, A., Seller, R., Rohacs, D. & Renner, P. (2017). Multilateration based UAV detection and localization. *IEEE Conf. Pub.,* pp. 1–10.

Thayaparan, T. Abrol, S. Riseborough, E. Stankovic, L. L. D. & Duff, G. (2007). Analysis of radar

micro-Doppler signatures from experimental helicopter and human data. *J. IET Radar Sonar Nav.* **1**: 289–299.

Vilimek, J. & Burita, L. (2017). Ways for copter drone acoustic detection. *6th Int. Conf. Military Tech. ICMT 2017.* pp. 349–353.

Weiß, M. (2014). Compressive sensing for passive surveillance radar using DAB signals. *Int. Radar Conf.,* pp. 1–6.

Willis, N. J. (2005). *Bistatic Radar* (Vol. 8). USA: SciTech Publishing Inc., Georgia USA.

Wit, J.J.M., Harmanny, R.I.A & Prémel-Cabic, G. (2012). Micro-Doppler analysis of small UAVs. *9th Int. Euro. Radar Conf. (EuRAD), 2012.* pp. 210–213.

Xia, P., Wan, X., Yi, J. & Tang, H. (2016). Micro-Doppler imaging for fast rotating targets using illuminators of opportunity. *J. IET Radar Sonar Nav.,* **10**: 1024–1029.

Yang, X., Huo, K., Jiang, W., Zhao, J. & Qiu, Z. (2016). A passive radar system for detecting UAV based on the OFDM communication signal. *Prog. Electromag. Research Sympo., (PIERS) Proc. 2016.* pp. 2757–2762.

Yu, Q. & Peng, H. (2015). Target detection technology in passive radar based on broadcasting satellite signals. *Int. Conf. Comp. Sci. Mech. Auto.*, pp. 191–195.

Zhang, Z. & Andreou, A. G. (2008). Human identification experiments using acoustic micro-Doppler signatures. *Argentine Sch. Micro-Nano Elect. Tech*., pp. 81–86.

Zhang, Z., Pouliquen, P., Waxmant, A. & Andreou, A. G. (2007). Acoustic micro-Doppler gait signatures of humans. *41st Annual Conf. Infor. Sci. Sys.,* pp. 627–630.

SPACEBORNE SYNTHETIC APERTURE RADAR (SAR) SENSORS IN LOW EARTH ORBIT (LEO) FOR REAL-TIME DETECTION AND MONITORING OF FLOODS

Arun Kumar Verma[1*], Ranbir Nandan[2] & Aditi Verma[3]

[1]Vidyadaan Institute of Technology and Management, Aryabhatta Knowledge University, India
[2]Geology Department, B.N. College, Patna University, India
[3]Qualcomm India Pvt. Ltd., India

[*] Email: arun@vidyadaan.org

ABSTRACT

Earth observation system (EOS) consists of optical or microwave sensors on spaceborne systems in the low Earth orbit (LEO) and provides crucial information for effective flood disaster management by supporting decision makers or emergency response organisations in their activities during the time critical crisis response phase of natural disasters. It is well known that the applications of satellite images of multi-spectral sensors in optical spectrum is not suitable for detection and monitoring of floods during rainy seasons with clouds in the sky due to non-penetrating capability of signals restricting its applications during clear sky condition. The other limitation of multi-spectral sensors in optical spectrum is its acquisition of satellite imageries during day time only. Synthetic aperture radar (SAR) is the preferred tool for flood detection and mapping from space due to continuous observation of earth surface from the polar orbit, where SAR sensors provides its own source of illumination and is characterised by near all-weather / day-night imaging capability independent of atmospheric conditions in the microwave spectrum. Open water surface areas during flooding period in rivers behave like flat water surface for radar bands in the microwave spectrum and act as specular reflector responsible for scattering of radar signals incident from spaceborne SAR sensors resulting into dark pixels in the radar image in contrast to non-flooding areas of the Earth surface. Change detection techniques using multi-temporal SAR images based on the behaviour of backscattered signals for threshold value for detecting the flood between non-flooding and flooding periods provide information related to the status of water surface of river systems. Recently, radar sensors have received interest in the development of spaceborne bi-static and multi-static SAR sensors due its potential to reduce the revisit (repeat orbit) time for monitoring the changes on the Earth surface depending upon the repeat orbit and SAR payloads on the satellites. Spaceborne SAR payloads can be placed in the orbit into fully active or semi-active configuration based on both transmit and receive capability of signals. In this paper, the concept of the bi-static and multi- static space-borne SAR sensors is described for the development of real time space-borne SAR surveillance system for monitoring of various characteristics of river basins and detection of floods using threshold / change detection techniques. Furthermore, the concept for the development of constellation of multi-static SAR satellite imaging receivers in LEO and geostationary radar illuminating system is described for real time detection and monitoring of floods.

Keywords: Spaceborne synthetic aperture radar (SAR); radar backscattering coefficient; detection and monitoring of floods; bi-static and multi-static SAR sensors; rain drop size distribution (RDSD).

1. INTRODUCTION

Earth observation system (EOS) consists of optical or microwave sensors that can provide crucial information for effective flood disaster management by supporting decision makers or emergency response organisations in their activities during the time critical crisis response phase of natural disasters. The information with respect to detection, monitoring and mapping of flooded regions is very critical for emergency and rescue operations during flooding periods. Spaceborne optical sensors in the visible and

infrared range during favourable weather conditions can be the preferred information source for flood mapping due to their straightforward interpretability and rich information content. However, it is well known that flood events often occur during long lasting periods of persistent cloud cover during rainy seasons, which restrict the use of optical sensors for continuous monitoring of flood disasters. Synthetic aperture radar (SAR) is the preferred tool for flood detection and mapping from space due to continuous observation of earth surface, where SAR sensors provides its own source of illumination and characterised by near all-weather / day-night imaging capability in the polar orbit independent of atmospheric conditions in the microwave spectrum. Smooth open water areas during flooding period behaves like flat water surface acting as a specular reflector responsible for scattering of radar signals incident from spaceborne SAR sensors in different bands of the microwave region resulting in dark pixels in the radar image data in contrast with non-flooding areas of the Earth surface. SAR sensors provide unique opportunity to detect to a certain extent standing flooding water beneath vegetation / forest due to the multiple bounce effect of radar signals depending upon its wavelength and characteristics of vegetation, such as branches, leaves, trunks and pattern. This is due to penetrating capability and backscattering characteristics of radar signals from horizontal water surface and lower sections of vegetation / forest. The applications of satellite images of multispectral sensors in optical spectrum is not suitable for detection and monitoring of flood during rainy season and clouds in the sky. The other limitation of multispectral sensors in the optical spectrum is the acquisition of satellite imageries during day time only (Vilches, 2013; White *et al*., 2015; Liu, 2016).

The development of spaceborne SAR technology due to its imaging capability during day and night as well as during rainy periods makes it most appropriate for monitoring and prediction of flood management in recent years. One of the major advantages of SAR images is its characteristic to generate high contrast between surfaces such as soil and water due to very low backscattering coefficient of radar signals from water bodies acting as a mirror reflecting surface. Furthermore, the Earth surface gives higher backscattering coefficient due to surface roughness, which consists of soil characteristics and vegetation, resulting into increased radar reflectivity of the surface (Verma *et al*., 2017, 2018). Therefore, the comparison of multitemporal SAR images before and during the flooding provides the mapping of flooded areas with high degree of precision. Change detection techniques using multi-temporal SAR images based on back-scattered signals for threshold value provide information related the status of water surface of river systems, an overflow stream and the flooding of the surrounding area. In coherence maps of a pair of SAR images acquired before and during floods, the flood-affected areas have significantly lower coherence than in dry areas, making it possible to clearly identify these areas (Vilches, 2013).

The Ganges, Brahmaputra and Yangtze are three major Himalayan rivers of South and East Asia, where around 500 million people, or 50% of the population in India and Bangladesh, and about 300 million people, or about 25 % of the population of China, live within the flood basins of these three Himalayan rivers. Southern Asia is already the wettest area on the continent and one of the wettest regions in the world, which receives at least 1,000 mm of rainfall a year. Due to increasing severe weather conditions triggered by climate change, heavy rainfall events are expected to increase in the next 30 years in Asia, putting hundreds of millions of people at risk across the rapidly developing countries of southern Asia (Zheng *et al*., 2018). As rainfall events increase, more people in India, Bangladesh and China will be put at risk of coastal or inland flooding as compared to the rest of the Asia-Pacific combined due to aggravating flooding through poor drainage and short-sighted planning of urban growth across South Asia to accommodate the millions of rural residents moving to cities. Ganga, Brahmaputra and Indus originate from the Himalayan snow and ice fields. The water yield from a higher Himalayan basin is roughly twice as high as that from an equivalent basin located in the peninsular part of India. The Himalayan region and its foothills covering the adjoining plain area of Ganga River basin experiences thunderstorms and convective rainfall of very high rain rate intensity frequently, which is responsible for causing flooding in the Ganga river basin and its catchment area, apart from melting of Glacier (Goswami ,1985; Anand *et al*., 2018). Flooding in rivers is caused due to excessive rainfall and discharge of water in the river basins. The spatial and temporal characteristics of rain rate and RDSD plays very important role to cause flooding in the river basin, apart from siltation from plain / hilly areas of terrain (Verma *et al*., 2017).

The recent development of space borne SAR systems is focused on the reduction of the repeat pass period (revisit time) from 35 days to sub-days for acquisition of SAR images using bi-static or multi-static micro SAR receivers (payloads) on satellite in the low Earth orbit (LEO) in fully active or semi-active configuration suitable for real time surveillance of the Earth surface including flood disaster management (Krieger *et al*., 2006). In this paper, the characteristics of Indian river basins and rainfall characteristics are described for the understanding the causes of river floods. Furthermore, the potential advantages of backscattering of SAR signals for separating between flooding and non-flooding water surface areas are discussed in addition to the modelling of SAR-backscattering of water bodies for different SAR sensors having multifrequency and multipolarised radar signals in the L, C and X-bands. In this paper, the concept of the bi-static and multi-static space-borne SAR sensors is described for the development of space-borne SAR surveillance system for the Indian sub-continent as a Disaster Management System (DMS). The concept of geostationary radar illuminator and constellation of multi-static SAR receivers on micro-satellites in LEO or medium Earth orbit (MEO) are described for real time space-borne SAR systems for flood detection, monitoring and surveillance for disaster management.

2. ASIAN RIVER SYSTEMS AND RAINFALL CHARACTERISTICS

South Asia is home to 54 rivers of varying sizes linked to the Indus, Ganges and Brahmaputra river basins, all originating in China's Tibet Autonomous Region. While the Indus basin connects China with Afghanistan, India and Pakistan, the Brahmaputra and Ganges basins connect Bangladesh, Bhutan, China, India and Nepal (Benn & Owen, 1998). A recent study by the UN's Intergovernmental Panel on Climate Change (IPCC) reveals a wetter future of South Asia based on global climate change models. It is expected to have 20 - 30% increase in mean annual run off in the South Asia region for the period 2046 - 2075 relative to the study baseline period of 1976 - 2005 based on the study carried out by the Commonwealth Scientific and Industrial Research Organisation, Australia. According to the study, the change will be driven by higher temperatures from global warming, leading to more rain. Average daily temperatures would rise by 2.9 – 4.0 °C in 2046 – 2075, relative to the baseline, which predicts that the winter seasons will be slightly warmer and the summer seasons may see noticeably higher temperatures, especially in the northern (high altitude) regions (IPCC Press Release, 2018). The Ganges, Brahmaputra and Yangtze are three major Himalayan rivers of South and East Asia, where around 500 million people, or 50% of the population in India and Bangladesh, and about 300 million people, or about 25 % of the population of China, live within the flood basins of these three Himalayan rivers (Anand *et al*., 2018). Every major city in Asia, such as Mumbai, Shanghai, Hanoi, Beijing, and Phnom Penh, has had a major flooding event, which is urban flooding, in the last five years as a result of expected impacts of climate change of the world's weather due to hotter temperature, higher sea levels and heavier rainfall event (Anand *et al*., 2018; Zheng, 2018).

A heavy rainfall event means very high precipitation over the course of one day or one hour, resulting in urban flooding depending upon the topography and infrastructure of the city, which puts lives in danger across Asia. Flooding in urban environments is due to the absence of adequate provisions of the natural way to disperse the floodwaters due to heavy rainfall events causing the damage beyond the scope of realriver flooding. As the cities expand into floodplains and built hurriedly to accommodate their citizens in the fast developing cities of the Asian region in an unplanned manner, urban flooding is becoming important for urban disaster risk management (Susantono & Schellnhuber, 2017). According to the World Bank Data (2016), 17 % of the population of China residing as urban population in major cities in 1976 has grown to 56 % of the population, whereas, during the same period in India, urban population growth has doubled with 33% of its people in large cities. India, Nepal and Bangladesh are among the countries with the highest flood risk. Some 12% of the territory of India (400,000 km^2) is made up of potential flood zones along the banks of rivers, while in Bangladesh, three quarters of the country is affected. More than half the population of Nepal lives in the 20% flood zone area. Urban flooding in most of the major cities in Asian countries is caused due to very heavy / torrential rainfall rate of the

order of more than 100 mm rain within 1 h in addition to long-term monsoon / summer rainfall events causing river flooding.

The National Atlas and Thematic Mapping Organization (NATMO) of India have divided the country's drainage into 11 major basins, 30 minor basins and the West Coast Drainage. Among the major rivers, the Ganga–Brahmaputra–Meghna (Barak) system is the largest. Three major basins, viz. Indus, Ganga and Brahmaputra are snow-fed, while the remaining is purely rainfall dependent. The water yield from a high Himalayan basin is roughly twice as high as that from an equivalent basin located in the peninsular part of India. The Himalayan sector receives 500 cm of rainfall per year, the lower ranges receiving more than the higher area. There are increasing trends of rainfall over the Indus, Ganga, Brahmaputra, Krishna and Cauvery river basins from 1954, 1993, 1988, 1953 and 1929 onwards respectively. Similarly, there are decreasing trends of rainfall over Sabarmati, Mahi, Narmada, Tapi, Godavari and Mahanadi river basin from 1960, 1964, 1950, 1965, 1964 and 1962 onwards respectively (Verma *et al*., 2018).

2.1 Rain Drop Size Distribution (RDSD) Spectra

For tropical climate such as in the Indian sub-continent, the characteristics of RDSD were measured by many research scientists, which follow lognormal RDSD. Verma & Jha (1996) developed a log-normal RDSD model for Indian climate based on the measurement of rain drop size data using a distrometer during 1989 - 1993 at the Defence Electronics Applications Lab (DEAL), Dehradun. The Indian Space Research Organisation (ISRO) also conducted rain drop size measurements using distrometers at various locations such as Shillong, Kharagpur, Ahmedabad, Trivendrum, and Hassan during 2004 - 2007 of the Indian sub-continent for log-normal RDSD model. The rain drop size distribution confirms log - normal distribution as number of rain drops increases rapidly and then decreases gradually (Jassal *et al*., 1994; Verma & Jha, 1996). The tropical RDSD follows log-normal distribution of rain drop sizes and can be written as:

$$N(D_i)= \frac{N_T}{\sigma D_i \sqrt{2\pi}} \exp[\, -0.5\{(lnD_i - \mu)/\sigma\ \}^2] \qquad (1)$$

where N_T is the total number of drops of all sizes, μ and σ are the mean and standard deviation of D_i (drop size i-channel, i varies from 1 to 20 drop sizes). Here, N_T, μ and σ are the functions of rain rate and can be written as:

$$N_T = a_0 R^{b_0}\ ;\ \mu = A_\mu + B_\mu lnR\ \ ; \sigma^2 = A_\sigma + B_\sigma lnR \qquad (2)$$

The log-normal RDSD model developed based on the rain drop size data measurement at different locations in the Indian tropical region have different value of coefficients of N_T, μ and σ.

Figure 1 shows the variability of the rain drop size characteristics of the rainfall using RDSD models developed for Indian climate based on the rain drop size measurements at Dehradun during 1989 - 1993 (Verma & Jha, 1996), and Shillong, Kharagpur, Ahmedabad, Trivendrum and Hassan during 2004 - 2007 (Das *et al*., 2010 ; Verma *et al*., 2018). It is observed that larger rain drop pattern exists in the southern part of Indian subcontinent, while the dominance of smaller rain drop spectra in the northern part of the Indian subcontinent for the same rain rate. The number of rain drops increases to a maximum for particular rain drop diameter (D_m) and then decreases during the rainfall. With the increase of rain rate during the rain event, the value of D_m increases differently, which depends on the climatic conditions as well as characteristics of Indian Summer Monsoon.

Figure 1 further explains the variation of rain drop spectra with rain rate for different locations of tropical climate following the lognormal distribution. The rain drop size (D) for $N(D)_{max}$ varies with rate from 0.65 to 1.75 mm for Dehradun, Ahmedabad. However, the corresponding rain drop size (D) for $N(D)max$ varies from drop size of 1.1 to 2.85 mm for the same rain rate for other locations such as Shillong, Kharagpur, Hassan and Trivendrum.

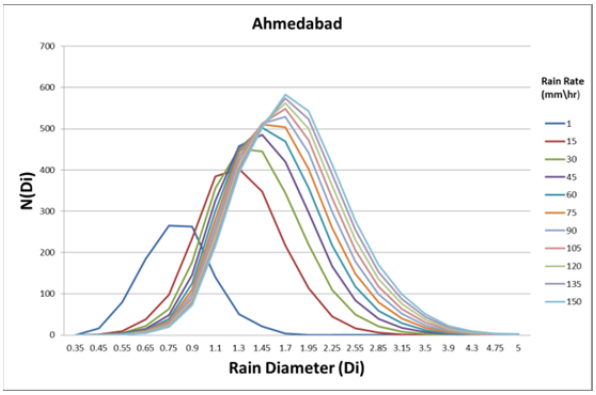

Figure 1(a): RDSD Spectra at Ahmedabad.

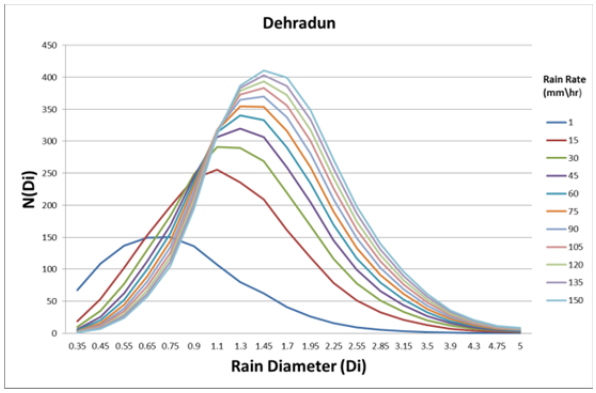

Figure 1(b): RDSD Spectra at Dehradun.

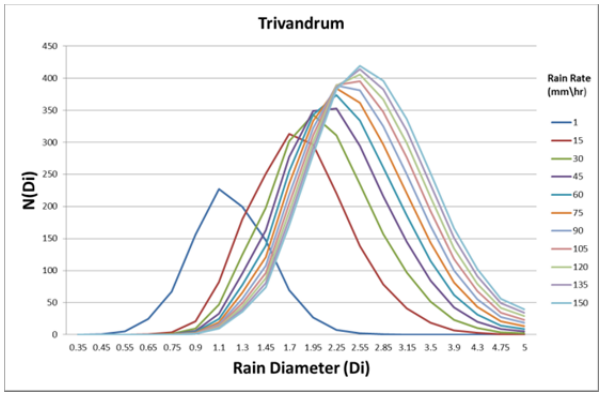

Figure 1(c): RDSD Spectra at Trivandrum.

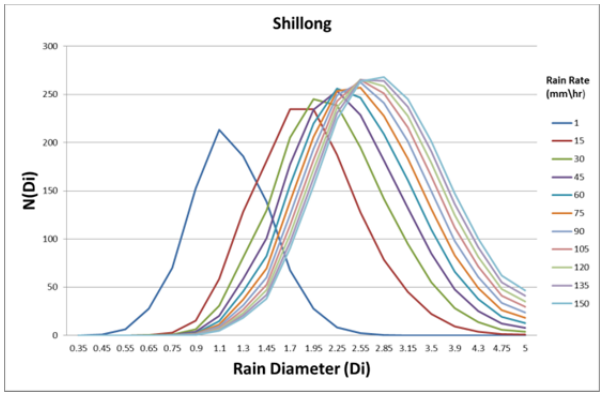

Figure 1(d): RDSD Spectra at Shillong.

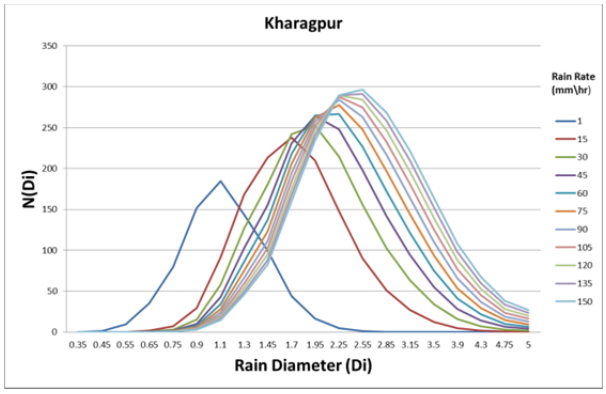

Figure 1(e) : RDSD Spectra at Kharagpur.

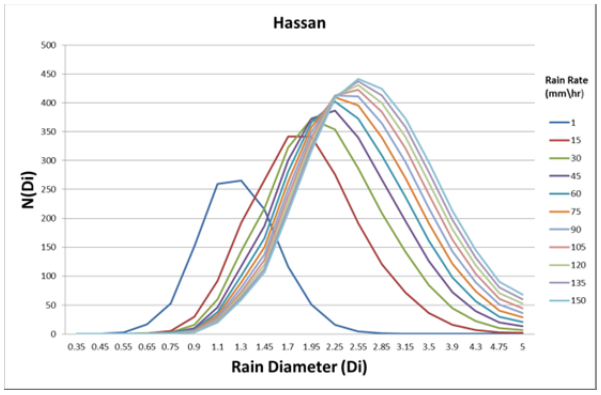

Figure 1(f) : RDSD Spectra at Hassan.

The variation in the drop size spectra for the different locations is due to variation in the climatic condition and the process of rain formation causing the rain events. The analysis of different models shows maximum $N(D)$ for Ahmedabad and rain characteristics consist of smaller rain drops between 0.55 and 3.15 mm with the variation of rain rate compared to other locations. The RDSD patterns of Shillong and Kharagpur follow the similarity and consist of larger rain drops between 0.75 and 4.5 mm for the same rain events as compared to Dehradun and Ahmedabad. Similarly, RDSD spectra of Trivandrum and Hassan consist of larger rain drop sizes due to similar climatic conditions. The rain drop size spectra for Dehradun consists of both smaller and larger rain drop sizes with moderate $N(D)$ values

from 0.35 to 4.5 mm drop size due to variation of the formation of rain process in the Himalayan climatic condition.

3. SAR BACKSCATTERING CHARACTERISTICS FROM WATER BODY FOR FLOOD DETECTION

3.1 SAR Backscattering in Forest and Wetland Covers Including Smooth Surface Water

Radar backscattering mechanisms that occur in forest and wetland land cover types including open surface water are shown in Figure 2, which vary as a function of the types and amount of vegetation, and the presence of standing water (Townsend, 2002). Smooth water surfaces can easily be detected by their very low backscattering value due to the fact that the transmitted radiation is almost completely scattered away from the SAR (radar) sensor. For the open surface water category, radar backscattering is specular or mirror like with little energy returning back to the sensor, which results in the dark image tones on SAR images. This dark image tones is used to discriminate this open water surface class from upland land cover. The radar backscattering increases significantly for rougher water surfaces induced by winds or currents, which requires sophisticated methods for identifying water surface. On the other hand, flooded vegetation produces double-bounce backscattering resulting in bright tones on SAR images; whereas, non-flooded vegetation leads to volume backscattering with SAR image diffuse in nature, not generally as bright as double-bounce scattering. SAR sensors operating in longer wavelengths (L-Band), radar signal penetrates the canopy and images underlying vegetation (Jussi, 2015; Martinis & Rieke, 2015).

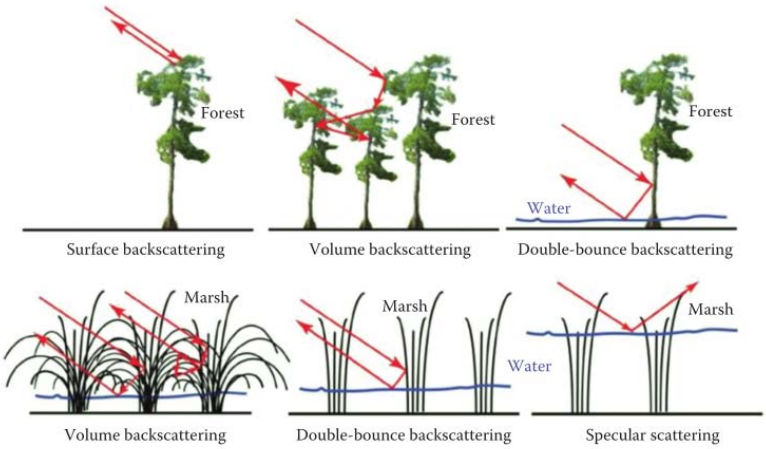

Figure 2: Radar backscattering process for forest and wetland covers (Brisco, 2015).

However, single polarised SAR intensity images cannot distinguish whether the radar signals received comes from canopy or ground / water surface. Thus, multi-polarized SAR sensors are required for distinguishing of different backscattering mechanisms such as volume backscattering, surface backscattering and di-plane (double bounce) backscattering involved in identifying water surface beneath vegetation or forest cover. Surface backscattering occurs when the Earth surface is rough enough to reflect radar signals, but the surface is still smooth in relation to the wavelength of radar sensors, such as C-band for RADARSAT-2, L-band ALOS PALSAR and X-band Terra SAR (Schmitt and Brisco, 2013; White *et al*., 2015). Di-plane backscattering or double-bounce backscattering occurs when two perpendicular planes are imaged by SAR sensors by means of radar signal reflection twice before reception. Double-bounce backscattering is rare and occurs as soon as vegetation / forest cover (grass or even trees) is flooded, and the culms or trunks respectively form a di-plane target in conjunction with the water surface. Volume backscattering is a purely diffuse backscattering behaviour caused by a huge number of disordered dipoles, e.g., inside a backscattering object or volume. Volume backscattering is applicable due to radar signal interaction with tree crowns of vegetation or forest cover, while surface

backscattering is applicable for the Earth surface or the canopy dependent on leave size and density (Schmitt & Brisco, 2013; Brisco, 2015).

3.2 Potential of SAR Images for Identifying Surface Water for Flood Detection

Standing water is generated by rainfall failing to infiltrate due to low infiltration capacity or by rainfall falling on the already saturated ground. The backscattering of SAR sensors from water surface is also determined by many other factors such as soil moisture, vegetation characteristics, soil surface conditions (roughness and standing water), SAR image acquisition characteristics (wavelength, incidence angle, polarisation) and smoothness of surface (soil surface roughness, vegetation biomass). Therefore, it is very important for the study of identification of standing water surface based on low backscattering of SAR signals to consider ancillary data such as soil moisture, in-situ-rainfall and normalised difference vegetation index (NDVI) for verification by adopting the methods used by Sentinal-1A (first member of constellation of two satellite operational from 2014; revisit time with maximum of five days) working in C-band in four imaging modes (Liu, 2016).

Sentinal-1 provides selectable polarization capability (VV or HH) for wave mode and selectable dual polarization capability (VV+VH or HH+HV). Since, HH-polarized data is less influenced by surface roughness on open water surface by waves, single polarized mode HH is used for flood mapping. The dielectric constant increases with soil moisture content, influencing the radar wavelength penetration. The longer the wavelength, the greater the sensitivity of the dielectric constant moisture content in soil. This means that in the L-band SAR images tend to be more sensitive to moisture in the soil than the bands of shorter wavelength such as C-band or X-band. SAR sensors with multi-polarisation of radar signals provide better information on inundated vegetation areas during flooding as compared to single polarised SAR sensors. SAR sensors with multi-polarised signals (HH or VV) are used for studying the separation of flooded and non-flooded forests. The backscattered ration between flooded and non-flooded forests is higher for HH-polarised radar signals as compared to VV polarised signals. A cross-polarised radar signal (HV or VH) provides lower backscattering due to very small effect of depolarisation of signals from flooded or non-flooded areas. Thus, the uses of multiple-polarised SAR sensors are suitable for detecting flooded water below the vegetation canopy as compared with single polarised SAR sensors. This capability further makes SAR sensors suitable for wetland mapping and monitoring purpose (White *et al*., 2015).

3.3 Radar Backscattering for Flooded and Non-Flooded Water Surface Area

SAR polarisation is a key factor in flood detection and HH-polarised images are considered more adequate for flood detection than VV- or cross-polarised images due to the fact that HH-polarisation gives the highest distinction in backscatter values between dry and wet forested areas. However, combining different polarisations can lead to improved flood maps, as HV polarisation is less sensitive to surface conditions of water bodies. The variation of double bouncing backscattering in flooded vegetation between flooded and dry conditions, and empirical backscattered threshold value are used for flooded vegetation with open flooded areas. The backscattering of SAR increases due to flooding in all SAR bands (L, C and X-band) over vegetation. The backscattering difference of SAR sensors between flooded and non-flooded areas varies differently for different SAR sensor bands, such as X-band: 10 dB, C-band: 6.9 dB and L-band: 9.7 dB, due to very heterogeneous characteristics of vegetation and SAR sensors parameters. Thus, threshold values of back-scattered signals are used for detecting the flood due to distinct threshold value separating the flooded and non-flooded regions. Therefore, multi-polarised SAR sensors are used to generate multi-polarised SAR backscattering data for detecting water below the vegetation canopy as compared to single polarised radar data and monitoring of the wetland (Townsend, 2002; Schmitt & Brisco, 2013; White *et al*., 2015). However, during the flood monitoring, which comprises most of open water bodies during flooding, SAR sensors collect backscattered signals with prior knowledge about the existence of flooded vegetation, then single polarised SAR sensors with HH

polarised radar signals can be used to derive the flood extent in high resolution mode for monitoring of large flood events (Schmitt & Brisco, 2013).

3.4 Analysis of SAR Backscatter Signals using TerraSAR-X, ALOS PALSAR and RADARSAT-2

Backscattering analysis over flooded vegetation areas in the central Europe was carried out in the context of flood mapping using multi-temporal, multi-frequency single polarized SAR sensors with partially submerged vegetation during flooding periods using TerraSAR-X (X-band: HH polarised: 3.1 cm) , ALOS PALSAR (L-band: 23.5 cm) and RADARSAT-2 (C-band: 5.6 cm) from 17 December 2009 to 9 June 2013 with nearly identical image acquisition parameters to understand the backscattering behaviour of radar signals in the different environments such as (a) permanent water surface; (b) deciduous forest (dense, flooded); (c) deciduous forest (dense, non-flooded); (d) deciduous forest (sparse, flooded); and (e) cropland (White *et al*., 2015). The variation of backscattered signals from permanent water surface ranges from -27.08 to -17.27 dB, which leads to variation of -10 dB over the same incidence angle due to different surface roughness conditions, is due to wind effects and seasonal freezing in TerraSAR-X (X-band) as compared to variation of -4.5 dB (ranging from -20.45 dB to -15.96 dB) in ALOS-PALSAR (L-band). The optimum threshold value of backscattered signal to separate open surface water and non-water surface during flood detection is -13.4 dB for X-band and -14.3 dB for L-band time series SAR image data. The high variability of the backscattered signal from water surface for flood detection threshold is set for each of the scene in X-band for separating water surface and non-water surface areas. Backscattered variation in L-band and X-band are found identical for both flooded dense forest (X-band: -4.42 dB and L-band: -4.23 dB) and flooded sparse forest (X-band: -1.81 dB and L-Band: -1.62 dB), but in partially flooded cornfield, the backscattered difference between flooded and non-flooded conditions is nearly identical (X-band: -9.86 dB and L-band: -8.58 dB).

4. BI-STATIC AND MULTI-STATIC SPACE BORNE SAR SENSORS IN POLAR LEO ORBIT FOR SURVEILLANCE OF RIVER FLOODS AND DISASTER MANAGEMENT

Recently, bi-static radar has received interest in the development of space-borne bi-static and multi-static SAR sensors due its potential to reduce the revisit (repeat orbit) time for monitoring the changes on the earth surface for detecting surface water for flood monitoring and different radar missions depending upon the repeat orbit and SAR payloads on satellite. Space-borne bi-static or multi-static radar is an active microwave sensor (SAR) operating with transmitting and receiving antennae separated by a large distance, depending upon wavelength to avoid de-correlation and phase ambiguities (Verma *et al*., 2018). Space-borne bi-static SAR based on a small satellite (BISSAT) flying in formation are equipped with a receiving-only microwave system for receiving the backscattered / forward scattered radar signals from existing mono-static space-borne SAR. As a result, the baseline attains a minimum value at the poles, which requires a safety value to be maintained. Bi-static SAR system with close formation with existing SAR system provides the effective bi-static coverage to the test area. Small satellites are suitable for formation flying missions in LEO orbit, where a large number of small satellites serve as distributed sensors for a large distributed antenna sensor platform, or make a large distributed antenna aperture for imaging of earth surface for surveillance and monitoring of multi-missions and other applications (Krieger & Moreira, 2006).

A formation flying (FF) mission involves a set of spatially distributed satellites in the desired earth orbits. It is possible to launch multiple small satellites due to their small size and modular nature of sensors in order to accomplish a mission instead of a much bigger and costlier conventional satellite and its launching system. There are two possible configurations for space-borne bi-static and multi-static SAR imaging, which are active and semi-active configurations, as shown in Figure 3. Bi-static and multi-static SAR sensors in the semi-active / active configuration of flying formation of satellites in space orbits have many advantages such as (a) distributed functionality allows separation of radar payloads supporting the use of small and low cost SAR satellites; (b) satellite constellation allows modular design, where the

reuse of major blocks shortens the development time, increases the reliability and reduces the cost; and (c) satellite constellation allows re-configurability and scalability suitable for a broad spectrum of remote sensing applications (Lombardo *et al*., 2016).

Figure-3 : Bi-static or multi-static SAR configurations (Lombardo & Pastina, 2016).

In space-borne SAR systems, the antenna is considered as the eye of the radar system, which is responsible for the transmission of radar signals for backscattering from the Earth surface and reception of the backscattered radar signals to form radar images. Thus, antenna gain imposes challenges to transmit high power to obtain wide swath coverage and demands to develop lightweight reflector antenna with digital feed array for cost effective generation of a narrow and high gain antenna beam steerable in real time to the varying direction. This innovative SAR concept allows for the use of small satellite bus for shorter radar wavelength system (X, Ku or Ka-band) for achieving high gain antenna with smaller antenna for reducing the weight of the satellite payloads. The concept of passive SAR sensors further reduces the weight of SAR payloads due to only the receiver chain and much reduced power requirement of the SAR receiver as compared to the SAR transmitter. The concept of lightweight SAR payloads at different radar bands opens up the opportunity for the development of micro-passive SAR sensors (receivers) for its deployment in polar LEO orbit in flying formations or constellations of satellite for multiple space missions for surveillance and monitoring of the Earth surface. This concept can be achieved by placing the radar illuminator in geosynchronous orbit or MEO by combining active radar illuminator with one or more passive SAR receivers. The separation of the transmitter from the receiver hardware allows for the use of low-cost microsatellites passive SAR receiver for backscattered radar signals, thereby enabling the cost-efficient implementation of a sparse array SAR with multiple baselines (Krieger & Moreira, 2006).

The revisit times of the space-borne SAR sensors are very important for applications such as surveillance and monitoring of the Earth surface; risk and flood disaster management; and development of flood or landslide warning system. The near real-time detection and monitoring of floods by space-borne SAR sensors requires frequent revisit of the sensors. Satellite constellations have the potential to shorten the revisit times substantially by using bi-static or multi-static SAR sensors in fully active or semi-active configurations. The Earth rotates under the polar LEO orbit allowing space-borne SAR sensors to see every point at some point of time. Space-borne SAR sensors in the LEO orbit revisit more frequently the point on Earth surface by increasing the higher latitude of interest towards the pole as compared to equator. Although revisit to the Arctic region occurs daily for current SAR systems, the existing coverage, particularly in the time domain, is not significant for the totality of the Arctic region. Specifically, multiple SAR payloads optimally configured in number and orbital planes within a polar orbiting LEO constellation can provide maximum coverage performance of the Arctic region for surveillance. For the Indian sub-continent and Asian regions with flood prone areas close to the equatorial with lower latitude, space-borne SAR sensors revisit the orbit after few days (Cooper, 2013).

Walker constellations are used for the SAR constellation to reduce the revisit time of space-borne sensors by satellites systematically spacing circular orbits to meet the requirement of missions. There are four parameters to characterise a Walker constellation, which are (a) inclination (*i*); (b) total number of satellites (*T*); (c) total number of satellite orbital planes (*P*); and (d) spacing between satellites in adjacent planes (*F*). The Walker constellation notations of *i T*/*P*/*F* describe the constellation of SAR payloads. For example, the Walker constellation notation of 98.6 4/4/1 describes that there are four SAR satellites in

four separate planes inclined at 98.6° with *F*=1 for the phase difference of 90° ((360°/4) * 1). The Walker constellation notation of 80 6/3/1 describes that there are six total satellites in three orbital planes (two per plane) at inclinations of 80° with a phase differential of 1, which means phase differential in adjacent planes to equal 60° (360°/6 * 1) (Cooper, 2013).

If RADARSAT-2 is considered as a SAR sensor for monitoring the Arctic region, then the number of SAR payloads within a single orbital plane of RADARSAT-2 increase to the limit of eight sensors due to orbital period of 100.7 min. The time to transit 48° of latitude of the Arctic region by RADARSAT-2 is determined as 13.3% of a complete orbit. As the orbital period for a full 360° orbit is 100.7 min, the estimated time to cover the Arctic region for each SAR satellite: 0.133 * 100.7 min or 13.4 min. Thus, the Arctic Circle will be in view of a SAR payload for 13.4 min. The theoretical minimum number of payloads to persistently monitor the Arctic region from an orbital plane is optimised for resolution and coverage (RADARSAT-2): 100.7 min / 13.4 min = 7.5. This means that eight SAR payloads are theoretically necessary to constantly view at least part of the Arctic Circle from a single orbital plane (Cooper, 2013). Figure 4 (a), (b) and (c) describe Polar orbits, Walker Constellation of 80 6/3/1: 6 satellite in three separate planes (two per orbiting plane), and view of all eight SAR sensors in a single polar orbital plane for the Arctic region respectively.

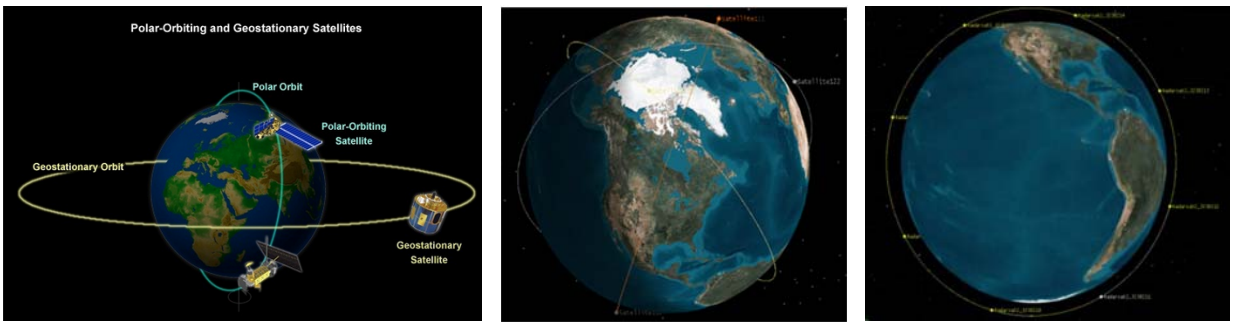

(a) Polar Orbit **(b) Walker constellations** **(c) View of eight SAR satellites**

Figure 4: View of polar orbit and SAR constellations (Cooper, 2013).

The German Space Agency developed TerraSAR-X in the sky as the first bi-static radar with repeat orbit cycle of 11 days, known as second generation SAR sensors, by launching the TanDEM-X SAR system for global DEM generation. The first multi-static space-borne SAR sensor, COSMO-SkyMed-1/4 with constellation of four satellites, is operational to provide resolution of 1 m with four days repeat orbit. ISRO also launched its first space-borne SAR sensor at C-band in 2012 as RISAT-1 with 25 days of repeat cycle of the orbit, which is further followed by X-band RISAT-2 with capability of 14 days of repeat cycle of the orbit and near revisit period of three to four days. The distributed functionality of bi or multi-static SAR sensors supports small and low cost satellite (Krieger and Moreira, 2006).

In the semi-active configuration of bi-static or multi-static SAR system, there will be one active SAR with transmitter and receiver as an active illuminator with one or more passive SAR receiver as shown in Figure 5, where Walker constellations of passive SAR payloads (receivers) in polar LEO orbit can be used for constellations of satellites in different circular planes for frequent revisit of SAR sensors for near real-time monitoring of floods for disaster management mission (Cooper, 2013). This configuration requires deployable antenna of smaller sizes and reduced power demands of passive receiver. This potential leads to enable an accommodation of many SAR payloads on micro-satellites in LEO orbit, which reduces the revisit time of SAR sensors to hours. In this semi-active configuration, the SAR sensor from communication or navigational satellites illuminate the Earth surface with very large radar footprint for backscattered signals, which are received by multi-SAR sensors (receivers) placed in LEO orbit for radar imaging. This results into highly reconfigurable and scalable satellite constellations for various remote sensing missions including surveillance as well as risk and disaster management system in the sky. The flexible imaging geometry of space-borne SAR sensors in multi-static configuration allows

multi-missions to dynamically adapt to different operational tasks. In the future, SAR concepts for higher orbits in MEO or geosynchronous mission require very large antenna apertures with beam steering capability as the radar illuminator requires apertures on the order of several hundreds of square metres for transmitting radio frequency (RF) signals up to 60 kW. For geosynchronous SAR missions, a large deployable hexagonal antenna of 30 m by 30 m antenna aperture is deployed, which is integrated with the active electronics for proper beam formation and transmit / receive signal amplification. The MEO SAR system architecture requires a smaller antenna of the order of 400 m^2 with flexibility in antenna geometry and lower power as compared to the geosynchronous SAR system concept. There are a number of emerging technologies for the development of ultra-lightweight antenna in progress for MEO or GEO radar illuminator and to reduce mass, power of lightweight small antenna to make LEO SAR receiver mission affordable to launch as constellation of satellites (Edelstein *et al*., 2005).

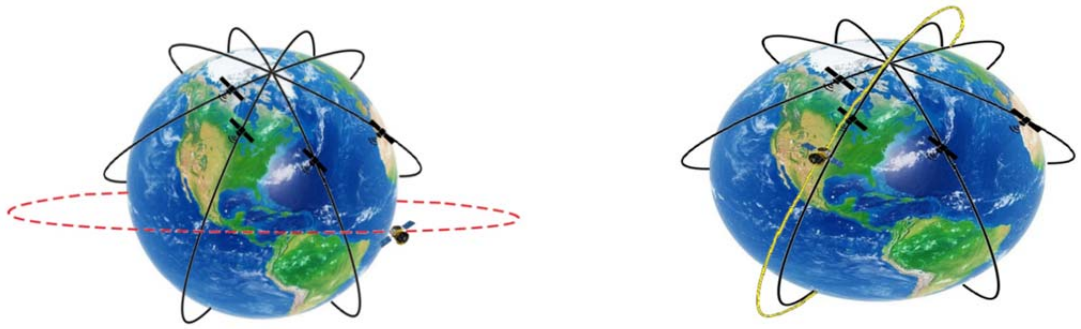

Geostationary radar illuminator with LEO receivers **LEO / MEO radar illuminator with LEO receivers**

Figure 5: Frequent monitoring of the Earth surface with SAR satellite constellation.

5. CONCLUSION

Space-borne bi-static and multi-static SAR configurations have the potential for different applications such as frequent monitoring of selected areas of the Earth surface (flood, landslide, earthquake), cross track interferometry, differential interferometry, wide swath high resolution imaging and scene classification / traffic monitoring. The following potential of bi-static and multi-static configurations can be used for different applications for surveillances of the Earth surface such as:

(a) Several SAR configurations are appropriate for real-time flood detection and management.

(b) A combination of geostationary radar illuminator with multiple SAR receivers in LEO orbit can also perform multiple missions depending upon the constellation of micro / small SAR receiver satellites.

(c) The configuration of constellation of SAR receivers can be upgraded or reconfigured.

Based on the regular events of flood occurrence in the Asian region causing disasters, a collaborative platform can be evolved amongst different space agencies in the Asian region for the development of near real-time surveillance and monitoring of floods, such as flood warning system as well as risk reduction and disaster management systems considering the recent river flooding and urban flooding due to very heavy rainfall characteristics and global climatic change in the region.

REFERENCES

Anand, J., Gosain, A.K., Khosa, R. & Srinivasan, R. (2018). Regional scale hydrological modeling for prediction of water balance analysis trends in stream flow and variation in stress flow: the case study of Ganga River basin. *J. Hydrol. Recent Stud.*, **16**: 32-53.

Benn, D.I. & Owen, L.A. (1998). The role of the South Asian monsoon and the mid-latitude westerlies in controlling Himalayan glacial cycles: review and speculative discussion. *J. Geol. Soc.*, **155**: 353-363.

Brisco, B. (2015). Mapping and monitoring of surface water and wet land with synthetic aperture radar.

Remote Sensing of Wetlands: Applications and Advances, CRC Press, Boca Raton, Florida.

Cooper, C.W. (2013). *Enhancing Arctic Surveillance with Spaced-Based Radars*. Thesis, Master of Science in System Technology (Command, Control & Communication), Naval Postgraduate School, Monterey, California

Das, S., Mitra, A. & Shukla, A.K. (2010). Rain attenuation modelling in the 10-100 GHz frequency using drop distribution for different climatic zones in tropical India. *Prog. Electromagn. Res. B*, **25**: 211 -224.

Edelstein, W., Madsen, S., Moussessian, A. & Chen, C. (2005). Concepts and technologies for synthetic aperture radar from MEO and geosynchronous orbits. *Proc. SPIE*, **5659**: 195-205

Goswami, D.C. (1985). Brahmaputra River, Assam, India: Physiographic, basin denudation and channel aggradation. *Water Resour. Res. Am. Geophys. Union,* **21**: 959-978.

IPCC Press Release (2018). Summary for Policymakers of IPCC: Special Report on Global Warming of 1.5 degree centigrade approved by governments. *Intergovernmental Panel on Climate Change (IPCC),* 2018/24/PR, Incheon, Republic of Korea, pp 1-4, 8 October.

Jassal, B.S., Verma, A.K. & Singh, L. (1994). Rain drop size distribution and attenuation for Indian climate. *Indian J. Radio Space Phys.*, **23**: 193-196.

Jussi M. (2015). *Synthetic Aperture Radar Based Flood Mapping in the Alam-Pedja Nature Reserve in Years 2005-2011*. Master thesis, Geo-informatics and Cartography, Institute of Ecology and Earth Science, University of Tartu, Estonia.

Krieger, G. & Moreira, A. (2006). Space-borne bi- and multi-static SAR: Potential and challenges. *IEEE Proc. Radar Sonar Nav.,* **153**: 184-198.

Liu, C. (2016). *Analysis of Sentinal-1 SAR data for Mapping Standing Water in Twente Region*. Thesis, M.S. in Geo-Informatics Science and Earth Observation, University of Twente, Netherlands.

Lombardo P. & Pastina D. (2016). Bi-static and multi-static radar. *2016 Eur. Radar Conf.,* London.

Martinis, S. & Rieke, C. (2015). Backscatter analysis using multi-temporal and multi -frequency SAR data in the context of flood mapping at River Saale, Germany. *Int. J. Remote Sens.,* **7**: 7732-7752.

Schmitt, A. & Brisco, B. (2013). Wetland monitoring using the curvelet -based change detection method on polarimetric SAR imagery. *Water*, **5**: 1036-1051

Susantono, B. & Schellnhuber, H.J. (2017). *A Region at Risk : The Human Dimensions on Climate Change in Asia and the Pacific*. Asian Development Bank (ADB) Report Publication, Manila, Philippines.

Townsend, P.A. (2002). Relationship between forest structure and the detection of flood inundation in the forested wetlands using C-band SAR. *Int. J. Remote Sens.,* **22**: 443-460.

Verma A.K., Nandan R., and Verma A. (2017). Space - borne synthetic aperture radar (SAR) system for real-time surveillance of earth surface for detection and management of flood disaster in Indian sub-continent. *38th Asian Remote Sens. Conf.,* New Delhi ; (2018) *J. Appl. Math. Comput.*, **2**:166-177.

Verma A.K. & Jha K.K. (1996). Rain drop size distribution model for Indian climate. *Indian J. Radio Space Phys.,* **25**:15-21.

Vilches, P.J.(2013). *Detection of Area Affected by Flooding River Using SAR Images*. Master in Space Applications for Emergency Early Warning and Response. CONOE, IG.

White, L., Brisco, B., Dabboor, M., Schmitt, A. & Pratt, A.(2015). A collection of SAR methodologies for monitoring wetlands. *Int. J. Remote Sens.,* **7**: 7615-7645

Zheng, H., Chiew, H.S.F., Charles, S. & Podger G. (2018). Future climate and runoff projections across South Asia from CMIP5 global climate models and hydrological modeling. *J. Hydrol. Recent Stud.,* **18**: 92-109.

DEVELOPMENT OF HF MODELLING IN PENINSULAR MALAYSIA DURING THE RISE OF SOLAR CYCLE 24

Rafidah Abd Malik[*1], Mardina Abdullah[2], Sabirin Abdullah[2], Yokoyama Tatsuhiro[3] & Clara Y. Yatini[4]

[1]Communications Branch, Science & Technology Research Institute for Defence (STRIDE), Malaysia
[2]Space Science Centre (ANGKASA), Universiti Kebangsaan Malaysia (UKM), Malaysia
[3]National Institute of Information and Communications Technology (NICT), Japan
[4]Space Science Centre, Indonesian National Institute of Aeronautics and Space (LAPAN), Indonesia

[*]Email: rafidah.abdmalik@stride.gov.my

ABSTRACT

The modelling of maximum useable frequency (MUF) is important in high frequency (HF) radio frequency management. Thus, the aim of this study was to develop MUF models and verify the models obtained with experimental data. The development of the models were carried out in Peninsular Malaysia during the rise of Solar Cycle 24 (2009 to 2011). The modelling parameters were the ionospheric F2-layer parameters obtained from the frequency modulated-continuous wave (FM-CW) ionosonde at Kototabang, Indonesia (0.2 ºS, 100. 3ºE; 10.36 ºS magnetic latitude), and sunspot number (SSN) data obtained from Space Weather Services, Bureau of Meteorology, Australia. The experimental MUF data was obtained from STRIDE, Ministry of Defence, Malaysia. The regression method was used to derive the mathematical models. MUF_{Time} *and* MUF_{SSN} *were derived from the regression method. Observation from the comparison of plots between* MUF_{Time} *and* MUF_{SSN} *with MUF experimental revealed that the magnitudes for* MUF_{Time} *and* MUF_{SSN} *with MUF experimental were of similar trend. The mean absolute error (MAE) between* MUF_{Time} *and* MUF_{SSN} *with MUF experimental were 0.77 and 0.86 respectively. In order to obtain HF operating frequencies, both models would need to be combined to implement MUF prediction.*

Keywords: *High frequency (HF); maximum usable frequency (MUF); MUF modelling; ionospheric F2 layers; sunspot number (SSN); regression method.*

1. INTRODUCTION

High frequency (HF) radio signal propagates using the ionosphere as a transmission medium and it is important for long range communications systems, especially in the military (Raab *et al.*, 2002; Mudzingwa *et al.*, 2013; Mudzingwa & Chawanda, 2018). Militaries use HF radio for tactical and strategic purposes, and for certain military scenarios. For civilian users, HF radio is used in the occurrence of any disaster, such as hurricanes, tornados and earthquakes. Therefore, frequency management is important to determine the right frequencies to establish reliable communication over a given path. The HF propagation medium, namely the ionosphere, is space-time variable. Hence, the variation of the ionosphere makes it impossible to rely upon a single assigned frequency since a frequency that may provide successful communication now may not achieve so an hour later (Hargreaves, 1992; Raab *et al.*, 2002). This phenomenon of HF propagation behaviour is dependent on the transmitted frequency, the properties of the ionosphere and solar activity indices, such as sunspot number (SSN) and solar flux (F10.7) (Maslin,1987; Raab *et al*., 2002; Goodman, 2005; Zhao & Li, 2010; Mudzingwa *et al*., 2013; Mudzingwa & Chawanda, 2018).

The HF radio frequency that is used for transmission in ionospheric prevailing conditions is called maximum usable frequency (MUF) (Bradley, 1973; Maslin, 1987; Mudzingwa *et al*., 2013;

Mudzingwa & Chawanda, 2018). *MUF*(3000)F2 is a MUF that can be received at a distance of 3,000 km when reflected by the ionosphere (Kouris *et al*., 2000; Adeniyi *et al*., 2003; Wichaipanich *et al*., 2013; Nagar *et al*., 2015). Liu *et al*. (2004) reported that the accuracy of MUF modelling is important for managing and designating the HF radio frequency. Ionospheric parameters, especially F2-layer parameters, are the key factor in the modelling of MUF (Kouris & Nissopoulos, 1994; Liu *et al*., 2004; Sharma *et al*., 2008; Souza *et al*., 2013). Meanwhile, solar activity indices are important in determining the variation of MUF within an hour, throughout the day, from season to season and within the 11-year solar cycle (Kouris & Nissopoulos, 1994; Sharma *et al*., 2008; Hadi & George, 2011; Joshua & Nzekwe, 2012; Wichaipanich *et al*., 2013). During the past few decades, there have been many published studies on MUF model development, including empirical models (Bradley, 1973; Kouris & Nissopoulos, 1994; Earle & Desourdis Jr, 1994; Joshua & Nzekwe, 2012; Lu & Liu, 2009; Chao *et al*., 2011).

To date, there has been no comprehensive study on MUF modelling and prediction in the Malaysian region. However, there have been several publications about HF prediction done by Zain & Abdullah (2000) and Abdullah *et al*. (2000). There have been also publications on HF data communication done by Sha'ameri & Boashash (1999) and Sha'ameri (2001, 2006, 2010). Nevertheless, of late, there have been a few studies on MUF in the Malaysian environment (Malik *et al*., 2010, 2011, 2014, 2015, 2016, 2017). Therefore, the main aim of this study is to develop MUF models in the Malaysian environment, and for verification purposes, the MUF models have been compared with MUF experimental. This paper introduces two models, which are MUF model based on ionospheric F2-layer and MUF model based on solar index, i.e., SSN. This study mainly contributes to the research on HF radio communication in the equatorial region / Southeast Asia (SEA), because the equatorial ionosphere has special features and consequently poses serious threats to communications and navigation systems as compared to the ionosphere in temperate regions (Akala *et al*., 2011). Furthermore, the equatorial and low latitude F region ionosphere presents some peculiar characteristics when compared to the middle and high latitude ionosphere (Oyekola & Fagundes, 2012; Athieno *et al*., 2015).

2. METHODOLOGY

The F2-layer parameters and SSN data have been designated to produce the MUF models. The F2-layer parameters were obtained from the frequency modulated-continuous wave (FM-CW) ionosonde at Kototabang, Indonesia (0.2 ºS, 100.3 ºE; 10.36 ºS magnetic latitude), which is located at the equator. It is one of the five SEALION (South East Asia Low-Latitude Ionospheric Network) ionosondes (Takashi *et al*., 2009). SEALION is an ionospheric observation network in SEA that is handled by the National Institute of Information and Communication Technology (NICT), Japan. The parameters used for the modelling were critical frequency of F2-layer (*fo*F2), height of F2-layer (*hm*F2) and *MUF*(3000)F2. The monthly SSN data was obtained from Space Weather Services, Bureau of Meteorology, Australia (Bureau of Meteorology, 1998). The MUF experimental data that was used for verification and comparison purposes were obtained from HF transmission tests conducted by the Science and Technology Research Institute for Defence (STRIDE), Ministry of Defence, Malaysia. The HF transmission tests were conducted between April 2009 to September 2011 at several places in Peninsular Malaysia, namely Kajang (101.8 °E, 2.98 °N) and Batu Arang (101.8 °E, 3.53 °N) in Selangor, and Lumut (100.6 °E, 4.22 °N) in Perak (Malik *et al*., 2010). The observation and experimental data in this study was obtained during Solar Cycle 24, which is a cycle that has risen much more slowly than any other space age solar cycle, with the solar activity in 2013 being the weakest peak in 100 years (Komitov & Kaftan, 2013; Hao *et al*., 2014; Kilpua *et al*., 2014).

3. RESULTS & DISCUSSION

The approach to MUF modelling adopted for this study was the regression method. This method is the most commonly used technique for investigating the relationship between two variables (Liu *et al*.,

2004; Sharma *et al*., 2008; Shanableh & Assaleh, 2010; Hadi & Aziz, 2012; Joshua & Nzekwe, 2012; Nagar *et al*., 2015). Before constructing the statistical models, it is important to consider the statistical relationship between the dependent and independent variables. This was carried out using correlation analysis, i.e., scatter plot between *MUF*(3000)F2 (dependent) and all the three independent variables namely *fo*F2, *hm*F2, and SSN. The results of the correlation analysis are illustrated in Figure 1. The observation from the scatter plots proves that correlation exists between MUF and all the three parameters. The correlation coefficient (*R*) shows strong correlation between MUF and *fo*F2 (0.96), followed by MUF and *hm*F2 (0.72), while the correlation between MUF and SSN is moderate (0.67). The *R* values from all the scatter plots indicate there are strong correlations between *MUF*(3000)F2 with *fo*F2 and *hm*F2, and moderate correlation between *MUF*(3000)F2 and SSN. The correlation between *MUF*(3000)F2 and SSN is moderate due to low solar activity from 2009 to 2011. However, SSN is considered in the equation because SSN is an important parameter in HF modelling.

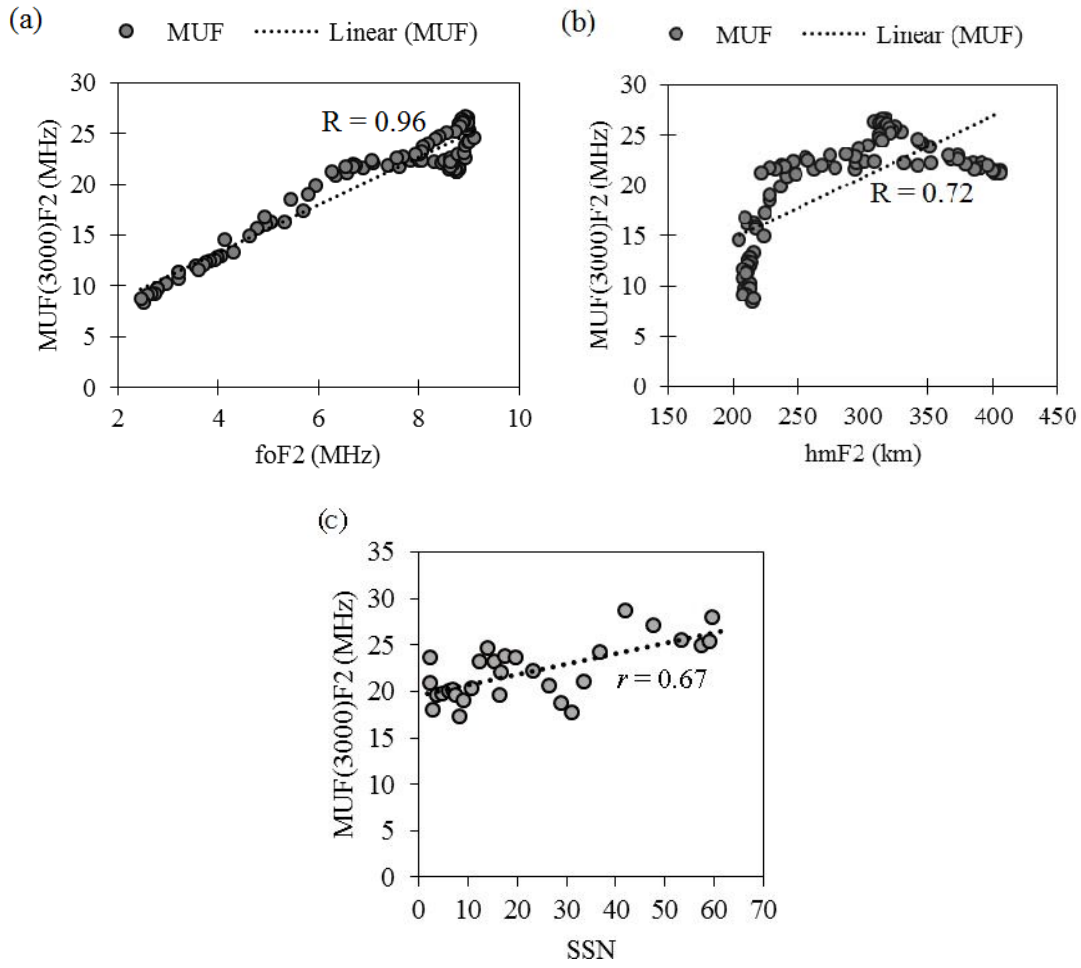

Figure 1: Scatter plots and *R* values between MUF with (a) foF2 (b) hmF2 and (c) SSN.

The following is the MUF modelling results; three regression methods have been implemented to obtain the MUF models in Peninsular Malaysia. The first regression model is a multiple stepwise regression to describe the relationship involving more than one independent variable. The goal of multiple regressions is to assess the relationship between a dependent variable and several independent variables. For this study, the dependent variable is *MUF*(3000)F2, while the independent variables are *fo*F2 and *hm*F2. The outcome is the formation of regression equations between the dependent variable and two independent variables as follows:

$$\text{Model 1} = A + B(foF2) \quad (1)$$

$$\text{Model 2} = A + B(foF2) - C(hmF2) \quad (2)$$

Using the multiple stepwise regressions, *A*, *B*, and *C* are regression coefficients. After performing the regression, there are two potential MUF models, which are Models 1 and 2, as in Equations 1 and 2 respectively. A comparison of Models 1 and 2 with MUF experimental is illustrated in Figure 2. The plots show that all the magnitudes are in the similar trend, but the plots for Models 1 and 2 are higher than MUF experimental. The reason for MUF from Models 1 and 2 being higher than MUF experimental is because of the different propagation distance and magnitude dip latitude between Peninsular Malaysia and Kototabang, Indonesia. The distance of stations in MUF experimental is approximately 200 km, while *MUF*(3000)F2 from the models are programmed for propagation distance of 3,000 km. The frequency is lower when the distance between the transmitter and receiver is nearer, while the frequency is higher when the propagation distance is much longer (Barringer & Springer, 1992; Lu & Liu, 2009; Wang *et al*., 2010). The different magnitude dip latitude between the areas of study that are located in Peninsular Malaysia (11.18°) and area of ionospheric parameters, namely Kototabang, Indonesia (10.36°) also cause a significant difference between Models 1 and 2 with MUF experimental. Thus, the difference in latitude affects ionospheric parameters even if it changed only by 1° (Zain *et al*., 2006).

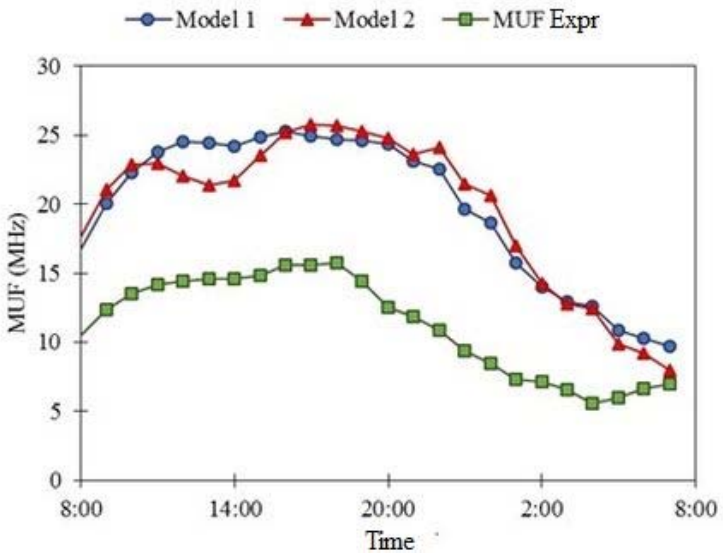

Figure 2: MUF experimental compared with Models 1 and 2 obtained from multiple stepwise regressions.

Improvements were made to the MUF models in Equations 1 and 2 to get the models to fit well with the Malaysian environment. The scaling method was used to lower the models to MUF experimental. Dongen (2004) and Lohninger (2012) stated that the scaling method changes the original values to different values, involving replacement data and the scale of changes, whether for enlargement or reduction of data. Analysis of error through mean absolute error (MAE) was used to analyse the errors between MUF experimental with Models 1 and 2. After data scaling, Model 1 is selected for further modification because when levelled with MUF experimental, as shown in Figure 3, the MAE for Model 1 is lower than Model 2, i.e., 0.96 and 1.32 respectively.

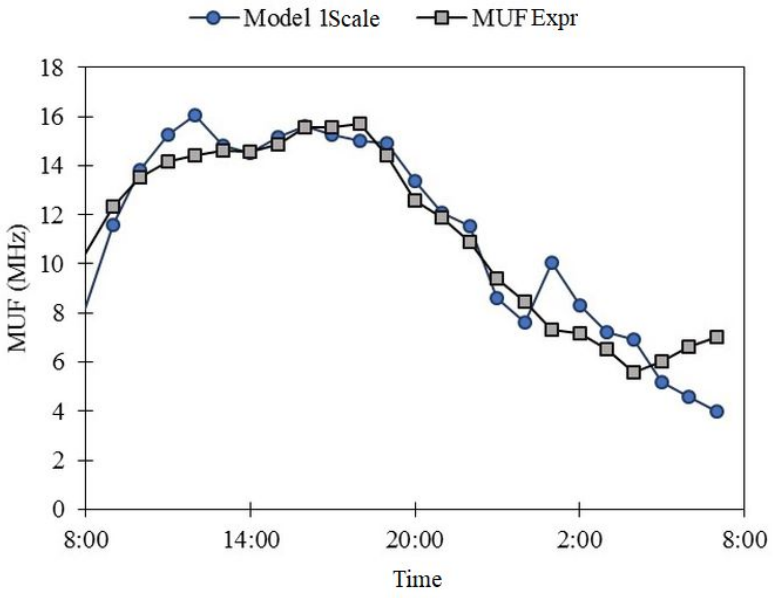

(a)

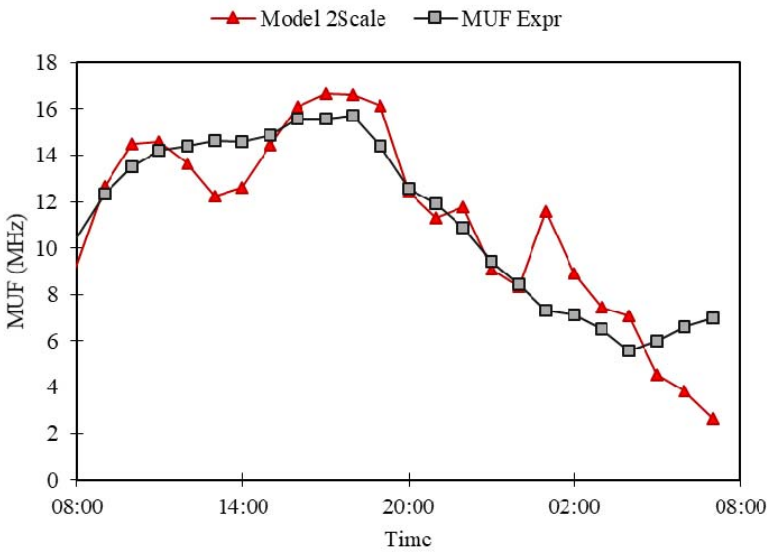

(b)

Figure 3: Models (a) 1 and (b) 2 that have been modified, which are levelled with MUF experimental.

Polynomial regression as shown in Figure 4 was implemented to Model 1 to get a new model that fitted with MUF experimental and was based on time of the day. Polynomial regression is used when the independent parameter is not linear, that is, the scatter plot is non-linear or curvilinear (Ostertagová, 2012; Sinha, 2013). According to Daehler *et al*. (1986) and Hanbaba (1998), a model that is based on daily variation according to time of the day is often used to design HF radio systems to predict the HF frequency. According to Equation 1, Model 1 only consists of *fo*F2 parameters, so it indicates that *fo*F2 is the most suitable parameter for MUF modelling for this study. Lakshmi (1994) stated that the increase of *fo*F2 values will increase the values of MUF, but the increase of *hm*F2 values will degrade the MUF values. Therefore, *hm*F2 becomes important in determining MUF values when the link distance is more than 1,000 km, while for short links, MUF is only determined by *fo*F2. The importance of *fo*F2 in determining the MUF value is also expressed by Liu *et al*. (2004), Rush *et al*. (1974) and Xue & Boon (2004).

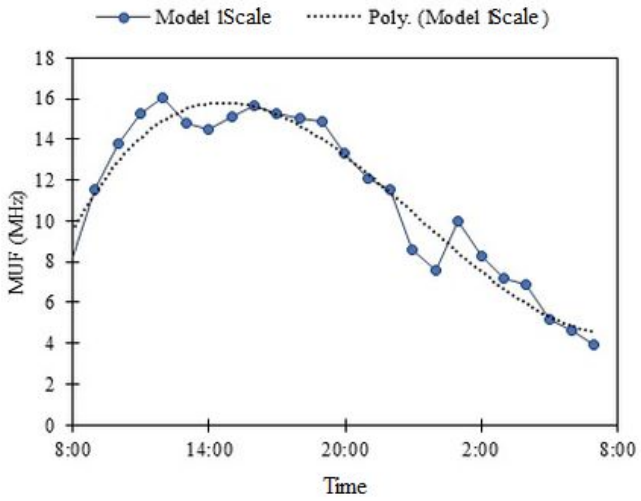

Figure 4: Polynomial regression of Model 1.

The polynomial regression equation was derived for up to the 3rd order as in Equation 3, with value of *R* being 0.97, which is strong correlation at the 3rd order polynomial.

$$MUF_{Time} = -A + B*t - C*t^2 + D*t^3 \quad (3)$$

Using Equation 3, approximation of hourly MUF values could be determined, where *t* is the number times of day, while *A*, *B*, *C* and *D* are regression coefficients. Figure 5 shows the comparison between MUF experimental and model MUF_{Time}, where it was found that the MAE between the experimental and prediction is 0.77.

The plots from Figure 5 show MUF that is constantly changing over a 24 h period. The MUF is high during the day, especially during noon and evening, which reaches the peak value at 1500. Then the MUF starts to drop before sunset at 1800 and gets lower at dawn until before sunrise (0600). The figure shows that both plots of MUF_{Time} and MUF experimental vary according to the time of day (TOD). This is because HF radio frequency is influenced by TOD and days of year (DOY), which affects the electrons density in the ionosphere that is changing according to solar activity (Gonzalez *et al*., 2007; Hadi & Aziz, 2012). During the day time, the electron density in the ionospheric layer is high and this allows higher frequency of HF radio to be reflected. Contrarily in night time, electron density is lower, and thus, absorbed HF radio waves are fewer, which causes lower frequencies being transmitted better. Hence, MUF is higher during the day and lower during the night until dawn.

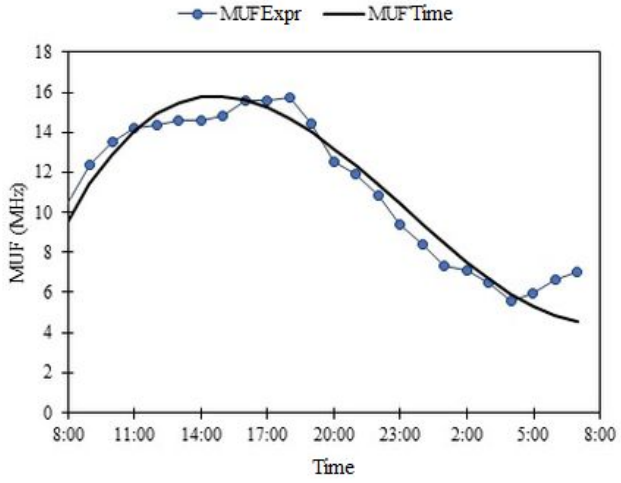

Figure 5: Verification of MUF_{Time} by comparison with MUF experimental.

Further regression modelling was carried out to complete the MUF model using a linear approximation to describe the relationship between MUF and SSN, in which SSN is used to estimate MUF values for each month. It is important to find variations of MUF based on SSN because HF predictions are usually based on estimates of SSN. Higher SSN allows for better HF transmission between two points, but too high SSN will disturb the transmission of HF signals (Dong & Li, 2007; Blaunstein & Plohotniuc, 2008; Keller, 2010). Thus, it indicates that SSN influences MUF values (Malik *et al*., 2010, 2014), so to make MUF predictions, SSN must be considered in the MUF modelling:

$$MUF_{SSN} = A + B*SSN \quad (4)$$

Using a linear regression relation, coefficients *A* and *B* for MUF_{SSN} were calculated. The variable SSN was monthly median data for year 2009 to 2011, so from Equation 4, monthly MUF value could be estimated. Subsequently, the MAE between MUF experimental and MUF_{SSN} is 0.86. Figure 7 is the plots of MUF_{SSN} compared with MUF experimental.

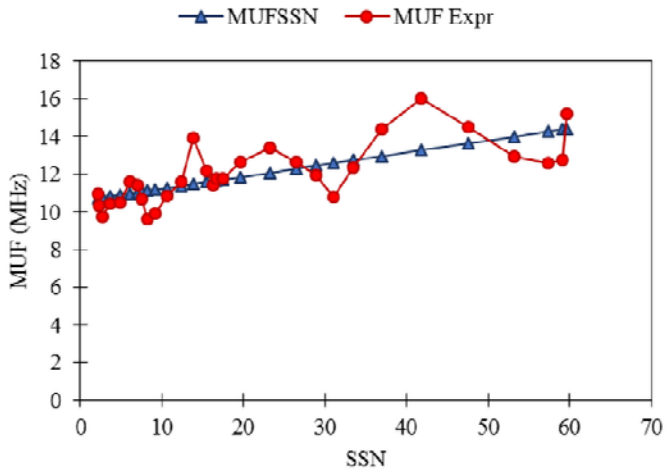

Figure 6: Validation of MUF_{SSN} by comparison with MUF experimental.

As a whole, to make MUF predictions, the two models, namely MUF_{Time} and MUF_{SSN} ,must be used in the prediction, as illustrated in Figure 8. The figure illustrates that the combination of MUF_{Time} and MUF_{SSN} will produce the MUF prediction. The HF operating frequencies that will be used in HF transmission will be obtained from MUF prediction in the form of hourly monthly median values.

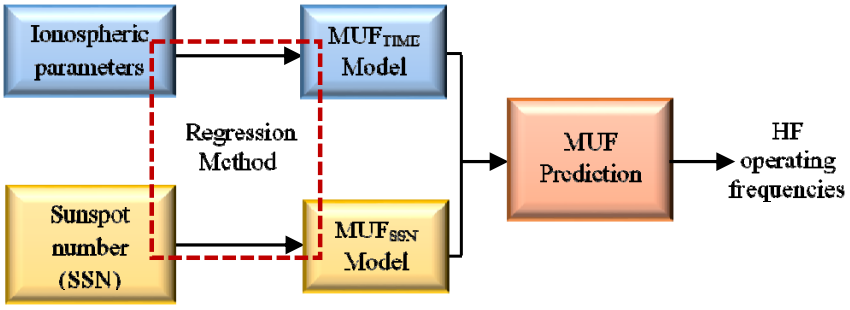

Figure 7: The MUF prediction process illustrating the two models involved, namely MUF_{TIME} and MUF_{SSN}.

4. CONCLUSION

The purpose of this study was to develop MUF models in Peninsular Malaysia. The MUF models are based on ionospheric F2-layer parameters, namely *fo*F2, *hm*F2 and *MUF*(3000)F2, and solar activity, i.e., SSN. Statistical methods, namely linear, multiple stepwise and polynomial regressions, were implemented to develop the MUF models. Based on the modelling, two models were derived from regression method, which are MUF_{Time} and MUF_{SSN}. MUF_{Time} predicts MUF values based on time of the day, while MUF_{SSN} predicts MUF values on monthly basis based on SSN. Analysis of MAE indicated that the MAE between the predicted MUF_{Time} and hourly monthly median MUF experimental is 0.77, while the MAE between the predicted MUF_{SSN} and monthly median MUF experimental is 0.86. In order to obtain HF operating frequencies, both models would need to be combined to implement MUF prediction. The present study fills a gap in the study of HF communications systems especially MUF modelling and prediction in the Malaysian environment. However, further studies and continued efforts need to be carried out in order to develop better MUF models, particularly in Malaysia and the equatorial region in general.

REFERENCES

Abdullah, M., Zain, A.F.M. & Jamaludin, M.Y. (2000). Forecasting of short-term radio propagation using expert systems. *Proc. Int. Conf. Artificial Intelligence Sci. Technol., AISAT'2000.* Hobart, Australia.

Adeniyi, J.O., Bilitza, D., Radicella, S.M. & Willoughby, A.A. (2003). Equatorial F2-peak parameters in the IRI model. *Adv. Space Res.,* **31**: 507–512.

Akala, A.O., Somoye, E.O., Adeloye, A.B. & Rabiu, A.B. (2011). Ionospheric foF2 variability at equatorial and low latitudes during high, moderate and low solar activity. *Indian J. Radio Space Phys.,* **40**: 124–129.

Athieno, R., Jayachandran, P.T., Themens, D.R. & Danskin, D.W. (2015). Comparison of observed and predicted MUF(3000)F2 in the polar cap region. *Radio Sci.,* **50**: 509–517.

Barringer, M.H. & Springer, K.D. (1992). *Radio Wave Propagation, 8th. Ed*., NAB, Washington, DC.

Blaunstein, N. & Plohotniuc, E. (2008). *Ionosphere and Applied Aspects of Radio Communication and Radar*. CRC Press, Boca Raton, Florida.

Bradley, P. (1973). A simple model of the vertical distribution of electron concentration in the ionosphere. *J. Atmos. Sol-Terr. Phy.*, **35**: 2131–2146.

Bureau of Meteorology, (1998). Monthly Sunspot Numbers. Available at: http://www.sws.bom.gov.au/ Solar/1/6 (Last access date: 15 June 2009).

Chao, L., Xiaopeng, Y., Feng, W., Hengyang, Z. & Yunjiang, L. (2011). A frequency prediction method based on estimation of the ionospheric characteristics. *Proc. Int. Conf. Elect. Mech. Engin. Inform. Technol., (EMEIT) 2011*, **8**: 3881–3884.

Daehler, M., Division, S.S. & Branch, I.E. (1986). Sounder updates for statistical model predictions of maximum usable frequencies on HF sky wave paths. *Radio Sci.*, **21:** 1001–1008.

Dong, B. & Li, S. (2007). Current status and developing tendency for high frequency communications. *Proc. Int. Conf. Inform. Elect. Engin.*, **1**: 10–17.

Dongen, H.P.A.V. (2004). Comparison of mathematical model predictions to experimental data of fatigue and performance. *Aviat. Space Environ. Med.,* **75**: A15–A36.

Earle, G.D. & Desourdis Jr, R.I. (1994). Advanced modeling of HF radio propagation. *Proc. Int. Conf. Mil. Comm., MILCOM'94*, pp. 895–899.

Gonzalez, G., Hanna, R., Hong, L. & Jones, W.L. (2007). HF communications analysis for varying solar and seasonal conditions. *Proc. Int. Conf. Southeast Con 2007*, pp. 182–186.

Goodman, J.M. (2005). Operational communication systems and relationships to the ionosphere and space weather. *Adv. Space Res.,* **36**: 2241–2252.

Hadi, K.A. & Goerge, L.E. (2011). A simplified mathematical model to calculate the maximum usable frequencies over Iraqi territory. *Diyala J. Pure Sci.,* **7**: 120–129.

Hadi, K.A. & Aziz, A.Z. (2012). Studying the impact of the solar activity on the maximum usable frequency parameter over Iraq territory. *IOSR J. Comput. Eng.*, **5**: 35–39.

Hanbaba, R. (1998). Performance prediction methods of HF radio systems. *Ann. Geophys.*, **41**: 715–742.

Hao, Y.Q., Shi, H., Xiao, Z. & Zhang, D.H. (2014). Weak ionization of the global ionosphere in solar cycle 24. *Ann. Geophys.,* **32**: 809–816.

Hargreaves, J.K. (1992). *The Solar-Terrestrial Environment*. Cambridge University Press, New York.

Joshua, E.O. & Nzekwe, N.M. (2012). foF2 correlation studies with solar and geomagnetic indices for two equatorial stations. *J. Atmos. Sol-Terr. Phy.*, **80:** 312–322.

Keller, J. (2010). Military HF radio communications may prove effective for Internet relay chat in land, sea, and air applications. *Mil. Aerosp. Electron.*, **21:** 9-19.

Kilpua, E.K.J., Luhmann, J.G., Jian, L.K., Russell, C.T. & Li, Y. (2014). Why have geomagnetic storms been so weak during the recent solar minimum and the rising phase of cycle 24? *J. Atmos. Sol-Terr. Phy.*, **107**: 12–19.

Komitov, B. & Kaftan, V. (2013). The sunspot cycle no. 24 in relation to long term solar activity variation. *J. Adv. Res.*, **4**: 279–282.

Kouris, S.S., Fotiadis, D.N. & Hanbaba, R. (2000). On the day-to-day variation of the MUF over Europe. *Sol., Terr. Planet. Sci.*, **25**: 319–325.

Kouris, S.S. & Nissopoulos, J.K. (1994). Variation of foF2 with solar activity. *Adv. Space Res*, **14**: 51–54.

Lakshmi, D.R. (1994). Tropical ionosphere and radio communications. *Proc. Int. Conf. Indian Nat. Scie. Acad. Part A 60*, New Delhi, India, pp. 243–262.

Liu, L., Weixing, W. & Ning, B. (2004). Statistical modelling of ionospheric foF2 over Wuhan. *Rad. Sci.*, **39**: 1–10.

Lohninger, H. (2012). Fundamental of Statistics. *Scaling of Data*. http://www.statistics4u.com /fundstat_eng/cc_scaling.html (Last access date: 26 June 2016).

Lu, J. & Liu, H. (2009). Modelling and simulations of high frequency propagation over China Sea-surface. *Proc. Int. Conf. Inform. Sci. Eng. (ICISE) 2009,* pp. 2653–2657.

Malik, R.A., Abdullah, M., Abdullah, S. & Homam, M.J. (2014). The influence of sunspot number on high frequency radio propagation. *Proc. Int. Conf. Asia-Pacific Appl. Electrom., APACE 2014*, pp. 107–110.

Malik, R.A., Abdullah, M., Abdullah, S. & Homam, M.J. (2016). Comparison of maximum usable frequency (MUF) variability over Peninsular Malaysia with IRI model during the rise of solar cycle 24. *J. Atmos. Sol-Terr. Phy.*, **138–139**: 87–92.

Malik, R.A., Abdullah, M., Abdullah, S., Homam, M.J., Yokoyama, T. & Michi, N. (2015). Ionospheric empirical model: Initial approach to MUF modeling in the Malaysian region. *Proc. Int. Conf. Space Sci. Commun., ICONSPACE 2015,* pp. 252–255.

Malik, R.A., Abdullah, M., Abdullah, S., & Homam, M.J. (2017). Comparison of measured and predicted HF operating frequencies during low solar activity. *In* Suparta, W., Abdullah, M. & Ismail, M. (Ed.) *Space Science and Communication for Sustainability*, Springer, Berlin, pp. 73–86.

Malik, R.A., Khamis, K., Zakariya, A.S., Tompang, A., Mohamed, H.T., Kamal, M.R.A., Rajab, A.R., Zahary, N., Hambali, H., Mustafa, M. & Zuraini, M. (2010). Determination of maximum usable frequency (MUF) for high frequency (HF) communications. *Defence Sci. Technol. Tech. Bull.,* **3**: 1–13.

Malik, R.A., Sathyamoorthy, D., Zakariya, A.S., Tompang, A., Mohamed, H.T., Kamal, M.R.A., Rajab, A.R., Zahary, N., Hambali, H., Mustafa, M. & Zuraini, M. (2011). The effect of smoothed sunspot number on HF radio communications in Peninsular Malaysia for the year 2009 to 2011. *Defence Sci. Technol. Tech. Bull.,* **4**: 165–182.

Maslin, N.M. (1987). *HF Communications: A Systems Approach*. Pitman Publishing, London.

Mudzingwa, C., Nechibvute, A., Chawanda, A. & Author, C. (2013). Maximum useable frequency prediction using vertical incidence data. *Int. J. Eng. Res. Tech,*. **2**: 2050–2056.

Mudzingwa, C. & Chawanda, A. (2018). Radio propagation prediction for HF communications. *Commun.*, **6**: 5–12.

Nagar, A., Mishra, S.D. & Vijay, S.K. (2015). Correlation of foF2 and M(3000)F2 over low latitude stations during low solar activity period. *Indian J. Rad. Space Phys.*, **44**: 78–87.

Ostertagová, E. (2012). Modelling using polynomial regression. *Procedia Eng.*, **48**: 500–506.

Oyekola, O.S. & Fagundes, P.R. (2012). On the variations of ionospheric parameters made at a near equatorial station in the African longitude sector : IRI validation with the experimental observations. *Earth Planets Space*, **64**: 567–575.

Raab, F.H., Caverly, R., Campbell, R., Eron, M., Hecht, J.B., Mediano, A., Myer, D.P. & Walker J.L.B. (2002). HF , VHF , and UHF systems and technology. *IEEE T. Microw. Theory Tec.,* **50**: 888–899.

Rush, C.M., Miller, D. & Gibbs, J. (1974). The relative daily variability of foF2 and hmF2 and their implications for HF radio propagation. *Rad. Sci.,* **9**: 749–756.

Sha'ameri, A.Z. (2010). *ALE Radio technology for public protection and disaster relief operations.* .my Convergence, **4**: 34–42.

Sha'ameri, A.Z. (2001). Analysis of HF data communication signals using the lag-windowed Wigner-Ville distribution. *Proc. Int. Conf. Symp. Sig. Proces. Appli. (ISSPA),* pp. 250–253.

Sha'ameri, A.Z. (2006). *Secured HF Image Transmission System*. Universiti Teknologi Malaysia (UTM), Malaysia.

Sha'ameri, A.Z. & Boashash, B. (1999). The lag windowed Wigner-Ville distribution: An analysis method for HF data communication signals. *J. Tech., UTM*, **30**: 33–54.

Shanableh, T. & Assaleh, K. (2010). Neurocomputing Feature modeling using polynomial classifiers and stepwise regression. *Neurocomputing*, **73**: 1752–1759.

Sharma, K., Dabas, R.S., Das, R.M., Sethi, N.K., Pillai, K.G. M. & Mishra, A.K. (2008). Modelling of ionospheric F-region parameters for Indian zone. *Proc. Int. Conf. XXIX URSI General Assembly*, pp. 1–4.

Sinha, P. (2013). Multivariate polynomial regression in data mining: methodology, problems and solutions. *Int. J. Scien. Eng. Res.,* 4: 962–965.

Souza, J.R., Batista, I.S., Costa, R.G.D.F. & Inpe, D.D.A. (2013). A simple method to calculate the maximum usable frequency. *Proc. Int. Conf. 13th Congress Brazilian Geophysical Society*, Rio de Janeiro, Brazil, pp. 1–5.

Takashi, M., Susumu, S., Masabumi, K., Kenro, N., Jyunpei, U., Takuya, T., Hidekatsu, J., *et al*. (2009). Ionospheric irregularities and the SEALION project. *J. Nat. Inst. Inform. Comm. Technol.,* **56**: 243–256.

Wang, J., Feng, X. & Cheng, L. (2010). Basic MUF observation and comparison of HF radio frequency prediction based on different ionosphere models. *Proc. Int. Conf. Antennas Propagation EM Theory, (ISAPE) 2010*, pp. 403–406.

Wichaipanich, N., Supnithi, P., Tsugawa, T., Maruyama, T. & Nagatsuma, T. (2013). Comparison of ionosphere characteristic parameters obtained by ionosonde with IRI-2007 model over Southeast Asia. *Adv. Space Res.,* **52**: 1748–1755.

Xue, Z.R. & Boon, T.K. (2004). The variation of foF2 in the equatorial ionosphere. *Proc. Int. Conf. Asia-Pacific Rad. Sci.*, pp. 350–354.

Zain, A.F.M., Ho, Y.H., Abdullah, S. & Abdullah, M. (2006). First ionospheric monitoring campaign at Fraser's Hill Malaysia. *Proc. Int. Conf. Ionospheric Rad. Sys. Tech., pp.* 162–167.

Zain, A.F.M. & Abdullah, M. (2000). Application of artificial intelligence to ionospheric radio propagation. *Proc. Int. Conf. TENCON 2000*, pp. 82–87.

Zhao, L.P & Li, Y.G. (2010). Modelling and simulation of useable frequencies in the ionosphere on HF sky-wave band. *Proc. Int. Conf. Inform. Engin. Elect. Commerce (IEEC), 2010,* pp. 1–4.

REVIEW OF MACHINE LEARNING BASED HARDWARE TROJAN DETECTION METHODS

Chee Hoo Kok[1*], Chia Yee Ooi[1], Michiko Inoue[2], Nordinah Ismail[1], Mehrdad Moghbel[1] & Hau Sim Choo[1]

[1]Embedded System Research Laboratory, Malaysia-Japan International Institute of Technology (MJIIT), Universiti Teknologi Malaysia (UTM), Malaysia
[2]Dependable System Laboratory, Graduate School of Information Science, Nara Institute of Science and Technology (NAIST), Japan

[*]Email: chkok2@live.utm.my

ABSTRACT

The rapid development of electronic hardware is strongly supporting the need of modern computing technologies and communication systems, but at the same time it is facing the threats of hardware Trojans posed by malicious intenders. In this paper, we explore machine learning assisted hardware Trojan detection methods as state-of-the-art counter mechanisms. First, we present the possible scenarios of hardware Trojan attacks. We provide options and guide of the possible ways of implementation to tackle different situations with the examples from previously-proposed methods. Finally, we evaluate the methods and provide the future roadmap for this research.

Keywords: *Hardware Trojan detection; integrated circuit (IC); hardware security; machine learning; feature extraction*

1. BACKGROUND OF HARDWARE TROJAN

In today's terminology, "Trojan" is a term often used for describing the tricks employed by individuals or organisations with malicious intents for implanting a malicious component (backdoor) into the target system while disguising it as normal component (Kapersky, 2018). In hardware terminology, Trojans often refer to malicious and stealthy circuits that are integrated into the design of integrated chips (IC). Upon receiving the trigger signal(s), the Trojan circuit will initiate the attack; otherwise, it will remain hidden and undetected. However, there are scenarios that require the Trojan circuit(s) to activate all the time. The malicious activity by the Trojan can range from leaking of secretive information and denial-of-service (DoS) attacks to the degradation of the system performance. Unlike software Trojans that are inserted and triggered by programming and affect the software side of the system, hardware Trojans often have a more sophisticated triggering mechanism and can not only affect the payload of the system but also the side-channel parameters of different devices in the system. As the circuits are getting more complicated and the size of ICs shrinking due to the manufacturing advances, detection of hardware-based Trojans is considerably more difficult than software based Trojans. This is as hardware Trojans can be implemented by just modifying several transistors, which makes it very difficult to detect inside an IC comprised of millions of transistors (Amin *et al.*, 2014).

While security concerns regarding IC designs may not have been an issue until recently, the emergence of technologies such as 5G and Internet of Things (IoT) has put every internet connected device at risk. If one of the nodes in the network is breached by a hardware Trojan, other devices connected to the network will become vulnerable. Making matters worse, it is possible to insert hardware Trojans at every stage of the IC's hardware development as this development is often outsourced to third-party designers and foundries (Yang *et al.*, 2016). Even if the client does not have any intention of inserting any Trojans into their designs, the intellectual property (IP) core designers, electronic design automation (EDA) tool vendors and semiconductor foundries may manipulate the design to introduce a

backdoor. The clients, especially military organisations, government intelligence agencies and financial organisations, are always at high risk to suffer great losses if they do not incorporate Trojan screening and countermeasures, with various governments and research groups around the world looking to develop hardware vulnerability screening systems such as the trusted IC projects carried out by the Intelligence Advanced Research Projects Activity (IARPA) of the US government (Mitra *et al.*, 2015). The failure of Syria's radar systems in 2007 can be considered as an example case of successful hardware Trojan utilisation, where experts suspect that a secret built-in kill switch had been planted into the radar system which caused Syria failed to detect incoming missiles (Adee, 2008). Recently, the world was shocked again by a report of attempts by Chinese spies to infiltrate US technology manufacturers by implanting a tiny chip into electronic systems via the supply chain (Robertson & Riley, 2018).

The past decade has seen machine learning based classification and screening algorithms being increasingly employed by researchers to screen and detect Trojan-infected circuits based on hardware Trojan features extracted. Although the application of machine learning for hardware Trojan detection is still new, the results obtained by these methods are promising. In this paper, hardware Trojan detection methods utilising machine learning techniques along with feature extraction concepts and publicly accessible datasets are discussed.

2. TRUST ISSUES IN THE IC MANUFACTURING INDUSTRY

Figure 1 illustrates the relationship between different industries and companies involved in IC development and manufacture. It is observed that there is a possibility of implementing the hardware Trojan at each step of the manufacture and design process (Bhunia *et al.*, 2014; Li *et al.*, 2016). Therefore, hardware Trojan countermeasures should be implemented by every party to ensure that the design is always Trojan-free at each of the development stage, as different parties are capable of inserting Trojans using different methods at different abstraction levels (Dabrowski *et al.*, 2014; Francq & Frick, 2015). Table 1 summarises different scenarios where these Trojans could be inserted into the hardware (Xiao *et al.*, 2016).

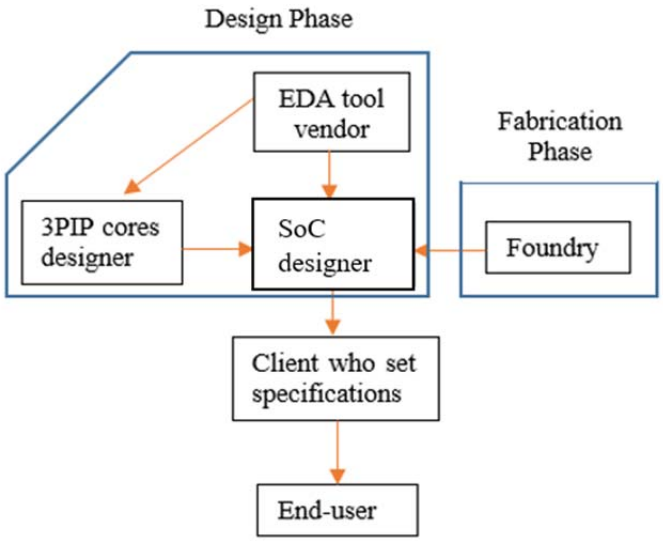

Figure 1: The parties involved in IC development and their relationship.

Table 1: Trojan insertion models as proposed in Xiao *et al.* (2016).

Model	Description	3PIP Vendor	SoC Developer	Foundry
A	Untrusted 3rd Party IP (3PIP) vendor	Untrusted	Trusted	Trusted
B	Untrusted foundry	Trusted	Trusted	Untrusted
C	Untrusted EDA tool or rogue employee	Trusted	Untrusted	Trusted
D	Commercial off-the-shelf component	Untrusted	Untrusted	Untrusted
E	Untrusted design house	Untrusted	Untrusted	Trusted
F	Fabless SoC design house	Untrusted	Trusted	Untrusted
G	Untrusted SoC developer with trusted IPs	Trusted	Untrusted	Untrusted

2.1 Hardware Trojan Classification

While categories of hardware Trojans are not specifically separated in the literature, there are a few categorisations proposed. The first taxonomy was proposed by Xiaoxiao *et al.* (2008) and later extended by other researchers to add in more attributes (Karri *et al.*, 2010; Rajendran *et al.*, 2010; Salmani *et al.*, 2013; Tehranipoor & Koushanfar, 2010). Although some researchers categorise hardware Trojans in terms of trigger and payload (Chakraborty *et al.*, 2009; Bhunia *et al.*, 2014), such an approach provides insufficient information about the Trojan as it only defines the behaviours and not the insertion techniques. The most widely referred classification scheme is the one used by a Trojan benchmarks library, known as Trust-Hub (Trust-Hub, 2013), proposed by Shakya *et al.* (2017), which is capable of covering all attributes of hardware Trojan in terms of insertion methods and Trojan behaviours, with Figure 2 illustrating this taxonomy.

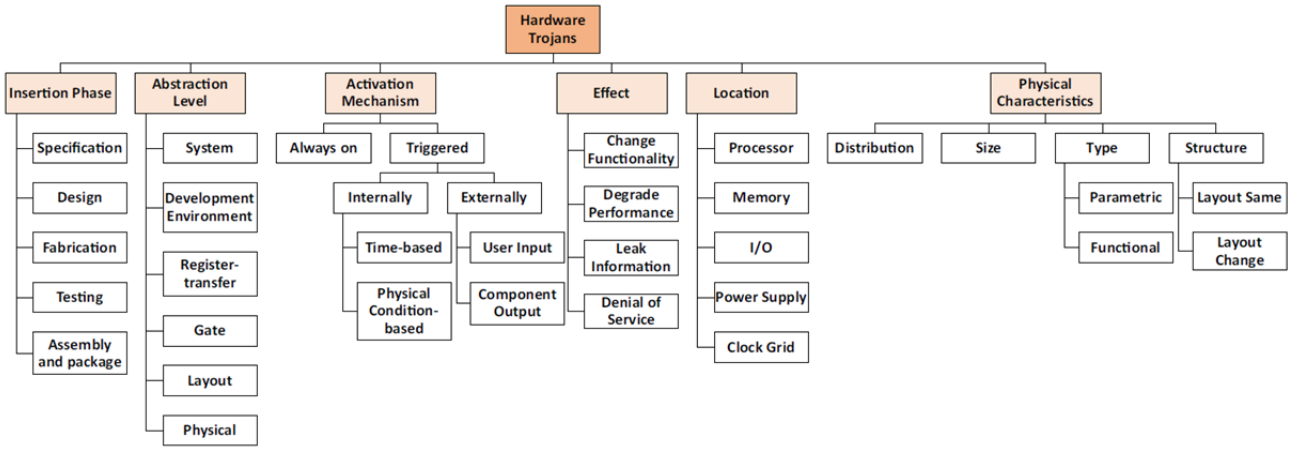

Figure 2: Hardware Trojan taxonomy proposed by Shakya *et al.* (2017).

2.2 Systematic Threat Modelling Using Hardware Trojan Classification Criteria

To design a hardware Trojan countermeasure, the threat model has to be determined first. A threat model is defined as a structured representation of different kinds of Trojans with different attributes. A threat model is important for defining the attributes of the hardware Trojan targeted by a proposed countermeasure as it is almost impossible to have a universal screening method capable of screening for all Trojan types. The threat model is constructed based on the classification criteria by adding the abilities of each design party into consideration with the insertion medium preferred over the insertion phase, as the insertion phase lists out all the phases in the IC manufacturing flow. Considering how a Trojan could be inserted by different parties involved in the phase, insertion medium would be more appropriate as it defines the channel used by the adversary to insert the Trojan.

The insertion medium attribute can be classified into more refined classes such as specification, electronic design automation (EDA) tools, IP core, system-on-chip (SoC) design, mask data and semiconductor parameters. Each of these classes is used by different parties although some of them can fall into the same manufacturing phase, as discussed in Table 2. The other attributes that could be used to form a threat model are abstraction level, location, effect, activation mechanism and physical characteristics, as shown in Table 3 while an example of a threat model posed by a Trojan is given in Table 4.

Table 2: The hardware Trojan insertion abilities of each party.

Party	**Insertion Medium**	**IC Manufacturing Phase**	**Abstraction Level**
IC Client	Specification	Specification	-
EDA tool vendor	EDA tool	Design	System, Register Transfer Level (RTL), Gate-level, Physical, Layout
3PIP core designer	IP core		
SoC designer	SoC design		
Foundry	Mask data & semiconductor parameters	Fabrication and assembly	Physical, Layout

Table 3: Attributes that could be used to form a threat model.

Attributes	**Description**	**Examples**
Abstraction level	Level of implementation used for inserting Trojans in a very-large-scale integration (VLSI) flow	System level, register-transfer level, gate-level and physical level
Location	Location on an IC where the Trojan is inserted	Processor, memory module, system bus, Input and Output (I/O) module and clock
Physical characteristic	Physical changes caused by the Trojan insertion	Changed layout, unchanged layout
Effect	The effect caused by Trojan attacks	leaking secretive information, denial-of-service issues, reduced system performance
Activation mechanism	The technique used for triggering the Trojan	A Trojan can be always on, internally triggered or externally triggered by digital logic signals or analog signals

Table 4: Example of attributes that could be used to form a threat model.

Trojan name	Differential fault analysis (DFA)-based advanced encryption system (AES) hardware Trojan (Bhasin *et al.*, 2013)
Description	The Trojan triggering circuit is implemented inside an AES core which injects a random “byte-flip” in the last encryption round which makes the cryptographic core to be “intentionally-leaky” and with compliance to Piret’s DFA algorithm, the guessing of the encrypted key becomes possible (Piret & Quisquater, 2003).
Insertion medium	IP core
Abstraction level	Gate-level
Location	Co-processor
Physical characteristic	Unchanged layout
Effect	Leak information
Activation mechanism	External combinational triggered

3. REVIEW ON MACHINE LEARNING IN HARDWARE TROJAN DETECTION

3.1 Performance Evaluation

In this section, the performance metrics commonly used for evaluating different machine learning methods are discussed. In the case of hardware Trojan detection, True Positive (TP) represents the events where Trojan-cases are identified correctly, while False Negative (FN) represents the incidences of Trojan cases wrongly identified as non-Trojan cases. Similarly, True Negative (TN) represents the events where events of non-Trojan cases are identified successfully, while False Positive (FP) represents the events of non-Trojan cases wrongly identified as Trojans.

Sensitivity, or true positive rate (TPR), measures the rate of success in detection of Trojan circuits. TPR is determined by:

$$TPR = \frac{Total\ True\ Positive\ (TP)}{Total\ True\ Positive\ (TP) + Total\ False\ Negative\ (FN)} \quad (1)$$

Specificity, or true negative rate (TNR), measures the rate of success in recognising genuine circuits. TNR is determined by:

$$TNR = \frac{Total\ True\ Negative(TN)}{Total\ True\ Negative\ (TN) + Total\ False\ Positive\ (FP)} \quad (2)$$

The accuracy (ACC) is determined by:

$$ACC = \frac{Total\ TP + Total\ TN}{Total\ TP + Total\ FP + Total\ FN + Total\ TN} \quad (3)$$

Precision or positive predictive value (PPV) is determined by:

$$PPV = \frac{Total\ TP}{Total\ TP + Total\ FP} \quad (4)$$

It should be mentioned that relying on just one performance measure as a possible representation of the classification performance is strongly discouraged as the results would not be representative of the real performance. As an example, a classifier might have high accuracy but it does not mean that TNR is also high as the classifier might only perform well in recognising Trojan cases but not in non-Trojan cases. The accuracy will also be affected if the test samples are imbalanced with more Trojan samples as compared to non-Trojan sample or vice versa (Elnaggar & Chakrabarty, 2018), or in other words, accuracy could be manipulated by dishonest altering of the test samples. The performance of a detection method tends to be more reliable if more performance metrics are provided.

3.2 Publicly Accessible Trojan Library

Currently, the only known publicly accessible library for classification of hardware Trojan circuits is Trust-Hub (Trust-Hub, 2013). At the moment, there are 94 circuits with different Trojans classified based on attributes that are available in the Trust-Hub library. The Trojan designs inserted in different circuits are available in gate-level and RTL netlists available in Verilog (.v) or VHDL (.vhd) formats as well as layout formats such as GSDII or Design Exchange (.def) formats. The usage of Trust-Hub circuits as benchmark circuits can act as a standardised benchmark dataset while resulting in a fair comparison between different screening and detection methods.

So far, the Trust-Hub library is mostly used for pre-silicon gate-level detection, as the proposed methods do not have any target functionality. Hasegawa *et al.* (2016), Salmani (2017), and Xie *et al.* (2017) developed their detection methods using the gate-level netlists provided by Trust-Hub, with

these methods designed to look for similar behaviours between different kinds of Trojans by utilising machine learning.

In addition to the Trust-Hub library, self-designed Trojans are also utilised in many studies as the circuits in Trust-Hub are limited to several functionalities, such as cryptographic modules (AES and RSA), communication modules (RS232-UART and EthernetMAC10GE), simple microcontroller modules (8051 and PIC16F84) and sequential circuits specialised for design for test (DFT) (ISCAS'89 and ITC'99). In some cases where there is a need to design a detection method for an IP core with a specific functionality or any other Trojans which are not listed in Trust-Hub, the Trojan for the circuit needs to be self-designed. In such cases, researchers have to make sure that the design of Trojan circuitry meets the definition of a hardware Trojan, in which it has to be well-hidden and difficult to be triggered.

Currently, all the proposed methods for post-silicon Trojan detection utilise self-designed circuits as their data source. For example, Kulkarni *et al*. (2016b) proposed a detection method for a Trojan attack on core-to-core communication, in which its abstraction level is system level and demonstrated with their self-designed circuit hiding the Trojan modules capable of launching a DoS attack. Their proposed method achieved an average accuracy of 93% on a multi-core field-programmable gate Array (FPGA) infected with four different Trojans.

3.3 Classification of Data Using Machine Learning

Due to the increased performance of machine learning algorithms, hardware Trojan detection methods can have promising accuracy while greatly reducing the time and cost associated with the detection process. While both supervised and unsupervised machine learning methods could be utilised for the detection, supervised methods are by far the most popular as they are able to provide a far higher accuracy as compared to other methods.

3.3.1 Unsupervised Learning

In unsupervised learning, no prior knowledge regarding the nature of features is assumed as the learning algorithm will cluster the data according to their nearest distance from the centroid of the unlabelled clusters with the number of clusters usually determined manually. Figure 3 illustrates a sample detection flow using unsupervised learning.

In semiconductor manufacturing, inspection technologies such as colour charge coupled devices (CCD) sensors, confocal microscopy and scanning electron microscopy (SEM) are used to obtain decent quality images of wafers for further fault detection and analysis (Sankaran *et al.*, 1999). In the field of hardware Trojan detection, Bao *et al.* (2016) suggested a reverse engineering method that eliminates the tedious steps associated with the annotation and schematic recreation. In their proposed method, it is only required to capture the SEM image of the physical layout of the IC after d7elayering. Then, they extract the area differences between golden layout and layout of the circuit under test, in addition to the differences of the geometric centre of mass (centroid) between golden layout and layout under test being computed for identifying any malicious addition or deletion. The differences in area and centroid are used as input features for k-means clustering, with parameter K=2 indicating the Trojan and non-Trojan clusters.

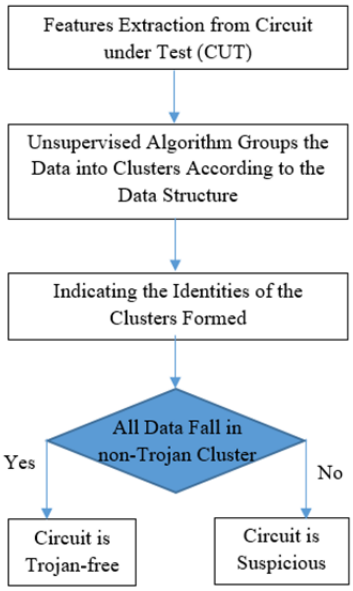

Figure 3: Suggested hardware Trojan detection flow using unsupervised learning.

Employing the controllability and observability of the netlist as Trojan features to train a classifier was first proposed by Salmani (2017), referred to as Controllability and Observability Trojan Detection (COTD) with the detection flow shown in Figure 4. This is plausible as the Trojan's activation signal is always stealthy while being very difficult to be triggered during verification steps using the test patterns generated by automatic test pattern generation (ATPG). In their study, three testability measures - CC0 (combinational controllability of signal '0'), CC1 (combinational controllability of signal '1') and CO (combinational observability) of each net inside a combinational netlist - were proposed with only combinational testability measures utilised as the tested circuits were loaded with scan chains, where the sequential testability is reduced to zero. Since each net has its own controllability and observability values, the dataset can be obtained from each net. The Sandia Controllability and Observability Analysis Program (SCOAP) (Goldstein & Thigpen, 1980) was used to generate the three values of the nets. CC0 and CC1 are combined to form a CC value, defined as:

$$CC(s) = \sqrt{(CC0^2\ (s) + CC1^2\ (s))} \qquad (5)$$

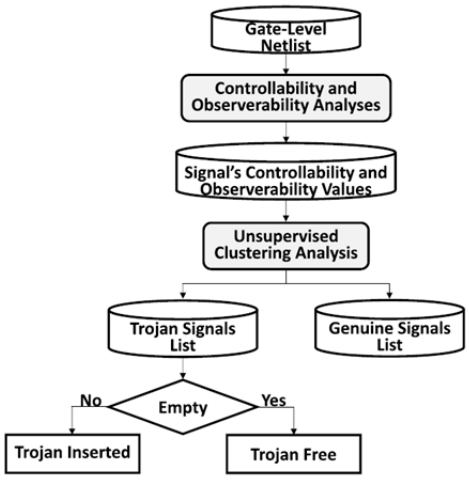

Figure 4: The COTD flow (Salmani, 2017).

Each dataset, therefore contains two features value, CC and CO. However, combining CC0 and CC1 into CC could reduce the Trojan detection rate as some Trojans need a specific signal (either 0 or 1) to trigger. In Salmani's (2017) proposed method, a k-means clustering approach is used with the number of clusters *K* set as 3, defined as genuine signals, Trojan signals with high CC and Trojan signals with high CO. If all the signals fall into the genuine signal's cluster, then the circuit is Trojan-free; otherwise, if any signal falls into Trojan's lists with either high CC or CO values, then Trojan is detected in the circuit. Their proposed method was able to achieve 100% TPR and 100% TNR in 21 out of 23 benchmark Trojan circuits.

3.3.2 Supervised Learning

For supervised learning, the samples representing Trojan-infected and Trojan-free circuits need to be defined before the learning process, with support vector machine (SVM), neural network (NN), k-nearest neighbour (k-NN), Bayesian classifier (BC) and decision tree (DT) being the most popular approaches. As new hardware Trojans are constantly developed and implemented in real life, the Trojan features library must be kept updated to ensure maximum performance, with Figure 5 illustrating the suggested supervised detection flow. Supervised learning hardware Trojan detection is comprised of training and detection steps. During the training, the dataset balancing and feature selection are optional but recommended with the trained model then used in the detection phase to classify the data from the circuit under test (CUT).

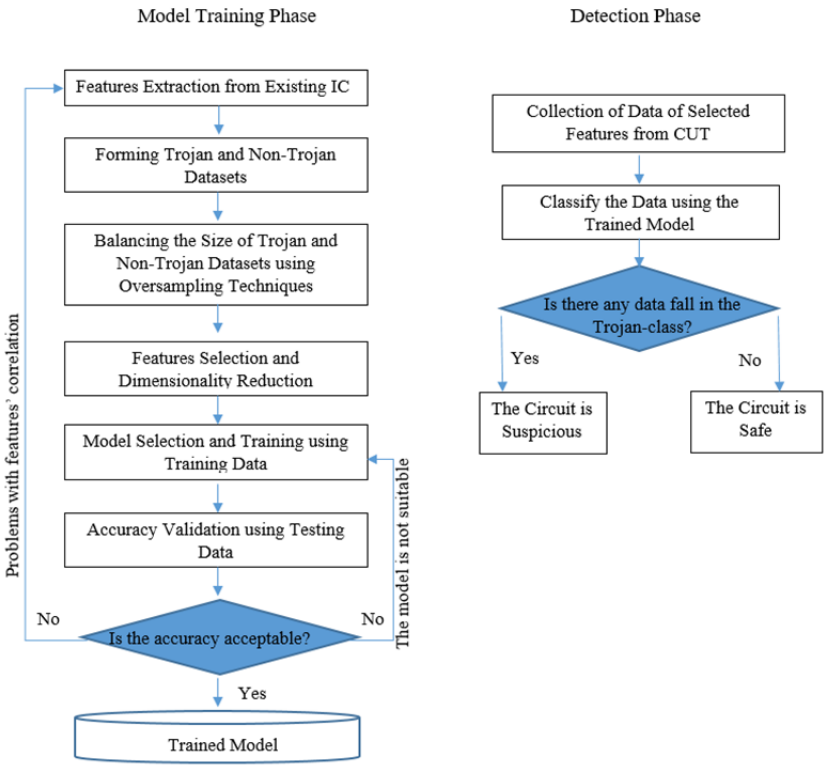

Figure 5: Suggested hardware Trojan detection flow using supervised learning.

Before training a classifier, it is advisable to conduct feature selection for increasing the training and classification performance of the classifier. As the number of features extracted from each circuit might range from several to many, there are often some features that might be redundant or irrelevant to hardware Trojans. Additionally, some of these features could be considered as noise that will affect the training and detection accuracy, learning time and computation requirement (Chandrashekar & Sahin,

2014; Cai *et al.*, 2018). Feature selection allows the classifier model to understand the data structure better by removing irrelevant variable and reducing the dimension. Hasegawa *et al.* (2017b) proposed 51 gate-level Trojans features as described in Table 5 and performed feature selection using the Random Forest classifier and computing the detection accuracy using the F-score measure. In the proposed features, *x* represents the level of depth away from the target net *n*. "Fan-ins" is a terminology used in VLSI which represents the logic-gates at the input side which converge on a point in the system. An example of defining the number of fan-ins from *x*=2 levels away from net *n* is depicted in Figure 6. The 11 features with the best average F-scores are selected for the final training and testing phases, as shown in Table 6. The main drawback of their proposed feature selection is the fact that the top-ranking Trojan features are selected based on F-score without taking the correlation among features into consideration. Correlation-based feature selection (CFS) and minimum redundancy & maximum relevance (mRMR) feature selection methods can be considered more appropriate as they consider the correlation between features with mRMR offering a better feature selection approach (Peng *et al.*, 2005).

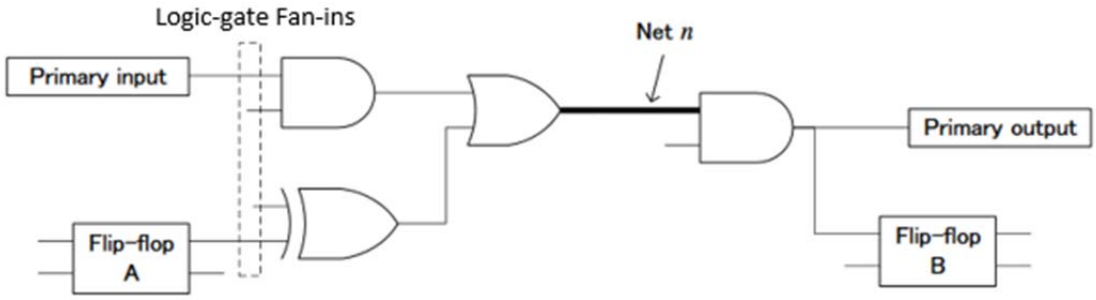

Figure 6: The number of fan-ins two levels away from net *n* is 4.

Table 5: The 51 initial features identified, where $1 \leq x \leq 5$ (Hasegawa *et al.*, 2017b).

Feature	No. of features
The number of logic-gate fan-ins up to *x*-level away from the net *n*	5
The number of flip-flops up to *x*-level away from the input side of the net *n*	5
The number of flip-flops up to x-level away from the output side of the net *n*	5
The number of multiplexers up to *x*-level away from the input side of the net *n*	5
The number of multiplexers up to *x*-level away from the output side of the net *n*	5
The number of up to *x*-level loops from the input side of the net *n*	5
The number of up to *x*-level loops from the output side of the net *n*	5
The number of constants up to *x*-level away from the input side of the net *n*	5
The number of constants up to *x*-level away from the output side of the net *n*	5
The minimum level to the primary input from the net *n*	1
The minimum level to the primary output from the net *n*	1
The minimum level to any flip-flop from the input or output side of the net *n*	2
The minimum level to any multiplexer from the input or output side of the net *n*	2

Table 6: The best 11 features ranked based on their importance values (Hasegawa *et al.*, 2017b).

Rank	Features	Importance Value
1	The minimum level to the primary output from the net *n*	0.200
2	The number of up to 5-level loops from the output side of the net *n*	0.133
3	The number of flip-flops up to x-level away from the output side of the net *n*	0.124
4	The number of multiplexers up to 3-level away from the input side of the net *n*	0.115
5	The number of flip-flops up to 4-level away from the input side of the net *n*	0.084
6	The number of logic-gate fan-ins up to 5-level away from the net *n*	0.070
7	The number of multiplexers up to 4-level away from the output side of the net *n*	0.070
8	The number of logic-gate fan-ins up to 4-level away from the net *n*	0.056
9	The number of up to 4-level loops from the input side of the net *n*	0.056
10	The minimum level to any multiplexer from the output side of the net *n*	0.048
11	The minimum level to the primary input from the net *n*	0.043

Dataset balancing should also be considered for ensuring the maximum classification accuracy as the dataset might have many samples representing a particular class and not enough samples representing other classes. For hardware Trojan classification, the Trojan data is very limited as compared to regular class data as the Trojan circuitry only makes up a very small part in a circuit. Thus, the data imbalance will cause biased classification in most cases. Therefore, if possible, oversampling of data in the Trojan-class has to be done before proceeding to the training phase. However, merely duplicating the minority class as done by Hasegawa *et al.* (2017b) has no tangible effect on the accuracy as the new data generated will only be duplicates of each other, which do not help the classifier to learn better but rather might cause it to over-fit. random over-sampling examples (ROSE) (Lunardon *et al.*, 2014) and synthetic minority oversampling technique (SMOTE) (Chawla *et al.*, 2002) can be considered as proven and effective techniques for dataset balancing. Figure 7 illustrates an example the SMOTE method balancing the data problem by simulating the data structure and trying to generate new data near the border of the existing minority (Trojan) data. In brief, each point of the Trojan-class will be connected and new points will be generated along the data boarders.

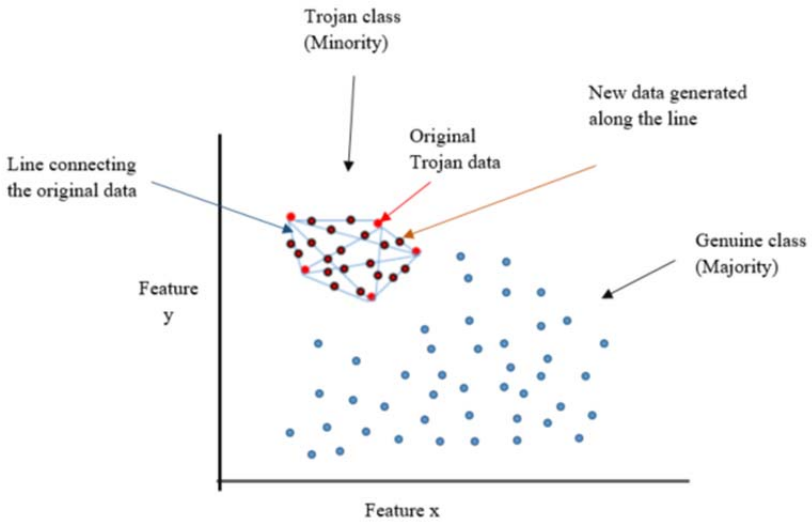

Figure 7: Illustration on how SMOTE helps to solve data imbalance problem for hardware Trojan data sets.

3.3.2.1 One-Class Classification

In some cases where only the genuine circuits are available and the features of the hardware Trojan remain unknown, one-class classification is being employed. The constructed one-class classifier will classify the data such that any new data that fall outside of the boundary of the class as outlier are considered as non-genuine data from the Trojan-free circuit.

Using the same features as previously mentioned by Bao *et al.* (2014), Bao *et al.* (2016) implemented a one-class SVM to classify the image of circuits containing any suspicious modifications by randomly injecting modifications to the layout of some benchmark circuits to be used as Trojan circuits for testing the accuracy of their proposed method. There were three types of Trojans inserted in the circuit, including Trojan by deletion (removing of components from the original layout), Trojan by addition (adding of components into the original layout) and Trojan by parametric (changes of transistors, gates and interconnects parameters). Depending on the type of the Trojan, their proposed method was able to achieve a minimum and maximum accuracy of 84 and 100% respectively.

Jap *et al.* (2016) proposed using a one-class SVM for detecting side-channel Electromagnetic (EM) leakage. Hardware Trojan was injected into a partially reconfigurable FPGA and the EM leakage was measured by a high precision EM probe based on the approach proposed by Bhasin *et al.* (2013), with the EM activity of the triggering circuit or payload observed. The EM trace was obtained by measuring 500 sample points on each EM wave with the trace measurement repeated for 200 times using the Trojan free device to generate the testing and training data. The features were then extracted from the traces, with the features used being the sum of absolute differences, all sample points in the traces and their local peaks. They trained the one-class SVM using the golden chip data, only achieving the highest accuracy of 93.7%.

Jin *et al.* (2012) proposed an on-chip detection method similar to the built-in self-test (BIST) technique by incorporating additional sensors and a one-class NN classifier chip into the CUT to analyse and classify the waveform from the circuit's DC voltage. Their proposed method was tested for cryptographic circuits inserted with different encryption key leaking Trojans. Their method achieved TPR and TNR greater than 97 and 99% respectively in classifying all power signals from each chip.

Wang *et al.* (2013) proposed using Karhunen-Love (K-L) expansion for the post-processing of power traces collected to improve the data quality and then classified the power traces of Trojan contaminated ICs from genuine ICs using one-class SVM. They utilised a data encryption standard (DES) circuit by simulation and added process variation (PV) noises of 2, 5, and 7% with added extra logic gates into the circuit as simple Trojan triggers for testing their method. Using power traces as the feature, the proposed method achieved an average of 96.81% TPR, 97.93% TNR and 97.18% ACC in recognising the power signals of nine different circuits.

3.3.2.1 Two-Class Classification

Lodhi *et al.* (2016) proposed a Trojan detection method using the timing signature of a few sets of test vectors. First, the timing signature from the original circuit is determined and the possible ranges of the delay of a normal circuit are obtained. If any delay is outside the defined normal range, it is theorised that the Trojans are the cause, while for delays inside the normal range, they are labelled as being a possible Trojan according to their respective delays. They obtained the training data by running 500 iterations per input vector using Monte Carlo simulation tool with Gaussian distribution applied to eliminate PV and dimension reduction using principal component analysis (PCA). The DT, BC and k-NN models were trained using the Rapid Miner machine learning tool. Their proposed method achieved an accuracy of 95.19% and PPV of 95.96% using DT. However, despite the good performance, the evaluation only involved their own circuit of macro synchronous micro asynchronous (MSMA) architecture pipeline (Lodhi *et al.*, 2014) coupled with a single hardware Trojan.

Lodhi *et al.* (2017) later suggested that the power consumption of each standard reduced instruction set computer (RISC) pipeline stage of Trojan-infected and uninfected circuits are different. Thus, a machine learning model can be trained by profiling the power consumption of the pipeline for each different instruction. To measure the instruction power profile, the power at each pipeline stage was measured. However, the authors did not clearly mention how they obtained the power profile of Trojan infected circuits. They achieved an accuracy of 99.02% and PPV of 96.62% using k-NN classifier and power profile of each pipeline instruction.

Wang *et al.* (2016) proposed using an extreme learning machine (ELM) based classifier using three Trojan-infected circuits with different overheads (area of Trojan occupation) on FPGA. They implemented different RS232 Trojan-infected circuits on an FPGA module, the power of the module was then examined using oscilloscopes and probes with the power consumption data analysed using a computer as illustrated in Figure 8. Their proposed method achieved an average accuracy of 89.549% in four different FPGA circuits using the current waveform as a feature.

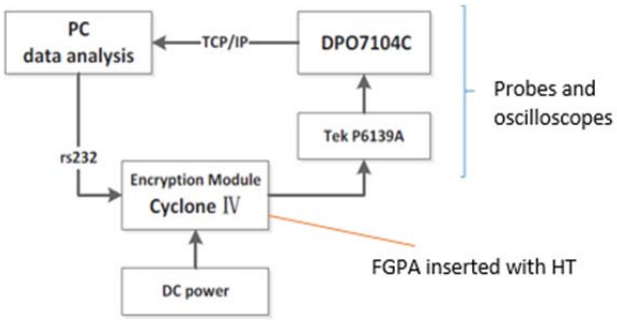

Figure 8: Power consumption data acquisition block diagram as mentioned in Wang *et al.* (2016).

Using a similar FPGA based platform and data acquisition approach, Li *et al.* (2016) proposed a back propagation (BP) neural network method for detecting the difference of power consumption between Trojan- infected circuits and normal circuits without providing any performance figures. The power consumption data was sampled into 1,200 points and BP neural network was employed to classify them. They proved that BP neural network is able to distinguish the very tiny increase of power consumption in Trojan circuits.

Iwase *et al.* (2015) measured the output power consumption in the time domain and transformed it into the frequency domain through discrete Fourier transform (DFT). Then, SVM was used as a classifying technique to classify Trojan-infected circuits and normal circuits. Their proposed method successfully detected Trojans caused by simple modifications of AES circuit implemented using an FPGA. Their method claimed to have correctly identified all the 12 Trojan-intruded circuits and a normal circuit.

Mingfu *et al.* (2016) proposed a method to inspect fabricated ICs by training a classifier in the design phase. To demonstrate the method, they designed 50 simple Trojans made up of a single comparator, counter or few gates inserted in to s38417 circuit. During the design phase, the transient power supply current (I_{DDT}) of each circuit was simulated and sampled into 500 points to be used as 500 feature vectors for the training of classifiers. Adaptive iterative optimisation was used to enhance the learning. The trained classifier was then used to classify the I_{DDT} measured from the fabricated ICs. The experiment was repeated with PV of 10, 15 and 20%, and achieved TPR and ACC of at least 72% and 74% respectively using different algorithms.

A real-time detection method specifically designed for hardware Trojans performing a DoS attack on inter-core communication was proposed by Kulkarni *et al.* (2016a, b). The authors modelled three types of DoS scenarios and extracted eight features during the packet transfer between cores for each

attack that also includes the distances of routes being chosen during the transferring. They proposed using a linear-SVM classifier for classifying the data into Trojan-free and Trojan-infected circuits, but not according to the types of attacks. If the route taken during the packet transfer is the same as a genuine circuit, then the circuit will be labelled Trojan-free; otherwise, it is classified as a Trojan-infected circuit. The training data set was obtained by randomly injecting attacks on the routers and the features for each communication were collected. For detection, the frameworks containing the trained linear-SVM classifier were placed into an FPGA, making it possible to detect intra-cluster and inter-cluster attacks separately.

Xie *et al.* (2017) claimed to have improved the hardware Trojan detection method proposed by Salmani (2017) with their proposed modifications illustrated in Figure 9. First, the inter-cluster distance between the Trojan and non-Trojan clusters based on CC and CO values is calculated using a k-means clustering approach. They theorised that the larger the inter-cluster distance, the more likely a Trojan exists in the circuit. Apart from the inter-cluster distance, they added the numbers of primitives, AND gates and OR gates as additional features, as it was assumed that the size of the circuit is related to the testability measures. These four features were then combined with their labels to form the dataset and a weight for each feature was set with an SVM classifier being used for the Trojan detection. Their proposed method achieved TPR and TNR of 100% in 28 gate-level Trojan-infected circuits from Trust-Hub and nine Trojan-free circuits.

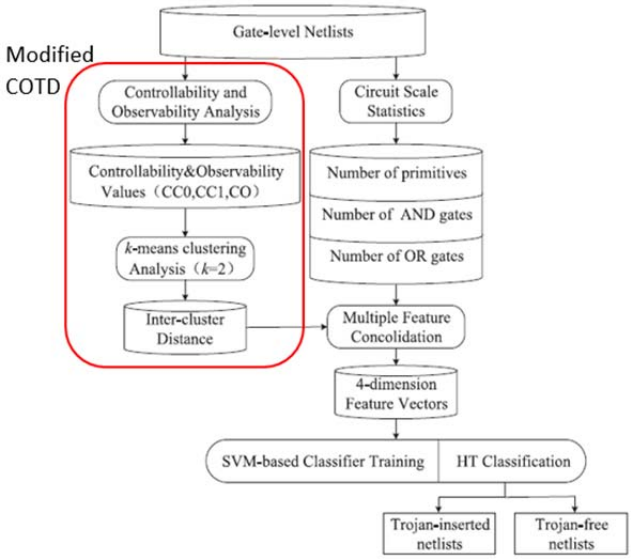

Figure 9: Flow of integrating COTD with circuit scale statistics (Xie *et al.*, 2017).

Hasegawa *et al.* (2016) and Inoue *et al.* (2017) both proposed similar Trojan detection approaches using gate-level netlist based on the structural features of the gate-level netlist. Five structural features were collected for each net in the netlist with the net labelled as Trojan net or normal net, and used in an SVM classifier. They validated their methods using gate-level netlists available on Trust-Hub using a leave-one-out-cross-validation (LOOCV) approach. The research was then expanded by identifying more features with strong correlation based on the Trojan library available from Trust-Hub. Hasegawa *et al.* (2017b) proposed 51 features that likely represented Trojans, as in Table 5, with the feature selection done based on F-score computed for each feature using the Random Forest algorithm, with the value of x (logic level from the target net) being fixed as $1 \leq x \leq 5$. The size of the circuit is not taken into consideration as it is expected that when the circuit size increases, the logic level will not remain the same. Inoue *et al.* (2017) obtained accuracies varying from 58.9% to 69.5% using self-

designed circuits while the method proposed by Hasegawa *et al.* (2016) obtained an average TPR of 82.59% utilising 17 Trust-Hub benchmarks.

Hasegawa *et al.* (2017a) later proceeded using NN to classify Trojan-infected net and normal net based on the 11 best features as determined previously (Hasegawa *et al.*, 2017b). After tuning the NN model, it was determined the three hidden layers with number of nodes of 200, 100 and 50 at each respective layer give the best result. Their proposed method achieved an average TPR of 84.8% and TNR of 70.1% using the best 11 gate-level structural features (out of the original 51) for 17 Trust-Hub benchmarks.

For RTL, a sub-graph isomorphism algorithm for hardware Trojan detection was developed by Piccolboni *et al.* (2017). The RTL coding of the entire design under verification is broken down into blocks and converted into sub-control flow graphs (CFG) as shown in Figure 10. Additionally, these sub-CFGs may come in a different number of nodes and edges as shown in Figure 11. By comparing to the topological structures available for known hardware Trojans, the algorithm is able to identify suspicious part inside the RTL coding. However, this does not resolve false positive issues arising for Trojans with similar structures with the genuine RTL coding. Therefore, Demrozi *et al.* (2017) proposed using probabilistic neural network (PNN) to assist in classifying the topological structure of the sub-CFG in suspicious locations more accurately. First, the PNN is trained using the known sub-CFG features extracted from the Trojan library with the features comprised of the number of occurrences of sub-CFG with a different number of nodes and the statistics with regards to the number of nodes and edges found in the graphs. The trained PNN model is used to differentiate between real Trojans and possible false positives achieving an accuracy of 100%.

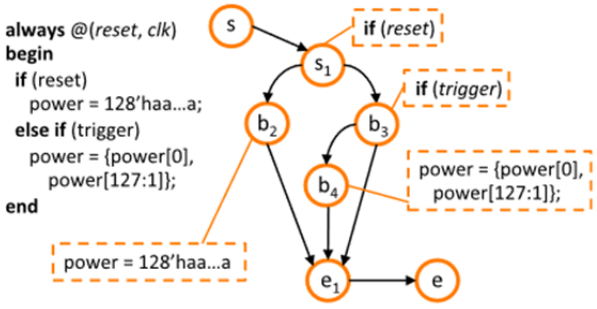

Figure 10: Example of conversion of an RTL block to a sub-CFG (Piccolboni *et al.*, 2017).

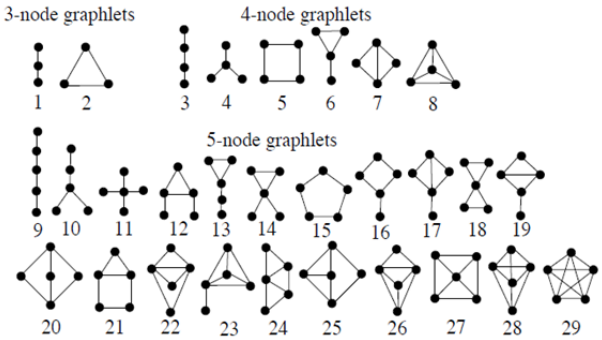

Figure 11: Features available in the structures of different patterns of sub-CFGs (Demrozi *et al.*, 2017).

4. DISCUSSION AND CONCLUSION

Table 7 summarises the different hardware Trojan detection methods based on the types of machine learning algorithm, features, source of Trojan data and performance. However, a fair comparison between these methods is almost impossible as all the circuits being experimented on have different aspects of complexity, functionality, and type of Trojans.

Table 7: Summary of previous works.

Author	Year	Machine Learning Algorithm	Features	Source of Trojan Data	ACC	Other Performance Measures
Bao *et al.*	2016	One-class SVM; k-means clustering	Area difference caused by: 1. Trojan-free 2. Trojan-addition 3. Trojan-deletion 4. Trojan- parametric	Self-designed	84% ~ 100 % at zero noise margin	-
Salmani *et al.*	2017	k-means clustering	CO, CC0, CC1	Trust-HUB gate-level netlists	-	100% TPR and 100% TNR for 21 out of 23 circuits
Jap *et al.*	2016	One-class SVM	EM trace	Self-designed	81.6% ~ 93.7%	-
Jin *et al.*	2012	One-class NN	Power consumption (Current trace)	Self-designed	-	More than 97% TPR; more than 99% TNR
Wang *et al.*	2013	one-class SVM	Power consumption trace	Self-designed	83.85% ~ 100%	-
Lodhi *et al.*	2016	Decision Tree	Time-latency	Self-designed	95.19%	95.96% TPR; 90.76% TNR
Lodhi *et al.*	2017	K-NN	Power consumed when running certain instructions	Self-designed	99.02%	96.62% PPV
Wang *et al.*	2016	ELM	Power consumption (Current trace)	Self-designed	-	89.55% TPR
Li *et al.*	2016	BP Neural Network	Power consumption trace	Self-designed	-	-
Iwase *et al.*	2015	SVM	Power consumption trace	Self-designed	-	-
Mingfu *et al.*	2016	Multiple algorithms	Transient power supply current (I_{DDT})	Self-designed	At least 74%	At least 72% TPR
Kulkarni *et al.*	2016	SVM	Packet transfer routes and destinations	Self-designed	93%	-
Xie *et al.*	2017	k-means clustering and SVM	Inter-cluster distance from COTD algorithm and circuit scale statistics	Trust-HUB gate-level netlists	-	100% TPR; 100% TNR
Inoue *et al.*	2017	SVM	Five gate-level structural features	Self-designed	58.90% ~ 69.50%	-
Hasegawa *et al.*	2016	SVM	Five gate-level structural features	Trust-HUB gate-level netlists	-	Average 82.59% TPR
Hasegawa *et al.*	2017	NN	11 best Trojan features selected from 51 gate features based on the score	Trust-HUB gate-level netlists	-	84.80% TPR; 70.10% TNR

			of F-measure.			
Demrozi *et al.*	2017	PNN	features of the structures of sub-CFG	Trust-HUB RTL netlists	-	17 out of 17 are successfully identified without FP

We can see that side-channel analysis is most popular among the post-silicon methods while power consumption is the most popular approach in-between different side-channel parameters as measurement-based data collection is easier and the data is more reliable if proper modelling on the noises from PV is done. Contrarily, although the destructive method proposed by Bao *et al.* (2014) gives high accuracy, it is not recommended for hardware Trojan detection as the tested chip is destroyed, in addition to the method being costlier and slower than side-channel analysis.

On the other hand, pre-silicon detection methods all utilise gate-level features. Although the method proposed by Xie *et al.* (2017) claims to achieve the highest accuracy, their claimed accuracy is questionable as they extracted only one dataset using one circuit. This means that the dataset utilised would have been very limited and the results are unlikely to be as accurate as other methods such as the method proposed by Salmani (2017). Moreover, there is no discernible relation between the number of gates and inter-cluster distance or Trojan features with the results depending on the controllability and observability. Utilising testability measures as features based on the proposal by Salmani (2017) is highly relevant to the Trojans but issues with false negatives and false positives are still of concern as mentioned earlier. Thus, it is recommended that testability measures be used alongside other gate-level features such as structural features proposed by Hasegawa *et al.* (2017a) for reducing false negatives and false positives.

Besides the accuracy, it should be mentioning that most researchers focus on true positive rate as a high true positive rate ensures that all Trojan-free circuits are identified with the false positives not being considered as the main concern as it is more important not to let any suspicious circuit evade the inspection rather than to falsely accuse a normal circuit. Machine learning based methods can greatly reduce the time and effort associated with this detection. There have been very few proposed detection methods for a register-transfer level or higher abstraction levels using machine learning concepts. This could be a focus for future hardware Trojan research as there are a lot of features available utilising RTL netlist. Additionally, it is possible to combine multiple level features for classification as it can help to reduce the false positive problems.

REFERENCES

Adee, S. (2008). The hunt for the kill switch. *IEEE Spectr.*, **45:** 34-39.

Amin, H.A.M., Alkabani, Y. & Selim, G.M.I. (2014). System-level protection and hardware Trojan detection using weighted voting. *J. Adv. Res.*, **5**: 499-505.

Bao, C., Forte, D., & Srivastava, A. (2014). On application of one-class SVM to reverse engineering-based hardware Trojan detection. *15th Int. Symp. Quality Electron. Des.*, 3-5 March 2014.

Bao, C., Forte, D. & Srivastava, A. (2016). On reverse engineering-based hardware trojan detection. *IEEE Trans. Comput. Aided Des. Integr. Circuits Syst.*, **35**: 49-57.

Bhasin, S., Danger, J. Guilley, S., Ngo, X. T., & Sauvage, L. (2013). Hardware Trojan horses in cryptographic IP cores. *2013 Works. Fault Diagnosis Tolerance Cryptogr.*, 20 August 2013.

Bhunia, S., Hsiao, M. S., Banga, M. & Narasimhan, S. (2014). Hardware Trojan Attacks: Threat Analysis and Countermeasures. *Proc. IEEE*, **102**: 1229-1247.

Cai, J., Luo, J., Wang, S. & Yang, S. (2018). Feature selection in machine learning: A new perspective. *Neurocomputing*, **300**: 70-79.

Chakraborty, R. S., Narasimhan, S. & Bhunia, S. (2009). Hardware Trojan: Threats and emerging solutions. *2009 IEEE Int. High-Level Des. Validation and Test Workshop*, 4-6 November 2009.

Chandrashekar, G., & Sahin, F. (2014). A survey on feature selection methods. *Comput. Electr. Eng.*, **40**: 16-28.

Chawla, N. V., Bowyer, K. W., Hall, L. O. & Kegelmeyer, W. P. (2002). SMOTE: Synthetic minority over-sampling technique. *J. Artif. Int. Res.*, **16**: 321-357.

Dabrowski, A., Hobel, H., Ullrich, J., Krombholz, K. & Weippl, E. (2014). Towards a Hardware Trojan detection cycle. *2014 9th Int. Conf. on Availability, Rel. Secur.*, 8-12 September 2014.

Demrozi, F., Zucchelli, R. & Pravadelli, G. (2017). Exploiting sub-graph isomorphism and probabilistic neural networks for the detection of hardware Trojans at RTL. *2017 IEEE Int. High Level Des. Validation Test Workshop (HLDVT)*, 5-6 October 2017.

Elnaggar, R. & Chakrabarty, K. (2018). Machine learning for hardware security: Opportunities and risks. *J. Electron. Test.*, **34**: 183-201.

Francq, J. & Frick, F. (2015). Introduction to hardware trojan detection methods. *2015 Des., Autom. Test Europe (DATE) Conf. & Exhibition*, Grenoble, France.

Goldstein, L. H. & Thigpen, E. L. (1980). SCOAP: Sandia controllability/observability analysis program. *17th Des. Autom. Conf.*, 23-25 June 1980.

Hasegawa, K., Oya, M., Yanagisawa, M. & Togawa, N. (2016). Hardware Trojans classification for gate-level netlists based on machine learning. *2016 IEEE 22nd Int. Symp. on On-Line Test. and Robust Syst. Des. (IOLTS*), 4-6 July 2016.

Hasegawa, K., Yanagisawa, M. & Togawa, N. (2017a). Hardware Trojans classification for gate-level netlists using multi-layer neural networks. *2017 IEEE 23rd Int. Symp. on On-Line Test. and Robust Syst. Des. (IOLTS)*, 3-5 July 2017.

Hasegawa, K., Yanagisawa, M. & Togawa, N. (2017b). Trojan-feature extraction at gate-level netlists and its application to hardware-Trojan detection using random forest classifier. *2017 IEEE Int. Symp. on Circuits and Syst. (ISCAS)*, 28-31 May 2017.

Inoue, T., Hasegawa, K., Yanagisawa, M. & Togawa, N. (2017). Designing hardware trojans and their detection based on a SVM-based approach. *IEEE 12th Int. Conf. on ASIC (ASICON)*, 25-28 October 2017.

Iwase, T., Nozaki, Y., Yoshikawa, M. & Kumaki, T. (2015). Detection technique for hardware Trojans using machine learning in frequency domain. *IEEE 4th Global Conf. Consum. Electron. (GCCE)*, 27-30 October 2015.

Jap, D., Wei, H. & Bhasin, S. (2016). Supervised and unsupervised machine learning for side-channel based Trojan detection. *IEEE 27th Int. Conf. on Appl-specific Syst., Archit. and Processors (ASAP)*, 6-8 July 2016.

Jin, Y., Maliuk, D. & Makris, Y. (2012). Post-deployment trust evaluation in wireless cryptographic ICs. *2012 Des., Autom. & Test Europe Conf. Exhib. (DATE)*, 12-16 March 2012.

Kapersky. (2018). *What is a Trojan Virus?* Available online at: https://www.kaspersky.com/resource-center/threats/trojans (Last access date: 11 December 2018)

Karri, R., Rajendran, J., Rosenfeld, K. & Tehranipoor, M. (2010). Trustworthy hardware: Identifying and classifying hardware Trojans. *Comput.*, **43**: 39-46.

Kulkarni, A., Pino, Y. & Mohsenin, T. (2016a). Adaptive real-time Trojan detection framework through machine learning. *2016 IEEE Int. Symp. Hardware Oriented Secur. Trust (HOST)*, 3-5 May 2016.

Kulkarni, A., Pino, Y. & Mohsenin, T. (2016b). SVM-based real-time hardware Trojan detection for many-core platform. *17th Int. Symp. on Qual. Electron. Des. (ISQED)*, 15-16 March 2016.

Li, H., Liu, Q. & Zhang, J. (2016). A survey of hardware Trojan threat and defense. *Integration, the VLSI J.*, **55**: 426-437.

Li, J., Ni, L., Chen, J. & Zhou, E. (2016). A novel hardware Trojan detection based on BP neural network. *2016 2nd IEEE Int. Conf. Comput. Commun. (ICCC)*, 14-17 Oct. 2016.

Lodhi, F.K., Abbasi, I., Khalid, F., Hasan, O., Awwad, F. & Hasan, S. R. (2016). A self-learning framework to detect the intruded integrated circuits. *2016 IEEE Int. Symp. Circuits Syst. (ISCAS)*, 22-25 May 2016.

Lodhi, F. K., Hasan, S.R., Hasan, O. & Awwad, F. (2014). Low power soft error tolerant macro synchronous micro asynchronous (MSMA) pipeline. *2014 IEEE Comput. Soc. Annu. Symp. VLSI*, 9-11 July 2014.

Lodhi, F. K., Hasan, S.R., Hasan, O. & Awwadl, F. (2017). Power profiling of microcontroller's instruction set for runtime hardware Trojans detection without golden circuit models. *Des., Autom. & Test Europe Conf. Exhib. (DATE)*, 27-31 March 2017.

Lunardon, N., Menardi, G. & Torelli, N. (2014). ROSE: A package for binary imbalanced learning. *R J.*,**6**: 79-89.

Mingfu, X., Jian, W. & Aiqun, H. (2016). An enhanced classification-based golden chips-free hardware Trojan detection technique. *2016 IEEE Asian Hardware-Oriented Secur. Trust (AsianHOST)*, 19-20 December 2016.

Mitra, S., Wong, H.P. & Wong, S. (2015). The Trojan-proof chip. *IEEE Spectr.*, **52**: 46-51.

Peng, H., Long, F. & Ding, C. (2005). Feature selection based on mutual information criteria of max-dependency, max-relevance, and min-redundancy. *IEEE Trans. Pattern Anal. Mach. Intell.* **27**: 1226-1238.

Piccolboni, L., Menon, A. & Pravadelli, G. (2017). Efficient Control-flow subgraph matching for detecting hardware Trojans in RTL models. *ACM Trans. Embed. Comput. Syst.*, **16**: 1-19.

Piret, G. & Quisquater, J.-J. (2003). A differential fault attack technique against SPN structures, with application to the AES and Khazad. *In* Walter, C.D., Koc, C.K. & Paar, C. (Eds), *Cryptographic Hardware and Embedded Systems - CHES 2003. Lect. Notes Comput. Sc., Col 2779.* Springer, Berlin, Heidelberg.

Rajendran, J., Gavas, E., Jimenez, J., Padman, V., & Karri, R. (2010). Towards a comprehensive and systematic classification of hardware Trojans. *2010 IEEE Int. Symp. Circuits Syst.*, 30 May-2 June 2010.

Robertson, J., & Riley, M. (2018). *The Big Hack: How China Used a Tiny Chip to Infiltrate U.S. Companies*. Available online at: https://www.bloomberg.com/news/features/2018-10-04/the-big-hack-how-china-used-a-tiny-chip-to-infiltrate-america-s-top-companies (Last access date: 11 December 2018)

Salmani, H. (2017). COTD: Reference-free hardware trojan detection and recovery based on controllability and observability in gate-level netlist. *IEEE Trans. Inf. Forensics Secur.*, **12**: 338-350.

Salmani, H., Tehranipoor, M. & Karri, R. (2013). On design vulnerability analysis and trust benchmarks development.*2013 IEEE 31st Int. Conf. on Comput. Des. (ICCD)*, 6-9 Oct. 2013.

Sankaran, V., Weber, C. M., Lakhani, F., & Tobin, J. K. W. (1999). Inspection in semiconductor manufacturing. *Webster's Encycl. of Electr. Electron. Eng.*, **10**: 242-262.

Shakya, B., He, T., Salmani, H., Forte, D., Bhunia, S. & Tehranipoor, M. (2017). Benchmarking of hardware trojans and maliciously affected circuits_. *J. Hardware Syst. Secur.*, **1**: 85-102.

Tehranipoor, M., & Koushanfar, F. (2010). A Survey of Hardware Trojan Taxonomy and Detection. *IEEE Des. & Test of Comput*, **27**: 10-25.

Trust-Hub. (2013). *Trust-Hub*. Available online at: http://www.trust-hub.org/home (Last access date: 11 December 2018).

Wang, C., Li, J., Yu, M. & Wang, J. (2013). An intelligent classification method for Trojan detection based on side-channel analysis. *IEICE Electron. Express*, **10:** 20130602-20130602.

Wang, S., Dong, X., Sun, K., Cui, Q., Li, D. & He, C. (2016). Hardware Trojan detection based on ELM neural network. *2016 1st IEEE Int. Conf. on Comput. Commun. and the Internet (ICCCI)*, 13-15 October 2016.

Xiao, K., Forte, D., Jin, Y., Karri, R., Bhunia, S. & Tehranipoor, M. (2016). Hardware Trojans: Lessons learned after one decade of research. *ACM Trans. Des. Autom. Electron. Syst.*, **22**: 1-23.

Xiaoxiao, W., Tehranipoor, M., & Plusquellic, J. (2008). Detecting malicious inclusions in secure hardware: Challenges and solutions. *2008 IEEE Int. Workshop on Hardware-Oriented Secur. and Trust*, 9-9 June 2008.

Xie, X., Sun, Y., Chen, H., & Ding, Y. (2017). Hardware Trojans classification based on controllability and observability in gate-level netlist. *IEICE Electron. Express*, **14**: 20170682-20170682.

Yang, K., Hicks, M., Dong, Q., Austin, T., & Sylvester, D. (2016). A2: Analog malicious hardware. *2016 IEEE Symp. on Secur. and Privacy (SP)*, 22-26 May 2016.

A MESSAGE CRYPTOGRAPHY TECHNIQUE USING DNA BASED HYBRID APPROACH

Vaibhav Godbole

Fr. Conceicao Rodrigues College of Engineering, India

Email: vai.godbole@gmail.com

ABSTRACT

Cryptography makes the transmitted message unreadable to unauthorised users. DNA cryptography is being explored worldwide and even in being in its primitive stages, it has revolutionised the area of network security. In this work, we take inspiration from DNA encryption schemes and use the biological alphabets to manipulate information. In this paper, we present a hybrid algorithm for cryptography using DNA and compare the performance of various DNA algorithms with the N^{th} degree truncated polynomial ring (NTRU) algorithm. Our research shows that the hybrid DNA algorithm performs better than three DNA based algorithms and the NTRU algorithm that we have mentioned in this paper in terms of key length, execution time and throughput

Keywords: *DNA cryptography; encryption-decryption algorithm; N^{th} degree truncated polynomial ring (NTRU) algorithm; message encryption; hybridisation.*

1. INTRODUCTION

The process of converting messages from plain text to cipher text iscalled cryptography. Cryptography is a technique of achieving security for communications by encoding plain text messages to make it unreadable (Bazil *et al.,* 2014; Thangavel *et al.,* 2017). DNA cryptography, a new branch of cryptography utilises DNA as an informational and computational carrier with the aid of molecular techniques (Manisha, 2015). Cryptography and data security help to secure transmission and storage of information via insecure internet. Most cryptographic systems apply encryption of valuable information and produce an encrypted output that may be meaningless to an eavesdropper who has no knowledge of the key. It is simply a technique for hiding the true meaning of the information from unauthorised users. The worst case of an attack within communication is complete control of the encryption system by illegitimate users. This happens by accessing the encryption algorithm to decrypt the data and access sensitive information. Cryptography relies on uncertainty in encoding the message to its cipher format (Roy *et al.,* 2011; Ubaidur Rahman *et al.,* 2015).

Symmetric or secret key can be classified as stream ciphers or block ciphers. Stream ciphers operate on a single bit (byte or computer word) at a time, and implement some form of feedback mechanism so that the key is constantly changing. A block cipher encrypts a block of data at a time using the same key on each block (Gupta *et al.,* 2013). DNA based bimolecular cryptography design is a technique that uses the huge parallel processing capabilities of bio-molecular computation that converts short messages from hexadecimal and ASCII forms and then back to encrypt and decrypt the information (Amin *et al.,* 2009). This has been used on different applications, but we consider using this technique to safeguard sensitive information with the addition of the key generation technique from the bio-molecular properties of the DNA sequences (Wilson *et al.*,1999).

In this paper, we propose a novel algorithm for message encryption, which is a hybridisation of three different DNA based algorithms. The rest of this paper is organised as follows. Section 2 describes related work, while Section 3 describes the different algorithms used for DNA cryptography. Section

4 describes the proposed algorithm, while Section 5 describes the experimental analysis of the proposed algorithm and its comparison with all other algorithms that we have mentioned in this paper. Section 6 describes the conclusion and future scope

2. RELATED WORK

DNA refers to de-oxyribo nucleic acid, which is a nucleic acid that contains genetic information (Ning, 2009; El-Seoud *et al.,* 2017). It is a collection of the most complex organic molecules. The instructions in DNA is required to the construct other components of cells such as protein, ribonucleic acid (RNA) molecules, etc. DNA and RNA are appealing media for data storage due to very large amounts of data that can be stored in compact volume. They far exceed the storage capacities of conventional electronic, magnetic and optical media. For instance, a gram of DNA contains about 108 terabytes. Hence, a few grams of DNA may have the potential of storing all the data stored in the world (Chen *et al.,* 2003) DNA strand encoding include four bases that are represented by the letters A (Adenine), T (Thymine), C (Cytosine) and G (Guanine) (Aggarwal *et al.,* 2014). Each alphabet is related to a nucleotide is very long. For instance, the DNA sequence of length of 10 nucleotides long can be represented as ATCGAATTCG.

mRNA is a messenger RNA (mRNA) is a large family of RNA molecules that convey genetic information from DNA to the ribosome, where they specify the amino acid sequence of the protein products of gene expression. tRNA is a transfer RNA (tRNA) is an adaptor molecule composed of RNA, typically 76 to 90 nucleotides in length, which serves as the physical link between the mRNA and amino acid sequence of proteins (Najaftorkaman *et al.,* 2015).

DNA computing and cryptography came into picture in 1990s. DNA computing was initialised by L Adleman in 1990 where he solved a directed Hamiltonian path problem. It indicated the feasibility of a molecular approach to solve combinatorial problems (Ubaidur Rahman *et al*., 2015). DNA computing in the fields of cryptography and steganography have been identified as a possible technology that may bring forward a new hope for unbreakable algorithms. The following are advantages of DNA computing (Najaftorkaman *et al.,* 2015)

1. **Speed:** Conventional computers can perform approximately 100 MIPS (millions of instruction per second). Combining DNA strands as demonstrated by Adleman made computations equivalent to 10 to the power 9 or better, arguably over 100 times faster than the fastest computer.
2. **Minimal Storage Requirements:** DNA stores memory at a density of about 1 bit per cubic nanometre, where conventional storage media requires 10 to the power 12 cubic nanometres to store 1 bit (Wang *et al.*, 2009).
3. **Minimal Power Requirements:** There is no power required for DNA computing while the computation is taking place. The chemical bonds that are the building blocks of DNA happen without any outside power source. There is no comparison to the power requirements of conventional computers (Wang *et al.*, 2009).

3. CRYPTOGRAPHY BASED ALGORITHMS BASED ON DNA AND NTRU

This section describes the three algorithms used in DNA cryptography and the N^{th} Degree Truncated Polynomial Ring (NTRU) algorithm. We have implemented all those algorithms and compared their performance with our proposed algorithm.

3.1 Algorithm 1 (Ubaidur Rahman *et al.*, 2015)

There are two stages in this algorithm - Encryption and Random Key Generation. In the first stage, the source data is encrypted, which is the input to the second stage. In second stage, random key is generated, say P_k, which is used for the next level of encryption

The input for stage one is the source data, which is in the text format. Each character of the source data is converted to its corresponding ASCII value, which is in turn converted to its binary value. This process is explained in detailed in Algorithm 1.

Algorithm 1

```
1: INPUT: Plain text
2: Procedure EncryptText(String text)
3: asc: Ascii(text)
4: bin: BinaryValue(asc)
5: for pair ∈ PairsFrom(bin) do
6:    if pair = 00 then
7:       dnaSeq+=A
8:    else
9:       if pair = 01 then
10:         dnaSeq+=C
11:      else
12:         if pair = 10 then
13:            dnaSeq+=G
14:         else
15:            if pair = 11 then
16:               dnaSeq+=C
17:            end if
18:         end if
19:      end if
20:   end if
21: end for
22: PK: random combination(A T G C)
23: Index table: generate combinations(Pk)
24: encryptedMessage:
    findEncryptedKeys(indexTable, dnaSeq)
25: return encryptedMessage
```

A random key, say P_k (Step 22) in the range 1 to 256, is generated for further encryption. Corresponding to each value of P_k, an index table of size 256 is generated, where each value of the table corresponds to a combination of A, T, G and C, as shown in Table 1, $4^4 = 256$, hence size of index table is 256, which corresponds to the permutation of four characters, A, T, G and C. As the value of P_k varies, the index table will also vary. The encrypted binary data from the Stage 1 is the input for this stage. First, the input data is selected as pairs. Each pair is replaced by the DNA nucleotides, A, T, G, and C, corresponding to the values 00, 01, 10 and 11. From the index table, the index key corresponding to the combination of A, T, G, and C is obtained, which is, the final encrypted value corresponding to the character of source data.

Table 1: Index table generated from combination of letters ATGC

1	AAAA	33	CAAA	65	GAAA	97	TAAA	129	CAAG	161	CGAA	193	GGAA	225	TGAA
2	AAAC	34	CAAC	66	GAAC	98	TAAC	130	AGAC	162	CGAC	194	GGAC	226	TGAC
3	AAAG	35	AGAA	67	GAAG	99	TAAG	131	AGAG	163	CGAG	195	GGAG	227	TGAG
4	AAAT	36	CAAT	68	GAAT	100	TAAT	132	AGAT	164	CGAT	196	GGAT	228	TGAT
5	AACA	37	CACA	69	GACA	101	TACA	133	AGCA	165	CGCA	197	GGCA	229	TGCA
6	AACC	38	CACC	70	GACC	102	TACC	134	AGCC	166	CCGC	198	GGCC	230	TGCC
7	AACG	39	CACG	71	GACG	103	TACG	135	AGCG	167	CGCG	199	GGCG	231	TGCG
8	AACT	40	CACT	72	GACT	104	TACT	136	AGCT	168	CGCT	200	GGCT	232	TGCT
9	AAGA	41	CAGA	73	GAGA	105	TAGA	137	AGGA	169	CGGA	201	GGGA	233	TGGA
10	AAGC	42	CAGC	74	GAGC	106	TAGC	138	AGGC	170	CGGC	202	GGGC	234	TGGC
11	AAGG	43	CAGG	75	GAGG	107	TAGG	139	AGGG	171	CGGG	203	GGGG	235	TGGG
12	AAGT	44	CAGT	76	GAGT	108	TAGT	140	AGGT	172	CGGT	204	GGGT	236	TGGT
13	AATA	45	CATA	77	GATA	109	TATA	141	AGTA	173	CGTA	205	GGTA	237	TGTA
14	AATC	46	CATC	78	GATC	110	TATC	142	AGTC	174	CGTC	206	GGTC	238	TGTC
15	AATG	47	CATG	79	GATG	111	TATG	143	CATT	175	CGTG	207	GGTG	239	TGTG
16	AATT	48	AGTG	80	GATT	112	TATT	144	AGTT	176	CGTT	208	GGTT	240	TGTT
17	ACAA	49	CCAA	81	GCAA	113	TCAA	145	ATAA	177	CTAA	209	GTAA	241	TTAA
18	ACAC	50	CCAC	82	GCAC	114	TCAC	146	ATAC	178	CTAC	210	GTAC	242	TTAC
19	ACAG	51	CCAG	83	GCAG	115	TCAG	147	ATAG	179	CTAG	211	GTAG	243	TTAG
20	ACAT	52	CCAT	84	GCAT	116	TCAT	148	ATAT	180	CTAT	212	GTAT	244	TTAT
21	ACCA	53	CCCA	85	GCCA	117	TCCA	149	ATCA	181	CTCA	213	GTCA	245	TTCA
22	ACCC	54	CCCC	86	GCCC	118	TCCC	150	ATCC	182	CTAC	214	GTCC	246	TTCC
23	ACCG	55	CCCG	87	GCCG	119	TCCG	151	ATCG	183	CTCG	215	GTCG	247	TTCG
24	ACCT	56	CCCT	88	GCCT	120	TCCT	152	ATCT	184	CTCT	216	GTCT	248	TTCT
25	ACGA	57	CCGA	89	GCGA	121	TCGA	153	ATGA	185	CTGA	217	GTGA	249	TTGA
26	ACGC	58	CGCC	90	GCGC	122	TCGC	154	ATGC	186	CTGC	218	GTGC	250	TTGC
27	ACGG	59	CCGG	91	GCGG	123	TCGG	155	ATGG	187	CTGG	219	GTGG	251	TTGG
28	ACGT	60	CCGT	92	GCGT	124	TCGT	156	ATGT	188	CTGT	220	GTGT	252	TTGT
29	ACTA	61	CCTA	93	GCTA	125	TCTA	157	ATTA	189	CTTA	221	GTTA	253	TTTA
30	ACTC	62	CCTC	94	GCTC	126	TCTC	158	ATTC	190	CTTC	222	GTTC	254	TTTC
31	ACTG	63	CCTG	95	GCTG	127	TCTG	159	ATTG	191	CTTG	223	GTTG	255	TTTG
32	ACTT	64	CCTT	96	GCTT	128	TCTT	160	ATTT	192	CTTT	224	GTTT	256	TTTT

3.2 Algorithm 2 (Ubaidur Rahman *et al.*, 2015)

This algorithm uses the complementary pair approach. In the RNA sequence, we often have the so-called base pairs (Aggarwal et al., 2014). We may just define our own complementary pairs. That is, for each alphabet, we assign a unique counterpart for it. For instance, we may have the following base pair rule: (A T) (C A) (G C) (T G). Then, the complementary sequence of AATGC will be TTGCA. In the sequence "ATCTG**AATGC**TTGTCTA**TTGCA**TCAAT", complementary substrings occur, as indicated by the bold characters. To find the longest complementary substrings, we may use the dynamic programming approach. This process is explained in Algorithm 2

Algorithm 2

1: *INPUT*: Plain text(M)
2: *Procedure EncryptText(String text)*
3: *Assume string L*
4: *Divide M into 2 equal parts*
5: *Replace M with DNA sequence*
6: *Generate 2 complementary substings and insert into L to form L'*
7: *Insert M into L'*
8: *Assign random integers to i and j*
9: *insert substring s[j,j+i] and s[2j,2j+1] in L' to form L"*
10: *Return L"*

3.3 Algorithm 3 (Chen *et al.*, 2003)

The encryption algorithm is shown in Algorithm 3, which converts plaintext to cipher text. Before encryption starts, the encoding process is carried out for plaintext to DNA sequence conversion (Manisha, 2015).

Algorithm 3

1: *INPUT*: Plain textM
2: *Procedure EncryptText(String text)*
3: *Divide M into 2 halves equally*
4: *Convert M into DNA sequence using Encoding table*
5: *Convert DNA to Binary A:00, T:01, C:10, G:11*
6: *Divide binary string into 2 halves and XNOR*
7: *Convert binary to DNA sequence A:00, T:01, C:10, G:11*
8: *Covert to mRNA*

$$(T \Rightarrow U)$$

9: *Covert to tRNA*

$$(A \Rightarrow U)$$

$$(U \Rightarrow A)$$

$$(G \Rightarrow C)$$

$$(C \Rightarrow G)$$

10: *Reverse Trascription*

$$(U \Rightarrow T)$$

11: *Right Shift the sequence*
12: *Replace DNA with the corresponding values in Amino acid table*
13: *Return the Encrypted Message*

3.4 NTRU ENCRYPTION ALGORITHM (Hoffstein *et al.*, 1998)

NTRU is an open source public-key cryptosystem that uses lattice-based cryptography to encrypt and decrypt data (Hoffstein *et al.*, 1998). NTRU is a lattice-based alternative to the RSA (**R**ivest, Adi

Shamir and Leonard **A**dleman) and ECC (**E**lliptical **C**urve **C**ryptography) algorithms, and is based on the shortest vector problem in a lattice. In 2009, the Institute of Electrical and Electronics Engineers (IEEE) approved the NTRU Cryptosystem for standardisation. The IEEE standard for NTRU algorithm is IEEE P1363. This algorithm is based on polynomial rings and used for message encryption (Singh *et al.*, 2016)

NTRU operates by mixing and reduction modulo of two prime numbers. NTRU operates primarily on the use of polynomials, which undergo the following operations: sum, product, inverse and modulus. NTRU operates in the convolution ring *R*, which denotes the set of such polynomials, with a maximum degree of $(N-1)$ and *N* terms, where *N* is the parameter size (Gaithuru *et al.*, 2016).

NTRU considers a few properties of a polynomial ring $Z[x]/(x^N-1)$. (Gaithuru *et al.*, 2016). The elements of this ring are polynomials of degree at most *N* -1 with integer coefficients. Ring addition is performed component wise and the product is the convolution product of polynomials:

For

$$a = a_0x^0 + a_1x^1 + a_2x^2 + \dots a_{N-2}x^{N-2} + a_{N-1}x^{N-1}. \quad (1)$$

and

$$b = b_0x^0 + b_1x^1 + b_2x^2 + \dots b_{N-2}x^{N-2} + b_{N-1}x^{N-1} \quad (2)$$

This is calculated as:

$$a*b = \sum_{i=0}^{N-1}\Big(\sum_{j+k\equiv i(N)} a_jb_kx^i\Big) \quad (3)$$

For example:

$$(1+2x^2+x^5)*(x^2+3x^4 = x^2+5x^4+6x^6+x^7+3x^9 = 1+4x^2+5x^4+6x^6 \quad (4)$$

is a polynomial ring of $Z[x]/(x^7-1)$ (Meskanen, 2005)

System parameters: The cipher would have three integer parameters, *n*, *p* and *q*. The integer *n* has to be 2^l, *p* is a small prime, and *q* is large prime such that the greatest common divisor, $\gcd(p,q)=1$, and p < q. Table 2 displays the system parameters required for this algorithm (Huang *et al.*, 2018). Algorithms 4 and 5 show the key generation and encryption algorithm for NTRU.

Table 2: System parameters.

1	n-degree parameter
2	q-Large Modulus
3	Ring Parameters, $R_{n,q} = \frac{z_q[x]}{x^n+1}$
4	p-Plaintext space modulus
5	a_1, a_2, a_3-Non-zero coefficient counts for product form polynomial terms.
6	μ-Plaintext
7	c-Cyphertext
8	k-Secret key
9	r-Ephemeral key
10	$\mathcal{D}_\mu$-Plaintext space
11	$\mathcal{D}_c$-Ciphertext space
12	$\mathcal{D}_k$-Secret key space
13	$\mathcal{D}_r$-Ephemeral key space
14	$\mathbb{B}$ ={Binary Polynomials}
15	$\mathbb{T}_n$ ={Ternary Polynomials}
16	$\mathbb{T}_n(a,e)$-{Ternary polynomials with exactly a ones and e minus ones}
17	$\mathbb{P}_n(a_1,a_2,a_3)$ ={Product form of polynomials $A_1 * A_2 + A_3 : A_i \in \mathbb{T}_n(a_i,a_i)$}

Algorithm 4 Key generation

1: *INPUT*: Set of input parameters
2: $k' \leftarrow \mathbb{P}_n(a_1, a_2, a_3)$
3: $k = 1 + p.k \in R_{n,q}$
4: until k is invertible in $R_{n,q}$
5: *OUTPUT*:secret key k

Algorithm 5 Encryption

1: *INPUT*: Secret key k, message $\mu \in \{(-p-1)/2, ... + (p-1)/2\}^n$, and set a parameter, $p = 3$
2: $r \leftarrow \mathbb{P}_n(a_1, a_2, a_3)$
3: $c = (p.rk1 + \mu)(mod\, q) \in R_{n,q}$
4: *OUTPUT*: Ciphertext c

4. PROPOSED ALGORITHM

Our proposed algorithm is a hybridisation of the three DNA algorithms that was discussed in the previous section. Figure 1 shows the flowchart of our proposed algorithm and Algorithm 6 shows the steps for our proposed algorithm. Consider the message the *M* to be transmitted to the receiver, the different steps for encryption is as follows:

Step 1: The text to be transmitted is first converted to ASCII code (in decimal format).

Step 2: The ASCII message (decimal values) is then converted to binary format (0s and 1s).

Step 3: The binary format is converted into DNA sequence. DNA strand encoding includes four bases, which are represented by the letters A (Adenine), T (Thymine), C (Cytosine) and G (Guanine). Each alphabet is related to a nucleotide. The encrypted binary data from the Step 2 is the input for this stage. First, the input data is selected as pairs. Each pair is replaced by the DNA nucleotides A-00, T-01, G-10, and C-11.

Step 4: The DNA sequence obtained in Step 3 is converted to mRNA sequence by replacing Thymine (T) with Uracil (U).

Step 5: The mRNA sequence is converted into tRNA sequence by replacing every DNA alphabet with its complement DNA alphabet. For e.g. A-U, U-A, G-C, C-G conversions are carried out.

Step 6: The tRNA sequence is converted into DNA sequence by replacing Uracil (U) with Thymine (T) in the tRNA sequences. This process is a simulation of biological reverse transcription.

Step 7: The DNA sequence from reverse transcription is right shifted

Step 8: Assume a reference string S=ACGG of length *k* (random number) and a complimentary reference string S'=TACC obtained by replacing ((A-T) (C-A) (G-C) (T-G)).

Step 9: Append the reference string *S* before the message bits and the complimentary reference string *S*' after the message bits.

Step 10: Replace DNA sequence obtained with corresponding values in the index table as shown in Table 1.

Step 11: The resultant sequence is the encrypted message.

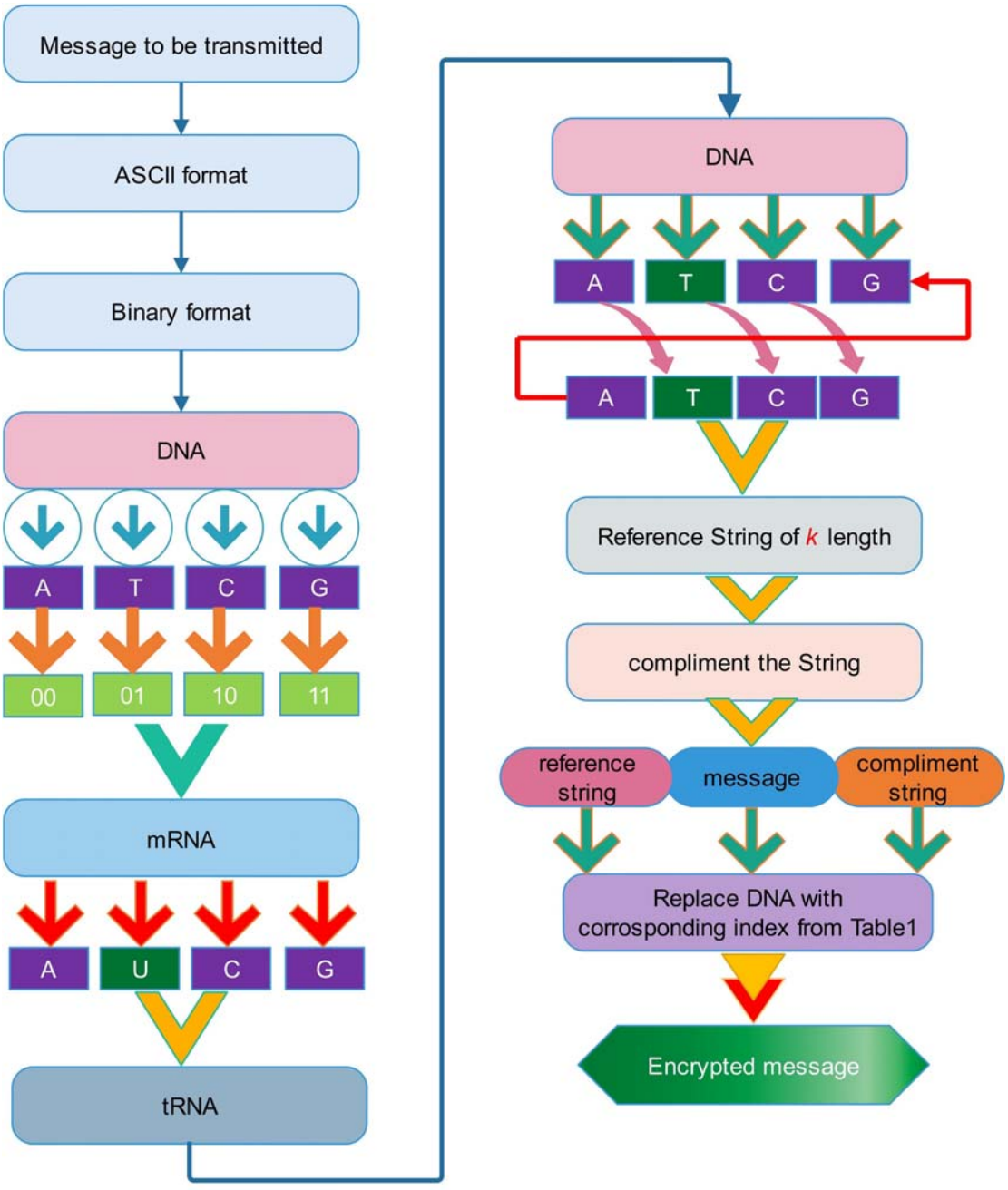

Figure 1: The proposed algorithm.

Algorithm 6 Proposed Algorithm

1: *INPUT*: Plain textM
2: *Procedure EncryptText(String text)*
3: *Convert Text to ASCII*
4: *Convert ASCII to binary*
5: *Convert Binary to DNA A:00, T:01, G:10, C:11*
6: *Covert to mRNA*

$$(T \Rightarrow U)$$

7: *Covert to tRNA*

$$(A \Rightarrow U)$$

$$(U \Rightarrow A)$$

$$(G \Rightarrow C)$$

$$(C \Rightarrow G)$$

8: *Reverse Trascription*

$$(U \Rightarrow T)$$

9: *Right Shift the sequence*
10: *Assume a string sequence S and find its complementary string S'*
11: *Append S before the message and S' after the message*
12: *PK*: random combination(A T G C)
13: *Index table*: generate combinations(Pk)
14: *encryptedMessage*: findEncryptedKeys(indexTable, dnaSeq)
15: *return encryptedMessage*

5. EXPERIMENTAL ANALYSIS AND DISCUSSION

In this section, we present the experimental analysis and comparison of our proposed algorithm with Algorithms 1, 2 and 3, and the NTRU algorithm. We implemented all these algorithms in Java on an Intel I-3 processor system with 2 GB RAM. We considered a string having length of 128 characters for our experimentation.

Figure 2 shows the key sizes for the different algorithms. We have considered 128- and 256-bit encryption standards for our experiments. The experiments show that the key length of the proposed algorithm is almost same as that of the NTRU algorithm, but nonetheless smaller than all the other algorithms.

Figure 3 shows execution times for encryption of a string with 128 characters. The experiment shows that the execution speed of the proposed algorithm is smaller than the other algorithms.

Figure 4 shows the throughput of the proposed algorithm. The experiments show that the throughput of the proposed algorithm is higher than all the other algorithms. The basic terminology is that as throughput increases, the power consumption decreases. Hence, the proposed algorithm consumes less power as compared to the other algorithms.

Table 3 shows the comparison of all algorithms that we have mentioned in this paper. The comparison shows that the number of lines of codes required for the proposed algorithm is less as compared to the other algorithms. For the proposed algorithm, the index of coincidence is smaller than the other algorithms.

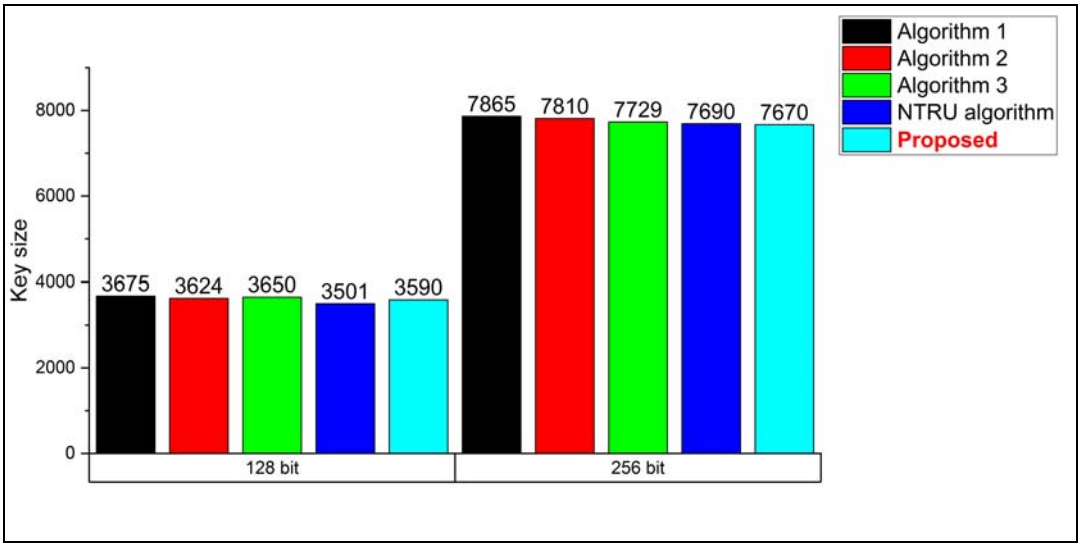

Figure 2: Key sizes with different security levels.

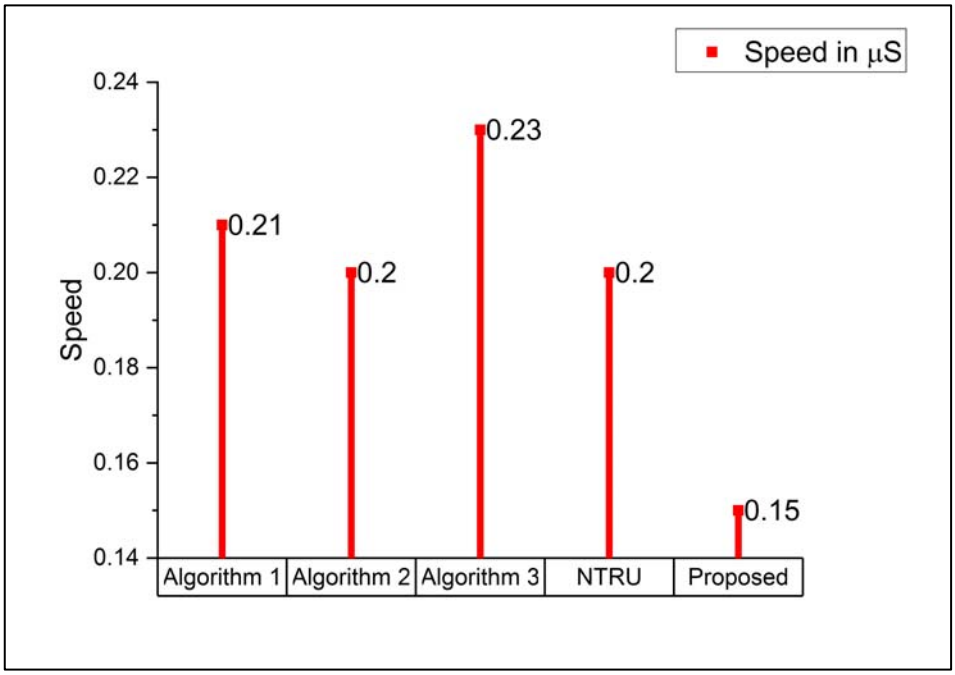

Figure 3: Execution time (speed) of the algorithms.

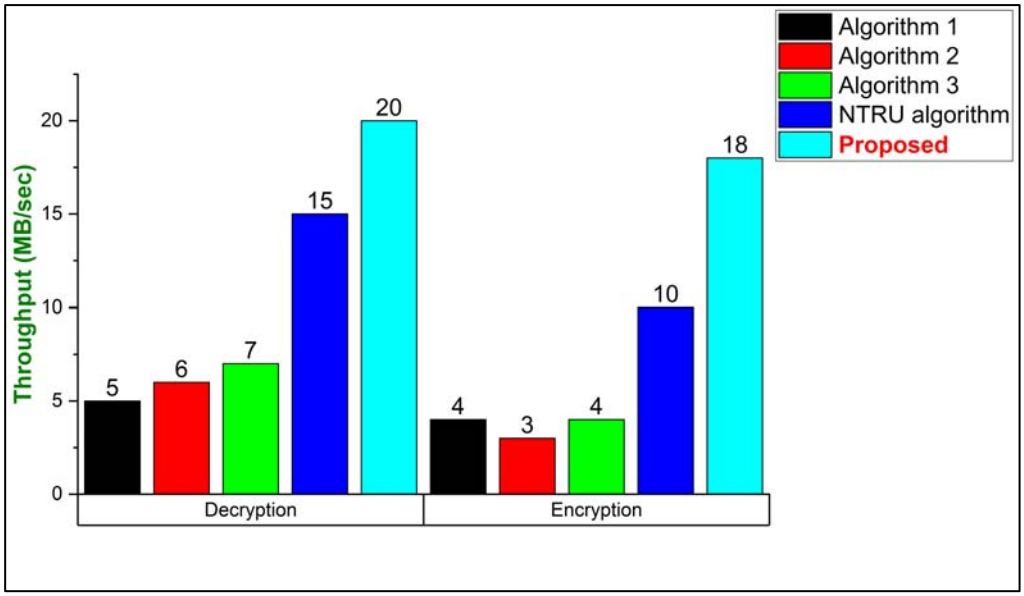

Figure 4: Throughput of the algorithms.

Table 3: Comparison of the algorithms.

	Algorithm 1	Algorithm 2	Algorithm 3	NTRU	Proposed
Time complexity	N	n^2	n	n	n
Space complexity	N	2^k	n^k	n	n
Lines of codes	151	171	310	165	160
Index of coincidence	0.3111	0.2688	0.3023	-	0.2679
Cipher pattern	Fixed	Variable	Fixed	Fixed	Fixed

6. CONCLUSION AND FUTURE WORK

In this paper, we have pointed out that DNA sequences have the special properties that we can utilise for encryption purposes. We have given three methods that based upon a reference sequence known only to the sender and the receiver. We have presented three algorithms using DNA cryptography and NTRU algorithm for message encryption. We also have proposed a new algorithm based on symmetric key encryption after understanding the previously implemented algorithms. The proposed algorithm performs better than the other DNA based algorithms and NTRU algorithm in the context of time requirements for encryption, index of coincidence, key length, and throughput (power consumption).

In the future, we will analyse the performance of our proposed algorithm with large sized text. In addition, we will extend our work to encrypt images and compare its performance with other algorithms used for image encryption.

`

REFERENCES

Aggarwal, A. & Kanth, P. (2014). Secure data transmission using DNA encryption. *Int.J. Adv.Res. Comp. Sci.*, **5**:10-15

Amin, S. Saeb, M. & El-Gindi, S. (2006). A DNA-based implementation of yaea encryption algorithm. *In* Amin, S.T. & El-Gind, S. (Eds), *Computational Intelligence*, 120–125.

Bazil, B. & Tuncel, M.A. (2014). Data encryption using bio-molecular information. *Int. J. Crypt. Inform. Secur.*, **4**: 21-33

Chen, J. (2003). A DNA-based, biomolecular cryptography design. *Int. Sym. Cir. Sys.*, **3:** III

El-Seoud, S. Mohamed, R. & Ghoneimy, S. (2017). DNA computing: Challenges and application. *Int. J. Inter. Mob. Tech.*, **11**:74-87.

Gaithuru, J. Salleh, M. & Mohamad, I. (2016). Mini n^{th} degree truncated polynomial ring (mini-ntru): A simplified implementation using binary polynomials. *Int. Conf. Eng. Edu.*, pp. 270-275

Gupta, K. & Singh, S. (2013). DNA based cryptographic techniques: A review. *Int. J. Adv. Res. Comp. Sci. Soft. Eng.*, **3**: 607-610.

Hoffstein, J. Pipher, J. & Silverman, J. (1998). NTRU: A ring-based public key cryptosystem. *Int. Algo. Num. Theo. Sym.*, Springer, Berlin, pp. 267-288

Manisha, P. (2015). A survey on DNA based cryptography. *Int. J. Sci. Eng.. Res.* **3**:132-134.

Meskanen, T. (2005). On the NTRU cryptosystem. *In Meskanen, T. (Eds), Turku Centre for Computer Science*, 28-29.

Mi, B. Huang, D. & Wan, S. (2018). NTRU implementation of efficient privacy-preserving location-based querying in vanet. *Wireless Commun. Mobile Comput.*, **2**: 1-11

Najaftorkaman, M & Kazazi, N. (2015). A method to encrypt information with DNA-based cryptography. *Int. J. Cy. Sec. Dig. Fore.*, **4**:417–427.

Ning, K (2009). A pseudo DNA cryptography method. *arXiv preprint arXiv:0903.2693*

Rivest, R. Shamir, A. & Adleman, I (1978). A method for obtaining digital signatures and public-key cryptosystems. *Comm. ACM*, **2**: 120–126.

Roy, B. Rakshit, G. Singha, P. Majumder, A. & Datta, D. (2011). An improved symmetric key cryptography with DNA based strong cipher. *IEEE Int. Conf. Dev. Comm., pp.* 1-5

Singh, S. & Padhye, S., (2016). Generalisations of NTRU cryptosystem. *Sec. Comm. Net,* **9**:6315-6334.

Thangavel, M. Varalakshmi, P. & Sindhuja, R (2017). A comparative study on DNA based cryptosystem. *Res. Rec. Dev. Intel. Comm. Apps.*, IGI Global, 496–528.

Ubaidur Rahman, N. Balamurugan, C. & Mariappan, R. (2015). A novel DNA computing-based encryption and decryption algorithm. *Proc. Comp. Sci.*, **46**:463–475.

Wang, X. & Zhang, Q. (2009). DNA computing-based cryptography. *Int. Conf. Bio. Insp. Comp., pp.* 1-3.

Wilson, B. (1999). *SEC1: Elliptic Curve Cryptography*. *Certicom Corporation,* Toronto, Canada.

INVESTIGATION OF VEHICLE OCCUPANT RESPONSE SUBJECTED TO UNDER-VEHICLE EXPLOSION

Khalis Suhaimi, Risby Mohd Sohaimi*, Muhammad Fahmi Md. Isa, Muhd Azhar Abu Bakar,Norazman Mohamad Nor, Ariffin Ismail& Victor Feisal Knight

Protection and Survivability Research Unit (PROTECT), Faculty of Engineering
National Defence University of Malaysia (NDUM), Malaysia

*Email: risby@upnm.edu.my

ABSTRACT

An improvised explosive device is regarded as one of the primary threats that can cause fatalities to armoured vehicle occupants. Upon detonation, the shock wave injures the crews as they are in direct contact with the blast impact through their feet and seating position. It is crucial to disperse the shock wave within a short time thus reducing the potential injury towards the vehicle's occupants. Traditional experimental processes typically use an actual vehicle and specialised anthropometric test dummy which is costly and non-repeatable if the asset is damaged during tests. This paper presents a scaleddown blast testing approach which comprises of an instrumented general-purpose dummy and a blast capsule. The capsule was designed to accommodate dummy at different seating position and a recumbent position. The main structural component of the blast capsule was designed and analysed using the strength of materials principle. Accelerometers were installed on specific areaof the blast capsule and an instrumented dummy for data measurement. The blast testing was performed using PE4 and at a fixed standoff distance under the capsule hull. Results have shown that the measured data have similarity in terms of shock history curves with other published works. Results obtained can also be used in validation of future simulation work.

Keywords: *Capsule; dummy; explosion; injury criteria; blast.*

1. INTRODUCTION

Improvised explosive devices (IEDs) have contributed about 50% of fatalities among military personnel in Afghanistan, whereas in Iraq the casualty percentage recorded was 10% higher for similar threats. For mine related attacks, the distinctive injuries sustained by vehicle crew were reported at the lower leg and brain region (Galarneau *et al.*, 2008; Nguyen *et al.*, 2018). Typical anti-tank landmine contains about 9.0 kg of high explosive, and upon the detonation, it creates tremendous impulses which may damage the vehicle body. Nowadays, an armoured vehicle with 150 mm thick plate is susceptible to IED or landmine with shaped charge capability (Sliwinski, 2011). Critical injury or even death can occur whenever the shock waves are not effectively dissipated and the impact load is higher from the prescribed threshold injury value (Maciej *et al.*, 2018). The insurgent attacks in Afghanistan and Iraq has gained a lot of interest amongst researchers in vehicle crews protection systems.

Several studies have been made by other researchers on the vehicle occupant blast response which involved numerical simulation and experimental investigation(Arepally *et al.*, 2008; Bir *et al.*,2008; Panowicz *et al.*, 2010; Sławiński *et al.*, 2013; Mackiewicz *et al.*, 2016). They performed finite element analysis using Hybrid III male anthropometric test dummy (ATD) model from Livermore Software Technology Corporation (LSTC). Bailey *et al.* (2013) had conducted lab-based experimentations to simulate the effect of occupants' response inside a vehicle from the mine blast.

Their study had adopted the sled impact test procedure that focused mainly on the lower extremities part of the human anatomy. However, the sled impact test can be considered an alternative testing method other than the blast capsule type of experiment. Vlahopoulos *et al.* (2010) and Dooge *et al.* (2011) studied the vehicle crew response using the blast capsule approach. Both studies had designed a custom-built capsule system to evaluate the anthropometric test dummy in a typical seating position. In this paper, a blast capsule design and an ATD blast response are discussed. The capsule was designed with consideration of the crew position at sitting and recumbent position. Recumbent position depicted the scenario of an injured occupant placement inside an armoured vehicle (ambulance variant).

2. CAPSULE DESIGN

The blast capsule design should resemble the characteristics of an armoured vehicle. For this work, the ground clearance for the capsule was determined in reference to SIBMAS AFSV 6x6 armoured vehicle. The vehicle base clearance was measured at 400 mm from the ground. Aside from the SIBMAS AFSV vehicle, NATO AEP-55 testing standard for armoured vehicle mine protection evaluation was also referred for ATD seating arrangements (NATO, 2011). A general purpose test dummy equipped with accelerometers (installed at the sole, pelvic and head region) was used as the test object in the proposed blast testing procedure. The positioning of the ATD at seating and recumbent position was used in determining the capsule overall length, width, and height.

A chassis structure was constructed using T-beam structural elements. The length of the total capsule was established by arranging three chassis structures (front, center, rear) according to the length of a field stretcher, in order to accommodate the ATD at a recumbent position. Figure 1(a) exhibits the design of the capsule main structure with respect to the rear, upper and seating height limit. Figure 1(b) depicts the arrangement of the three main structures prior to the length of the standard NATO stretchers arrangement (NATO, 2013).

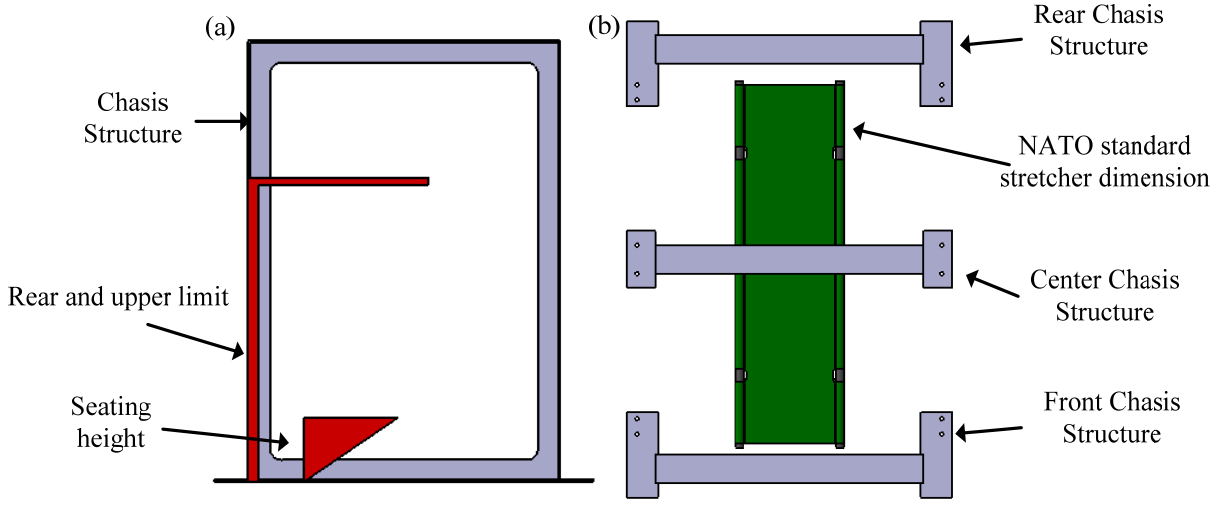

Figure 1: (a) Side view of the positioning of ATD prior to capsule frame reconstruction. (b) Top view of the recumbent position of ATD on a stretcher with frame structures.

2.1 Chassis Structure

T-beam structure was selected as the main capsule frame due to its availability in the local market. The loading condition for the T-Beam was based from several published works which reported the air blast pressure ranges from 80 to 100 MPa (Chung *et al.,* 2012; Karlos & Solomos, 2013; Saeimi-Sadigh *et al.,* 2014).The reported load distribution was then used in the determination of the T-Beam sizes. The maximum bending point of the T-BEAM was computed using the equation reported by Young *et al.*(2012):

$$y = \theta_1 x + \frac{M_1 x^2}{2EI} + \frac{R_1 x^3}{6EI} - \frac{w_a}{24EI} < x-a >^4 - \frac{(w_L - w_a)}{120EI(L-a)} < x-a >^5 \qquad (1)$$

where R is the reaction force at the beam support, M is the bending moment, E is the modulus of elasticity of the T-beam material, θ is the angle of the elastic slope, x is the distance in between each support, L is the length of supported beam, w is the distributed load at designated point and I is the moment of inertia of the cross section about the neutral axis of the T-beam. The T-Beam free body diagram and its designated parameters are shown in Table 1. The required beam dimension was determined from Table 1, which was calculated using Equation 1.

The T-beam with the smallest deflection and with the lowest mass was selected as the frame structure. The selected T-beam properties are shown in Table 1.

Table 1: Free body diagram for simple analytical chassis structure and calculated parameters.

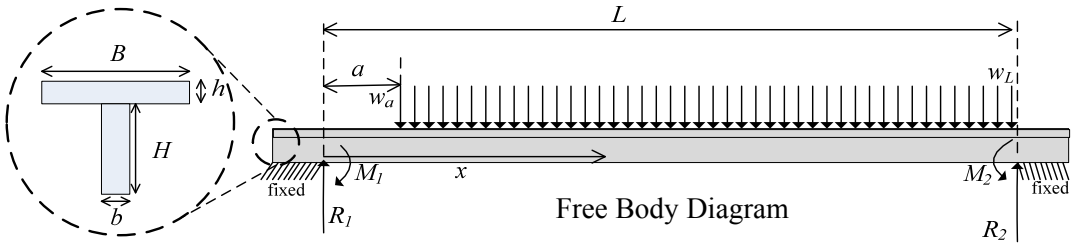

Parameter	*Unit*	Parameter	*Unit*
Reaction Force 1, R_1	68.85 kN	Reaction Force 1, R_2	68.85 kN
Reaction Moment 1, M_1	-19.5075 kN	Reaction Moment 1, M_2	-19.5075 kN
Maximum deflection, y_{max}	0.00128 m	Maximum Bending Stress, σ_{max}	66.2 Mpa
Distributed load at a , w_a	81 kN	Distributed load at L , w_L	81 kN
Web height, H	135 mm	Web thickness, *b*	10 mm
Flange width, B	150 mm	Flange thickness, *h*	15 mm
Distance, a	0 m	Distance, L	1.7 m
Distance, x	0 to 1.7 m	Material	A36 steel

2.2 Capsule Shape Design and Testing

The blast capsule hull was fabricated using A36 steel of 5 mm thick panels for the side-wall and roof section. The capsule floor was fabricated using 10 mm thick A36 steel panel in order to withstand the full impact of the blast. A steel instrumentation box with a spring-based absorber system was installed at the capsule rear section. The function of the box was to secure any instruments or data logger unit during the testing event. The shock wave acceleration data from the published work of Dooge *et al.* (2011) and Denefeld *et al.* (2014), reported at 175 G to 350 G, were used in the selection of the spring absorber system. From obtained values, a helical spring system produced by Socitec, United Kingdom

was selected for the project. The helical spring (product code: CB1400-50IM) can withstand the maximum static force of 206 daN and shock force of 618 daN to 1648 daN depending on tension or compression mode. The complete design of the blast capsule is as shown in Figure 2.

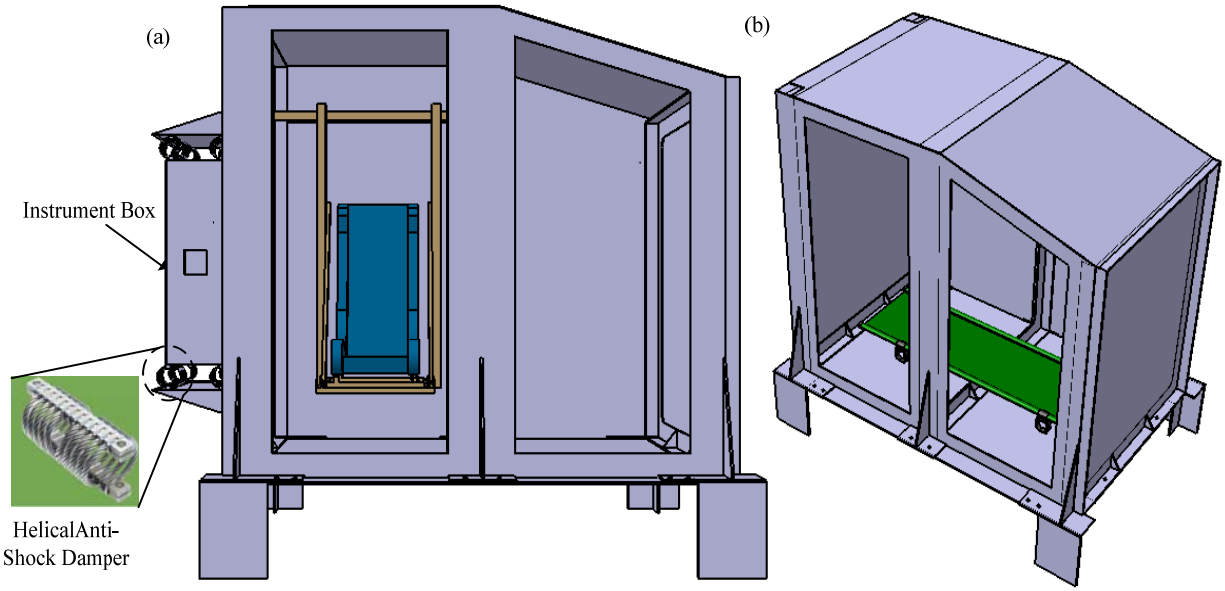

Figure 2: (a) Side view of the capsule with seat installed to the wall of the capsule. (b) Isometric view of the capsule with the stretcher placed on the capsule floor.

Based from Table 1, the physical properties such as mass, the centre of gravity and moment of inertia values of the blast capsule was estimated using a computer-aided drawing software. The computed properties are shown in Table 2. The capsule fabrication work was outsourced to a local vendor and the testing was conducted at a military site as shown in Figure 3.

Table 2: Physical properties of the blast capsule.

Center of gravity	
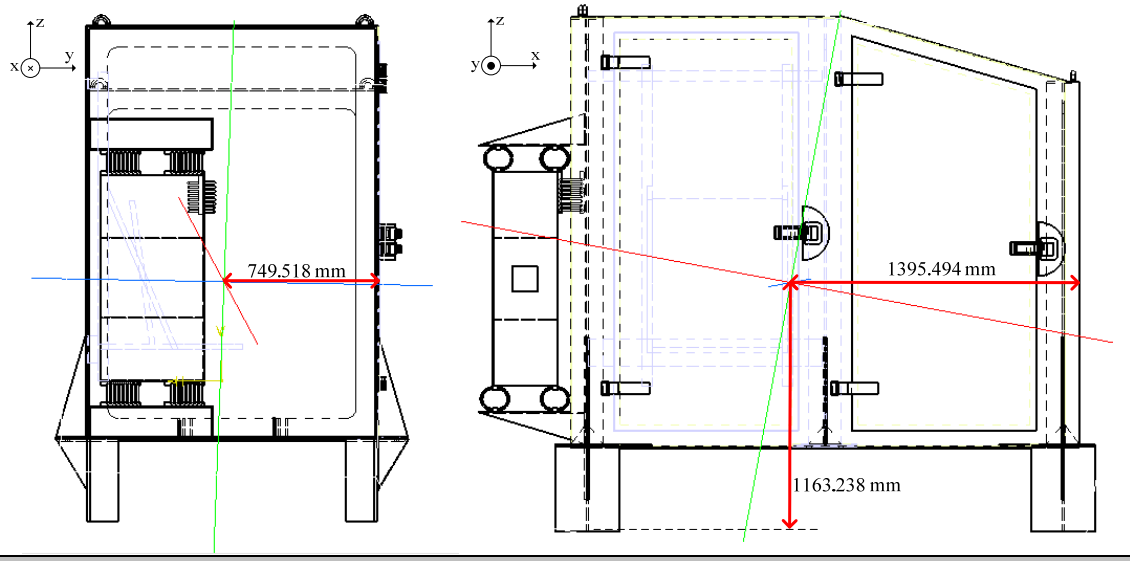	
Properties	*Data*
Mass	1556.425kg
Moment of inetia along x-axis, I_x	1296.885kgm^2
Moment of inetia along x-axis, I_y	1651.034 kgm^2
Moment of inetia along x-axis, I_z	2002.567kgm^2

Figure 3: Fabricated blast capsule: (a) Side view (b) Rear view.

For the testing procedure, an explosive charge was placed under the capsule. The weight of the charge was estimated according to the Hopkinson-Cranz scaling law (Caçoilo *et al.*, 2018), as shown in the following equation:

$$Z = \frac{R}{\sqrt[3]{W}} \qquad (2)$$

where Z is the scaled distance, R is the stand-off distance and W is the scaled TNT weight. The explosive mass (PE4) of 200 g was used in the testing scheme. The PE4 mass has the equivalency of 1.002 kg TNT blast tenacity at a target distance of 1 m. The blast testing was performed using an ATD as per specified in NATO AEP-55 standard. The ATD (rigged with several accelerometers and load cells) was tested in two categories; ATD at sitting position and ATD at horizontal recumbent position (as shown in Figure 4). The explosive charge PE4 of 75 g was placed inside a steel pot under the blast capsule with standoff distance of 400 mm. The ATD was restrained at the seat using a SABELT 5 point harness belt whereas for the recumbent position, the ATD was strapped to the stretcher at the chest, pelvic and knee region. The explosive material was detonated using an electrical detonator as shown in Figure 5.

Figure 4: Dummy positioning: (a) Sitting (b) Horizontal recumbent

Figure 5: Blast testing of the capsule and ATD.

3. RESULTS AND DISCUSSION

The blast responses were measured using PCB Piezotronics, Inc. accelerometers (350B03 and 350B01) and the data was recorded using NlPXle-1078 data acquisition module. Figure 6(a) depicts the blast capsule floor acceleration in "g" or shock endured of 4,752 g when the blast wave impacted the hull at 0.175 ms. The shock wave from the blast was transmitted to the dummy pelvic and head (in horizontal recumbent position). Data obtained from the sensor showed the peak shock of 4.36 g and 8.02 g respectively at approximately 0.19 ms, as shown in Figures 6(b) and (c).

Based from the result, it can be assumed that the stretcher to floor gap distance and the stretcher poles hollow structure were able to produce a significant shock attenuation capability. These parameters reduced the transmitted shock wave from the floor to the dummy.The ATD pelvic endured less shock transmission than the head section because the pelvic region is located farther from the blast location as compared to the head. Badshah *et al.* (2017) reported that hollow structures and stand-off distance plays a very effective role in shock wave energy absorption and attenuationof blast protection.

Figure 7(a) shows the blast capsule floor acceleration measured at 5,621 g when the blast wave impacted the hull at 0.170 ms. The slight difference of the shock value when compared to Figure 6(a) maybe attributed to the packing density of the PE4 and the atmospheric condition during the detonation period. The shock wave from the blast was transmitted to the dummy pelvic and head (at sitting position). Data obtained from the sensor showed the peak shock values of 172 g and 7.2 g at approximately 0.19 ms, as shown in Figures 7(b) and (c).

The foot region exhibits higher shock value due to the foot's close contact with the flooring section. As the shock wave travels through the ATD structure (foot, tibia, knee, torso to the pelvic), the wave propagation is attenuated by the ATD material and structures. This trend was similarly observed by Tabiei & Nilakantan (2007) in their work.

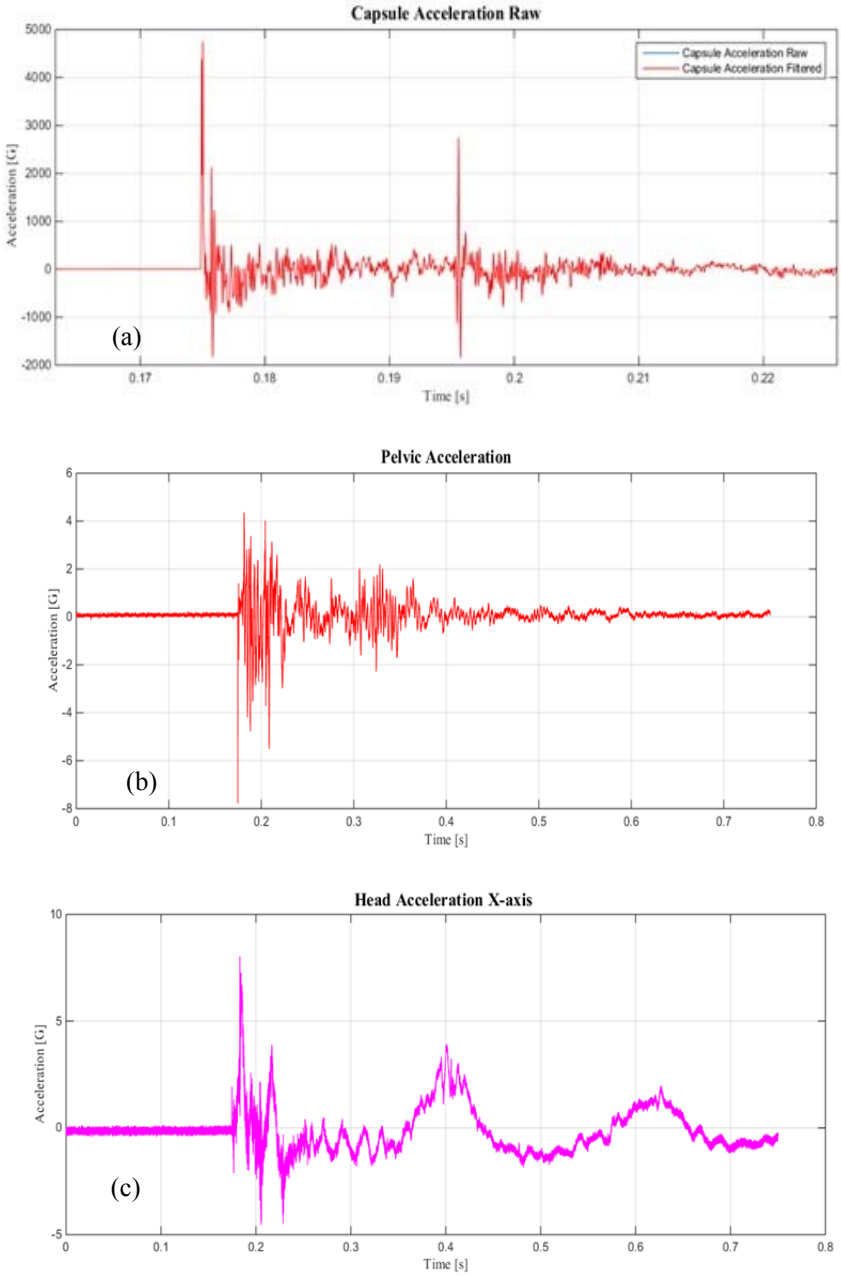

Figure 6: Recumbent position shock history curves for: (a) Blast capsule floor (b) ATD pelvic (c) ATD head.

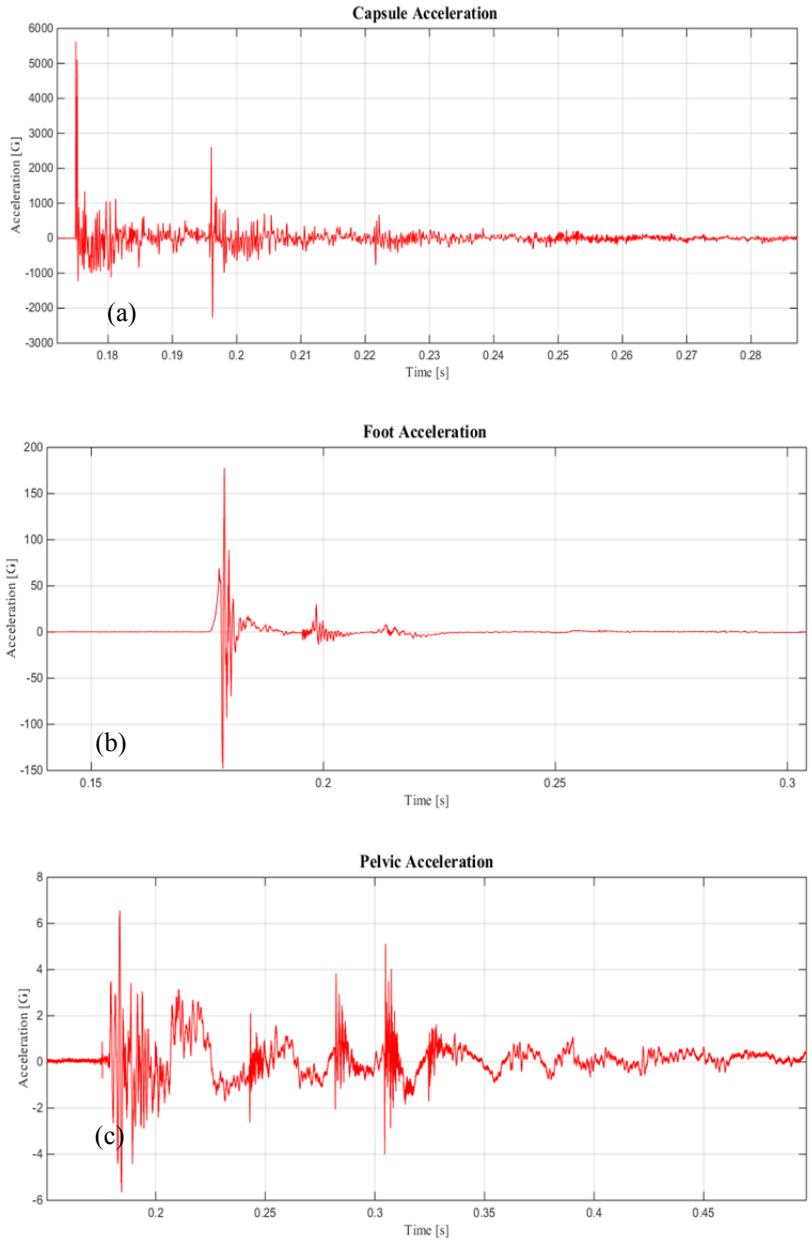

Figure 7: Seating position shock history curves for: (a) Blast capsule floor (b) ATD foot (c) ATD pelvic.

4. CONCLUSION

Investigation of occupant response (using an ATD as surrogate) during mine blast detonation was conducted at designated site. The scaled down experimental approach was found to be feasible in order to simulate actual vehicle occupant's response. In this work, the capsule design was able to fit an ATD at seating and recumbent position. An analytical calculation was performed to estimate the maximum deflection of the capsule chassis structure, which was computed at 0.00128 m. From the blast test results, the pelvic, head and foot data showed trends similarly observed in other published works. The ATD foot region exhibited the highest shock value due to its close proximity to the blast capsule floor. The experimental results obtained can be used to validate future numerical simulation work related to mine blast survivability.

ACKNOWLEDGEMENT

The authors wish to acknowledge the research grant provided by the Long Term Research Grant Scheme (LRGS/B-U/2013/UPNM/DEFENCE&SECURITY-P3) from the Malaysian Ministry of Education that lead to the realisation of this work.

REFERENCES

Arepally, S., Gorsich, D., Hope, K., Gentner, S. & Drotleff, K. (2008). Application of mathematical modeling in potentially survivable blast threats in military vehicles.*26th Army Sci. Conf.2008*, 1-4 December 2008, Orlando, Florida.

Badshah, E., Naseer, A., Ashraf, M., Shah, F. & Akhtar, K. (2017). Review of blast loading models, masonry response, and mitigation. *Shock Vib.*,**2017**: Article ID 6708341.

Bailey, A.M., Christopher, J.J., Henderson, K., Brozoski, F. & Salzar, R.S. (2013). Comparison of hybrid-III and PMHS response to simulated underbody blast loading conditions.*IRCOBI Conf.* 2013, **7288**: 158–170.

Bir, C., Barbir, A., Dosquet, F., Wilhelm, M., Horst, M. &Wolfe, G. (2008). Validation of lower limb surrogates as injury assessment tools in floor impacts due to anti-vehicular land mines, *Mil.Med.*,**173**: 1180–1184.

Caçoilo, A.,Mourão, R., Belkassem, B., Teixeira-Dias, F., Vantomme, J. & Lecompte, D. (2018). Blast wave assessment in a compound survival container: Small-scale testing. *Int. Conf. Exp. Mechanics.*,**2**: 540.

Chung, K.Y.S., Langdon, G.S., Nurick, G.N., Pickering, E.G. & Balden, V.H. (2012). Response of V-shape plates to localised blast load: Experiments and numerical simulation. *Int. J. Impact Eng.*, **46**: 97–109.

Denefeld, V., Heider, N., Holzwarth, A., Attler, A.S. & Salk, M. (2014). Reduction of global effects on vehicles after IED detonations. *Def. Tech.*, **10**:219–225.

Dooge, D., Ramesh, D., Schaffner, G., Miller, A., Thyagarajan, R., Vunnam, M. & Babu, V., (2011) Evolution of occupant survivability simulation framework using FEM-SPH coupling, *2011 NDIA Ground Vehicle Syst. Eng. and Tech.Symp.*.

Galarneau, M.R., Woodruff, S.I., Dye, J.L., Mohrle, C.R. & Wade, A.L. (2008). Traumatic brain injury during Operation Iraqi Freedom: findings from the United States Navy- Marine Corps Combat Trauma Registry. *J Neurosurg.*,**108**:950–957.

Karlos, V. & Solomos, G. (2013). Calculation of blast loads for application to structural components. *JRC Technical Report*.

Maciej, S., Eren, A. & Namas,C. (2018). On the accurate determination of shock wave time-pressure profile in the experimental models of blast-induced neurotrauma. *Front Neurol*., **9**:52.

Mackiewicz, A., Sławiński, G., Niezgoda, T. & Będziński, R. (2016). Numerical analysis of the risk of neck injuries caused by IED explosion under the vehicle in military environments. *Acta Mech. Autom.*, **10**:258–264.

NATO.(2011). *Protection Level Of Armored Vehicles*. vol. 2, AEP-55, Allied Engineering Publication.

NATO. (2013). *Standard Stretchers, Bearing Brackets*. AMedP-2.1.

Nguyen, T., Pearce, A.P., Carpanen, D., Sory, D., Grigoriadis, G., Newell, N., Clasper, J., Bull, A., Proud, W.G. & Masouros, S.D. (2018). Experimental platforms to study blast injury. *J R Army Med Corps.*,1–5.

Panowicz, R., Sybilski, K. & Niezgoda. T. (2010). Numerical analysis of a light armoured loaded with a mine or IED explosion. *J. KONES*.,**17**:3.

Saeimi-Sadigh, M.A., Paykani, A., Afkar, A. & Aminollah, D. (2014). Design and energy absorption enhancement of vehicle hull under high dynamic loads.*J. Cent. South Univ.*,**21**:1307–1312.

Sławiński, G., Niezgoda, T., Barnat, W. & Wojtkowski, M. (2013). Numerical analysis of the influence of blast wave on human body.*J. KONES*, **20**:3.

Sliwinski, J. (2011). Protection of vehicles against mines, *J. KONES*, **18**:1.

Tabiei, A. & Nilakantan, G. (2007). Reduction of acceleration induced injuries from mine blasts under infantry vehicles, *6th Eur. LS-DYNA Users' Conf.*, 1–28,

Vlahopoulos, N. & Zhang, G., (2010). Validation of a simulation process for assessing the response of a vehicle and its occupants to an explosive threat.*27th Army Sci. Conf*.

Young, W. C., Budynas, R.G.& Sadegh, A.M. (2012). *Roark's Formulas for Stress and Strain (8th Ed.)*. McGraw-Hill, New York.

OPTIMISATION OF HYBRID COMPOSITE REINFORCED CARBON AND GLASS USING AHP METHOD

Nur Aizatul 'Ain Md Zahir[1,3], Ahmad Fuad Ab Ghani[2,3], Mohd Ahadlin Mohd Daud[1,3*], Sivakumar Dharmalingam[1,3] & Ridzuan Mansur[1,3]

[1]Fakulti Kejuruteraan Mekanikal (FKM)
[2]Fakulti Kejuruteraan Teknologi Mekanikal dan Pembuatan (FTKMP)
[3]Centre for Advanced Research on Energy (CARe)
Universiti Teknikal Malaysia Melaka (UTeM), Malaysia

[*]Email: ahadlin@utem.edu.my

ABSTRACT

Aiming for the selection of carbon fibre reinforced polymer (CFRP) and glass fibre reinforced polymer (GFRP) hybrid composite with the best combination of strength, weight and cost, the analytical hierarchy process (AHP) method was applied. Ten composite configurations were arranged with different design criteria such as flexural strength, flexural modulus, strain to failure, density and cost and were then ranked by AHP method. AHP results revealed that C1with relative PV of 23.24% was the preferred hybrid composite for CFRP/GFRP design configuration. It was also concluded that the flexural strength of the design criteria was the most significant property which may affect the mechanical properties of the hybrid composite.

Keywords: *Hybrid composite; carbon fibre reinforced polymer (CFRP) and glass fibre reinforced polymer (GFRP); optimisation; analytical hierarchy process (AHP).*

1. INTRODUCTION

In engineering field, design techniques and analysis often become complicated when it comes to design improvement and optimisation (Ab Ghani & Mahmud, 2017). For example, in order to improve the mechanical properties of composite sandwich structure, the design variables that should be taken into considerations include ply orientations, face sheets stacking sequence, and thickness of the core. Thus, the analysis and design of the sandwich structure is far more complicated than the traditional sandwich structure with isotropic material properties. To cope with these complexities, the techniques and methodologies of design optimisation should be developed.

The optimisation of composite laminates has been initiated by the American aerospace industry with fibre volume and orientation angles as design variables. This method of optimisation is also restricted to simple laminates design and load cases only (Schläpfer, 2013). The optimisation could unlock the next level of hybrid composite capabilities because the large number of design variables could be provided. This will bring a great potential for tailoring the composite laminates properties to meet certain requirements but it will implies a complex engineering problem. Thus a better solution in optimisation that requires less time can be found by using computational optimisation method (Schläpfer, 2013).

A few modern approaches for the design of composite structures have been studied by Axinte *et al*. (2013) which covered genetic algorithm (GA), simulated annealing method (SAM), particle swarm optimisation (PSO) and ant colony optimisation (ACO). Another powerful tool that has been used for optimisation of composite material is analytical hierarchy process (AHP) (Mansor *et al*., 2014;

Zafarani *et al*., 2014). Baragetti (2014) stated that AHP is capable in formulating and handling a complex problem hierarchally.

Certain constrains can be found in a number of research dealing with optimising the hybrid composite materials Carbon Fibre Reinforced Polymer (CFRP) and Glass Fibre Reinforced Polymer (GFRP). One of the most studied industries for composite application is the defence industry where numerous researchers attempt to improve the existing part in the defence industry such as body armour and ballistic composite components (Supian *et al.,* 2018). In addition, Sapuan *et al*. (2011) systematically organised the database of material selection for natural fibres that can be used in the application of AHP for development of automotive dashboard panel. Throughout the study, the kenaf 60% + polypropylene (PP) shows a domination of three out of four simulated scenarios in AHP. The sensitivity analysis that have been conducted to verify the results have also shown similar results thus the AHP approach was proven as a useful method to solve decision problem by providing clear criteria and priority during material selection process. The reduction of weight and manufacturing cost of automotive armrest is achievable by replacing the steel frame with Vinylester resin when the AHP approach was implemented. AHP was used to evaluate the data and select the best alternative based on the criteria to decide the thermoset matrix for natural fibre composites automotive armrest (Rosli *et al*., 2017).

In this study, the process and methodologies for optimisation process were developed and briefly discussed from the design configurations of composite material until the selection of the best composite design configurations. The finite element analysis was implemented, and the steps involved were explained in detail including flexural analysis modelling step and failure criteria. In addition, this section explains the optimisation method by using AHP approach to determine the optimised design configurations of composite material.

2. METHODOLOGY

2.1 Material Properties

The composite laminates structure consisted of CFRP and GFRP layup, represented by orange region – CFRP and blue region – GFRP in Figure 1. The mechanical properties of CFRP and GFRP are tabulated in Table 1. There are ten different arrangement of composite structure with the purpose to investigate the behaviour under the same condition. All cases consist of unidirectional fibre direction and symmetry arrangement as shown in Figure 1.

Table 1: Material database for CFRP and GFRP.

Mechanical Properties	CFRP	GFRP
Longitudinal elastic modulus, E1 (GPa)	128.80	45.20
Transverse elastic modulus, E2 (GPa)	9.30	14.10
Major Poisson's ratio, V12	0.34	0.29
Shear Modulus, G12 (GPa)	3.37	6.30
Thickness per layer (mm)	0.20	0.187

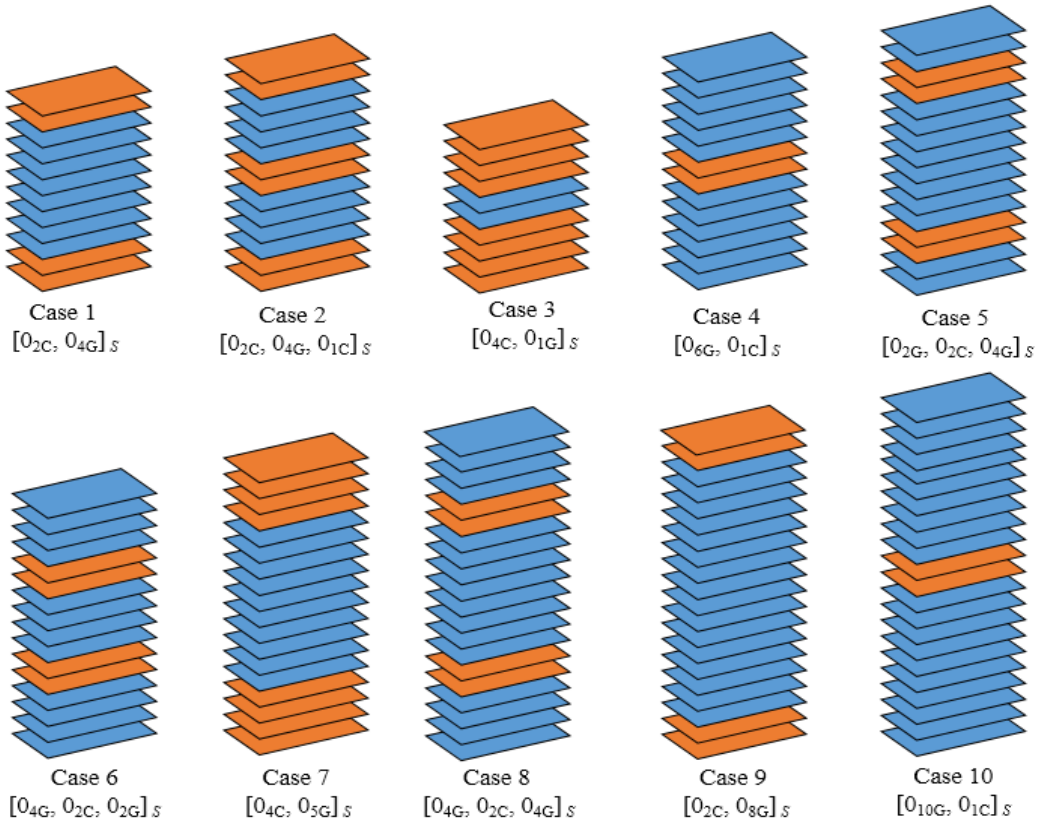

Figure 1: Ten composite laminates configurations.

The cost for each composite material CFRP and GFRP was based on the current price from Rockwest Composite (TORAY T700S Data Sheet, 2018). The cost of the hybrid composite material is calculated based on its weight and the price of material per unit weight. The price is then calculated according to the dimension of the sample in this study which is 40 mm × 15 mm.

2.2 Finite Element Analysis (FEA)

In FEA simulations, the composite structure was divided into finite number of elements. The stress and strain results under flexural loading were obtained by FEA using ANSYS APDL. Composite specimen was modelled with dimension of 40 mm in length, 15 mm in width and specific thickness according to each case. An example of hybrid composite CFRP/GFRP finite element model under the three point bending in ANSYS APDL is shown in Figure 2.

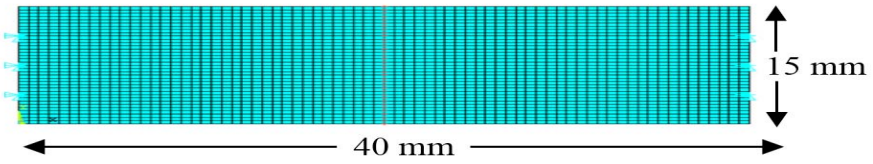

Figure 2: Composite model in ANSYS APDL.

In order to replicate three-point-bending test in the experiment, the model was mapped mesh at the area with quad element and refined at each node. The element type is SHELL181. Distributed load with sinusoidal distribution was applied which include downward distributed load (*P*) in the load point, and half of an upward distributed load (*P/2)* at the left and right ends of bottom surface. The two central points at each end of laminate (*z=h/2*) were restrained as *UX=UY=UZ=0* to eliminate the DOFs. Load was applied gradually along the middle nodes as line load (Force/Width) until the whole layers failed by using the concept of Last Ply Failure (LPF). Failure criteria are presented using the notion of failure index, $I_F$in ANSYS APDL where failure is predicted if the $I_F > 0$ for all layers in the composite laminates. The flexural strength (σ_F), strain to failure (ε_F) and flexural modulus (E_F) are determined given by Equation 3.1, Equation 3.2 and Equation 3.3 respectively (Standard ASTM D790, 1997):

$$\sigma_F = \frac{3F_{\max}L}{2bh^2} \tag{1}$$

$$\varepsilon_F = \frac{6Dh}{L^2} \tag{2}$$

$$E_F = \frac{L^3 m}{4bh^3} \tag{3}$$

where *L, b* and *h* are the span length, width and thickness of the specimen, *m* is the slope of the tangent to the straight line of load vs. deflection curve, *D* is the maximum deflection before failure, and $F_{max}$is the maximum load before specimen failure.

2.3 Analytical Hierarchy Process (AHP)

AHP is one of the decision-making tools developed by Prof. Thomas L. Saaty in 1980. AHP is implemented when there are multiple and conflicting criteria present, as well as when both of the qualitative and quantitative aspects of a decision need to be considered. It is an effective choice in dealing with a complex decision making since it reduces complex decision to a series of pair-wise comparison. AHP works by considering a set of evaluation criteria along with the alternatives scenarios to decide which decisions is the best.

For decision making process, a weight for each evaluation criterion and scenario is generated following the information provided and the ranking of the scenarios will be determined. There are three fundamental steps in AHP, (i) defining a multi-criteria problem hierarchically, (ii) assigning relative priorities to the various elements using pair-wise comparison techniques and (iii) integrating these priorities to converge at an overall evaluation of decision alternatives. The concept of relative importance by Saaty (1980) in Table 2 is used when assigning weights to the alternatives as well as criteria for constructing the decision matrix and pair-wise comparison matrices.

In AHP, the decision matrix and pair-wise comparison matrices are in the form of square matrices. Eigen values and Eigen vectors are used to check the consistency of the judgment values assigned to the decision alternatives and criteria and if required, the decision-maker revises and modifies judgment values. Before evaluation process takes place, the goal in this study is to analyse and evaluate different design configurations of composite laminates to obtain the most optimum design.

Table 2: Intensity of relative importance.

Intensity of relative importance	Definition
1	Equally important
3	Moderately preferred
5	Essentially preferred
7	Very strongly preferred
9	Extremely preferred
2,4,6,8	Intermediate importance between two adjacent judgments

In this study the selection of the best design configurations of the composite laminates CFRP/GFRP depends upon six evaluation criteria. The optimisation of hybrid composite can be measured in terms of flexural strength, flexural modulus, strain to failure, density and cost. All the evaluation criteria were selected based on the most studied criteria for hybrid composite material based on the literature study. Table 3 displays the identified criteria with their operational definitions.

Table 3: Selected criteria for optimisation of hybrid composites.

No.	Criteria and Code	Operational Definition
1.	Flexural Strength, F_1	Highest stress experienced within the material at its moment of yield.
2.	Flexural Modulus, F_2	Tendency for a material to resist bending.
3.	Strain to Failure, F_3	The maximum elongation of material, i.e. at break.
4.	Density, F_4	Ratio of weight of the composite material to the volume of the composite material
5.	Cost, F_5	Composite materials costs

Ten composite plate configurations (Figure 1) are considered and coded as C_1, C_2, C_3, C_4, C_5, C_6, C_7, C_8, C_9 and C_{10}. It is presumed that the behaviour/performance of these ten alternatives (composite configurations) with respect to each of the six criteria is known. The list of the set of design configurations is listed in Table 4.

Next, the pair-wise comparison matrices were developed for each design criterion in Figure 3 to identify the ranking of importance of design criteria. Pair-wise comparison begins with comparing the relative importance of two design criteria by using relative pair-wise comparison by AHP template from SCBUK. The decision matrix was developed by assigning weights to each design criteria based on the relative importance of its contribution according to the nine-point scale. The judgments or assigned values are based on the experience, knowledge, through journals and handbooks.

For each of the pair-wise comparison matrices, the normalised score (NS) is determined to calculate the priority vectors (PV) for decision matrix. The sum of each of the column is multiplied by the corresponding PV value as in Figure 3. Calculation of the sum of these products, i.e., the principal eigen value (λ_{max}) is done in order to check the consistency index and consistency ratio. The consistency is less than 10% thus the judgment is acceptable.

Table 4: List of the set of design configurations (C1 to C10).

Case	Laminate Configuration	Symbol
Case 1	$[C_2/G_4]s$	C_1
Case 2	$[C_2/G_4/C_1]s$	C_2
Case 3	$[C_4/G_1]s$	C_3
Case 4	$[G_6/C_1]s$	C_4
Case 5	$[G_2/C_2/G_4]s$	C_5
Case 6	$[G_4/C_2/G_2]s$	C_6
Case 7	$[C_4/G_5]s$	C_7
Case 8	$[G_4/C_2/G_4]s$	C_8
Case 9	$[C_2/G_8]s$	C_9
Case 10	$[G_{10}/C_1]s$	C_{10}

Pairwise Comparison Matrix

	Design criteria				
	Flexural Strength	Flexural Modulus	Strain to failure	Density	Cost
Flexural Strength	1	2	9	6	7
Flexural Modulus	1/2	1	8	2	6
Strain to failure	1/9	1/8	1	1/4	1/4
Density	1/6	1/2	4	1	2
Cost	1/7	1/6	4	1/2	1

Figure 3: Pair-wise comparison matrix for design criteria.

A consistency indicates how a given matrix compares to a purely random matrix in terms of their consistency indices, and acceptable consistency is when Consistency is ≤ 10%. Thus, larger consistency value requires the judgment to be reiterated until Consistency of < 10% is reached (Mansor *et al*., 2014). Priority vectors (PV) indicates how important a criterion is among the other criteria. For instance, the flexural strength (F1) contributes the highest to the goal with priority vector of 48.8% while the strain to failure (F3) contribute the lowest with the priority vector of 3.4% only.

This means that flexural strength is the most important consideration with respect to the hybrid composite laminates criterion to the other criteria. The ranking of the design criteria decisions are shown in Figure 4. It shows that the most important criteria is flexural strength, followed by flexural modulus, density, cost and strain to failure.

	AHP		Consistency check
1	0.488	48.8%	Consistency OK
2	0.281	28.1%	7%
3	0.034	3.4%	
4	0.120	12.0%	
5	0.077	7.7%	

Figure 4: Priority vector (PV) for criterion decision matrix.

The criteria that influence the selection process factor of design configurations were then translated into the hierarchy structure in Figure 5. The pair-wise comparison for design configurations for each design criteria is performed. Based on tabulated data in Table 5, the weights to each of the alternatives (design configuration) were assigned, based on its relative importance, according to nine-point scale.

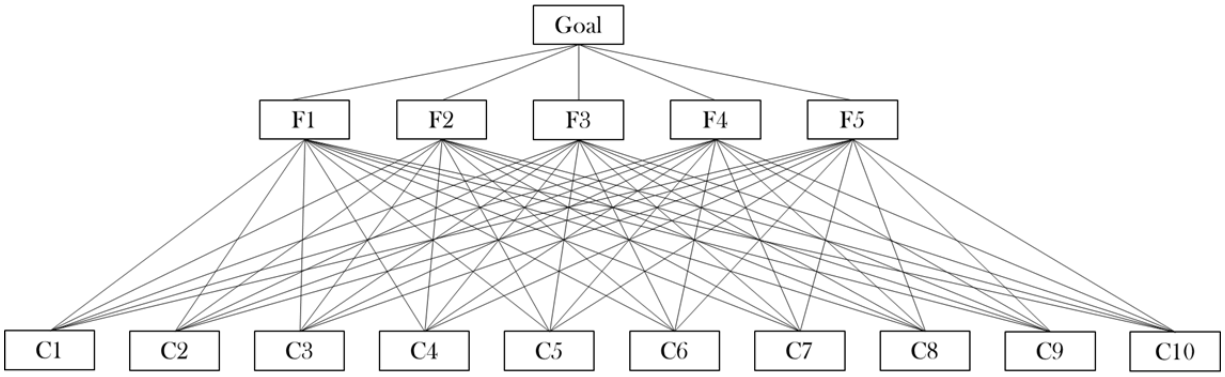

Figure 5: Hierarchy structure of design criteria and design configurations.

Table 5: Criteria values for AHP.

Case	Flexural Strength (MPa)	Flexural Modulus (GPa)	Strain to failure	Density (kg/m^3)	Cost ($)
1	1714.8442	73.2451	0.0234	2.9036	0.2194
2	1447.3580	68.3092	0.0212	2.7201	0.2631
3	1611.6300	90.4862	0.0178	2.0263	0.2079
4	1384.6897	39.4143	0.0351	3.2779	0.2416
5	1705.1704	51.3319	0.0332	3.0661	0.2853
6	1683.5860	43.3880	0.0388	3.0661	0.2853
7	1162.7038	66.4912	0.0175	2.6897	0.3398
8	1641.2523	41.3398	0.0397	3.1646	0.3512
9	1349.1650	54.0735	0.0250	3.1646	0.3512
10	1225.2328	33.9737	0.0361	3.3816	0.3735

3. RESULTS & DISCUSSION

The ten design configurations of composite laminates CFRP/GFRP were evaluated in order to determine the most optimum composite laminates design concept which has high flexural properties, and at the same time possess low cost and low densities. In general, AHP composed of three basic steps; decomposition, comparative judgment and synthesis. The pair-wise comparison that has been made to the design configurations for each design criteria are shown in Figure 6 – Figure 10.

Flexural Strength

Pairwise Comparison Matrix

	Case 1	Case 2	Case 3	Case 4	Case 5	Case 6	Case 7	Case 8	Case 9	Case 10
Case 1	1	6	5	7	2	3	9	4	8	9
Case 2	1/6	1	1/2	2	1/4	1/3	4	1/3	3	3
Case 3	1/5	2	1	2	1/3	1/3	5	1/2	3	4
Case 4	1/7	1/2	1/2	1	1/5	1/4	3	1/3	2	2
Case 5	1/2	4	3	5	1	2	8	2	6	7
Case 6	1/3	3	3	4	1/2	1	7	2	5	6
Case 7	1/9	1/4	1/5	1/3	1/8	1/7	1	1/6	1/3	1/2
Case 8	1/4	3	2	3	1/2	1/2	6	1	4	5
Case 9	1/8	1/3	1/3	1/2	1/6	1/5	3	1/4	1	2
Case 10	1/9	1/3	1/4	1/2	1/7	1/6	2	1/5	1/2	1

Figure 6: Pair-wise comparison of design configurations with flexural strength.

Flexural Modulus

Pairwise Comparison Matrix

	Case 1	Case 2	Case 3	Case 4	Case 5	Case 6	Case 7	Case 8	Case 9	Case 10
Case 1	1	2	1/2	7	4	5	2	6	3	8
Case 2	1/2	1	1/2	6	3	4	2	5	2	7
Case 3	2	2	1	8	5	6	3	7	4	9
Case 4	1/7	1/6	1/8	1	1/3	1/2	1/5	1/2	1/4	2
Case 5	1/4	1/3	1/5	3	1	2	1/2	2	1/2	4
Case 6	1/5	1/4	1/6	2	1/2	1	1/3	2	1/2	3
Case 7	1/2	1/2	1/3	5	2	3	1	4	2	6
Case 8	1/6	1/5	1/7	2	1/2	1/2	1/4	1	1/3	2
Case 9	1/3	1/2	1/4	4	2	2	1/2	3	1	5
Case 10	1/8	1/7	1/9	1/2	1/4	1/3	1/6	1/2	1/5	1

Figure 7: Pair-wise comparison of design configurations with flexural modulus.

Strain to Failure

Pairwise Comparison Matrix

	Case 1	**Case 2**	**Case 3**	**Case 4**	**Case 5**	**Case 6**	**Case 7**	**Case 8**	**Case 9**	**Case 10**
Case 1	1	2	2	1/3	1/2	1/5	3	1/6	1/2	1/4
Case 2	1/2	1	2	1/4	1/3	1/6	2	1/7	1/2	1/5
Case 3	1/2	1/2	1	1/5	1/4	1/7	2	1/8	1/3	1/6
Case 4	3	4	5	1	2	1/2	6	1/3	2	1/2
Case 5	2	3	4	1/2	1	1/3	5	1/4	2	1/2
Case 6	5	6	7	2	3	1	8	1/2	4	2
Case 7	1/3	1/2	1/2	1/6	1/5	1/8	1	1/9	1/4	1/6
Case 8	6	7	8	3	4	2	9	1	5	2
Case 9	2	2	3	1/2	1/2	1/4	4	1/5	1	1/3
Case 10	4	5	6	2	2	1/2	6	1/2	3	1

Figure 8: Pair-wise comparison of design configurations with strain to failure.

Density

Pairwise Comparison Matrix

	Case 1	Case 2	Case 3	Case 4	Case 5	Case 6	Case 7	Case 8	Case 9	Case 10
Case 1	1	1/2	1/3	3	2	2	1/2	2	2	4
Case 2	2	1	1/2	4	2	2	1/2	3	3	5
Case 3	3	2	1	6	4	5	2	5	5	7
Case 4	1/3	1/4	1/6	1	1/2	1/2	1/5	1/2	1/2	2
Case 5	1/2	1/2	1/4	2	1	1	1/3	2	2	3
Case 6	1/2	1/2	1/5	2	1	1	1/3	2	2	3
Case 7	2	2	1/2	5	3	3	1	4	4	6
Case 8	1/2	1/3	1/5	2	1/2	1/2	1/4	1	1	2
Case 9	1/2	1/3	1/5	2	1/2	1/2	1/4	1	1	2
Case 10	1/4	1/5	1/7	1/2	1/3	1/3	1/6	1/2	1/2	1

Figure 9: Pair-wise comparison of design configurations with density.

Cost

Pairwise Comparison Matrix

	Case 1	Case 2	Case 3	Case 4	Case 5	Case 6	Case 7	Case 8	Case 9	Case 10
Case 1	1	2	1/2	2	3	3	4	5	5	6
Case 2	1/2	1	1/3	1/2	2	2	2	3	3	4
Case 3	2	3	1	2	4	4	5	6	6	7
Case 4	1/2	2	1/2	1	2	2	3	4	4	5
Case 5	1/3	1/2	1/4	1/2	1	1	2	2	2	3
Case 6	1/3	1/2	1/4	1/2	1	1	2	2	2	3
Case 7	1/4	1/2	1/5	1/3	1/2	1/2	1	2	2	2
Case 8	1/5	1/3	1/6	1/4	1/2	1/2	1/2	1	1	2
Case 9	1/5	1/3	1/6	1/4	1/2	1/2	1/2	1	1	2
Case 10	1/6	1/4	1/7	1/5	1/3	1/3	1/2	1/2	1/2	1

Figure 10: Pair-wise comparison of design configurations with cost.

The composite priority (CP) of the design configurations were then determined by multiplying the PV values for a particular criterion with the corresponding PV value of that criterion, and adding up these products. Design configurations that have the highest CP showed the design configuration that is best in terms of evaluated criteria. The result for CP for all design configurations is shown in Table 6.

Based on the % of CP, the ranking of the design configurations decisions are determined as shown in Figure 11. Among all design configurations, C1 is the only one that has the % CP of above 20% which is the largest one considering there is ten competitive configurations. Between the composites configurations with the same % of CFRP and GFRP, same manufacturing cost, and same density (C5 & C6; C8 & C9), the controlling parameter is the flexural strength, flexural modulus and strain to failure. It showed that the design concept Case 1 (C_1) with a % CP of 0.2325 (23.25%) is the first choice, the second choice is the design concept Case 3 (C_3) with a %CP of 0.1662 (116.62%) and third choice is the design concept Case 5 (C_5) with a % CP of 0.1274 (12.74%).

Table 6: Composite Priorities.

	F_1	F_2	F_3	F_4	F_5	Total	% CP
	0.488	0.281	0.034	0.12	0.077		
Case 1	0.302	0.201	0.044	0.102	0.193	0.232454	23.2454
Case 2	0.059	0.153	0.033	0.139	0.106	0.097749	9.7749
Case 3	0.076	0.27	0.025	0.267	0.264	0.166176	16.6176
Case 4	0.042	0.025	0.113	0.035	0.142	0.046497	4.6497
Case 5	0.191	0.061	0.083	0.072	0.072	0.127355	12.7355
Case 6	0.147	0.044	0.201	0.071	0.072	0.104998	10.4998
Case 7	0.018	0.113	0.019	0.19	0.052	0.067987	6.7987
Case 8	0.11	0.033	0.27	0.048	0.037	0.080742	8.0742
Case 9	0.032	0.083	0.061	0.048	0.037	0.049622	4.9622
Case 10	0.024	0.019	0.151	0.026	0.026	0.027307	2.7307

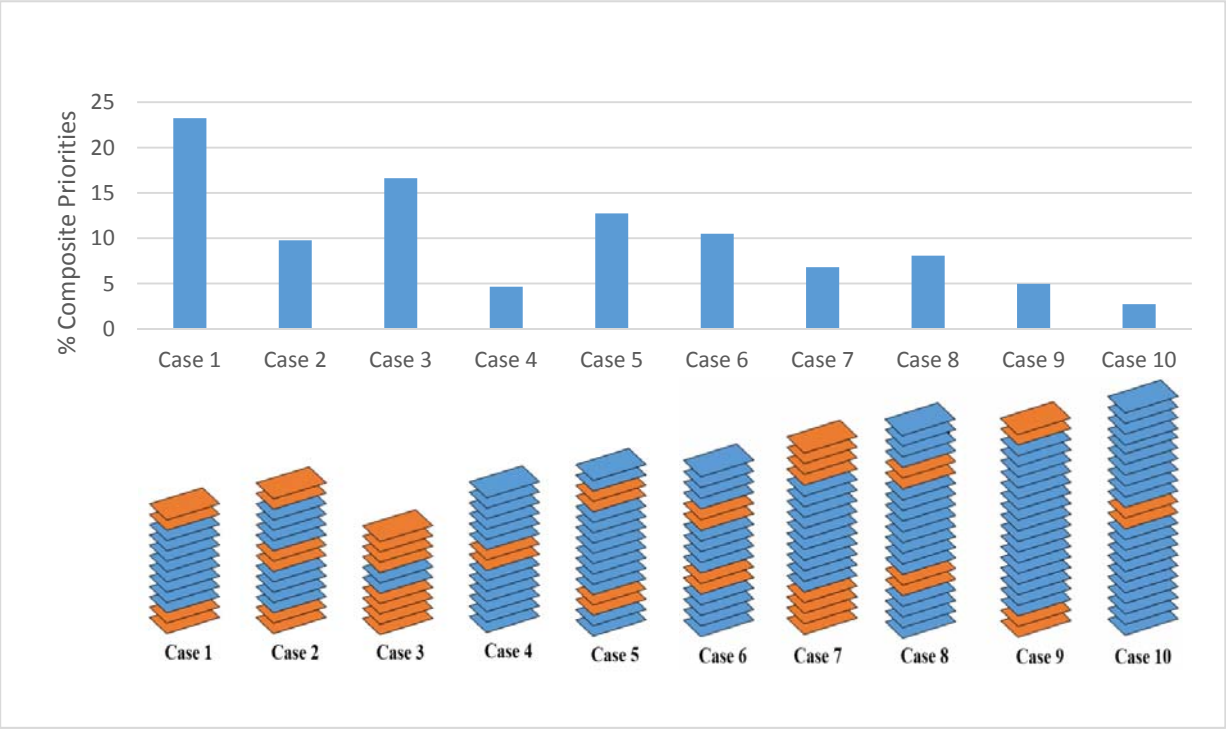

Figure 11: Ranking for design configurations.

The design configurations were found to have great influences on flexural properties of CFRP/GFRP hybrid composite. From Table 6, even though Case 1 has dominated only one out of the five evaluated criteria, however, Case 1 showed the highest global priorities followed by Case 3 and Case 5. The stacking sequence of composite laminates like Case 1 with CFRP plies placed at the outer layer of hybrid composite laminates could promote to the higher flexural strength that can withstand higher stress experienced within the composite laminates at its moment of yield. Besides that, by altering the stacking sequences of CFRP/GFRP hybrid composite, the lesser cost with lighter weight of composite laminates can be achieved. This can be shown with the comparison between Case 1 and Case 5. Case 1 possess a lighter weight and cost less than Case 5 with higher flexural properties which proved that the stacking sequence like Case 1 could promote more advantages compared to stacking sequence like Case 5.

Thus, it can be concluded that Case 1 is the best hybrid composite design configuration to be considered for the hybrid composite laminates formulation that satisfy all the required design specification for the intended application, which has the highest flexural properties while maintaining low cost and density. Similarly, the potential of configuration of Case 1 as the best design of composite laminates was also reported by Subagia *et al*. (2014) through the case study on effect of stacking sequence on flexural properties by hybrid composites reinforced carbon and basalt fibres. Their findings revealed that the interply hybrid composite with carbon fibre at the compressive and tension sides exhibited higher flexural strength and modulus than when basalt fabric was placed at the compressive side (Subagia *et al*., 2014).

4. CONCLUSION

The aim of this work is to select the optimal composite configurations that have the best combination of strength, weight and cost which is significant in structural applications in defence, automotive and aerospace industries. Analytic Hierarchy Process (AHP) was selected to be used as the multi-criteria decision making method. Ten design configurations of composites laminates were evaluated with the same design criteria which are flexural strength, flexural modulus, strain to failure, density and cost. Findings from AHP method showed that the choice of C1 with relative density of 23.24% is the preferred alternative. It also showed that flexural strength is the most significant design criteria which can affect the mechanical performances of the hybrid composites CFRP/GFRP due to its highest PV among the design criteria.

ACKNOWLEDGEMENT

The authors would like to send gratitude to Faculty of Mechanical Engineering for ANSYS software utilization and many thanks to Ministry of Education Malaysia as this project was supported by Research Acculturation Grant Scheme: RAGS/1/2015/TK0/FKM/03.

REFERENCES

Ab Ghani, A.F. & Mahmud, J., (2017). Material characterization of hybrid composite: Experimental using strain gauge and Digital Image Correlation (DIC) with finite element modelling macro/micro scale. *Key Eng. Mater.*, **740**: 31-40.

ASTM (1997). *D790-07: Standard Test Method for Flexural Properties of Unreinforced and Reinforced Plastics and Electrical Insulation Materials*. ASTM, West Conshohocken, Pennsylvania.

Axinte, A., Bejan, L., Taranu, N. &Ciobanu, P. (2013). Modern approaches on the optimization of composite structures.*Bul. Inst. Polit. Iaşi.*, **59:**43.

Baragetti, S. (2014). Analytic hierarchy process application for the selection of a metal matrix composite. *Open Mater. Sci. J.*, **8:**63-70.

Mansor, M.R., Sapuan, S.M., Zainudin, E.S., Nuraini, A.A. &Hambali, A. (2014). Conceptual design of kenaf fiber polymer composite automotive parking brake lever using integrated TRIZ–Morphological Chart–Analytic Hierarchy Process method. *Mater. Des.*, **54:** 473-482.

Rosli, M.U., Jamalludin, M.R., Khor, C.Y., Ishak, M.I., Jahidi, H., Wasir, N.Y., Faizal, W.M., Draman, W.N.A.T.W., Lailina, N.M. & Ismail, R.I. (2017). Analytical hierarchy process for natural fibercomposites automotive armrest thermoset matrix selection. *MATEC Web of Conferences.* EDP Sciences. **97**: 01039.

Saaty, T.L. (1980). The analytical hierarchy process, planning, priority. *Resource Allocation. RWS Publications, USA*.

Sapuan, S.M., Kho, J.Y., Zainudin, E.S., Leman, Z., Ali, B.A. &Hambali, A. (2011). Materials selection for natural fiber reinforced polymer composites using analytical hierarchy process.*Indian J. Eng. Mater. Sci*.,**18:** 255-267.

Schläpfer, B.G. (2013). *Optimal Design of Laminated Structures with Local Reinforcements.* Doctoral dissertation, Eth Zurich.

Subagia, I.A., Kim, Y., Tijing, L.D., Kim, C.S. & Shon, H.K. (2014). Effect of stacking sequence on the flexural properties of hybrid composites reinforced with carbon and basalt fibers. *Composites Part B.*, **58:**251-258.

Supian, A.B.M., Sapuan, S.M., Zuhri, M.Y.M., Syams, Z.E. &Ya, H.H. (2018). Hybrid reinforced thermoset polymer composite in energy absorption tube application: A review. *Defence Tech.,***14:** 291-305.

TORAY T700S Data Sheet. *Rockwest Composite.* Available online at: www.rockwestcomposites.com (Last access date: 31 July. 2018).

Zafarani, H.R., Hassani, A. &Bagherpour, E. (2014). Achieving a desirable combination of strength and workability in Al/SiC composites by AHP selection method. *J. Alloys Compd*., **589:**295-300.

THE INFLUENCE OF FIBRE STACKING CONFIGURATIONS ON THE INDENTATION BEHAVIOUR OF PINEAPPLE LEAF / GLASS FIBRE REINFORCED HYBRID COMPOSITES

Ng Lin Feng[1], Sivakumar Dhar Malingam[1*], Kathiravan Subramaniam[1], Mohd Zulkefli Selamat[1], Mohd Basri Ali[1] & Omar Bapokutty[2]

[1]Centre for Advanced Research on Energy, Fakulti Kejuruteraan Mekanikal
[2]Fakulti Teknologi Kejuruteraan Mekanikal dan Pembuatan
Universiti Teknikal Malaysia Melaka (UTeM), Malaysia

[*]Email: sivakumard@utem.edu.my

ABSTRACT

Composite materials have gained wide acceptance among industries since the past decades. They have been widely employed in a wide variety of engineering applications. In this research, the influences of fibre stacking configurations on the indentation behaviour of pineapple leaf/glass fibres reinforced polypropylene hybrid composites were investigated. The indentation behaviours of hybrid composites were then compared to non-hybrid composites. Composites were fabricated through the hot press moulding compression technique using hydraulic hot press machine. The indentation behaviours of composites were presented in terms of maximum indentation force, energy absorption and specific energy absorption. The damage mechanism of composites was also studied after the indentation test. From the findings, it was concluded that the partial incorporation of glass fibre in the composite laminates improved the indentation resistance and energy absorption. In overall, non-hybrid glass fibre reinforced composite laminates showed the highest indentation resistance and energy absorption. However, the hybrid composites with the substitution of middle glass fibre with pineapple leaf fibre had a comparable indentation resistance and energy absorption to the non-hybrid glass fibre based composites. Therefore, these results have evidenced the potential of hybrid composites to supersede non-hybrid glass fibre based composites.

Keyword: *Hybrid composites; pineapple leaf fibre; fibre stacking configuration; indentation behaviour; energy absorption.*

1. INTRODUCTION

Metallic alloys are contemporary materials being widely employed in structural applications. However, the material requirements in the engineering applications have inclined towards lightweight and high specific properties. Therefore, effort has been given to search for alternative materials with high specific properties. It was evidenced that composite materials have demonstrated excellent specific properties over metallic alloys (Feng *et al*., 2018). Thus, composite materials have received great attention for engineering applications due to their excellent specific properties. It is undeniable that the increasing exploration of natural fibres is because of the awareness on increasing product performance by employing lightweight components (Arpitha *et al*., 2017). Apart from the high specific properties in composite materials, the substitution of metallic alloys to composite materials could offer the flexibility to tailor the materials properties by the specific industrial applications. Currently, composite materials have been the well-known materials that are widely used in outdoor and load-bearing applications such as automotive, aerospace, sports equipment and marine structures (Sivakumar *et al*., 2016; Pickering *et al*., 2016; Habibi *et al*., 2018). In spite of various advantages by using composite materials, they have arisen several environmental issues since the main reinforcement used is dominated by glass fibres owing to their high mechanical strength and they are

inexpensive. In the military application, glass fibres are widely used to make military mine hunters (Chawla, 2006). The extensive use of glass fibre could lead to severe occupational health issues (Le Duigou *et al*., 2010). Due to the shortcomings of synthetic fibre based composites, several attempts have been provoked to explore alternative materials to resolve such problems (Yang *et al*., 2011; Feng *et al*., 2017; Ng *et al*., 2017).

To rectify the drawbacks of synthetic fibre based composites, the use of natural resources as the reinforcement is indispensable. Renewability, recyclability and biodegradable are those desired properties for alternative environmental friendly materials. Most of the natural fibres are abundant, low cost, lightweight and encompass relatively good mechanical properties and thus shows a high potential to be used in composite materials. Besides, natural fibres are insensitive to fatigue loading, non-abrasive, carbon dioxide neutral, consuming less energy and having high specific properties (Asgarinia *et al*., 2015; Feng & Malingam, 2019). Owing to their advantages, natural fibres have recently received the interest among technologist and scientists particularly for military applications (Alam *et al*., 2014). In this context, pineapple leaf fibre (PALF) is among the potential cellulosic fibre which possesses high mechanical strength relative to other natural fibres while having a lower density than glass fibres. PALF is considered as a secondary fibre crop as the plants are mainly grown for its fruit rather than their fibres. Owing to the high availability and good mechanical strength, PALF has shown a great potential to replace the glass fibres. Nonetheless, PALF is similar to other natural fibres which are susceptible to high moisture sensitivity due to their intrinsic hydrophilic behaviour. The high moisture sensitivity eventually retards the use of natural fibres in industrial applications. Therefore, hybridisation of natural fibres with synthetic fibres represents a great alternative technique in this context.

Recently, there is a growing interest in exploring the mechanical properties of hybrid composites. Hybrid composites are formed through the blending of two or more types of fibres into a single polymer matrix. There are three distinct types of hybrid composites, namely, synthetic/synthetic, synthetic/natural and natural/natural hybrid composites. However, the most commonly studied hybrid composites are based on synthetic/natural fibres. Previous works have concluded hybrid composites offer many benefits compared to non-hybrid composites such as reduction in the moisture uptake and improvement in the mechanical properties (Karahan & Karahan, 2015; Malingam *et al*., 2018). The hybridisation of two different types of fibres within a single matrix could lead to positive hybrid effect in which the advantage of one fibre could compensate for the shortcomings of other fibres. Thus, balance properties such as lightweight, high mechanical strength, modulus and toughness could be achieved. Although the environmental friendliness of the composites could be reduced, this is compensated with the improvement in the mechanical properties and a reduction in the moisture sensitivity.

In general, composite materials have been subjected to localised impact load through the solid objects during their service (Zhou *et al*., 2017). This localised load eventually leads to damage to the structures, which is known as indentation behaviour. Furthermore, it is stated that the indentation resistance of the composite materials also indicates the energy dissipating characteristic of the structures under out-of-plane loading without the consideration of rate effects. To date, several research studies have been conducted on the indentation behaviour of composite materials at the quasi-static rate. Bulut & Erklig (2018) investigated the quasi-static indentation behaviour of laminated composite plates based on carbon, glass and Kevlar fabrics with different stacking sequences. They concluded non-hybrid carbon fibre reinforced epoxy composites showed higher energy absorption compared to glass and Kevlar reinforced composites. In overall, hybrid composite laminates demonstrated the highest indentation force and absorbed energy in comparison with non-hybrid composites. Mohamad *et al*. (2017) studied the quasi-static indentation of sandwich panels based on polyurethane and kenaf foam. The fibre content was in the range of 0 % to 30 % while the thickness of the foam was fixed at 15 mm, 30 mm and 45 mm. The findings showed fibre content of 20 % and foam thickness at 45 mm evidenced the highest indentation resistance. Salman *et al*. (2018) conducted an indentation test at a quasi-static rate on the kenaf/Kevlar fibre reinforced polyvinyl butyral hybrid composite laminates. They revealed that the hybrid composites had higher energy

absorption compared to non-hybrid kenaf reinforced composites. Furthermore, hybrid composites showed a comparable energy absorption to those of non-hybrid aramid fibre reinforced composites. Yahaya *et al*. (2014) studied the effect of hybridisation on the quasi-static indentation behaviour of woven kenaf/aramid reinforced epoxy composite laminates. They found the hybrid composites absorbed more energy than non-hybrid kenaf and aramid fibre reinforced composites. Erkendirci & Haque (2012) compared the indentation behaviour of S-2 glass and E-glass fibres based composites using different types of polymer matrices. The results showed high density polyethene based composites exhibited lower indentation properties than epoxy based composites.

Majority of the energy absorbed during low velocity, high velocity and even ballistic is due to the static deformation (Lin & Fatt, 2006). Thus, quasi-static indentation behaviour of composite materials is vital in determining the impact characteristics of such materials. The aforementioned studies have shown the potential of thermoset based hybrid composites in terms of indentation resistance and energy absorption. Nevertheless, there are still very limited studies that focus on the thermoplastic based hybrid composites. Moreover, the quasi-static indentation behaviour of PALF/glass fibre reinforced polypropylene still remains unexplored. Therefore, this study aims at exploring the influence of fibre stacking configurations on the quasi-static indentation behaviour in terms of maximum indentation force, energy absorption, specific energy absorption and the associated damage mechanism.

2. METHODOLOGY

2.1 Materials

Plain weave PALF and glass fabrics as shown in Figure 1 (a) and (b) were employed as reinforcement in this study. Woven glass fabric with an areal weight of 600 g/m^2 was supplied by ZKK Sdn. Bhd, Malaysia. Woven PALF fabric with an areal weight of 315 g/m^2 was provided by Mecha Solve Engineering, Malaysia. Polypropylene (PP) granules with a density of 0.91 g/cm^3 were purchased from Al Waha Petrochemical Company, Saudi Arabia. The tensile properties of PALF and glass fibre are shown in Table 1.

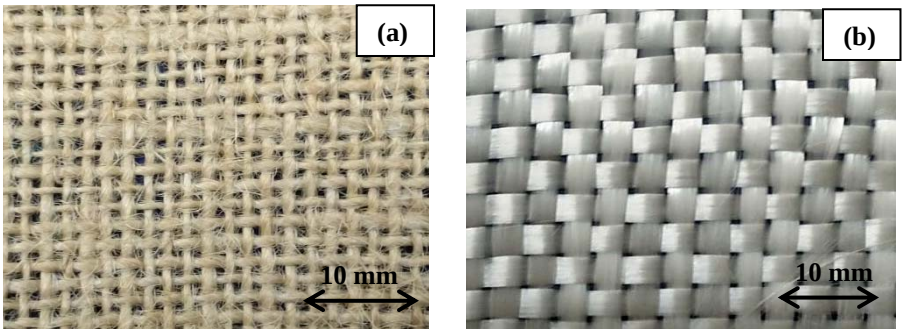

Figure 1: Plain weave woven: (a) PALF (b) glass.

Table 1: Tensile properties of PALF and glass fibre (Gurunathan *et al*., 2015; Dittenber & GangaRao, 2012).

Properties	PALF	Glass fibre
Tensile strength (MPa)	170 – 1627	2000 – 3500
Tensile modulus (GPa)	60 – 82	70 – 76
Strain at break (%)	1 – 3	1.8 – 4.8
Density (g/cm^3)	1.5	2.5

2.2 Composite Preparation

PP granules were mixed with 3 % of Maleic Anhydride Polypropylene (MAPP) before the composite fabrication. According to Beg & Pickering (2008), optimum fibre-matrix adhesion could be achieved by the introduction of 3 - 5 % of MAPP in the composites. The mixing process of PP granules with MAPP was conducted using an internal mixer (Haake Rheomix OS) at a temperature of 175 ºC. The mixture was then pelletized and compressed to form PP films. Non-hybrid and hybrid composite laminates were then formed through hot press moulding compression technique using hydraulic hot press machine.

Non-hybrid and hybrid composite laminates with a nominal thickness of 3 mm were fabricated by stacking the woven fabrics and PP films alternatively to allow optimum fibre impregnation. The stack was arranged in the picture frame mould with a dimension of (250 mm X 250 mm X 3 mm). After that, the stack was subjected to the heat compression moulding at a temperature of 175 ºC and pressure of 3.5 MPa. Preheating for 2 minutes was conducted prior to the heat compression moulding process to ensure the heat was evenly distributed throughout the composite laminates. Subsequent cooling process was performed on the composite laminates until room temperature before it was taken out from the hot press machine.

A total number of four fibre stacking configurations were fixed in the composite laminates. Non-hybrid PALF and glass fibre reinforced PP composite laminates consist of three layers of woven PALF and glass fibre, which are referred as [P/P/P] and [G/G/G]. One of the hybrid composites was arranged by replacing the outermost skin layers of woven glass fibre with woven PALF, which is represented as [P/G/P]. Another hybrid composite laminate, [G/P/G], was fabricated by substituting the middle woven glass fibre with woven PALF. Figure 2 shows the fibre stacking configurations in composite laminates. The fibre weight and volume fraction of non-hybrid and hybrid composite laminates are summarised in Table 2. The standard deviations of the fibre weight and volume fraction are included in the parentheses. The fibre volume fraction of was determined in accordance with Equation 1.

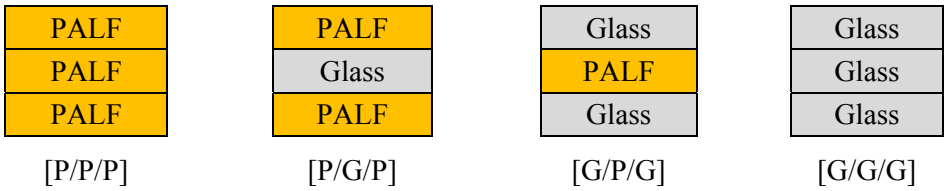

Figure 2: Fibre stacking configurations in composite laminates.

Table 2: Fibre weight and volume fraction in composite laminates.

Fibre layup	Fibre weight fraction (%)	Fibre volume fraction (%)		
		PALF	Glass	Total
[P/P/P]	31.07 (2.65)	21.09 (0.15)	–	21.09 (0.15)
[P/G/P]	36.08 (0.58)	13.75 (0.27)	7.86 (0.16)	21.61 (0.43)
[G/P/G]	42.56 (1.68)	7.16 (0.37)	16.35 (0.86)	23.51 (1.23)
[G/G/G]	47.08 (1.32)	–	24.47 (0.98)	24.47 (0.98)

$$V_{fibre} = \frac{\frac{w_{PALF}}{\rho_{PALF}} + \frac{w_{Glass}}{\rho_{Glass}}}{\frac{w_{PALF}}{\rho_{PALF}} + \frac{w_{Glass}}{\rho_{Glass}} + \frac{w_{PP}}{\rho_{PP}}} \quad (1)$$

where w_{PALF} is the weight of PALF, w_{Glass} is the weight of glass fibre, w_{pp} is the weight of PP, ρ_{PALF} is the density of PALF, ρ_{Glass} is the density of glass fibre and ρ_{pp} is the density of PP.

2.3 Experimental Works

The indentation test in edge support configuration was conducted according to ASTM D6264 at room temperature using the universal testing machine, Instron 5585 with 150 kN load cell. Non-hybrid and hybrid composite laminates with various fibre stacking configurations were cut into the dimension of 100 mm X 100 mm (Length X Width) for the indentation test. The quasi-static crosshead displacement rate was fixed at 1.27 mm/min. The specimen was clamped between the top and bottom support plate, which was tightened using four screws to avoid slippage during the test. The setup of the quasi-static indentation test for composite laminates is depicted in Figure 3. A hemispherical tip indenter with a diameter of 12.7 mm was used to perform the indentation. The experiment was repeated three times for each fibre stacking configuration to obtain the average findings. The force-displacement curves from the indentation test were then recorded to evaluate the energy absorption and the maximum indentation load of each composite laminate. The damage mechanism of the front and rear fracture surfaces of each composite was subsequently investigated.

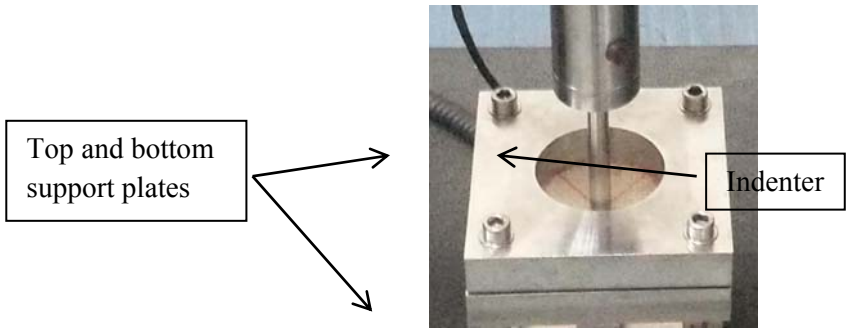

Figure 3: Setup of the quasi-static indentation test.

3. RESULTS AND DISCUSSION

3.1 Quasi-Static Indentation Properties

The quasi-static indentation test was conducted on the non-hybrid and hybrid composite laminates to study the indentation resistance and energy absorption behaviours. The indentation properties in terms of maximum indentation force, energy absorption and specific energy absorption of non-hybrid and hybrid composite laminates are summarised in Table 3.

Table 3: Indentation properties of non-hybrid and hybrid composite laminates.

Fibre stacking configurations	Maximum indentation force (N)	Energy absorption (J)	Specific energy absorption ($J.m^2/kg$)
[P/P/P]	860.76	8.47	2.76
[P/G/P]	939.62	8.92	2.78
[G/P/G]	1372.97	13.43	3.77
[G/G/G]	1474.55	15.10	3.95

The force-displacement curves of the non-hybrid and hybrid composite laminates are represented in Figure 4. The overall trend of the force-displacement curves is similar irrespective of the fibre stacking configurations. The indentation force increased along with the increase of the displacement up to the maximum point where the failure of the composite laminate occurred. As noticed in Figure 4, the indentation force increased at the initial stage until the maximum value, leading to the matrix cracking and initiation of the delamination. Then, it was followed by the penetration and fibre breakage which drastically reduced load carrying capacity of the fibres. Subsequently, the composite laminate was subjected to the perforation that resulted in the friction between the sample and the indenter prior to the final failure. Similar behaviour could be observed in the research study by Abisset *et al*., (2016) who found the indentation force increased initially until the load drop, which was followed by the delamination and finally fibre failure.

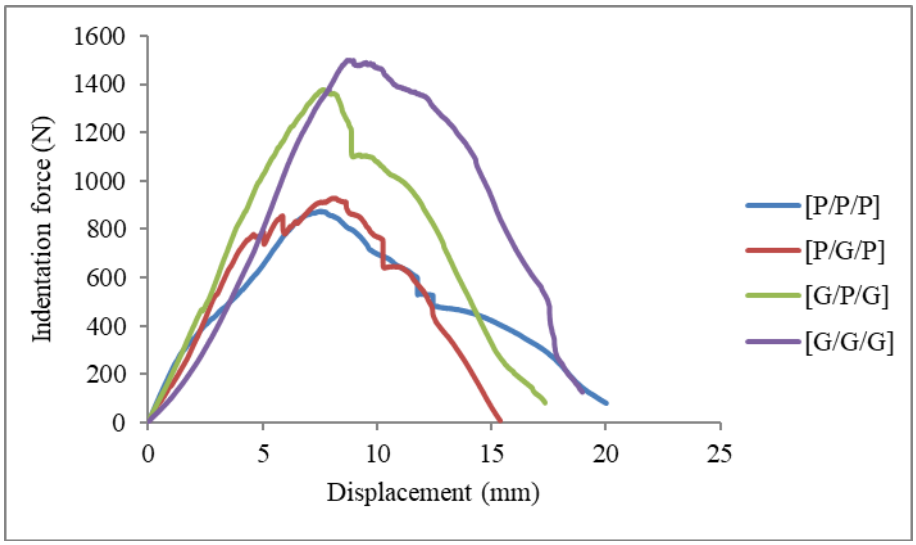

Figure 4: Force-displacement curves of non-hybrid and hybrid composite laminates.

The maximum indentation force and the energy absorption of each non-hybrid and hybrid composite laminate are shown in Figure 5. The energy absorption for each composite laminate was determined by obtaining the area under the force-displacement curves. From the findings, it was evidenced that non-hybrid glass fibre reinforced composites had the highest indentation force and energy absorption compared to other composite laminates. In contrast, non-hybrid PALF reinforced composites demonstrated the lowest indentation force and energy absorption. The maximum indentation force and energy absorption of non-hybrid glass fibre reinforced composites were 1474.55 N and 15.10 J which are 71.31 % and 78.28 % respectively higher than non-hybrid PALF reinforced composites However, the partial incorporation of glass fibre in the PALF based composites resulted in the positive hybrid effect where the overall indentation force and energy absorption were increased. When one middle layer of PALF was replaced by glass fibre, the maximum indentation force and energy absorption were improved by 9.16 % and 5.31 %. Furthermore, the maximum indentation force and energy absorption were enhanced by 59.51 % and 58.56 % when glass fibres substituted the outermost PALF fibre layers.

It is interesting to note that composite laminates with [G/P/G] fibre stacking configuration exhibited comparable maximum indentation force and energy absorption to those of [G/G/G] composite laminates. The maximum indentation force and energy absorption of [G/P/G] composite laminates were merely 6.89 % and 11.06 % lower than [G/G/G] composite laminates. These trends indicate the potential of hybrid composites to replace non-hybrid glass fibre reinforced composites. Besides, it was also noticed that the [P/P/P] composite laminates had comparable indentation properties to those of [P/G/P] composite laminates. It can be observed that the indentation properties of composite laminates are governed by the skin layers instead of the middle fibre layer. The skin layers in the composite laminates are the primary load carrier instead of the intermediate layer. The intermediate

fibre layer has a minor contribution to the indentation properties of composite laminates. Besides, the indentation behaviour of composite laminates depends on the bending stiffness of each fibre layer. Therefore, the incorporation of high strength glass fibre as the skin layers could provide higher indentation resistance to the composite laminates.

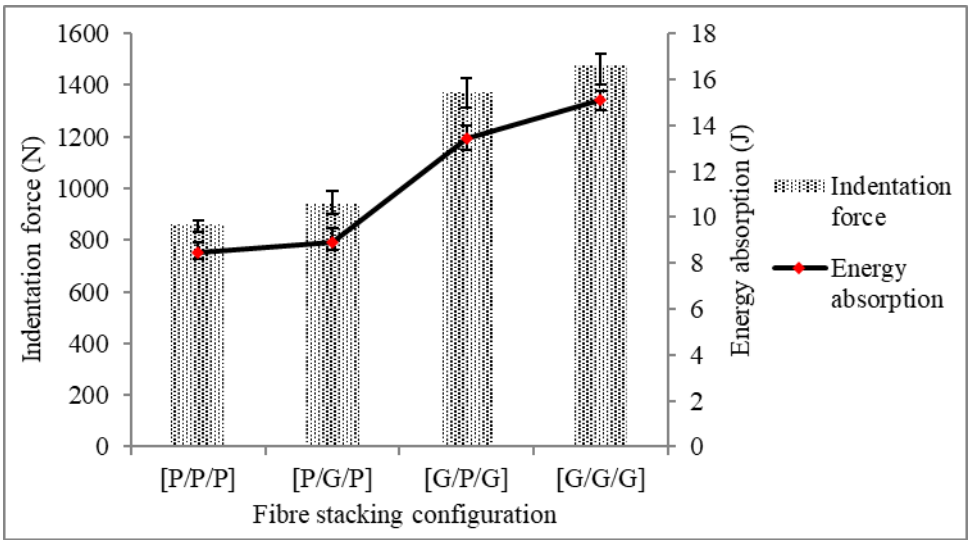

Figure 5: Maximum indentation force and energy absorption of composite laminates under quasi-static indentation.

Since lightweight characteristic is the advantage of natural fibres in comparison to synthetic fibres, thus it is paramount to study the specific indentation behaviour of the PALF based composite laminates. Figure 6 depicts the specific energy absorption of composite laminates subjected to indentation. The specific energy absorption of each composite laminates was obtained by dividing the total energy absorption ($E_{absolute}$) by the areal density, which is attested in Equation 2.

$$E_{specific} = \frac{E_{absolute}}{Areal\ density} \quad (2)$$

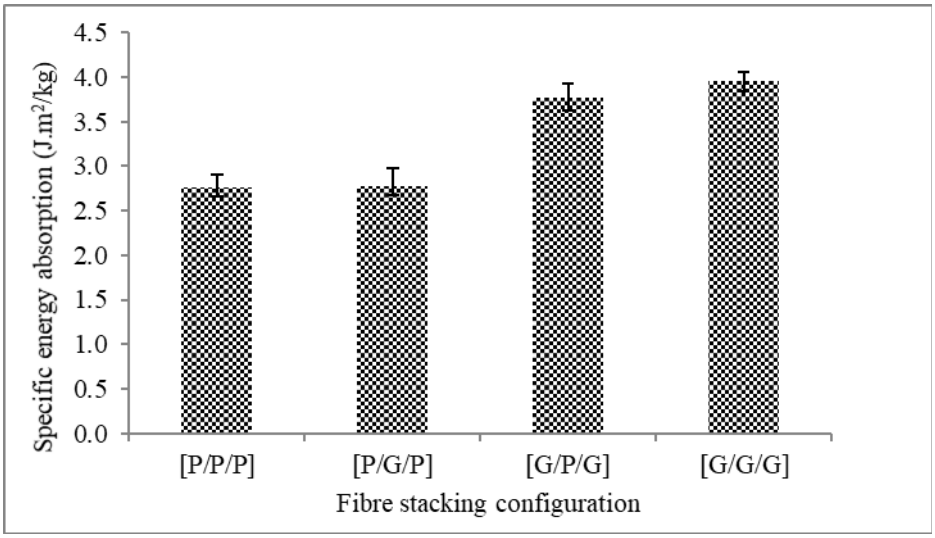

Figure 6: Specific energy absorption of composite laminates subjected to indentation.

The results indicate the difference in the specific energy absorption of each composite laminate was diminished with an increasing amount of PALF in the composite laminates. In spite of [G/G/G] composite laminates still demonstrated the highest specific energy absorption, however, the difference in the specific energy absorption between non-hybrid [G/G/G] composite laminates and [G/P/G] composite laminates reduced. The specific energy absorption of [G/P/G] composite laminate is only 4.53 % lower than [G/G/G] composite laminates. A similar trend was observed in the [P/P/P] and [P/G/P] composite laminates in which the specific energy absorption of [P/P/P] composite laminates is only 0.49 % lower than [P/G/P] composite laminates. Due to the intrinsic lower density of PALF as compared to glass fibre, therefore the incorporation of PALF in the composite laminates is considered beneficial to the specific properties.

3.2 Damage Assessment

The fracture mechanism of the non-hybrid and hybrid composite laminates was evaluated after the quasi-static indentation test. The fracture surfaces of the indented and rear sides of each composite laminate are shown in Table 4. The overall observation shows the fracture mechanisms of composite laminates are highly dependent on the fibre type in the outermost layers of composite laminates.

Table 4: Fracture surface of composite laminates subjected to quasi-static indentation.

Composites	Front	Rear
[P/P/P]	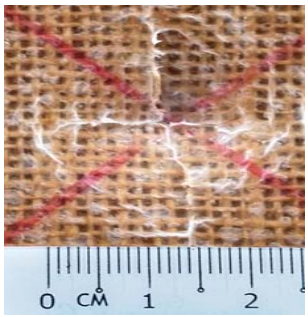	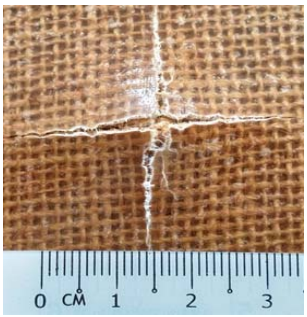
[P/G/P]	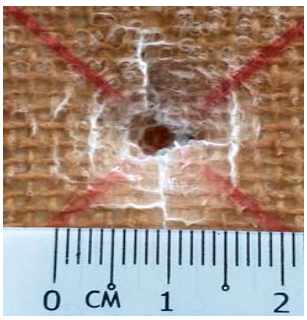	

[G/P/G]

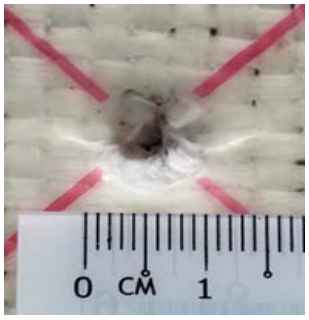

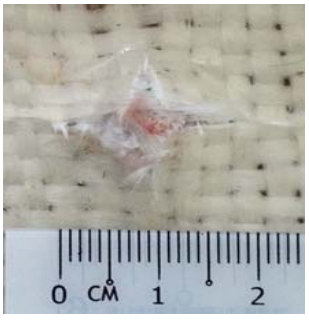

[G/G/G]

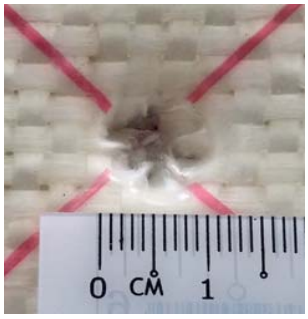

From Table 4, it was observed that [P/P/P] and [P/G/P] composite laminates exhibited similar fracture mechanism. Meanwhile, the fracture mechanism of [G/P/G] and [G/G/G] composite laminates was similar. The fracture mechanism of PALF based composite laminates demonstrated larger crack propagation as compared to glass fibre based composite laminates. However, the crack propagation was reduced when one layer of PALF was substituted by glass fibre. In overall, the crack propagation of composite laminates with glass fibre as the skin layers was significantly smaller compared to those composite laminates with PALF as the skin layers, which was evidenced in Table 4. The failures due to the quasi-static indentation are compression-shear and tension-shear which could occur at the indented and rear surface respectively. During the indentation, the failure occurred first at the indented surface with a dent which was followed by the crack initiation and propagation on the rear surface. The crack length on the rear surface increased with the increase of indentation displacement. Moreover, the crack on the rear surface was more severe than the indented surface, implying that rear surface exhibited more damage and deformation during the indentation.

4. CONCLUSION

In this research work, the influence of the fibre stacking configuration on the indentation behaviour of pineapple leaf/glass fibre reinforced PP composite laminates was investigated. The indentation behaviour of hybrid composites was compared to those of non-hybrid composites. From the results obtained, the following conclusions were drawn.

1. The quasi-static indentation behaviour of composite laminates was highly dependent on the fibre stacking configurations. Non-hybrid glass fibre reinforced composite laminates demonstrated the highest indentation force over other composite laminates. On the contrary, the lowest indentation force was noticed in non-hybrid PALF based composite laminates. The indentation force and energy absorption of hybrid composite laminates were in between non-hybrid composite laminates. However, hybrid [G/P/G] composite laminates exhibited a comparable indentation force and energy absorption which was only 6.89 % and 11.06 % lower than the [G/G/G] composite laminates.

2. In terms of the energy absorption, the same trend was observed in which the [G/G/G] composite laminates showed the highest value, which was followed by [G/P/G], [P/G/P] and finally [P/P/P]

composite laminates. The partial incorporation of glass fibre indeed leads to the positive hybrid effect which improved the energy absorption of the PALF based composite laminates. The results evidenced that the energy absorption was enhanced by 5.31 % when one middle PALF layer was replaced by glass fibre. In addition, the replacement of the outermost PALF layers with glass fibre resulted in the improvement up to 58.56 %.

3. When the areal weight of each composite laminate was taken into consideration, the advantage of incorporating PALF in the composite laminate become prominent due to the lower density of PALF compared to the glass fibre. In comparison with the absolute energy absorption, it was shown that the difference in the specific energy absorption of composite laminates was diminished with an increasing amount of PALF. The specific energy absorption of hybrid composite laminates with [G/P/G] fibre stacking configuration was only 4.53 % lower than [G/G/G] composite laminates while the specific energy absorption of [P/P/P] composite laminates was merely 0.49 % lower than [P/G/P] composite laminates. These findings have shown the potential of PALF based hybrid composites as a substitution for the non-hybrid glass fibre based composites.

ACKNOWLEDGEMENT

The authors would like to thank Universiti Teknikal Malaysia Melaka (UTeM) for the continuous support of this research project. The authors would also wish to express their gratitude towards Skim Zamalah UTeM provided by UTeM and Ministry of Education for research grant FRGS/1/2017/STG07/FKM-CARE/F00339.

REFERENCES

Abisset, E., Daghia, F., Sun, X.C., Wisnom, M.R. & Hallett, S.R. (2016). Interaction of inter- and intralaminar damage in scaled quasi-static indentation tests: Part 1 – Experiments. *Compos. Struct*., **136**: 712–726.

Alam, M.M., Maniruzzaman, M. & Morshed, M.M. (2014). Application and Advances in Microprocessing of Natural Fiber (Jute)–Based Composites. *In* Hashmi, S., Batalha, G.F., Tyne, C.J.V. & Yilbas, B. (Eds.), *Comprehensive Materials Processing*. Amsterdam, Netherlands, pp. 243–260.

Arpitha, G.R., Sanjay, M.R., Senthamaraikannan, P., Barile, C. & Yogesha, B. (2017). Hybridization effect of sisal/glass/epoxy/filler based woven fabric reinforced composites. *Exp. Tech*., **41**: 577–584.

Asgarinia, S., Viriyasuthee, C., Phillips, S., Dube, M., Baets, J., Van Vuure, A., Verpoest, I. & Lessard, L. (2015). Tension-tension fatigue behaviour of woven flax/epoxy composites. *J. Reinf. Plast. Compos*., **34**: 857–867.

Beg, M.D.H. & Pickering, K.L. (2008). Mechanical performance of kraft fibre reinforced polypropylene composites: influence of fibre length, fibre beating and hygrothermal ageing. *Compos. Part A Appl. Sci. Manuf*., **39**: 1748–1755.

Bulut, M. & Erkliğ, A. (2018). The investigation of quasi-static indentation effect on laminated hybrid composite plates. *Mech. Mater*., **117**: 225–234.

Chawla, K.K. (2006). Glass fibers. *In* Mortensen, A (Ed.), *Concise Encyclopedia of Composite Materials*. Elsevier, Amsterdam, Netherlands, pp. 415–419.

Dittenber, D.B. & GangaRao, H.V.S. (2012). Critical review of recent publications on use of natural composites in infrastructure. *Compos. Part A Appl. Sci. Manuf*., **43**: 1419–1429.

Erkendirci, O.F. & Haque, B.Z.G. (2012). Quasi-static penetration resistance behaviour of glass fibre reinforced thermoplastic composites. *Compos. Part B Eng*., **43**: 3391–3405.

Feng, N.L. & Malingam, S.D. (2019). Monotonic and fatigue responses of fiber-reinforced metal laminates. *In* Jawaid, M., Thariq, M. and Saba, N. (Eds.), *Mechanical and Physical Testing of Biocomposites, Fibre-Reinforced Composites and Hybrid Composites*. Woodhead Publishing, Duxford, United Kingdom, PP. 307–323.

Feng, N.L., DharMalingam, S., Zakaria, K.A. & Selamat, M.Z. (2017). Investigation on the fatigue life characteristic of kenaf/glass woven-ply reinforced metal sandwich materials. *J. Sandw. Struct. Mater*., 1–16. doi:10.1177/1099636217729910

Feng, N.L., Malingam, S.D., Jenal, R., Mustafa, Z. & Subramonian, S. (2018). A review of the tensile and fatigue responses of cellulosic fibre-reinforced polymer composites. Mech. Adv. Mater. Struct., 1–16. doi:10.1080/15376494.2018.1489086

Gurunathan, T., Mohanty, S. & Nayak, S.K. (2015). A review of the recent developments in biocomposites based on natural fibres and their application perspectives. *Compos. Part A Appl. Sci. Manuf*., **77**: 1–25.

Habibi, M., Laperrière, L. & Hassanabadi, H.M. (2018). Influence of low-velocity impact on residual tensile properties of nonwoven flax/epoxy composite. *Compos. Struct*., **186**: 175–182.

Karahan, M. & Karahan, N. (2015). Investigation of the tensile properties of natural and natural/synthetic hybrid fiber woven fabric composites. *J. Reinf. Plast. Compos*., **34**: 795–806.

Le Duigou, A., Davies, P. & Baley, C. (2010). Interfacial bonding of flax fibre/poly(l-lactide) bio-composites. *Compos. Sci. Technol*., **70**: 231–239.

Lin, C. & Fatt, M.S.H. (2006). Perforation of composite plates and sandwich panels under quasi-static and projectile loading. *J. Compos. Mater*., **40**: 1801–1840.

Malingam, S.D., Ng, L.F., Chan, K.H., Subramaniam, K., Selamat, M.Z. & Zakaria, K.A. (2018). The static and dynamic mechanical properties of kenaf/glass fibre reinforced hybrid composites. *Mater. Res. Express*., **5**: 1–12.

Mohamad, M.A.H., Mat, W.A.W., Zaidi, A.M.A., Ibrahim, M.H., Hassim, H.M., Mustapa, M.S. & Abdullah, S. (2017). Penetration resistance force of sandwich panels composite with kenaf foam as a core material against deformable projectiles. *Def. S T Tech. Bull*., **10**: 101–110.

Ng, L.F., Sivakumar, D., Zakaria, K.A., Bapokutty, O. & Sivaraos. (2017). Influence of kenaf fibre orientation effect on the mechanical properties of hybrid structure of fibre metal laminate. *Pertanika J. Sci. Technol*., **25**: 1–8.

Pickering, K.L., Efendy, M.G.A. & Le, T.M. (2016). A review of recent developments in natural fibre composites and their mechanical performance. *Compos. Part A Appl. Sci. Manuf*., **83**: 98–112.

Salman, S.D., Leman, Z., Ishak, M., Sultan, M. & Cardona, F. (2018). Quasi-static penetration behavior of plain woven kenaf/aramid reinforced polyvinyl butyral hybrid laminates. *J. Ind. Text*., **47**: 1427–1446.

Sivakumar, D., Ng, L.F. & Salmi, N.S. (2016). Eco-hybrid composite failure behavior of two serial bolted joint holes. *J. Eng. Technol*., **7**: 114–124.

Yahaya, R., Sapuan, S.M., Jawaid, M., Leman, Z. & Zainuddin, E.S. (2014). Quasi-static penetration and ballistic properties of kenaf–aramid hybrid composites. *Mater. Des*., **63**: 775–782.

Yang, Y., Ota, T., Morii, T. & Hamada, H. (2011). Mechanical property and hydrothermal aging of injection molded jute/polypropylene composites. *J. Mater. Sci*., **46**: 2678–2684.

Zhou, G., Zhang, B. & Pasricha, A. (2017). A study of indentation behaviour of sandwich panels supported rigidly. *Int. J. Struct. Integr*., **8**: 439–451.

MECHANICAL PROPERTIES OF CROSS-PLY BANANA-GLASS FIBRE REINFORCED POLYPROPYLENE COMPOSITES

Norizzati Zulkafli[1], Sivakumar Dhar Maligam[1]*, Siti Hajar Sheikh Md Fadzullah[1], Zaleha Mustafa[2], Kamarul Ariffin Zakaria[1] & Sivarao Subramonian[2]
[1]Centre for Advanced Research on Energy, Fakulti Kejuruteraan Mekanikal
[2]Fakulti Kejuruteraan Pembuatan
Universiti Teknikal Malaysia Melaka (UTeM), Malaysia

*Email: sivakumard@utem.edu.my

ABSTRACT

Banana fibre is a secondary crop fibre that could be profitably used in the manufacturing of fibre reinforced composites because they possess attractive mechanical and physical properties. The mechanical properties of banana-glass fibre reinforced polypropylene composite were studied. The composites were prepared using a hot press with four types of stacking sequence. Mechanical tests were carried out according to American Society for Testing and Materials (ASTM) D3039 for tensile test, ASTM D790 for flexural test and ASTM D6264 for quasi-static indentation. The results showed that banana fibre (B) reinforced composite was enhanced by incorporating glass fibres (G) by 302.27% and 24.45% for GBG, in terms of tensile and flexural strength respectively. For quasi-static indentation, the energy absorbed increased by 122.22% with the incorporation of glass fibre for GBG. The results show a positive hybrid effect on the mechanical properties, where hybrid GBG is comparable to GGG in the flexural application.

Keywords: *Natural fibre; hybrid composite; mechanical properties; banana fibre; glass fibre.*

1. INTRODUCTION

Environmental consciousness, as well as government legislations around the world, has encouraged the academic and industrial researches to develop eco-friendly, sustainable, and biodegradable composite materials, thus often referred to as green composites (Baillie, 2005). Natural fibre reinforced composites are currently dominating the composite field, which support the notion of creating a greener future. Natural fibres offer better specific stiffness and strength, biodegradability, availability, sustainability in production, and low cost per unit volume (Herrera-Franco & Valadez-Gonzalez, 2004). Many types of natural fibres such as kenaf, jute, hemp, sugar palm, sisal, pineapple leaf, coir, abaca and kapok, have been used as reinforcement in polymer composites (Mohammed *et al*., 2015). Environmentally friendly composites are more frequently applied to military applications, transportation, building and construction industries (Saba *et al*., 2014). Extensive research and investigations are dedicated to natural fibre reinforced polymer composites due to their advantageous features, such as biodegradable, recyclable, lightweight and cost-effective (Subramonian *et al*., 2016). Physical and mechanical properties of composites are dependent on the length of the fibre, matrix ratio, fibre arrangement, number of layers and fibre directions (Arthanarieswaran *et al*., 2014; Subramaniam *et al*., 2017).

One way to improve the mechanical properties of natural fibre reinforced composite is through hybridisation. There is a growing need for composite materials for use in military and civil applications, and there is a global search for materials with desirable structural characteristics (Razali *et al*., 2017). The study of woven banana and kenaf fibre composites by Alavudeen *et al*. (2015) showed that hybridisation of kenaf with banana fibres increase the mechanical properties which are superior to those of the individual fibres. Woven hybrid composites namely jute / sisal / glass and jute

/ banana / glass were tested, and the results showed that high strength hybrid composite made of jute / banana / glass has better mechanical properties and is applicable for a wide range of applications (Parandaman & Jayaraman, 2015). Venkatasubramaniam *et al*. (2014) studied the mechanical properties of the randomly oriented mats of abaca, banana and glass fibres and their hybrids. The result showed that abaca-glass composite had the highest tensile properties while abaca/glass/banana hybrid composite had better flexural and impact properties. Srinivasan *et al*. (2014) investigated the mechanical properties of woven flax, banana, glass and their hybrids. The results showed that the banana / glass composite had a higher tensile strength than the flax / glass composite. However, the flexural and impact properties of the banana / glass composite were slightly higher (15.79%) and lower (8.33%) respectively lower than the flax / glass composite. Navaneethakrishnan *et al*. (2015) investigated the mechanical properties of glass / banana fibre reinforced silica nano-particles with epoxy composites. The impregnated layers were made for six different types of composites with 0 - 5 % of silica, where each type composed of two layers of banana fibre and four layers of glass fibre. The results showed that the composite with 3% silica had the highest tensile strength. It was concluded that banana fibre in combination with glass fibre has proven to be excellent for making a cost-effective composite material. Samal *et al.* (2009) investigated the performance of banana / glass fibre reinforced polypropylene hybrid composites. The samples were fabricated using melt blending with different fibre ratio. The results showed that the mechanical properties of hybrid composites were enhanced to the maximum when the fibre was 15%:15% (glass: banana). Thiruvasagam *et al*. (2016) evaluated the mechanical properties of woven roving hybrid banana, jute and glass fibre reinforced polyester composite. The result showed that glass / banana / jute had the highest tensile properties followed by glass / banana and glass / jute. However, for the flexural test, glass/banana composite had the highest flexural strength since its strength increases with an increase in interfacial adhesion.

Rodriguez *et al*. (2016) studied the water uptake, chemical characterisation and tensile behaviour of modified woven banana plantain fibre and their polyester composites. The results showed that silane treated banana fibre increased the tensile strength by 11.32%. Kumar *et al*. (2013) investigated the mechanical properties of short banana fibreglass reinforced hybrid polypropylene composites with different fibre weight fraction. Based on the results, the tensile strength was maximum when the fibre weight fraction was 7.5%, and 10% for flexural strength. The composite can be regarded as a useful lightweight engineering material and reduces the manufacturing cost by adding banana fibre hybridised with glass fibre to the matrix. Rahman *et al*. (2018) investigated the mechanical properties of chemically treated banana and pineapple leaf fibre reinforced hybrid polypropylene composites. The short fibres of banana and pineapple leaf were alkali treated before fabrication. The results showed that the best mechanical properties were obtained when polypropylene was reinforced with 5 wt.% pineapple leaf and banana fibre at a ratio of 3:1. This is due to pineapple leaf fibre containing higher cellulose content as compared to banana fibre, thus making composite with more pineapple leaf fibre having better bending properties.

Boopalan *et al*. (2013) studied the mechanical and thermal properties of cross-ply jute and banana fibres reinforced in epoxy resin. The results showed that the mechanical properties increased up to a certain limit, then decreased due to poor interfacial bonding. The highest tensile and flexural strengths were observed for the composite with a 50/50 weight ratio of jute / banana fibres. Amir *et al*. (2017) studied the effect of fibre configuration on the mechanical properties of banana fibre / polypropylene (PP) / maleic anhydride grafted polypropylene (MAPP) reinforced composites. The composites were reinforced with different types of banana fibres; raw fibre, banana yarn and banana in mat form. The results showed that the PP / banana yarn had the highest tensile and flexural properties. This was because the yarn fibre is continuous in the composite and commingled by its configuration. Heckadka *et al*. (2018) compared the mechanical properties between jute / glass and banana / glass reinforced epoxy composite laminates. In this research, the tensile and flexural strengths of jute / glass composite was higher than the banana / glass composite. The hybridisation of natural and synthetic fibres enhanced the mechanical properties of the composite through the acquirement of the advantages of one fibre to overcome the disadvantage of another fibre, such as hydrophilicity (Dhar Malingam *et al*., 2017; Subramaniam *et al*., 2017).

However, thus far, the research on the hybridisation of cross-ply banana-glass fibre thermoplastic composites is scarce, especially on the effect of stacking on the mechanical properties. Thus, this paper investigates the mechanical properties of hybrid banana-glass fibre reinforced polypropylene composite in terms of its tensile, flexural and quasi-static indentation properties.

2. EXPERIMENTAL SETUP

2.1 Materials

J.C. Overseas Incorporation, India supplied cross-ply (0/90°) banana (B) fibre with the areal weight of 342.5 g/m^2. ZKK Sdn Bhd, Malaysia supplied cross-ply (0/90°) glass (G) fibre with the areal weight of 600 g/m^2. Al Waha, Saudi Arabia supplied polypropylene (PP) pellets with a density of 0.95 g/cm^3. The typical properties of banana fibre, glass fibre and polypropylene are tabulated in Table 1.

Table 1: Typical properties of banana fibre (Agarwal *et al.*, 2003; Paul *et al.*, 2008; Bhatnagar *et al.*, 2015;), glass fibre (Wallenberger *et al.*, 2001) and polypropylene (Maddah, 2016).

Properties	Banana Fibre	Glass Fibre	Polypropylene
Tensile Strength (MPa)	550	1700-3500	22-41.4
Young's Modulus (GPa)	22-32	65-72	1.5-2
Elongation at break (%)	3-4	3	3-700
Diameter (μm)	80-250	5-25	-
Density (g/cm^3)	1.35	2.58	0.89-0.95
Cellulose (%)	60-65	-	-
Hemicellulose (%)	6-19	-	-
Lignin (%)	5-10	-	-
Softening point, T_q (°C)	-	-	-10 to -23
Melting point, T_m (°C)	163	-	160-176

2.2 Composite Preparation

PP granules were compressed at 168 °C and pressure of 4.9 MPa in a hot press to form a thin film with a nominal thickness of 0.2 mm. The cross-ply glass and banana fibres were cut and stacked in four different sequences alternated with PP thin film in a picture mould frame with dimensions of 250 x 250 x 3.5 mm. A total of three layers of cross-ply fibres were fixed in a single composite laminate. The mould was then placed in a hot press and preheated at 170 °C for 5 min. Then, the composite was compressed at 170 °C for another 10 min at a constant pressure of 3.5 MPa and then left to cool for 15 min. The composites were divided into hybrid and non-hybrid composites, referred to as banana / banana / banana (BBB), banana / glass / banana (BGB), glass / banana / glass (GBG) and glass / glass / glass (GGG), as illustrated in Figure 1. BBB and GGG are the non-hybrid banana and glass fibre reinforced polypropylene composites. BGB is a hybrid composite with banana fibre as the skin layer, while GBG is the hybrid composite with glass fibre as the skin layer.

Table 2 shows the fibre and matrix volume fractions of the composites. The following Equation 1 is used to calculate the fibre volume fractions (V_{fibre}):

$$V_{fibre} = \frac{\frac{w_{banana}}{\rho_{banana}} + \frac{w_{glass}}{\rho_{glass}}}{\frac{w_{banana}}{\rho_{banana}} + \frac{w_{glass}}{\rho_{glass}} + \frac{w_{pp}}{\rho_{pp}}} \quad (1)$$

where w_{banana} and ρ_{banana} are the weight and density of banana fibre, w_{glass} and ρ_{glass} are the weight and density of glass fibre, and w_{pp} and ρ_{pp} are the weight and density of PP.

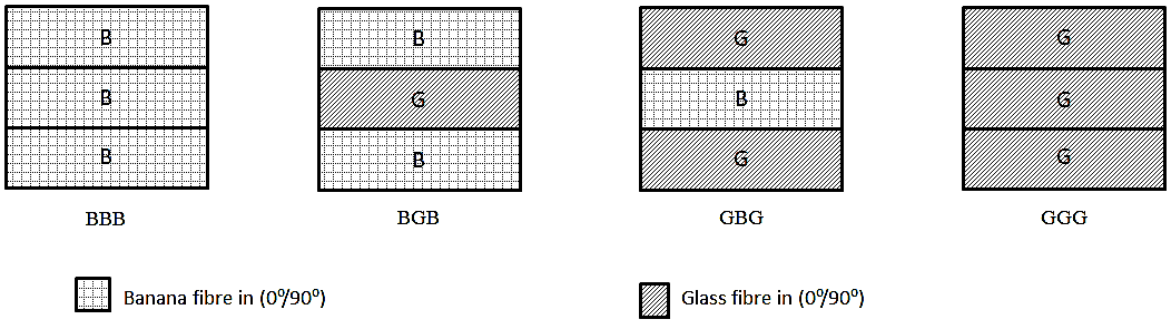

Figure 1: Stacking sequence of the composites.

Table 2 : Fibre and matrix volume fractions in the composites.

Composite	Fibre volume fraction (%)	Matrix volume fraction (%)
BBB	24.36	75.64
BGB	22.99	77.01
GBG	19.35	80.65
GGG	18.92	81.08

2.3 Mechanical Properties

Tensile and flexural tests were conducted according to American Society for Testing and Materials (ASTM) D3039 and ASTM D790 using a universal testing machine (UTM) model Instron 8872 with a 25 kN load cell. The composites were cut into dimensions of 200 x 25 mm and tested with a crosshead speed of 2 mm/mm until fracture. For the quasi indentation test, the samples were cut into dimensions of 100 x 100 mm according to ASTM D6264. The test was conducted using a UTM Instron 5585 with 150 kN load cell at a crosshead speed of 1.27 mm/min using a custom made fixture and 12.7 mm diameter stainless steel hemispherical tip indenter. Five samples were tested for each type of composite. The penetration energy absorbed by the composites was calculated based on the area under the penetration force-displacement curves. Following these tests, the tensile, flexural and quasi-static indentation fracture surfaces were examined using scanning electron microscope (SEM).

3. RESULTS AND DISCUSSION

3.1 Tensile Properties

Figure 2 shows that the tensile strength of the composite increases when the layer of glass fibre increases. The ultimate tensile strength for each layering sequence was determined, and the highest value was found for GGG at 191.27 MPa, while the lowest was observed for BBB at 38.80 MPa. The tensile strength for the BGB was 123.12% higher than BBB. GBG tensile strength was 80.29% and 302.27% higher than BGB and BBB respectively. This is due to the incorporation of glass fibre with higher strength and modulus as compared to banana fibre. The strength of the layered hybrid composites depends on the fibre stacking sequence in the composites (Dhar Malingam *et al.*, 2018a). The load applied on the composite was carried axially by the high strength fibres before multiple fractures occurred and beyond, where the load was redistributed to the PP matrix. The composite with higher fibre strength at the skin material is prone to yield an optimum mechanical property (Agarwal *et al*., 2003). The normalised tensile strength also followed the same pattern of tensile strength, where non-hybrid GGG had the highest value of 1,235.59 MPa/ (g/cm³), followed by the GBG, BGB and BBB composites with 1,059.57, 617.49 and 285.54 MPa/ (g/cm³). Figure 3 shows the tensile modulus of the fabricated composites. The BBB sample exhibited the lowest tensile modulus of 0.37 GPa. The addition of glass fibre in the BGB sample showed an increase in the value of tensile modulus by 56.76%, while for the GBG sample, there was a 232.43% increase when compared to the BBB sample. The composite stiffness increased with the increase of glass fibre layup.

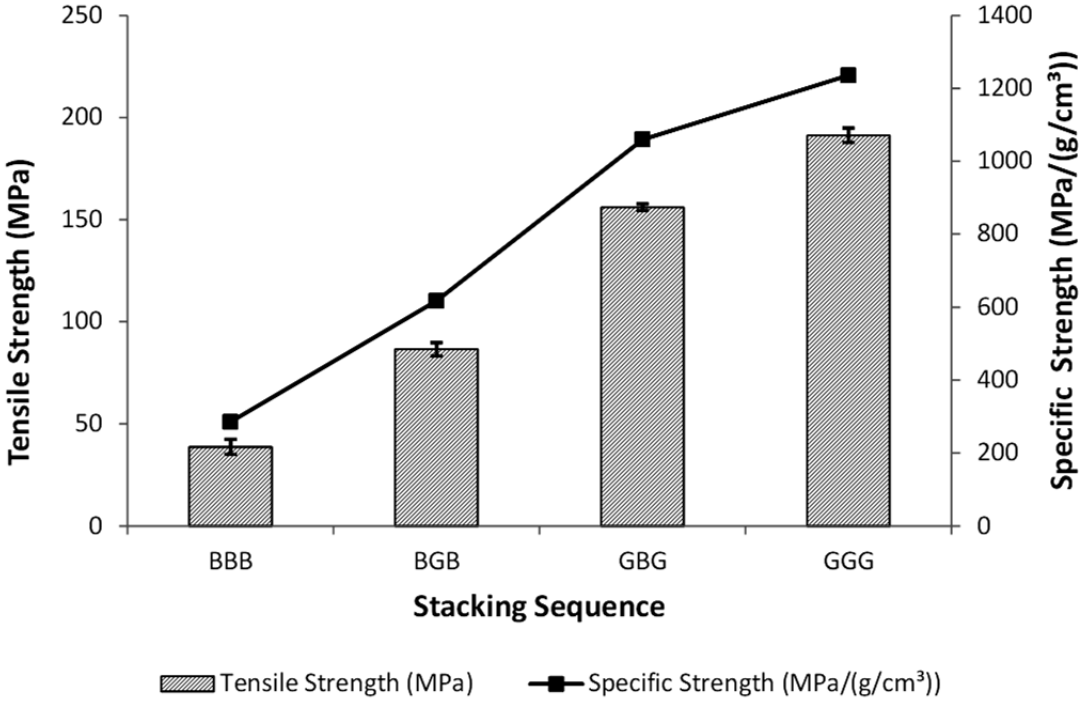

Figure 2: Tensile strength and specific tensile strength of each stacking sequence.

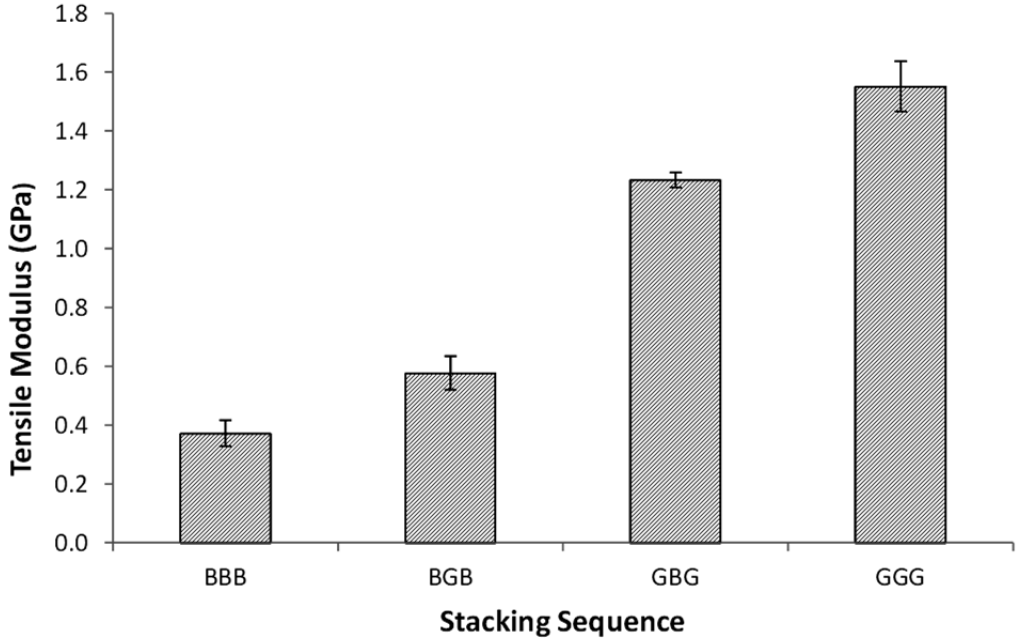

Figure 3: Tensile modulus of each stacking sequence.

3.2 Flexural Properties

Flexural strength is the combination of tension and compression stress, which vary with the inter-laminar shear strength. Figure 4 shows the flexural strength of each type of samples. The increasing glass fibre in the composites increased the shearing resistance and thus, increased the flexural performance (Sreekala *et al*., 2002). However, the GGG composite had a flexural strength of 68.26 MPa, which is 16.40% lower than the hybrid GBG composite due to poor interfacial adhesion between the fibre and matrix. Higher flexural strength in the hybrid composites is due to higher dispersion of banana fibre, where the glass fibre can pack well in the interstitial spaces available leading to a close-packed composite structure (Haneefa *et al*., 2008). Kretsis (1987) reviewed the flexural properties of hybrid fibre reinforced plastics, who found that flexural properties not only depend on the hybrid composition but also the arrangement of the material layers. The results depict that hybrid GBG has the highest flexural strength of 81.65 MPa when compared to hybrid BGB. This enhancement in flexural strength may be attributed to the ability of the fabric to withstand bending forces during the three-point bending test (Dan-mallam *et al*., 2015). The increased flexural strength of the hybrid composites with the loading of glass fibre was mainly owing to the increased resistance to shearing of the composites due to the inclusion of rigid glass fibre (Haque & Hasan, 2016). Failure of the composite was characterised by fibre breakage and matrix cracking, which was initiated from the tension side of the specimen, with fracture occurring in the middle of the beam (Jawaid *et al*., 2011). Once the compression failure occurs, the flexural stress in the composite is reduced as the fibre breakage, and matrix cracking continues to propagate along the fibre-matrix interphase. As stated in Sathish *et al*. (2015), composites made from banana fibres have high flexural strength and hence, can be used in various automotive applications such as seat trims and transmission covers. The flexural modulus in Figure 5 increased with increasing glass fibre in the composite. Joseph *et al*. (1999) attributed the increase in the flexural strength and modulus to the increasing fibre-to-fibre contact when the fibres were impregnated.

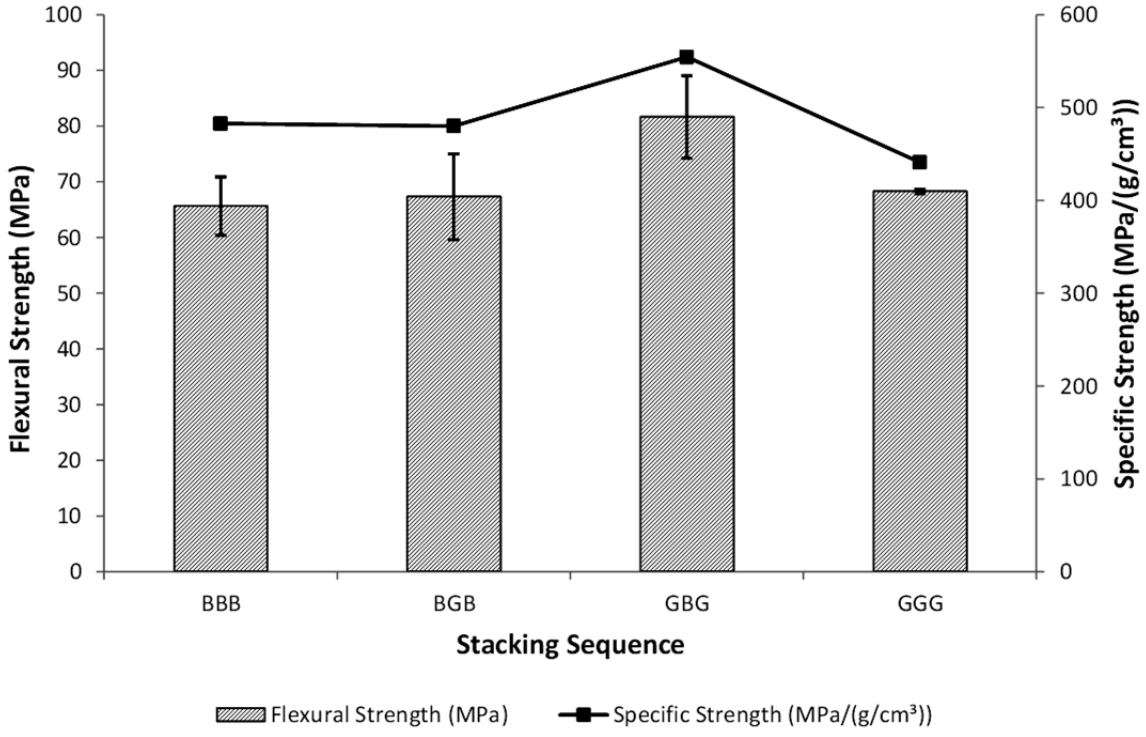

Figure 4: Flexural strength and specific flexural strength of each stacking sequence.

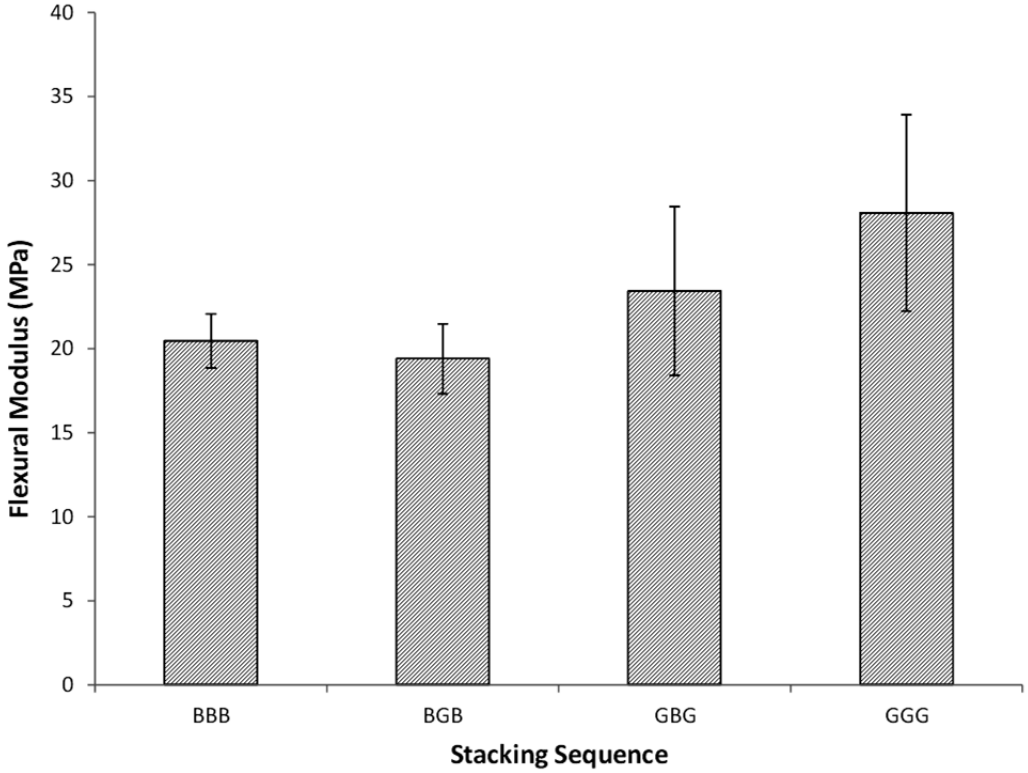

Figure 5: Flexural modulus of each stacking sequence.

3.3 Quasi-Static Indentation Properties

The average load-displacement curves of the indentation of the hybrid and non-hybrid composites are shown in Figure 6. The results of the test were analysed based on the force-displacement curves, total energy absorption and normalised energy absorption. Initially, the curve showed a linear behaviour, where it increased along with displacement until reaching a maximum peak load. This is due to a dent forming on the top surface of the composite, which eventually initiated a crack (Subramaniam *et al*., 2017). The indenter then moved through the thickness of the composite by pushing the matrix and fibres through the rear surface. Then, when the indenter penetrated the rear surface of the composite, the curve dropped drastically, which indicates that the specimen has failed (Saw *et al*., 2011).

Based on Figure 6, the GGG composite has the highest resistance to indentation for up to 6.65 kN. This is due to the strength of glass fibres, which resist the formation of a shear plug (Dhar Malingam *et al*., 2018b). However, the peak loads of the hybrid composite GBG was only 24.5% less than the GGG composite at 5.02 kN, followed by BGB and BBB at 3.07 and 2.25 kN respectively.

The area under the load-displacement curves in Figure 6 was calculated up to the peak load to determine the indentation energy absorbed by the composites. Figure 7 illustrates the energy absorbed and normalised energy absorption of the composites. The trend showed a positive hybrid effect where incorporation of glass fibre as the skin layer had greater energy absorption and load resistance. The glass fibre requires more force and elongation to fail, thus placing glass fibre as the skin layer of the composite enhance the energy absorption. The highest energy of 46.14 kJ was absorbed by GGG, followed by GBG and BGB with 32.30 kJ and 16.82 kJ respectively. BBB had the lowest energy absorption capability of 13.19 kJ. BBB had the lowest normalised energy of 0.36 kJ/g followed by BGB, GBG and GGG at 0.43, 0.80 and 1.04 kJ/g respectively. Hybrid GBG was 86% higher than hybrid BGB.

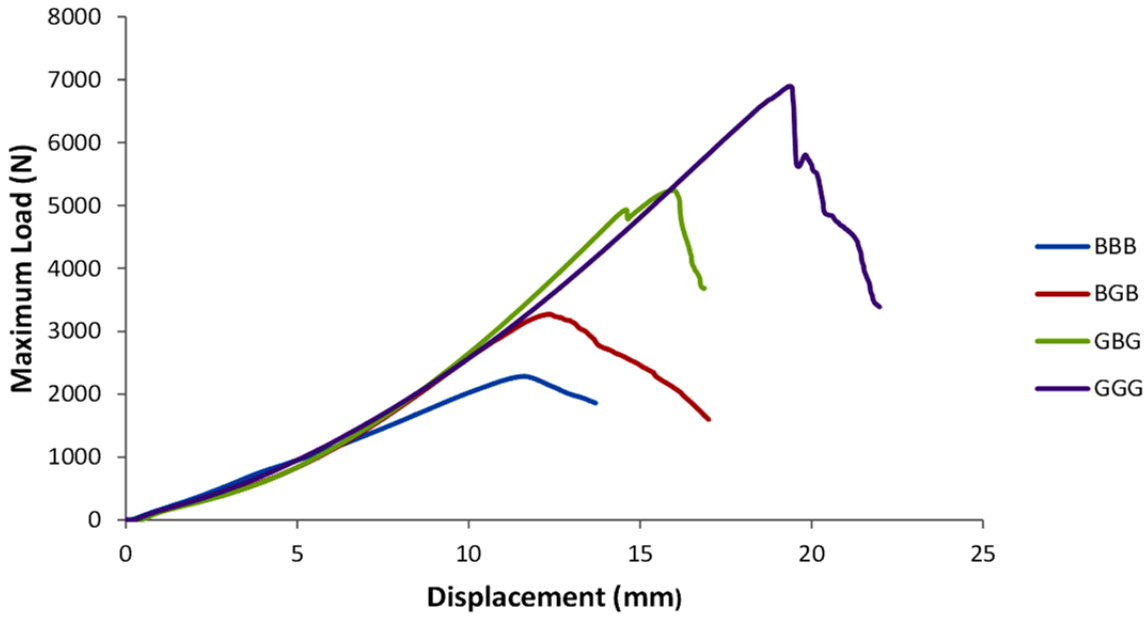

Figure 6: Load-displacement curve for each stacking sequence.

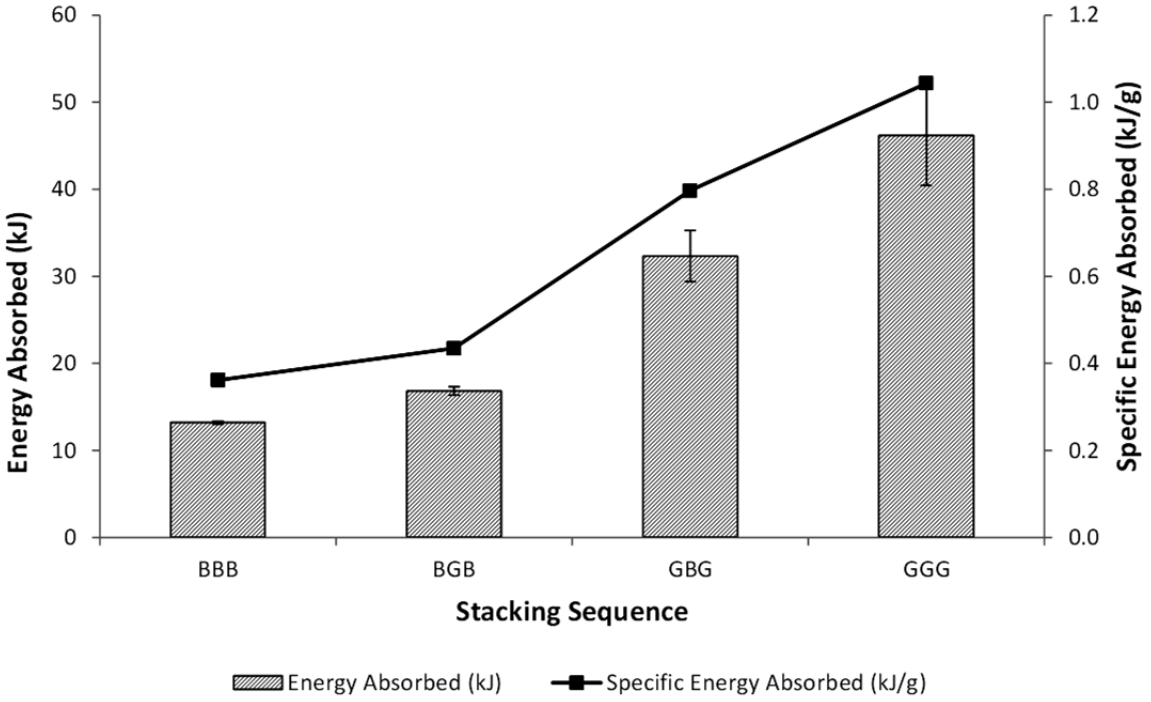

Figure 7: Energy and specific energy absorbed for each stacking sequence under quasi-static indentation.

3.4 Characterisation

Figure 8 depicts the SEM images of the failure surface of cross-ply composite due to tensile loading. The interlocking mechanism in both natural and synthetic fibres play an important role in resisting the load applied (Dhar Malingam *et al*., 2017). Based on Figure 8(a), it is apparent that fibre pull-outs occurred making the stress transfer between matrix and fibre less efficient. Figure 8(b) also shows banana fibres pull-outs and fractured glass fibres in BGB. Figure 8(c) has fewer fibre pull-outs but has traces of some delamination and matrix cracking in the composite GBG. Incorporation of glass fibres into the banana fibre reinforced composite increased the mechanical properties of the composites as the stresses were efficiently transferred from the matrix to the fibres for tensile and quasi-static. The staggered fractured matrix surface indicates the ductile behaviour of the matrix. Figure 8(d) shows the smooth surface of glass fibre, which indicates inefficient fibre wetting and matrix fracture. The matrix surface has few edges, which indicates that the composite is more brittle than the GBG composite in Figure 8(c) and thus, immediate failure occurred. A stronger fibre at the skin layer has better properties as compared to hybrid and BBB composites, thus resulting in hybrid GBG exhibiting better tensile properties when compared to hybrid BGB.

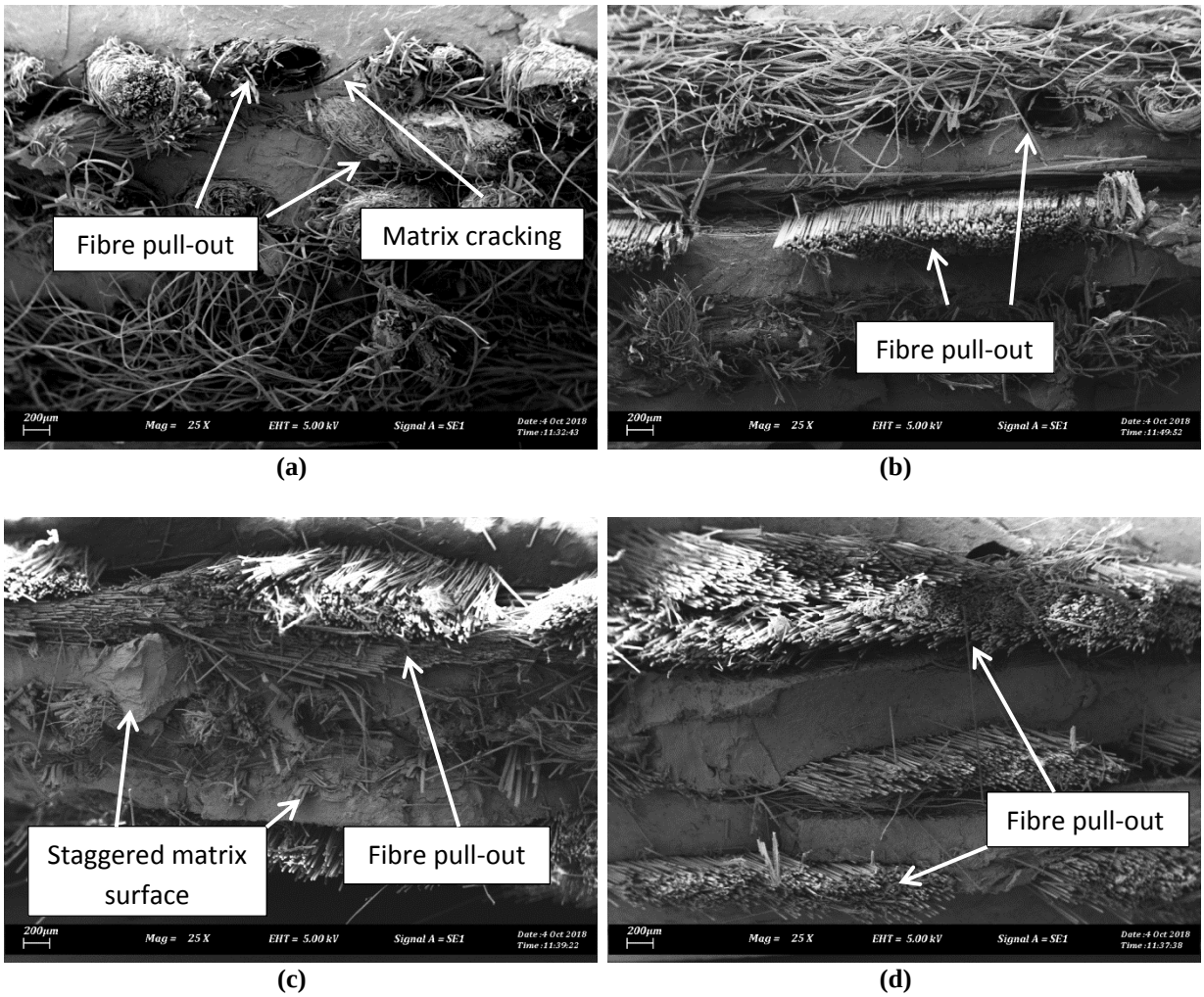

(a) **(b)**

(c) **(d)**

Figure 8: SEM micrograph of each stacking sequence (a) fibres pull-outs in BBB composite (b) banana and glass fibres in BGB composite (c) good adhesion between fibre and matrix of GBG composite (d) glass fibres in GGG composite.

4. CONCLUSION

Tensile, flexural and quasi-static indentations of hybrid banana / glass fibres in different stacking sequences were investigated. The tensile, flexural and quasi-static indentation properties were compared between hybrid and non-hybrid composites. The highest tensile strength was achieved by non-hybrid GGG composite with 191.27 MPa, which is 392.96% higher than non-hybrid BBB composite. Incorporation of glass fibres in the banana fibre reinforced composite showed enhancement of 302.27% and 123.12% for GBG and BGB respectively. The highest flexural strength was observed for hybrid composite GBG with 81.65 MPa, which is 21.32% higher than hybrid BGB. The highest energy absorbed is seen in the non-hybrid GGG composite with 46.14 kJ, which is 249.81% higher than non-hybrid BBB composite. The hybrid GBG composite had 32.30 kJ, which is 92.03% higher than hybrid BGB. Based on the results, the hybrid banana / glass fibres showed better mechanical properties with the incorporation of glass fibres, especially in flexural properties.

ACKNOWLEDGEMENT

The authors would like to thank Universiti Teknikal Malaysia Melaka (UTeM) for the continuous support given this research project. The authors also wish to express their gratitude to the Ministry of Education for the grant FRGS/1/2017/STG07/FKM-CARE/F00339.

REFERENCES

Agarwal, R., Saxena, N.S., Sharma, K.B., Thomas, S. & Pothan, L.A. (2003). Thermal conduction and diffusion through glass-banana fiber polyester composites. *Indian J. Pure Ap. Phy.*, **41**: 448–452.

Alavudeen, A., Rajini, N., Karthikeyan, S., Thiruchitrambalam, M. & Venkateshwaren, N. (2015). Mechanical properties of banana / kenaf fiber-reinforced hybrid polyester composites : Effect of woven fabric and random orientation. *Mater. Design*, **66**: 246–257.

Amir, N., Abidin, K.A.Z. & Shiri, F.B.M. (2017). Effects of fibre configuration on mechanical properties of banana fibre / PP / MAPP natural fibre reinforced polymer composite. *Procedia Eng.*, **184**: 573–580.

Arthanarieswaran, V. P., Kumaravel, A. & Kathirselvam, M. (2014). Evaluation of mechanical properties of banana and sisal fiber reinforced epoxy composites : Influence of glass fiber hybridization. *Mater. Design*, **64**: 194–202.

Baillie, C. (2005). *Green Composites: Polymer Composites and the Environment*. CRC Press, Boca Raton, Florida.

Bhatnagar, R., Gupta, G. & Yadav, S. (2015). A review on composition and properties of banana fibers. *Int. J. Sci. Eng. Res.*, **6**: 49–52.

Boopalan, M., Niranjanaa, M. & Umapathy, M.J. (2013). Study on the mechanical properties and thermal properties of jute and banana fiber reinforced epoxy hybrid composites. *Compos. Part B Eng.*, **51**: 54–57.

Dan-mallam, Y., Hong, T.W. & Abdul Majid, M. S. (2015). Mechanical characterization and water absorption behaviour of interwoven kenaf / PET fibre reinforced epoxy hybrid composite. *Int. J. Polym. Sci.*, **Vol. 2015**: 1–13.

Dhar Malingam, S., Jumaat, F.A., Ng, L.F., Subramaniam, K., & Ab Ghani, A.F. (2018a). Tensile and impact properties of cost-effective hybrid fiber metal laminate sandwich structures. *Adv. Polym. Tech.*, **37**: 2385–2393.

Dhar Malingam, S., Ng, L. F., Chan, K. H., & Subramaniam, K. (2018b). The static and dynamic mechanical properties of kenaf/glass fibre reinforced hybrid composites. *Mater. Res. Express*, **5**: 095304.

Haneefa, A., Bindu, P., Aravind, I., & Thomas, S. (2008). Studies on tensile and flexural properties of short banana/glass hybrid fiber reinforced polystyrene composites. *Compos. Mater.*, **42**: 1471–

1489.
Haque, M.M. & Hasan, M. (2016). Mechanical properties of betel nut and glass fibre reinforced hybrid polyethylene composites. *Int. J. Auto. Mech. Eng.*, **13**: 3763-3772.
Heckadka, S.S., Nayak, S.Y., Vishal, S.P. & Amin, N.M. (2018). Evaluation of flexural and compressive strength of E glass/jute and E glass/banana hybrid epoxy hollow composite shafts. *Key Eng. Mater.*, **777**: 438–445.
Herrera-Franco, P. & Valadez-Gonzalez, A. (2004). Mechanical properties of continuous natural fibre-reinforced polymer composites. *Compos. Part A Appl. Sci. Manuf.*, **35**: 339–345.
Jawaid, M., Abdul Khalil, H.P.S. & Abu Bakar, A. (2011). Woven hybrid composites: Tensile and flexural properties of oil palm-woven jute fibres based epoxy composites. *Mater. Sci. Eng. A.*, **528**: 5190–5195.
Joseph, P.V, Joseph, K. & Thomas, S. (1999). Effect of processing variables on the mechanical properties of sisal fiber-reinforced polypropylene composites. *Compos. Sci. Technol.*, **59**: 1625–1640.
Kretsis, G. (1987). A review of the tensile , compressive , flexural and shear properties of hybrid fibre- reinforced plastics. *Composites*, **18**: 13–23.
Kumar, N.R., Prasad, G.R. & Rao, B.R. (2013). Investigation on mechanical properties of banana fiber glass reinforced hybrid thermoplastic composites. *Int. J. Eng. Res. Technol.*, **2**: 3701–3706.
Maddah, H.A. (2016). Polypropylene as a promising plastic: A review. *Am. J. Polym. Sci.*, **6**: 1–11.
Mohammed, L., Ansari, M.N., Pua, G., Jawaid, M. & Islam, M.S. (2015). A review on natural fiber reinforced polymer composite and its applications. *Int. J. Polym. Sci.*, **Vol. 2015**: 1–15.
Navaneethakrishnan, G., Selvam, V. & Julyes, S.J. (2015). Development and mechanical studies of glass/banana fiber hybrid reinforced silica nano particles with epoxy bio-nanocomposites. *J. Chem. Pharm. Sci.*, **Vol. 2015**: 197–199.
Parandaman, P. & Jayaraman, M. (2015). Experimental investigation on the mechanical properties of jute/sisal/glass and jute/banana/glass hybrid composite materials. *Euro. J. Appl. Sci.*, **7**: 138–144.
Paul, S. A., Boudenne, A., Ibos, L., Candau, Y., Joseph, K. & Thomas, S. (2008). A effect of fiber loading and chemical treatments on thermophysical properties of banana fiber / polypropylene commingled composite materials. *Compos. Part A Appl. Sci. Manuf.*, **39**: 1582–1588.
Rahman, M., Das, S., & Hasan, M. (2018). Mechanical properties of chemically treated banana and pineapple leaf fiber reinforced hybrid polypropylene composites. *Adv. Mater. Proc Technol.*, **4**: 527–537.
Razali, N., Sultan, M.T.H. & Jawaid, M. (2017). A review on detecting and characterizing damage mechanisms of synthetic and natural fiber based composites. *BioResources*, **12**: 9502–9519.
Rodriguez, L. ., Cardona, C.A. & Orrego, C.E. (2016). Water uptake, chemical characterization, and tensile behavior of modified banana–plantain fiber and their polyester composites. *Polym. Compos.*, **37**: 2960–2973.
Saba, N., Tahir, P. M., & Jawaid, M. (2014). A Review on Potentiality of Nano Filler/Natural Fiber Filled Polymer Hybrid Composites. *Polymers*, ***6***(8), 2247–2273.
Samal, S.K., Mohanty, S. & Nayak, S.K. (2009). Banana / glass fiber-reinforced polypropylene hybrid composites : Fabrication and performance evaluation. *Polym. Plast. Technol. Eng.*, **48**: 397–414.
Sathish, P., Kesavan, R. & Ramnath, B.V. (2015). Effect of fiber orientation and stacking sequence on mechanical and thermal characteristics of banana-kenaf hybrid epoxy composite. Silicon, **9**: 577–585.
Saw, S. K., Sarkhel, G. & Choudhury, A. (2011). Dynamic mechanical analysis of randomly oriented short bagasse/coir hybrid fibre-reinforced epoxy novolac composites. *Fiber Polym.*, **12**: 506–513.
Sreekala, M. S., George, J., Kumaran, M.G. & Thomas, S. (2002). The mechanical performance of hybrid phenol-formaldehyde-based composites reinforced with glass and oil palm fibres. *Compos. Sci. Technol.*, **62**: 339–353.
Srinivasan, V.S., Boopathy, S.R., Sangeetha, D. & Ramnath, B.V. (2014). Evaluation of mechanical and thermal properties of banana–flax based natural fibre composite. *Mater. Design*, **60**: 620–

627.
Subramaniam, K., Dhar Malingam, S., Feng, N.L. & Bapokutty, O. (2017). The effects of stacking configuration on the response of tensile and quasi-static penetration to woven kenaf/glass hybrid composite metal laminate. *Polym. Composite*, **40**: 568–577.
Subramonian, S., Ali, A., Amran, M., Sivakumar, L., Salleh, S. & Rajaizam, A. (2016). Effect of fiber loading on the mechanical properties of bagasse fiber – reinforced polypropylene composites. *Adv. Mech. Eng.*, **8**: 1-5.
Thiruvasagam, C., Harish, R., Tamilarasan, S., Venkatesh, G. & Vimalathithan, K. (2016). Evaluation of mechanical properties of banana fiber – jute – glass fiber reinforced polyester composite. *Int. J. Inno. Res. Sci. Eng. Technol.*, **2**: 29–37.
Venkatasubramaniam, H., Chaithanyan, C., Raghuraman, D.S. & Panneerselvam, T. (2014). Evaluation of mechanical properties of abaca-glass-banana fiber reinforced hybrid. *Int. J. Inno. Res. Sci. Eng. Technol.*, ***3***(1), 8169-8177.
Wallenberger, F.T., Watson, J.C. & Li, H. (2001). Glass Fibers. ASM International, Materials Park, Ohio.

SOUND INSULATION PERFORMANCE OF KENAF FIBRE AS A NOISE CONTROL TREATMENT IN CAR USING STATISTICAL ENERGY ANALYSIS

Norzailan Azahari[*1], Azma Putra[2], Reduan Mat Dan[2] & Muhammad Nur Othman[2]

[1]Fakulti Kejuruteraan Mekanikal
[2]Centre for Advanced Research on Energy
Universiti Teknikal Malaysia Melaka (UTeM), Malaysia

[*]Email: M041620009@student.utem.edu.my

ABSTRACT

Low noise level in car cabin has always become an important target for automotive manufacturers. If low exterior noise is bounded by environmental regulation, low interior noise is subjected to customer's satisfaction, which thus offers a competitive advantage in the automotive industry. Common noise control treatment in car cabin is by applying sound absorbing materials attached to various vehicle components such as floor, roof and door panel. In this paper, the study is presented to discuss the performance of natural fibres as the noise control treatment materials. A three-dimensional plate attached with natural fibres namely kenaf, coir, oil palm and ijuk was simulated using VA-One and the sound transmission loss calculated based on the statistical energy analysis method is presented. The performances are then compared to that of felt materials, usually used in the current commercial vehicles. Parametric simulation was then conducted to study the effect of various designed parameters of the natural materials such as the thickness and flow resistivity. The methodology is presented and the results are discussed.

Keyword: *Transmission loss; statistical energy analysis (SEA); kenaf; parameters; natural fibre.*

1. INTRODUCTION

Towards green technology, natural fibres have been extensively studied as substitute materials to the existing synthetic materials which can be harmful to the environment in a long period. Natural fibres are gaining popularity, not only because of their non-toxic nature, but also their performances, such as structural integrity, thermal conductivity and sound absorption (Asdrubali *et al*., 2012).

One of the natural fibres which has been extensively studied is extracted from kenaf, where this plant has been cultivated in many countries including Malaysia. The fibres come from its stem, which consist of long bast fibres and short fine fibres. These fibres are used from engineering composite to pack materials (Khalil *et al.,* 2010). Tan *et al*., (2016) found that coir, kenaf, and kapok fibre could be used as the acoustical panels for the reduction of noise. Recently, Ying *et al.* (2016, 2018) showed that kenaf fibre also has excellent performance as sound absorber materials. Figure 1 shows the kenaf fibres compressed in the form of mat.

The objective of this paper is to study the sound transmission loss (TL) of the kenaf fibre to observe its feasibility as the noise control treatment (NCT) material in cars. The TL is calculated using Statistical Energy Analysis (SEA) technique in VA-One software. A three-dimensional SEA model of a rectangular plate is created together with a layer having material properties of kenaf fibres attached to the plate. The results of TL by varying the parameters of the kenaf layer are discussed in this paper.

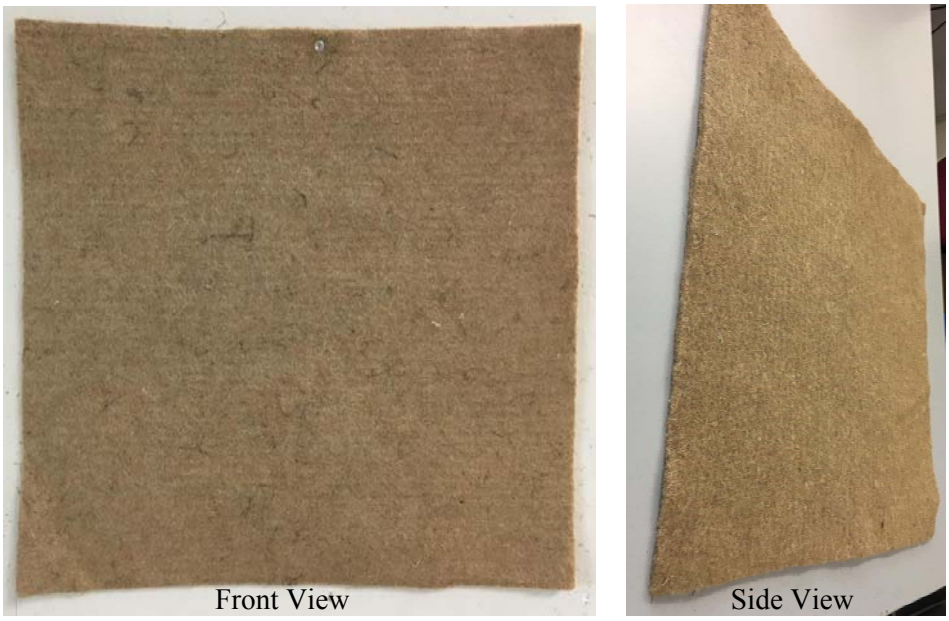

Figure 1: Kenaf fibre in the form of mat.

Figure 2 shows the common noise propagation from the source room to the receiver room. The noise transmitted to the receiver room can be either directly through air or can be through the vibration of structures, which produces noise radiation. The former is called airborne noise and the latter is called structure-borne noise. If the vibration of the partition of the room (which causes noise radiation to the receiver room) is due to the excitation of sound from the source room, the noise is called indirect airborne noise.

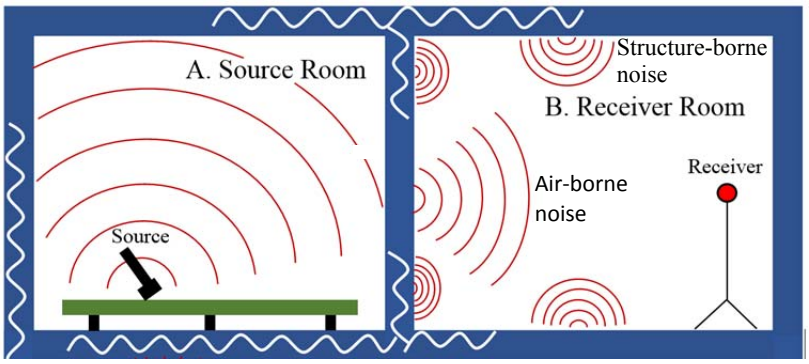

Figure 2: Sound transmission paths between a source and receiver room.

Sound transmitted through of a partition is categorised as the indirect airborne noise. Figure 3 shows the illustration of sound transmission through a partition. The sound waves produced in the source room strikes the partition where the sound energy is partially absorbed by the partition (due to damping), some energy is transmitted into the receiver room and the rest is reflected back into the source room. The sound transmission loss (TL) can be defined as the decrease of sound energy when it is transmitted.

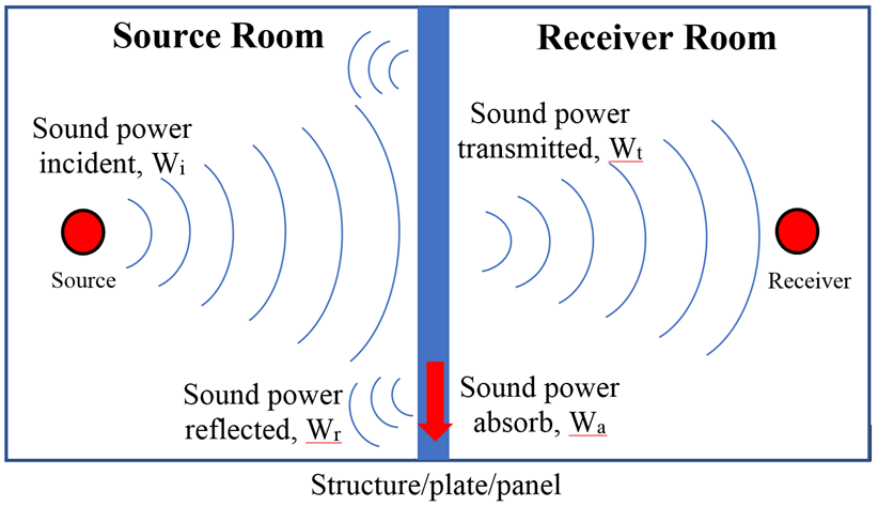

Figure 3: Basic concept of sound transmission through a partition.

Sound transmission loss (TL) is given by

$$TL = 10 \log \frac{W_i}{W_t} \tag{1}$$

where W_i denoted as the incident sound power and W_t denoted as the transmitted sound power. The incident sound power assuming the source room forms a diffuse field is given by,

$$W_i = \frac{\bar{P}^2}{4\rho c}(S) \tag{2}$$

where $\bar{p}^2$ is the mean sound pressure, ρ is the density of air (1.21 kg/m3) and c is the speed of sound in the air (343 m/s) and S is the surface area excited by the sound.

Theoretically, the TL of a partition can be divided into four regions as shown in Figure 4. The first region is the stiffness-controlled region at very low frequencies, where it is the stiffness of the panel which determines the level of TL. The second region is resonance-controlled region at low to medium frequencies. In this region, the response is identified by the static stiffness of the panel. Resonance can also occur depending on the internal damping in the panel which decreases the TL. The third region is the mass-controlled region, where the response is governed by the mass of the panel and the curve follows a typical 6 dB/octave slope. By doubling the mass of the panel, the TL increases by 6 dB. The fourth region is the coincidence region at high frequencies the acoustic wavelength is the same as the structural wavelength.

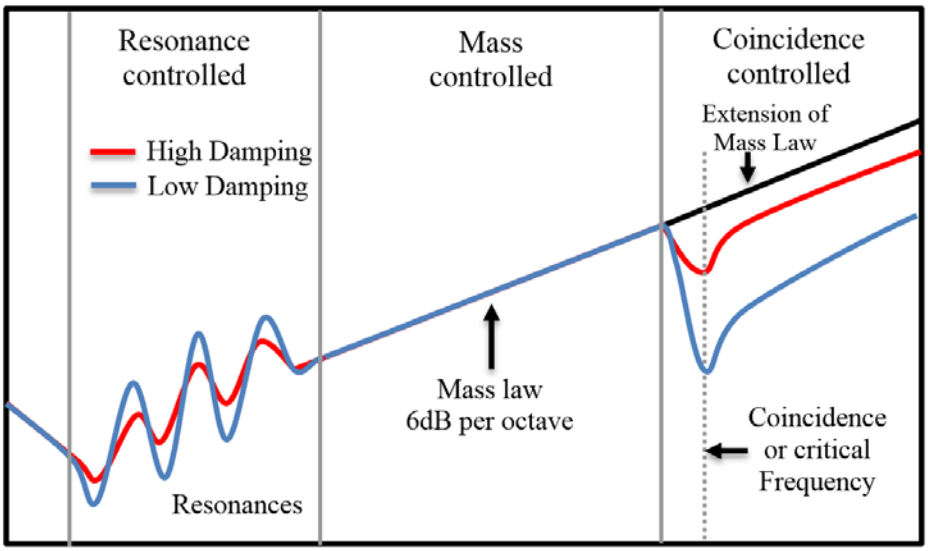

Figure 4: Theoretical TL for an isotropic plate.

2. METHODOLOGY

2.1 Model of SEA Plate

The Statistical Energy Analysis (SEA) was first introduced in 1959 and has been extensively used to predict the transmission of acoustic and vibration of complex structures, especially in a motor vehicle. The method breaches the structures into sub-systems consisting of plates, beams and cavity, and each of this subsystem acts as an energy reservoir. The SEA assumes that each subsystem must store energy with sufficient modal energy density so that statistical average at high frequencies is valid (Lyon, 1975). The subsystem must be dominated by the reverberant field and the direct field is neglected (Putra *et al*., 2015). To fulfil this requirement, the SEA is only valid when the propagating acoustics or vibration wavelength is much smaller than the dimension of the structure. Recently, a hybrid FE-SEA was proposed to accommodate the presence of low modal density structures and thus covers the analysis from low-to-high frequencies (Shorter & Langley, 2005).

In this study, a three-dimensional model of a rectangular plate is constructed in VA-One with an aluminium plate of dimensions 10 cm x 10 cm and thickness of 5 mm. The SEA cavities (dimensions of 10 cm x 10 cm x 10 cm) are applied to both side of the plate as the storage for the sound energy, representing source and the receiver subsystems. The diagram is shown in Figure 5.

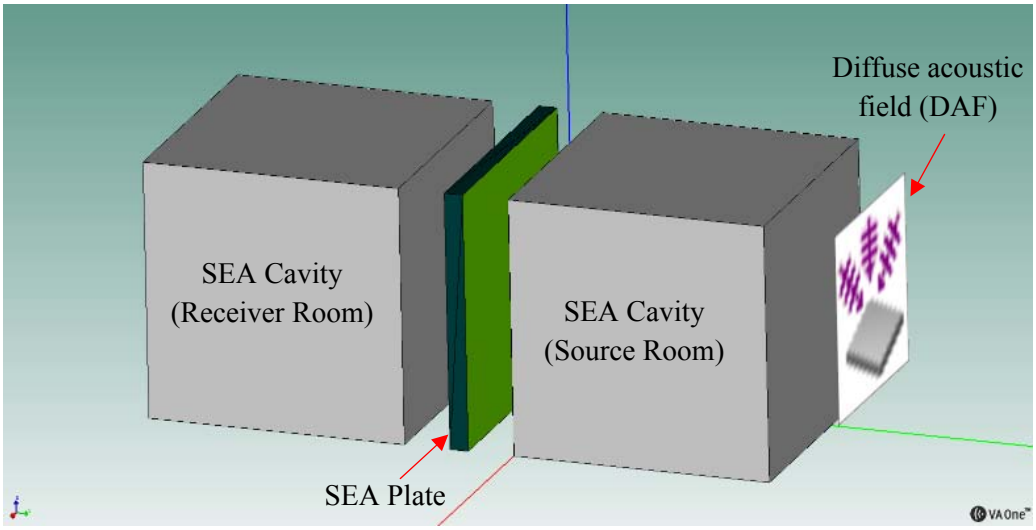

Figure 5: The SEA model of sound transmission loss of a rectangular plate.

The plate facing the source cavity is excited with a diffuse acoustic field (DAF) of 1 Pa sound pressure (as in Eq. (2)), which represents a diffuse acoustic pressure load acting over the surface area of a subsystem. The maximum solving frequency is set to 6 kHz. Coupling linkages between the SEA plate and SEA cavities (i.e. the contact area) are set with SEA area junction to represent the area of acoustic energy transmission between SEA plate and a SEA acoustic cavity.

2.2 Application of Natural Fibre to SEA Plate

Noise Control Treatment (NCT) material is defined as a single or multi-layered material attached to the surfaces of the SEA plate to absorb or to block the incoming sound energy. In this simulation, the natural fibre is applied to the receiver side of the SEA plate as shown in Figure 6. This simulates the NCT of a car body, where felt materials are applied in the inner side of the car body panels as the interior sound absorber and also to reduce the noise transmission from the exterior.

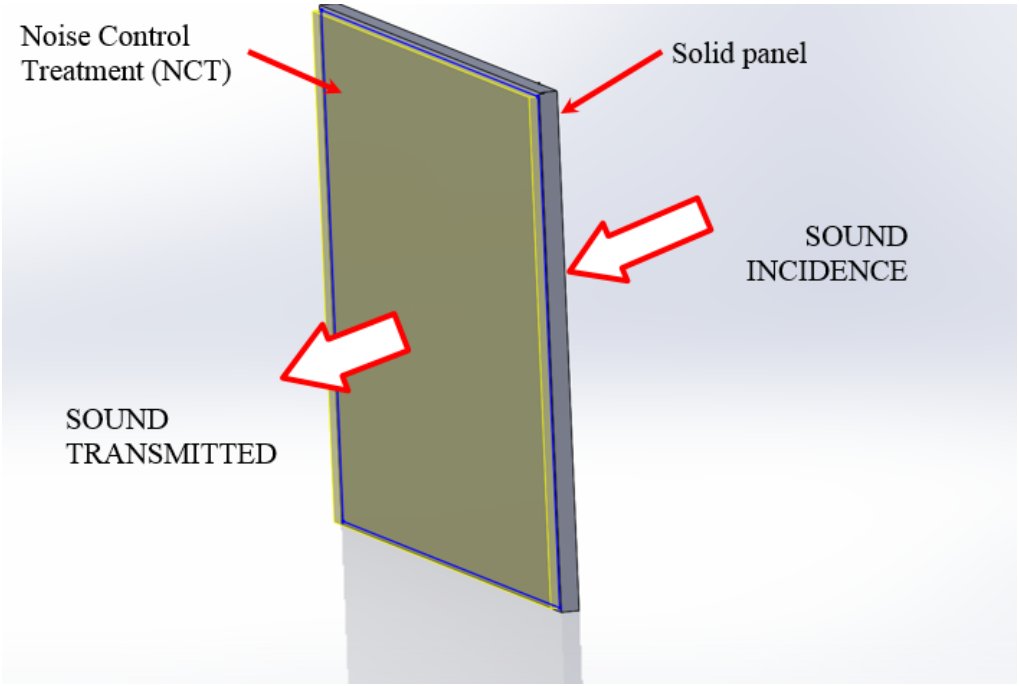

Figure 6: NCT attached to the SEA plate.

The NCT materials can provide substantial local subsystem damping when they are applied on a panel. They can affect: (i) the mass and stiffness (or reactive impedance) of the panel and (ii) the energy flows that occur between panel and any adjacent acoustic cavity subsystem.

This study is to simulate the performance of sound insulation of the kenaf fibre. Before the discussion is focused on the kenaf, performances of other natural fibres are presented. Table 1 lists the properties of the natural fibres, namely kenaf, coir, oil palm and ijuk extracted from existing studies. This includes the felt used as the baseline for the TL. The density can be seen to be different for each material.

Table 1: Material properties of natural fibres.

Item	Unit	Felt	Kenaf	Oil palm mesocarp	Ijuk	Coir
Density, ρ	kg/m^3	50	40	247	300	821
Flow Resistivity, σ	N.s/m^4	40000	6215	37415	11383	1359
Porosity, $\emptyset$	-	0.92	0.99	0.85	0.85	0.89
Tortuosity, α	-	1.50	1.05	1.09	1.09	1.06
Viscous Characteristic Length, Λ	μm	56	68	97.81	70	133.5
Thermal Characteristic Length, Λ'	μm	122	177	195.62	180	266.9
Reference	-	VA One (2015)	Shravage (2009)	Latif *et al.* (2016)	Sambu *et al.* (2016)	Jailani *et al.* (2010)

2.3 Simulation of Natural Kenaf Fibre as NCT Material in Car Interior

Transmission of noise from the engine, tyre and other exterior noise into the car cabin directly depends on the treatment applied to the car body as illustrated in Figure 7. This includes the acoustic trim materials and also the damping layer to the body panel. In the market, most car manufacturers use synthetic fibres, known as felt as the NCT as well as for the interior design of a car cabin.

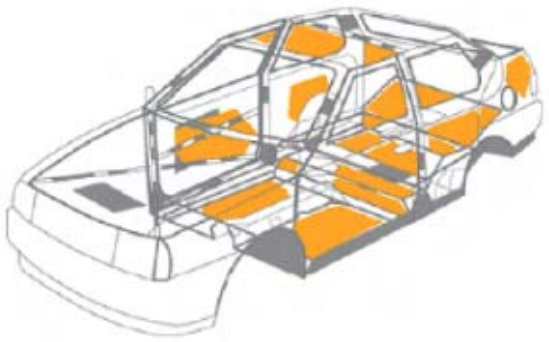

Figure 7: Locations of damping treatment in a car body (Furukava *et al.*, 2009).

In this study, a simulation is performed where kenaf fibre is used as the NCT material in a car. Figure 8 shows the 3D model of the car designed in the VA One software. The car body is divided into plates/shells representing the floor, dash, roof, windows, doors and firewall. The properties are listed in Table 2. The interior was subdivided into acoustic spaces where they are classified into front cavity and rear cavity.

The material properties of Kenaf and Felt can be seen in Table 1. In the simulation, Kenaf was replaced in the position of Felt to study the sound absorption of both materials and placed in floor, roof, firewall, door and window's frame.

Sound excitation using diffuse acoustic field (DAF) is applied on the outer surface of the firewall to represent the noise from the engine, on the floor to represent the noise from tires and on the side door and windscreen to represent the wind noise. The sound pressure level (SPL) in the front cavity and rear cavity is calculated. The results are compared for the case where no NCT is applied (white body)

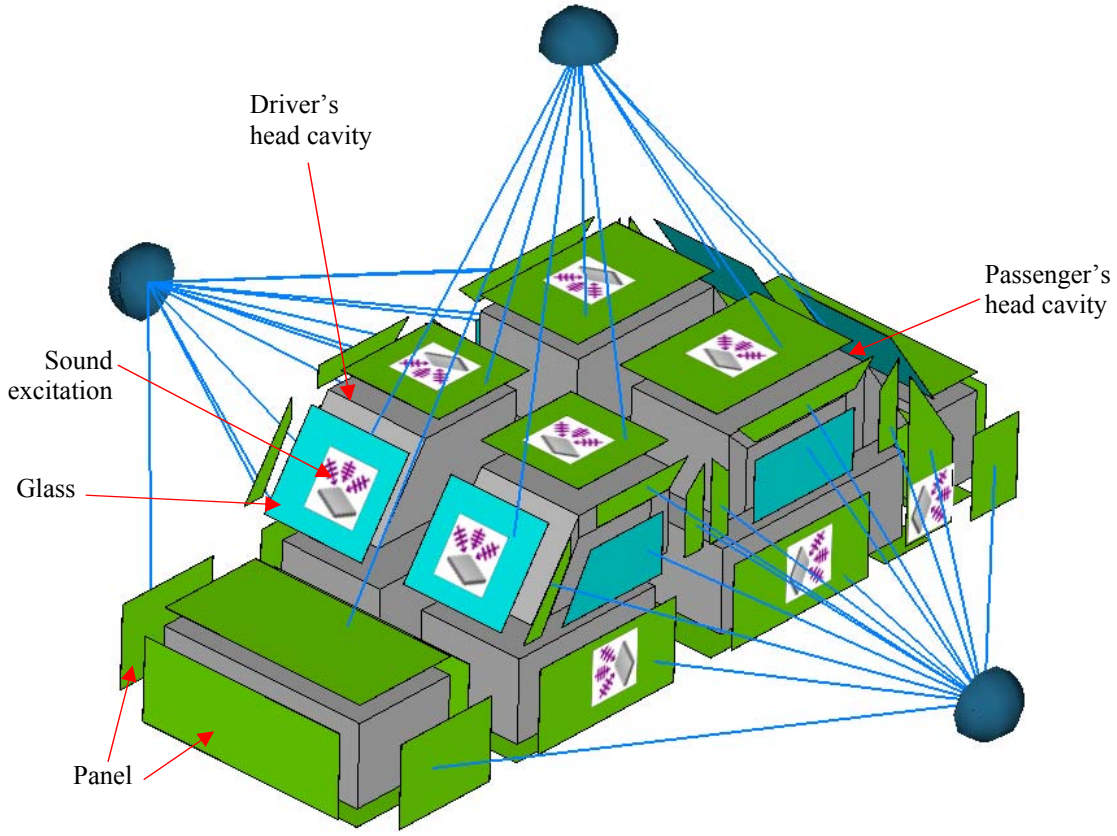

Figure 8: The 3D car model of SEA subsystems in VA One (shrink mode).

Table 2: Properties of car panels in VA One.

Structure	Material	Thickness (mm)
Roof panel	Steel	1
Floor panel	Steel	1
Door panel	Steel	1
Pillars	Steel	1
Glass panel	Glass	1.5

3. RESULTS AND DISCUSSION

3.1 The Simulated Transmission Loss of SEA Plate

Figure 10 shows the TL of the SEA panel obtained for five different fibres as listed in Table 1. All fibre layers are simulated with the same thickness of 5 mm. It can be seen that the TL of the plate increases when NCT materials are applied to the plate. The felt material can be seen to have superior insulation performance. Here, only the oil palm fibres have similar TL with that of the felt material. From Table 1, although both materials have different density, they have similar flow resistivity and are the greatest among other fibres. The direct relationship between the density of the fibrous material and its flow resistivity is given by

$$R = A\rho B \tag{3}$$

where ρ denoted as mass density of the material (mass per unit of volume) and A and B are the coefficients which depend on the type of the fibres.

Figure 10 shows the coincidence frequency of the panel can be seen to be at 1.6 kHz, which is the critical frequency of the 5 mm aluminium panel (see again Figure 4). The effect of different fibres can be observed to mostly affect at above the coincidence frequency, with almost no significant difference at the mass-controlled region below 1.6 kHz. This due to the weight of the fibres which is much smaller compared to weight of the aluminium panel. The effect of porosity and flow resistivity are discussed in the next sections and the focus is only for the kenaf fibres to observe the potential of this material for the future NCT in automotive.

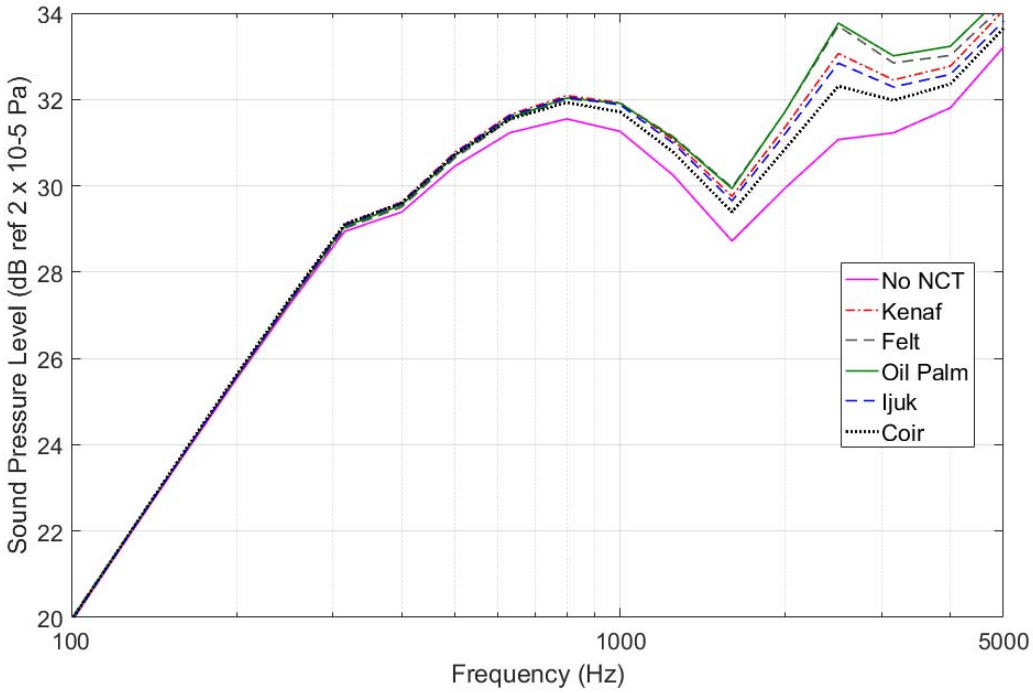

Figure 10: Results of TL of the SEA plate with noise control treatment of various fibres (based on data in Table 1 and with 5 mm thick).

3.2 Parametric Study of Kenaf fibres as NCT

Based on the designed model, the felt material used in automotive is set as the baseline performance and the sound insulation performance of the proposed natural kenaf material is compared against that of the felt. This study includes the NCT thickness, flow resistivity, porosity and tortuosity. Shravage *et al*., (2010) shows that flow resistivity, porosity and tortuosity are one of the most important parameters of acoustic behaviour of the porous material compare to elastic parameters which does not affected the acoustic behaviour of the poroelastic materials.

3.2.1 Effect of Thickness

The average thickness of the felt in automotive used was roughly 5.0 mm. To study the thickness effect on the STL of the plate, the analysis was performed using three different thickness of the kenaf fibres; 5.0 mm, 7.0 mm and 9.0 mm. In Figure 11, it can be seen that with additional of 2 mm fibre thickness (total thickness of 7 mm), the TL of the kenaf fibres can have the same performance to that of the felt for the frequency range from 100 Hz to 5 kHz.

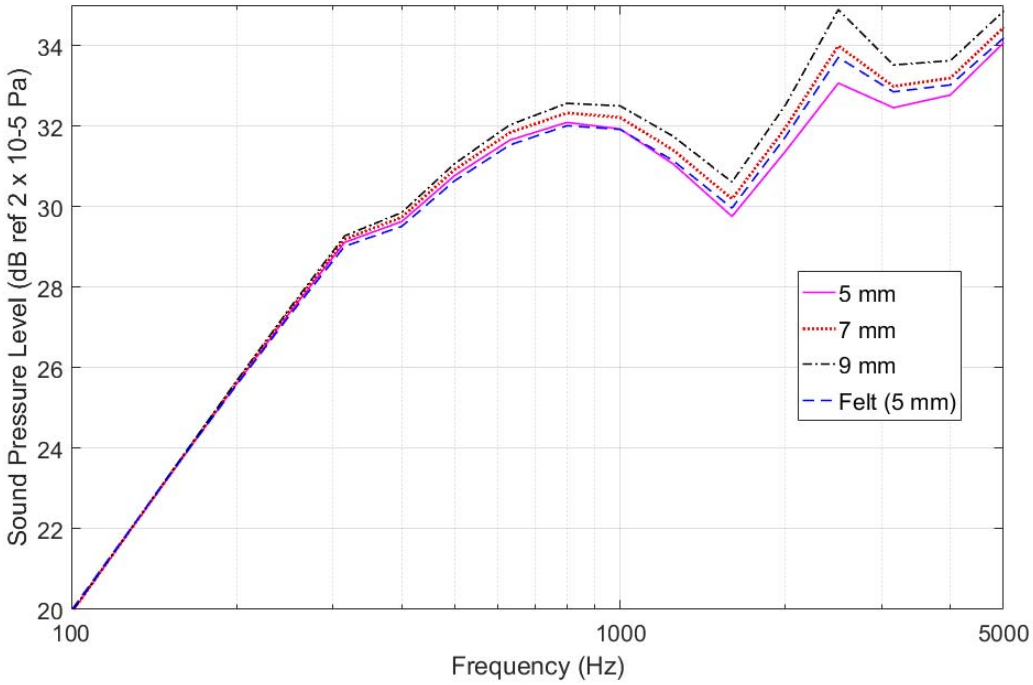

Figure 11: Effect of thicknesses on sound transmission loss.

The data use the same density of fibres, i.e. 40 kg/m^3, which means by increasing the thickness, more fibres are added to maintain the density. In this way, increasing the thickness means increasing the mass, and thus improvement at mass law region can thus be observed below 1.6 kHz.

Tan *et al*., (2016) also showed in their study that the most effective way to enhance the transmission loss of fibrous panel is by increasing the mass of the fibres.

3.2.2 Effect of Flow Resistivity

The flow resistivity can be defined as the viscous resistance to the steady flow of air in the acoustic material. Shravage *et al*., (2010) studied about the effect of flow resistivity on absorption and transmission loss of the poroelastic materials. Their study shows that by increasing the flow resistivity

up to a certain value, significant increase in sound absorption coefficient is obtained in the mid-frequency range and as well as in the TL.

In this study, flow resistivity of the material is varied from 6,215 to 40,000 N.s/m^4, while other parameters are kept constant. From Figure 12, it can be observed that by increasing the flow resistivity, the improvement is only effective above the coincidence frequency (above 1.6 kHz), while almost no improvement at the mass law region . The lower frequency can easily pass the through the fibre (the incoming acoustic wavelength is larger than the thickness of the panel), while the higher frequencies have greater resistance inside the fibre.

As the flow resistivity is proportional to the density of the fibres (Eq. (3)), the results above 1.6 kHz is consistent with those in Figure 11. The negligible effect obtained below 1.6 kHz is because the panel thickness is kept constant at 5 mm.

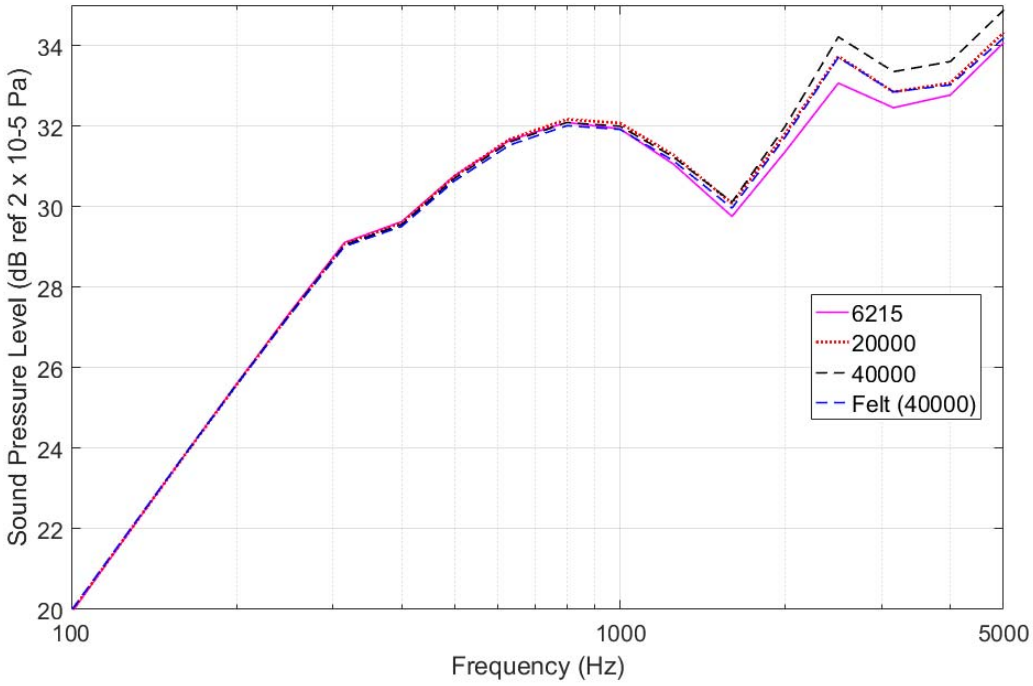

Figure 12: Effect of flow resistivity of kenaf fibres on sound transmission loss.

3.2.3 Effect of Porosity

The porosity refers to the degree of pores in the panel. As also observed by Shravage *et al*., (2010), the porosity has more influence on the TL at mid to high frequencies. The TL increases with increase in porosity.

Porous materials generally have porosity near 0.7-0.9. Here the porosity is varied from 0.5 to 0.9. From Figure 13, the TL improves as the porosity increases. The greater the porosity, the easier the sound penetrates the panel.

Note that the simulation assumes the panel to have a constant bulk density, i.e. constant ratio between the mass of the fibres to the total volume of the panel (including the air in the porous). In practice, increasing the porosity while maintaining the thickness of the panel can reduce the mass of the panel. Meanwhile, increasing the density of the fibres to maintain the mass can reduce the porosity as the fibres become more compact in the panel (Putra *et al.,* 2013).

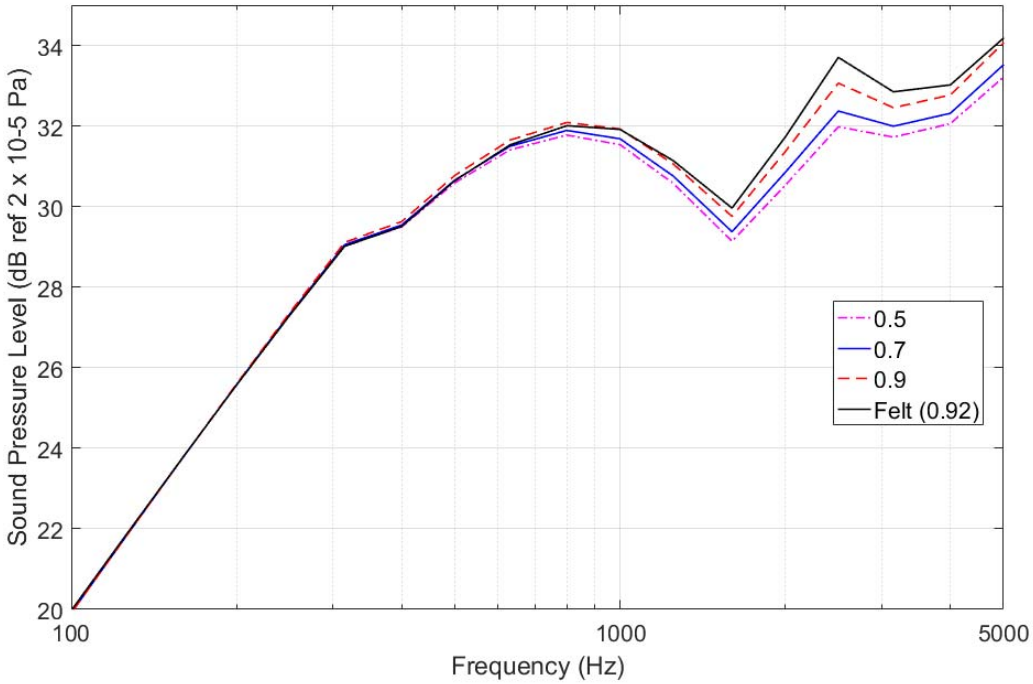

Figure 13: Effect of porosity on sound transmission loss.

3.2.4 Effect of Tortuosity

Tortuosity defines the curliness or complexity of pores of the material, which means the more complex the material path, the more time the sound wave is in contact with the fibres and the more energy dissipation obtained.

In this study, tortuosity of 0.8, 1 and 1.5 are used. In Figure 14, it is shown that the smaller the value of this parameter, the greater the TL. The simulation shown by Shravage *et al*. (2010) indicates the fluctuation of TL as the function of tortuosity values due to resonance and anti-resonance phenomena. The choice of 0.8-1.5 values here may be in the range of where the TL decreases as the tortuosity increases.

The difference of TL compared to the TL of felt is however is not significant as in Figure 14. The TL difference is almost negligible below 2 kHz, and only differs by less than 1 dB above 2 kHz.

3.3 Effectiveness of Kenaf Fibre as NCT

In this simulation, the performance of the kenaf and felt layer as the sound insulator is compared in terms of the sound energy built up in the car cabin due to the input of sound excitation from the exterior. Besides the sound energy is reduced due to insulation, it is also damped due to the sound absorption from the layer. The absorption coefficient for the felt is obtained from the study of Ricciardi & Lenti (2010) and for the kenaf is from Lim *et al.* (2015).

Figures 15 and 16 show the built-up sound pressure level (SPL) at the driver's and passenger's cavities, respectively. It can be seen that the performance of kenaf layer is almost similar to that of the felt layer, except at around 400 Hz - 1 kHz where the felt outperforms the kenaf by roughly 5 dB in average. This is due to the absorption coefficient of the felt is greater than the kenaf fibre for the frequency above 400 Hz.

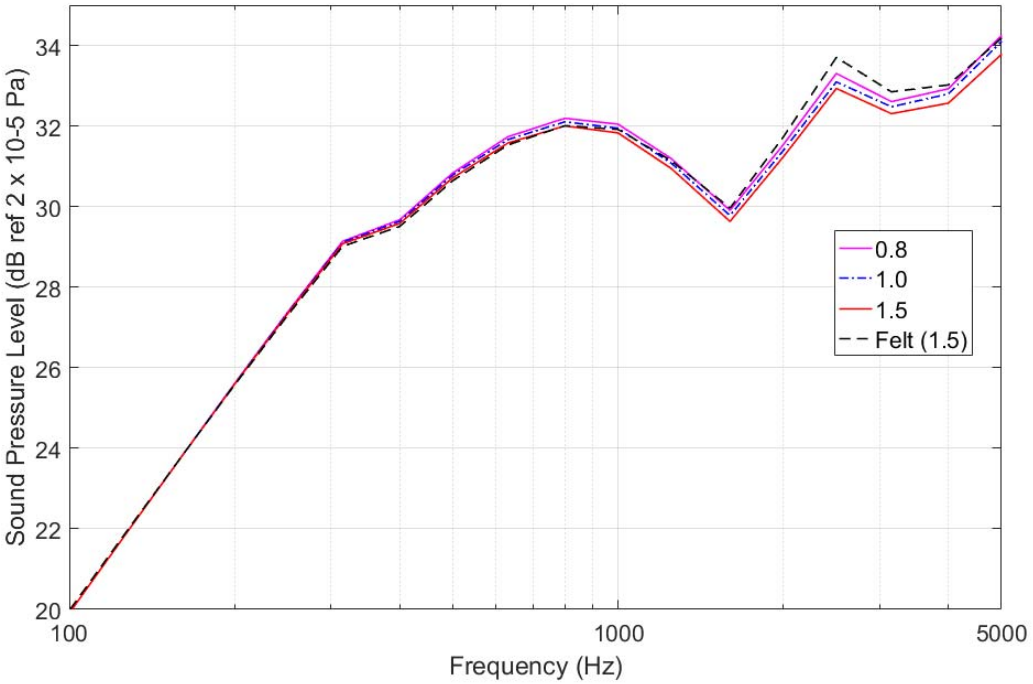

Figure 14: Effect of tortuosity on sound transmission loss.

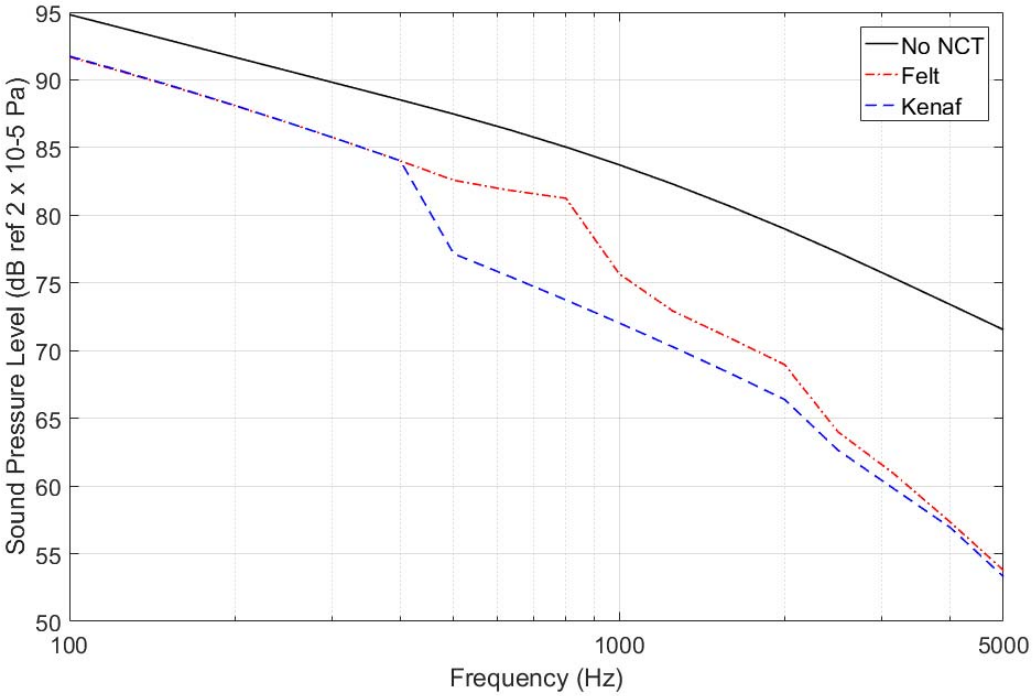

Figure 15: Effect of NCT on front driver cavity.

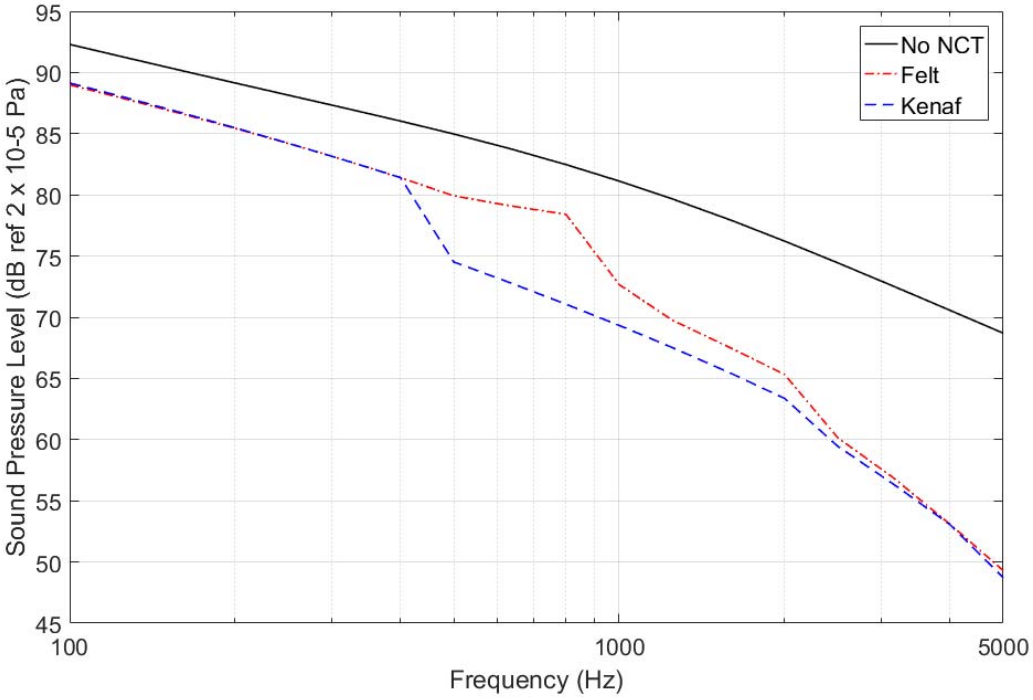

Figure 16: Effect of NCT on rear passenger cavity.

Note that the simulation is modelled with the NCT layer directly attached to the car body panel. In practice, the inner car body consists of other layers of additional steel panel or plastic-like materials before it is finished with felt layer, and thus the built-up SPL should be much lower than those shown in Figure 15 and 16.

The sound excitation in the simulation also assumes diffuse acoustic field with the sound energy level almost constant across the frequency. For the experiment with the input of real engine noise, the engine order of 2X (where X is the frequency related to the engine speed) will be the dominant peak frequency in the SPL spectrum. The transition of the airborne and structure borne sound transmission at frequency 300-500 Hz will also be evidence showing the effectiveness of partition (including NCT materials) to effectively block the airborne noise above this transition frequency (Putra *et al*. 2012).

4. CONCLUSION

The performance of kenaf fibres used as the noise control treatment in a car has been discussed in this paper. The results show that the natural kenaf fibres have a comparable performance with the commercial felt materials. For the same layer thickness, the felt still have greater sound transmission loss, but the difference is only within 1-2 dB with that of the kenaf fibres. The kenaf fibres can outperform the felt by controlling the acoustical parameters of the fibres, particularly by increasing the density of the fibres. This paper presents the initial stage of results for the performance of kenaf fibres as the noise control treatment in a motor vehicle towards utilising green material. The next study can be extended to present the data on the experiment and the treatment of the fibres to have the same quality as of the commercial felt, especially in terms of fire retardancy.

ACKNOWLEDGEMENT

This work is fully supported by research grant from Ministry of Higher Education Malaysia No. FRGS/1/2016/TK03/FTK-CARe/F00323 and collaboration with Proton Sdn Bhd. Acknowledgement is also addressed to ESI Group for the VA-One software.

REFERENCES

Asdrubali, F., Schiavoni, S. & Horoshenkov. K.V. (2012). A review of sustainable materials for acoustic applications. *Build. Acoust.,* **19**:283-312.

Furukava, M., Gerges, S., Neves, M.M., & Coelho, B.J. (2009). Analysis of structural damping performance in passenger vehicles chasis. *J. Acoust. Soc. Am*, **126**:22-80.

Jailani, M., Ayub, M. D., Zulkifli, R., Amin, N. & Hosseini, M. (2010). Effect of compression on the acoustic absorption of coir fibre. *Am. J. Appl. Sci.,* **7**:1285-1290.

Khalil, H. A., Yusra, A. I., Bhat, A. & Jawaid, M. (2010). Cell wall ultrastructure, anatomy, lignin distribution, and chemical composition of Malaysian cultivated kenaf fibre. *Ind. Crops. Prod.,* **31**:113–21.

Latif, H. A., Nizam, M., Zaman, I., Sambu, M., Imran, M. & Nasrul, M. (2016). Acoustical characteristics of oil palm mesocarp. *ARPN J. Eng. Appl. Sci.,* **11**:7670-7676.

Lim, Z.Y., Putra, A., Nor, M.J., & Yaakob, M.Y. (2015). Preliminary study on sound absorption of natural kenaf fibre. *Proc. Mech. Eng. Resear. Day 2015*, pp:95-96.

Lyon, R.H. (1975). *Statistical Energy Analysis of Dynamical Systems. Theory and Applications*. MIT Press, Massachusetts.

Or, K.H., Putra, A. & Selamat, M.Z. (2017). Oil palm empty fruit bunch fibres as sustainable acoustic material. *Appl. Acoust*., **119**: 9-16.

Putra, A., Munir, F. A. & Juis, C. D. (2012). On a simple technique to measure the airborne noise in a car interior using substitution source. *Int. J. Vehicle Noise Vib.*, **8**: 275-287.

Ricciardi, P. & Lenti, M. (2010). Sound absorption characterisation of woven materials. Case study: auditorium restoration. *Proc. 20th Int. Cong. Acoustics*, Sydney, Australia.

Sambu, M., Nizamyahya, M., Latif, H. A., Nasrul, M. & Imran, M. (2016). Acoustical performance and physical properties of nonwoven fibre; Arenga Pinnata (Ijuk) and natural rubbercomposite. *ARPN J. Eng. Appl. Sci.,* **11**:13292-13299.

Shorter, P. J., & Langley, R. S. (2005). Vibro-acoustic analysis of complex systems. *J. Sound Vib.,* **288**: 669-699.

Shravage, P. (2009). Effect of inverted geometric parameters on normal incidence sound absorption and transmission loss, *35th German Annual Conf. Acoustics (DAGA)*, pp: 155-158.

Shravage, P., Jain, S., & Karanth, N. (2010). Effect of intrinsic parameters on sound absorption and transmission loss-A parametric study. Proc. *INTER-NOISE NOISE-CON Cong.*, **2**:664-673.

Tan, W. H., Lim, E. A., Chuah, H. G., Cheng, E. M., & Lam, C. K. (2016). Sound transmission loss of natural fibre panel. *Int. J. Mech. Mech. Eng.,* **16**:33-42.

VA One Software. (2015). *VA One Software*. ESI Group, Paris.

Ying, L.Z., Putra, A., Jailani, M. & Noryani, M. (2016). Sound absorption of multilayer natural coir and kenaf fibres. *Proc. 23rd Int. Cong. Sound Vib.*, Greece.

Ying, L.Z., Putra, A., Jailani, M. J. M. & Yaakob, M. Y. (2018). Sound absorption performance of natural kenaf fibres. *Appl. Acoust.,* **130**:107-114.

PROPERTIES OF ELECTRODEPOSITED NICKEL COBALT COATED MILD STEEL DEVELOPED FROM ALKALINE BATH

Nik Hassanuddin Nik Yusoff[1,2*], Othman Mamat[1] & Mahdi Che Isa[2]

[1]Mechanical Engineering Department, Universiti Teknologi Petronas (UTP), Malaysia
[2]Marine Materials Research Group, Maritime Technology Division (BTM), Science & Technology Research Institute for Defence (STRIDE), Ministry of Defence, Malaysia

[*]Email: hassanuddin@stride.gov.my

ABSTRACT

Nickel-cobalt (Ni-Co) alloy coatings were deposited on mild steel surface from the alkaline bath with triethanolamine as the complexing agent. The effect of cobalt content was investigated on phase structure, surface morphology, mechanical properties and corrosion behaviour of the composite coating. It was observed that the cobalt content in the coatings increased correspondingly with increasing cobalt concentration in the bath. X-ray diffraction (XRD) patterns revealed that peak intensities were significantly varied by adding cobalt in the electrolyte. The phase structure of the deposits was changed from face-centred cubic (FCC) to FCC and hexagonal closed packed (HCP). The crystallite size became smaller at high Co content coatings, which produced smaller grains in their surface morphologies. It was found that higher Co content generated coatings with better microhardness values due to the grain refinement effect by modification of grain size. The adhesion strength of the coatings also increased with high Co content, with the critical load for cracking and chipping increasing with increasing Co content. However, high Co content tends to diminish the corrosion resistance of the coating due to phase structure and grain boundary.

Keywords: *Nickel-cobalt (Ni-Co); alkaline bath; phase structure; surface morphology; mechanical properties.*

1. INTRODUCTION

Electrodeposition is a process of incorporating metals to a substrate using the electrochemical method. The electrodeposition technique offers several advantages, such as precisely controlled near room temperature operation, low energy requirements, capability to coat complex component geometries, low cost, and simple scale-up (Saha & Khan , 2010; Shakoor *et al*., 2014). The ability of the technique to coat various types of materials, such as oxide, nitride, carbide and metallic, in a metal matrix allows it to provide coatings for multiple applications (Bakhit & Akbari, 2013). The advantages of this technique have encouraged researchers to further explore its potentials.

Studies on Ni-Co coating have suggested that the properties of this coating strongly depend on their cobalt content (Srivastava *et al*., 2006; Bakhit & Akbari 2013). Changes in the surface morphology from pyramidal to branch structure and microstructure changes from face-centred cubic (FCC) to hexagonal closed packed (HCP) are the findings reported from cobalt increment (Wang *et al*., 2005; Bakhit, 2015). On the other hand, deposit structure and texture also depends mainly on solution pH (Rafailović & Minić, 2009). The changing of coating microstructure not only influences their mechanical properties, but also their corrosion behaviour as reported by Srivastava *et al*. (2006) and Bakhit & Akbari (2013). Controlling the cobalt content is necessary in order to obtain the best coating performance. The amount of cobalt can be controlled by experimental parameters such as electrolyte composition, nickel cobalt ratio, temperature, agitation, current density and pH (Srivastava *et al*., 2006).

Nickel-cobalt (Ni-Co) is commonly deposited from acid bath, whereby the solution pH is varied between 3.5 to 5 (Tian & Cheng, 2007; Zhang *et al*., 2014). The other applicable method to deposit metal coatings is using an alkaline bath. In the beginning, the alkaline baths were developed from cyanide base chemicals which have been reported to be harmful to human health (Feng *et al*., 2015). The alternative methods were developed to provide the non-cyanide alkaline bath such as pyrophosphate, glucoheptonate, EDTA and others. However, the baths had not been applied commercially since the coatings had bad adhesion to the substrate (Ibrahim & Bakdash 2015). Zn-Fe, Zn-Ni and Fe coatings were widely prepared in alkaline bath (Lan et al., 2006; Long *et al*., 2013; Feng *et al*., 2015). This alkaline bath has been reported to be used for steel parts of complex dimension due to uniform metal distribution in the deposit (Feng *et al*., 2015). However, it is difficult to develop an eco-friendly alkaline bath for the electrodeposition process. Conversely, limited data is available in the literature concerning the properties of Ni-Co coating deposited from the alkaline bath.

In the present work, Ni-Co coatings were deposited from the alkaline bath using triethanolamine (TEA) as a complexing agent. Moreover, the effect of cobalt content was investigated on the coating's microstructure, composition and mechanical properties, including microhardness and adhesion. Simultaneously, the corrosion behaviour of the composite coating was examined using the electrochemistry method in order to estimate the corrosion rate of the substrate. The aim was to produce Ni-Co composite coatings with better mechanical properties and corrosion resistance.

2. EXPERIMENTAL PROCEDURE

The bath composition for electrodeposition processes is listed in Table 1. Samples were prepared with five different Ni and Co concentrations, with the total concentration of active species (Ni^{2+} and Co^{2+}) being 0.5 M. The substrate was prepared from 5 cm^2 of ASTM A36 mild steel plates, polished to a mirror finish surface by different grades of abrasive paper from 1,000 to 2,400, degreased with 20 wt% sodium hydroxide (NaOH) solution in ultrasonic bath for 5 min, then activated with 20 wt% hydrochloric acid (HCl) for 60 s. These were used as cathodes, which were weighed before and after electrodepositing. A pure nickel plate was used as an anode. The required pH of the bath was adjusted by 10 wt% hydrogen sulphate (H_2SO_4) solution. A hot plate that was equipped with a mechanical stirrer was used for bath agitation and temperature control.

Table 1: The bath composition for electrodeposition process.

Bath composition and process parameters	Value
$NiSO_4.6H_2O$	0.45, 0.4, 0.35, 0.3, 0.25 M
$CoSO_4.7H_2O$	0.05, 0.1, 0.15, 0.2, 0.25 M
Triethanolamine (TEA)	1 M
K_2CO_3	0.7 M
$Na_4P_2O_7.10H_2O$	0.1 M
pH	9-10
Current density	50 mA/cm^2
Temperature	50 $^{\circ}$C
Agitation speed	400 rpm

The phase compositions of the coating was characterised using a Bruker AXS X-ray diffractometer (XRD). The XRD patterns were obtained using CuKα radiation. The diffraction data was collected over a 2θ range of 0 to 80° with a step width of 0.04° and a counting time of 1s per step. The crystallite size of the coating was calculated using the Scherrer equation (Zhao *et al*., 2015):

$$D = k\lambda / \beta cos\theta \quad (1)$$

where D is the average grain size of the coatings, β is the full width at the half maximum intensity (FWHM), θ is the reflectance angle and k is the shape factor. The surface morphologies of the deposits were studied using a Phenom Pro scanning electron microscope (SEM) equipped with energy dispersive X-ray analyser (EDX) for elemental analysis. To measure the microhardness of the coatings, a HMV-2T Shimadzu microhardness tester was used with indentation load of 0.25 N and indentation time of 10 s. The average value of ten different measurements was reported as the microhardness of the coating.

The adhesion of the deposits was measured using a scratch tester (DUCOM, DUCOM Instruments Pvt. Ltd., Bangalore, India). The scratch load was increased from 1 up to 180 N with a loading rate of 2 N/mm, strike length of 9 mm and speed on 0.1 mm/s. The image of the wear track after testing was examined using SEM.

The electrochemical corrosion test of coating samples was performed in a three electrode cell using a graphite electrode as a counter electrode (CE), saturated calomel electrode (SCE) as reference electrode (RE) and the coated sample as the working electrode (WE). 3.5wt% NaCl solution was used as the test solution and maintained at room temperature.

3. RESULTS AND DISCUSSION

3.1 Phase Identification and Microstructure

The XRD patterns of the electrodeposited Ni-Co coatings prepared from the electrolytes with different Co concentrations are shown in Figure 1. The acquired XRD patterns were verified by referring to the Joint Committee for Powder Diffraction Studies – International Centre for Diffraction Data (JCPDS-ICDD), which was stored in EVA software by Bruker. All coatings exhibit a single phase of Ni and Co matrix with FCC crystal structure. The crystal planes of (111), (200) and (220) are observed at angular positions of 44.45, 51.8 and 76.3° respectively, for all electrodeposited Ni-Co coatings. According to Yang *et al*. (2010), the preferred orientations for pure Ni coating is (200), while the presence of Co element within the coating changed the preferred orientation to (111). As the Co content increased, the intensities of the (111) plane clearly decreased. Diffraction peaks (200) and (220) remarkably decreased when the Co concentration in the solution increased from 30 to 50 wt%, as shown in Figures 1(c) to (e). The presence of low diffraction peak corresponding to HCP phase structure is observed when the Co concentration in the electrolyte is more than 40 wt%. The (100) and (101) diffraction peaks of the HCP phase structure occurred at angular positions of 41.7 and 47.5° respectively, as shown in Figures 1 (d) and (e), due the change of Co phase structure, with higher Co concentration present within the coatings. The Co element becomes dominant as the phase structure commonly found in coatings provided from pure Co solutions (Wang *et al*., 2005). Consequently, it can be reported that a single FCC phase structure turns to a mixture of FCC and HCP phase structures with increasing Co ion concentration within the electrolyte, which increases the Co content within the coating.

The mean crystallite sizes for the major crystallite plane (111) of the coatings were determined using Equation 1. For the preferred orientation (111), it is shown that the coatings exhibit nanostructured properties since the mean crystallite sizes were estimated to be in the range of 7.1 to 11.5 nm. Furthermore, it was found that the mean crystallite size of the crystal plane (111) would decrease by increasing the Co concentration within the coating, as shown in Table 2.

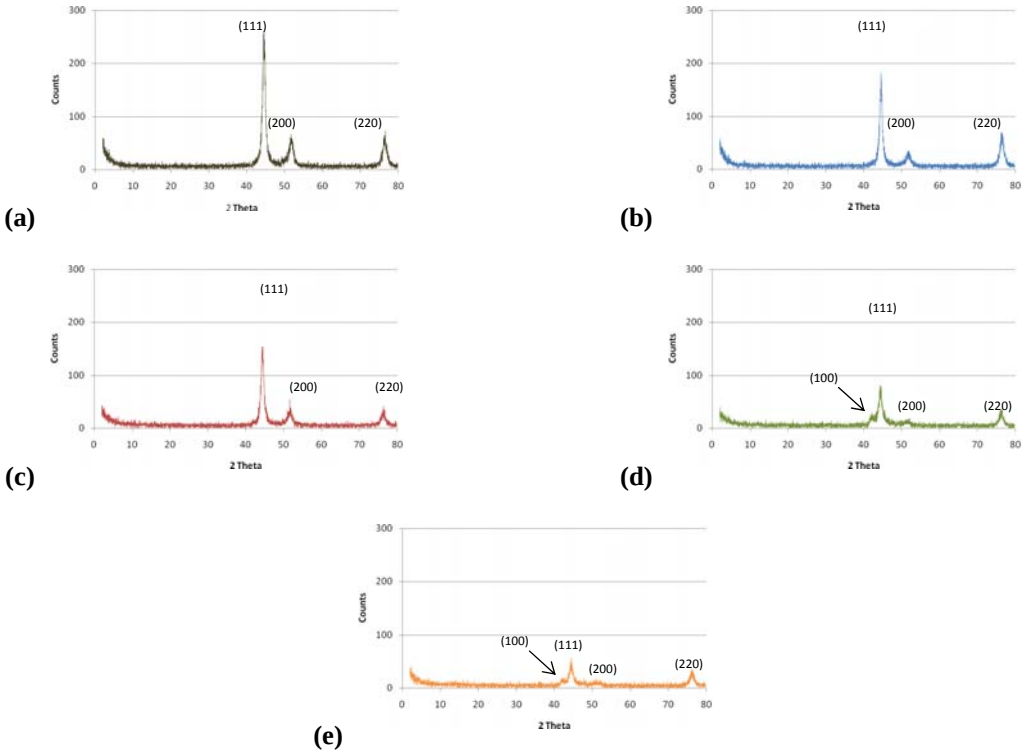

Figure 1: XRD pattern of Ni with (a) 10, (b) 20, (c) 30, (d) 40 and (e) 50 wt% Co concentration.

Table 2: The crystallite sizes of coatings as a function of Co content at different crystal planes.

Co content (%)	Crystallite size (nm)				
	(100)	(111)	(101)	(200)	(220)
10	-	10.5	-	6.8	12.0
20	-	11.5	-	5.9	8.8
30	-	11.3	-	6.3	8.5
40	22.9	9.1	-	126.2	112.3
50	33.6	7.1	18.2	15.7	20.9

The SEM technique was employed to study the surface morphological structure of the coatings with respect to Co ion concentration within the electrolyte. The SEM micrographs obtained for the results of Co ion concentrations are shown in Figure 2. The size and shape of the grains formed on the coating surface are consisting of grains with a rounded shape, covered by needle-like dendritic particles. The increment of Co concentration provided smaller grains together with more compact needle-like structure that was uniformly distributed. The changes on surface morphologies were prominent at the Co concentration of 40 wt%, as can be seen from Figure 2(d). Further increase of Co concentration to 50 wt% provided a cauliflower-like structure, whereby small rounded grains were embedded in a big rounded grain, as shown in Figure 2(e). It is clearly observed that the formation of Ni-Co coating morphology was strongly influenced by the chemical composition of the coating. The needle-like dendritic structure mostly appears due to the presence of Co. A higher Co content in the bath concentration would lead to increase of more Co to be deposited as applied current use provided for higher overpotential on Co deposition. Besides that, the size of crystal nuclei decreased, which increased their nucleation rate as describe previously (Rafailović *et al*., 2010; Tian *et al*., 2011).

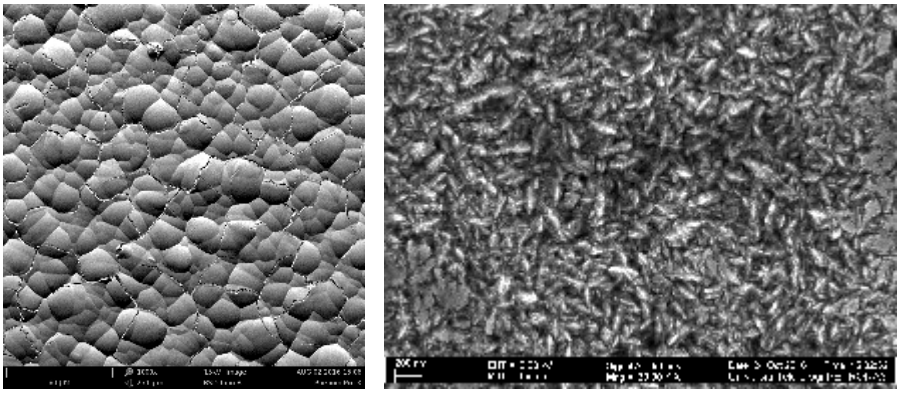

(a)

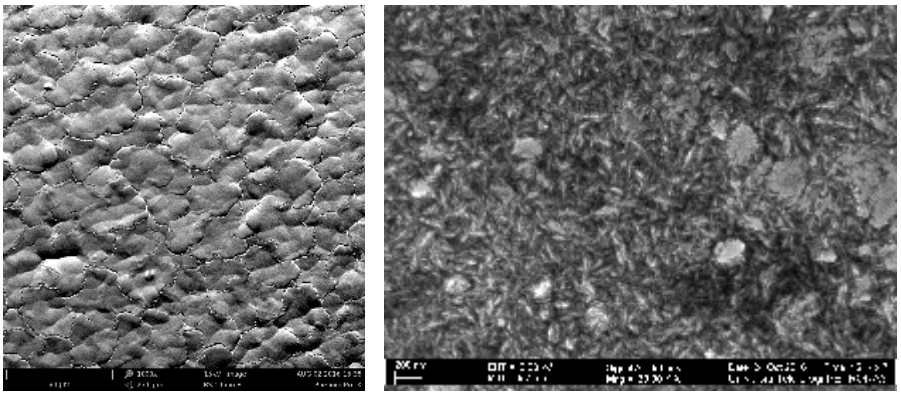

(b)

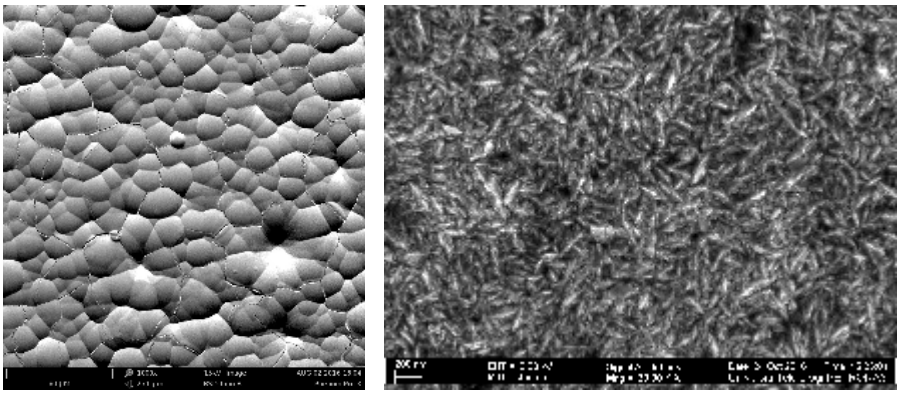

(c)

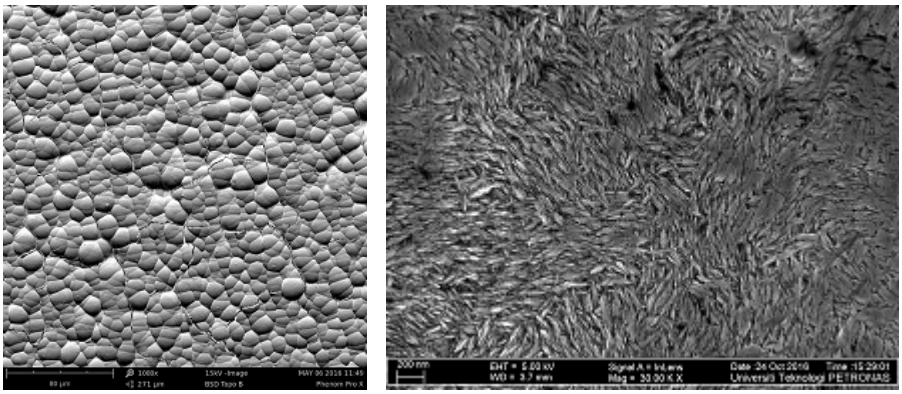

(d)

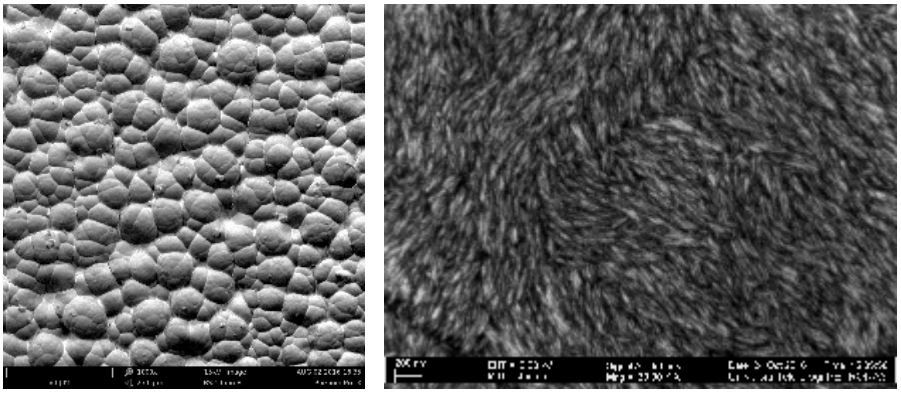

(e)

Figure 2: Surface morphologies of the Ni coatings with (a)10, (b) 20, (c) 30, (d) 40 and (e) 50 wt% Co concentration at low and high magnification.

3.2 Cobalt Content

Figure 3 shows the variation of the cobalt content in the Ni–Co coatings as a function of the cobalt concentration in the electrolyte. There is a significant growing trend in the cobalt content within the coating as a function of Co content in an electrolyte. The ratio of Co content within the coatings also does not differ much from the ratio of cobalt concentration in the electrolyte. However, these findings contradict the findings from previous studies (Bahadormanesh & Dolati 2010; Srivastava *et al*., 2006; Sarac *et al*., 2015). The 'anomalous co-deposition' or preferential deposition of less noble metal (Co) against noble metal (Ni) resulted in the Co content within the coating being higher than the Co concentration in an electrolyte, which was not significant in these studies.

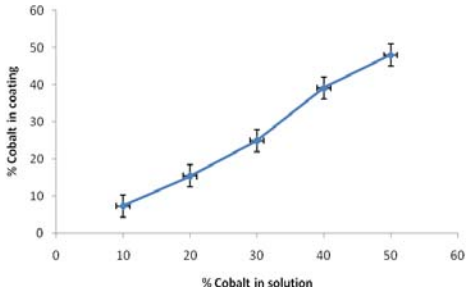

Figure 3: Percentage of Co in a solution as compared to the percentage of Co within the coatings.

3.3 Mechanical Properties of Ni-Co Coatings

The influence of Co content on the Ni Co coating microhardness is illustrated in Figure 4. The literature values for microhardness of pure Ni coating prepared in the alkaline bath are 380 to 450 HV depending on the deposition parameters (Bund & Thiemig, 2007). The Ni-Co coatings prepared using the alkaline bath in this study showed microhardness values greater than 550 HV. The increase in the percentage of Co from 10 to 20 wt% did not show a significant change in the microhardness value. Nevertheless, further increase of Co from 20 to 50 wt% Co demonstrated improvement in the microhardness properties of up to 740 HV. A few factors have been discussed previously that influence microhardness values. Marita *et al*. (2014) and Bakhit (2015) suggested that smaller grain size gives better effect to the microhardness value. According to the Hall-Petch relation, the nanocrystalline structure will possibly improve the coating microhardness (Pande & Cooper 2009). Coating microstructure also has its own contribution to the microhardness value, whereby the

columnar structure is superior than globular, as reported by Tury *et al*. (2007). Nonetheless, the increase in the microhardness value in this study is related more to the grain refinement effect due to the alteration of grain size by Co content as shown in Table 2. The morphology of all the coatings provided rounded shapes with no compromise to the percentage of the Co that was added to the coating.

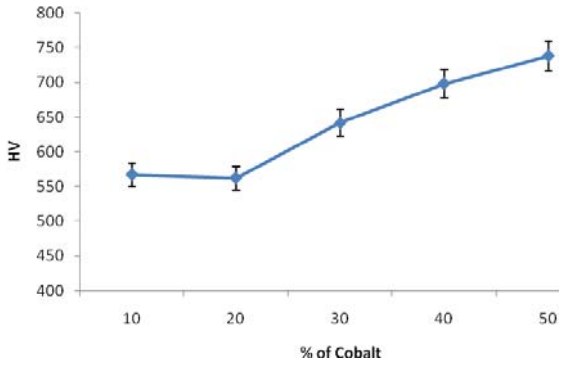

Figure 4: Coating microhardness as a function of Co content in the solution.

In order to measure the coating adhesion, the scratch test has achieved the most extensive use in assessing the mechanical stability and adhesive strength of coating / substrate interface (Narasimman *et al*., 2011; Schwarzer *et al*., 2011). The scratch caused deformation to the coating film from elastic to plastic until damage in the surface region. The damage on the surface is commonly characterised into several types, such as cracking, spalling and chipping, which can be determined by microscopic examination (Sander *et al*., 2011). The load at which a certain failure occurs is referred to as critical load (L_C). The scratch test conducted on the Ni-Co coatings revealed the failure modes that occurred. A few modes of failure clearly appear resulting from linearly increasing load from 1 to 180 N. Figure 5(a) shows that plastic grooves occurred at the beginning of the test followed by coating crack. At higher loads, the coating began to chip and peel off from the substrate. In order to confirm the point of coating deformation, elemental analysis was conducted using energy-dispersive x-ray spectroscopy (EDX). Figure 5(b) shows the EDX spectrum spotted at the initial point where the coating deformation occurs. The presence of ferum (as a major element of the substrate) indicates that the coating layer was demolished. The Fe element trace at the initial point of the plastic groove was very low while at the point of crack began to show higher percentage of Fe. The highest percentage of Fe could be found when the coating starts to chip or peel off.

The adhesion of the Ni-Co coatings with different Co concentrations was tested by the scratch test as shown in Figure 6. The critical load L_c1 represents the load where the coating started to crack while L_c2 corresponds to the load where the coating began to peel off. The coating with 10 wt% Co content started to crack when the normal load applied was greater than 54 N. Further increase of the load of up to 90 N had broken off the coating layer. Higher vol.% of Co within the coating had increased the L_c1 and L_c2. The coating with 30 wt% Co gave L_c1 value of 60 N and L_c2 value of 104 N, while the coating with 50 wt% Co provided L_c1 value of 80 N and L_c2 value of 114 N. This behaviour is consistent with the hardness test results and demonstrates that higher Co content contributes to better adhesive strength of the coatings.

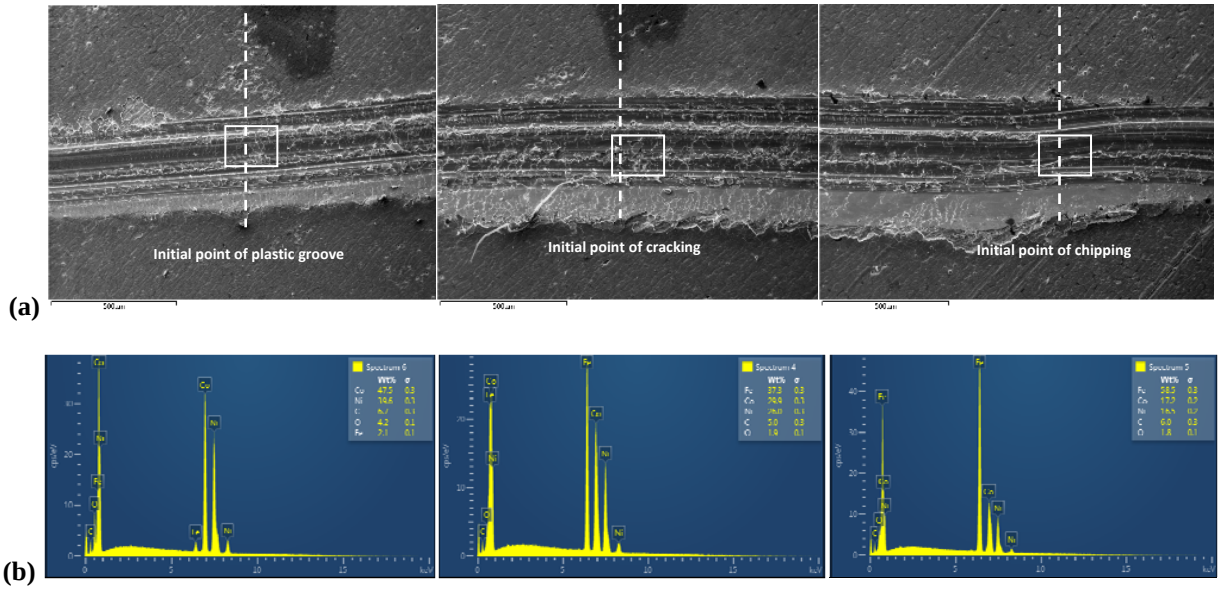

Figure 5: (a) SEM images of the grooves from the scratch test and (b) elemental analysis using EDX on the marked areas.

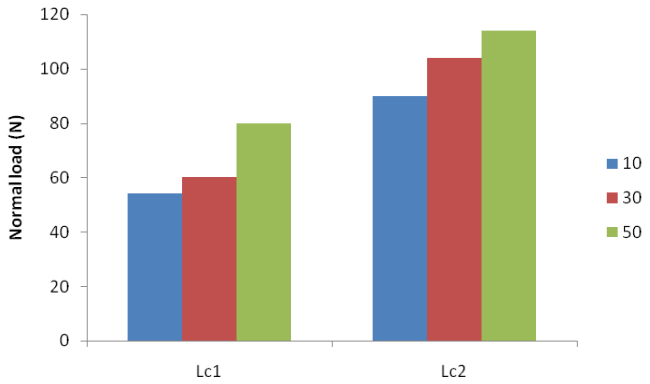

Figure 6: The critical load (L_c) obtained from the scratch test conducted on the Ni coatings with 10, 30 and 50 Co content.

3.4 Corrosion Behaviour of Ni-Co Coatings

The potentiodynamic polarisation curves of the mild steel substrate and Ni–Co alloy coatings with 10, 30 and 50 wt% of Co subjected to corrosive medium 3.5wt% NaCl solution are presented in Figure 7. The electrochemical parameters, such as corrosion potential (E_{corr}), corrosion current (I_{corr}) and corrosion rate, obtained from the potentiodynamic polarisation curves (Figure 7) are summarised in Table 3. The corrosion rate was determined using a software based on the following equation (Yusoff *et al*., 2013):

$$\text{Corrosion rate (μm/year)} = 3.27 * EW * i_{corr} / dA \quad (2)$$

where EW = equivalent weight (g/equivalent), d = density (g/cm^3) and A= sample area (cm^2).

The E_{corr} of mild steel was observed to be −487 mV. A positive shift of E_{corr} values would indicate better corrosion resistance, while a negative shift would indicate a vice versa effect. The shift observed for Ni 10 wt% Co was found to be -456 mV, indicating improved corrosion resistance of the coating. As the Co content was further increased to 30 and 50 wt% Co, the E_{corr} shifted towards a more negative value. This indicates that the corrosion resistance of the coatings deteriorated with the further addition of Co content. For the coating with 50 wt% Co, the corrosion resistance had clearly deteriorated as compared to the uncoated mild steel. Furthermore, the higher Co content within the coating accelerated the corrosion rate of the mild steel from 622 µm/year to the maximum of 853 µm/year. The degradation of corrosion protection provided by the Ni-Co coatings could be due to several factors. Chemical composition, phase structure and grain size are factors which have effective influences on the corrosion behaviour of composite coatings (Bakhit *et al*., 2014). Ni-Co composite coatings have been reported to give better corrosion resistance as compared to single Ni coating due to uniform and compact surface structure (Srivastava *et al*., 2006; Yang *et al*., 2010). However, high Co concentrations within the coating had changed their structures. Grain size was clearly diminished by increasing Co content, thus increasing the grain boundaries. It is well known that the grain boundaries are prone to corrosion attacks especially for the multi-phase structure materials (Cai *et al*., 2015). Other than that, the presence of different phases between coating and substrate encourages the galvanic corrosion to occur particularly when the Co concentration is high. Cobalt content could lead to an increase in electrochemical activity of the Ni–Co alloy matrix (Bakhit & Akbari 2012; Bakhit *et al*., 2014). This occurrence explains the cause of higher corrosion rate between high Co content of Ni-Co coated mild steel than uncoated mild steel.

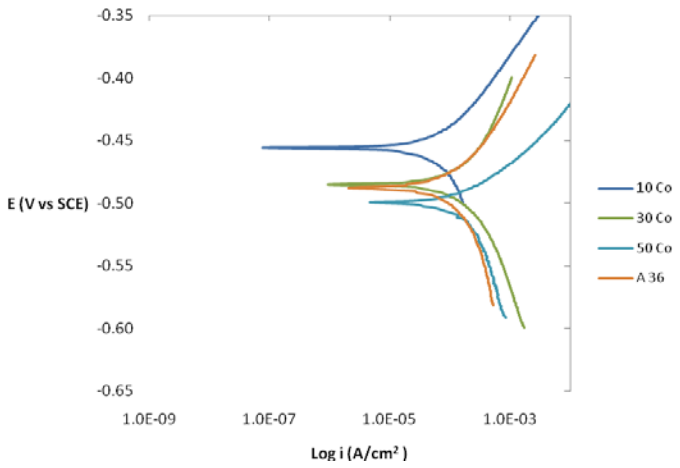

Figure 7: Potentiodynamic polarisation curves for Ni-Co composite coatings in 3.5wt% NaCl solution.

Table 3: The electrochemical parameters obtained from the Tafel slope.

	I_{corr} (µA)	E_{corr} (mV)	Corrosion Rate (µpy)
A36	252	-487	622
Ni 50 wt%Co	300	-500	739
Ni 30 wt%Co	294	-485	853
Ni 10 wt%Co	109	-456	313

4. CONCLUSION

The electrodeposition of Ni-Co coatings were successfully deposited on mild steel substrates prepared in an alkaline bath. The effects of cobalt content was characterised in terms of phase structure, crystallite size and coating surface morphology. In addition, the properties of the coatings were studied with respect to the microhardness value, adhesion strength and corrosion behaviour of the coated steel. Increase of the cobalt content in the solution correspondingly increased the cobalt content within the coating. Consequently, the single FCC phase structure turned to a mixture of FCC and HCP phase structures. The crystallite size became smaller at high Co content coatings, which produced smaller grains in their surface morphologies. Higher Co content generated coatings with better microhardness value due to the grain refinement effect by modification of grain size. The adhesion strength of the coatings also increased with high Co content, with the critical load for cracking and chipping increasing with increasing Co content. However, high Co content tends to diminished corrosion resistance of the coating due to changes in their phase structure and grain boundary. Ni with 10wt% Co concentration would be suggested to offer good mechanical strength together with corrosion protection to the mild steel.

REFERENCES

Bahadormanesh, B. & Dolati, A. (2010). The kinetics of Ni-Co/SiC composite coatings electrodeposition. *J. Alloy Compd.*, **504:** 514–18.

Bakhit, B. (2015). The influence of electrolyte composition on the properties of Ni–Co alloy coatings reinforced by SiC nano-particles. *Surf. Coat. Tech.*, **275**: 324–31.

Bakhit, B. & Akbari, A . (2012). Effect of particle size and co-deposition technique on hardness and corrosion properties of Ni–Co/SiC composite coatings. *Surf. Coat. Tech.*, **206:** 4964–75.

Bakhit, B. & Akbari, A. (2013). Synthesis and characterization of Ni–Co/SiC nanocomposite coatings using sediment co-deposition technique. *J Alloy Compd.*, **560:** 92–104.

Bakhit, B., Akbari, A., Nasirpouri, F. & Hosseini, M. (2014). Corrosion Resistance of Ni-Co Alloy and Ni-Co/SiC nanocomposite coatings electrodeposited by sediment codeposition technique. *Appl. Surf. Sci.,* **307**: 351–59.

Bund, A. & Thiemig, D. (2007). Influence of bath composition and ph on the electrocodeposition of alumina nanoparticles and nickel. *Surf. Coat. Tech.,* **201**: 7092–99.

Cai, F., Jiang, C., Fu, P. & Ji, V. (2015). Effects of co contents on the microstructures and properties of electrodeposited NiCo–Al composite coatings. *Appl. Surf. Sci,* **324**: 482–89.

Feng, Z., Li, Q., Zhang, J., Yang, P., Song, H. & An, M. (2015). Electrodeposition of nanocrystalline Zn–Ni coatings with single gamma phase from an alkaline bath. *Surf. Coat. Tech.,* **270**: 47–56.

Ibrahim, M.A.M. & Rashed, S.B. (2015). New cyanide-free ammonia bath for brass alloy coatings on steel substrate by electrodeposition. *Int. J. Electrochem. Sc.,* **10**: 9666–77.

Lan, C.J., Liu, W.Y., Ke, S.T. & Chin, T.S. (2006). Potassium salt based alkaline bath for deposition of Zn–Fe alloys. *Surf. Coat. Tech.,* **201**: 3103–3108.

Long, J.M., Xiu Z. & He, Z.P. (2013). Effect of triethanolamine addition in alkaline bath on the electroplating behavior, composition and corrosion resistance of Zn-Ni alloy coatings. *Adv. Mat. Res.,* **738**: 87–91.

Marita, Y., Ridwan, N. & Nurdin, S. (2014). Preparation of Ni-Co alloy by electrodeposition. *Appl. Mech. Mater.*, **525**: 58-61.

Narasimman, P., Pushpavanam, M. & Periasamy, V.M. (2011). Synthesis, characterization and comparison of sediment electro-codeposited nickel–micro and nano SiC composites. *Appl. Surf. Sci.,* **258**: 590–98.

Pande, C.S. & Cooper, K.P. (2009). Nanomechanics of Hall–Petch relationship in nanocrystalline materials. *Prog. Mater. Sci.,* **54**: 689–706.

Rafailović, L.D., Karnthaler, H.P., Trišović, T. & Minić, D.M. (2010). Microstructure and mechanical properties of disperse Ni–Co alloys electrodeposited on Cu substrates. *Mater. Chem. Phys.,* **120**: 409–416.

Rafailović, L.D. & Minić, D.M. (2009). Deposition and characterisation of nanostructured nickel-

cobalt alloys. *Hem. Ind.,* **63**: 557–69.
Saha, R.K. & Khan, T.I. (2010). Effect of applied current on the electrodeposited Ni–Al2O3 composite coatings. *Surf. Coat. Tech.,* **205**: 890–95.
Sander, T., Tremmel, S. & Wartzack, S. (2011). A modified scratch test for the mechanical characterization of scratch resistance and adhesion of thin hard coatings on soft substrates. *Surf. Coat. Tech.,* **206**: 1873–1878.
Sarac, U., Baykul, M.C. & Uguz, Y. (2015). Differences observed in the phase structure, grain size–shape, and coercivity field of electrochemically deposited ni–co thin films with different co contents. *J. Supercond. Nov. Magn.,* **28**: 3105–3110.
Schwarzer, N., Duong, Q.H.H., Bierwisch, N., Favaro, G., Fuchs, M., Kempe, P., Widrig, B. & Ramm, J. (2011). Optimization of the scratch test for specific coating designs. *Surf. Coat. Tech.,* **206**: 1327–35.
Shakoor, R.A., Kahraman, R., Waware, U.S., Wang, Y. & Gao, W. (2014). (2014). Synthesis and properties of electrodeposited Ni–B–CeO2 composite coatings. *Mater. Design*, **59**: 421–429.
Srivastava, M., Selvi, V.E., Grips, V.K.W & Rajam,V., (2006). Corrosion resistance and microstructure of electrodeposited nickel–cobalt alloy coatings. *Surf. Coat. Tech.*, **201**: 3051–3060.
Tian, B.R. & Cheng, Y.F. (2007). Electrolytic deposition of Ni–Co–Al2O3 composite coating on pipe steel for corrosion/erosion resistance in oil sand slurry. *Electrochim. Acta*, **53**:511–517.
Tian, B.R., Liangliang, Xu, J. & Xiao, S. (2011). The influence of Ph and bath composition on the properties of Ni–Co coatings synthesized by electrodeposition. *Vacuum,* **86**: 27–33.
Tury, B., Radnóczi, G.Z., Radnóczi, G. & Varsányi, M.L. (2007). Microstructure properties of pulse plated Ni–Co alloy. *Surf. Coat. Tech.,* **202**: 331–35.
Wang, L., Gao, Y., Xue, Q., Liu, H. & Xu, T. (2005). Microstructure and tribological properties of electrodeposited Ni–Co alloy deposits. *Appl. Surf. Sci.,* **242** : 326–32.
Yang, X., Li, Q., Zhang, S., Gao, H., Luo, F. & Dai, Y. (2010). Electrochemical corrosion behaviors and corrosion protection properties of Ni-Co alloy coating prepared on sintered NdFeB permanent magnet. *J. Solid State Electr.,* **14**: 1601–1608.
Yusoff, N.H.N., Ghazali, M.J., Isa, M.C., Daud, A.R. & Muchtar, A. (2013). Effects of powder size and metallic bonding layer on corrosion behaviour of plasma-sprayed Al_2O_3-13% TiO_2 coated mild steel in fresh tropical seawater. *Ceram. Int.,* **39**: 2527–33.
Zhang, Z., Jiang, C. & Ma, N. (2014). Microstructure and corrosion behavior of electrodeposited Ni-Co-ZrC coatings. *J. Mater. Eng. Perform.,* **23**: 4065–4071.
Zhao, Y., Jiang, C., Xu, Z., Cai, F., Zhang, Z. & Fu, P. (2015). Microstructure and corrosion behavior of Ti nanoparticles reinforced Ni–Ti composite coatings by electrodeposition. *Mater. Design,* **85**: 39–46.

WEAR BEHAVIOUR OF a-C:H HELICAL GEAR THROUGH PARTICLE GENERATION

Abdul Hakim Abdul Hamid[1,2], Reduan Mat Dan[1,2*], Azma Putra [1,2,], Mohd Nizam Sudin[1,2] & Rozdman Khaidir Mazlan

[1]Fakulti Kejuruteraan Malaysia
[2]Centre for Advanced Research on Energy
Universiti Teknikal Malaysia Melaka (UTeM), Malaysia

[*]Email: reduan.dan@utem.edu.my

ABSTRACT

This paper presents the wear performance of amorphous hydrogenated carbon (a-C:H) deposited on helical gears through wear debris analysis. Helical gears are tested on a power recirculating test rig with constant loads of 100 Nm and speed of 1,000 rpm. The tests are conducted for 9 million cycles or an initial pitting of 25% covering the surface of the teeth. Samplings are obtained for approximately 60 ml of the lubricant for every 3.6×10^5 cycles, which are then analysed through oil analysis that includes wear debris analysis as well as particle counting. The results reveal that the a-C:H coated gear reduces the particle generation by a factor of 3.11 as compared to the baseline testing. However, a-C:H does not affect the condition of the lubricant. It is found that the a-C:H gear had reduction in micro-pitting formation as compared to the uncoated gear. This study demonstrates an extension of the life of gears through the application of a-C:H coating.

Keyword: *Diamond-like carbon; helical gear; condition monitoring; fatigue life; power recirculating gear test rig.*

1. INTRODUCTION

Gears are one of the main mechanisms for power transmissions in almost all machines. The primary purpose of gear systems is to implement motion transmission, as well as to increase or to decrease the speed of shafts carrying rollers or loads. Recent developments on design and manufacturing of gearboxes strive for a more compact design that yields a larger capacity of power transmission. Due to the nature of the power transmission that involves variable speed of rotary mechanism and heavy loads, gears tend to experience failures at various cycle of the machine operation. The common failure modes of gear typically include bending fatigue, contact fatigue, scuffing, wear, cracking, fracture and plastic deformation (AGMA, 2014). However, countless analyses have identified that the factors in most occurring failure modes are tooth-bending fatigue, contact fatigue, scuffing and abrasive tooth wear (Edwards, 2004).

Surface technology is a feasible solution towards improving the service life of gears and is now extensively developed, which includes various methods such as surface hardening, shot penning and nitriding. Surface coating is a promising method to improve surface performance. The current generation of popular hard coatings is the “diamond like carbon” (DLC), where it has been proven to have profound tribological advantages in sliding-rolling contact components. Manier *et al.* (2010) found that the amorphous hydrogenated carbon (a-C:H) and the tetrahedral amorphous carbon (ta-C) coating surpasses the ceramic coating performance under slip rolling condition at a high Hertzian contact stress of 3.5 GPa. Various studies have also been conducted on the influence of DLC coatings towards the improvement of the common failure mode resistance, such as contact fatigue and scuffing resistance. Krantz *et al.* (2004) demonstrated an extension of life of tungsten DLC (a-C:H:W) coated

gears by a factor of six through accelerated fatigue testing. However, it is discovered that the performance of DLC coated gears changed with the load condition applied. Under low load conditions, the gears exhibited longer fatigue life, while in high load conditions, the fatigue life is comparatively shorter or equal to the non-coated gear (Fujii *et al.*, 2010). Although DLC coating provides an advantage on maximising resistance towards gear failures, the complex interactions for various parameters, such as the elastohydrodynamic lubrication (EHL), temperature and contact pressures yields various results of enhancements as well as deterioration.

The utilisation of a-C:H coating on the influence of gears is rarely discussed as most of the existing studies are conducted using a-C:H:W coating (Joachim *et al.*, 2002; Kalin & Vižintin, 2005; Kržan *et al.*, 2006; Michalczewski *et al.*, 2013a; Tuszynski *et al.*, 2015; Velmurugan & Vijayakumar, 2017). An experimental testing of a-C coating on cylindrical gears applied with a high contact stress was presented by Xiao *et al.* (2014), which suggested that the prolongation of the gear life is achievable by a factor of three. The study on a-C:H coating on spur gears lubricated under ecological oil is demonstrated by Michalczewski *et al.*(2013b), where the coated gears had an increased scuffing load capacity. Another a-C:H coating study was published by Fujii *et al.*, (2011), where fatigue testing is conducted on gears under vacuum condition. The study also suggested improved scuffing load capacity in comparison with the uncoated gear.

This paper focuses on the wear behaviour of a-C:H coated helical gear in terms of the wear debris generation as well as the surface fatigue formation. Its effect on the lubricant condition is also discussed.

2. METHODOLOGY

2.1 a-C:H Specification and Gear Specification

Prior to experimental investigation, the DLC coatings are selected based on the optimum condition for helical gear testing using pareto optimal analysis and weighted decision matrix. Tables 1 and 2 show the selected DLC coating and gear specification used in the experiment.

Table 1: a-C:H specification.

Coating	Material	Thickness range µm	Microhardness HV 0.05/ Hardness (GPa)	Coefficient of friction	Service temperature (°C)	Deposition temperature (°C)
Tribobond 43	a-C:H	1-5	2500-4000/ 12-20	0.1	300	160-200

The gears are made from low carbon steel (AISI 1020), which after hobbing are carburised at temperatures higher than 900 °C with an as-ground surface for the physical vapour deposition (PVD) deposition of the a-C:H coating. The standard specification of the AISI 1020 steel gives a hardness value of 130 HV, but through testing using a Shimadzu HMV-G Micro Vickers Hardness Tester, it was recorded that the core hardness was at 261 HV. Due to the low-cost consideration of gear fabrication, pack carburisation is utilised where the case depth proved to be difficult to control. Nevertheless, the range was approximately 1.2 to 1.5 mm. The carburised gear has a case hardness of 546 HV, whereby the a-C:H deposition has a case hardness of 769 HV. The adhesion layer of chromium (Cr) is deposited as an interlayer through the PVD process, which is followed by the deposition of a-C:H coating via plasma assisted chemical vapour deposition (PACVD) process. Table 1 and 2 shows the a-C:H specification as well as the test gear parameters respectively.

Table 2: Gear specifications.

	Specifications
Type of Gear	Helical
Helix angle	17.75
Pressure angle	20
Centre to centre distance	113 mm
Module of gear	3
Number of teeth	36
Face width	15 mm (preliminary) / 7 mm (pitting) / 3 mm (pitting)
Tip diameter	116.25 mm
Pitch diameter	110.25 mm
Applied Tangential Loading	1818 Nm
Lubricant	DEXRON III Pennzoil
Gear Material	AISI 1020, Casehardened

2.2 Selection of Machine and Experimental Setup

Figures 1 and 2 shows the setup and schematic diagram of the power recirculating test rig. The test rig for the wear analysis in the experiment utilised the power recirculating gear system consisting of four helical gears. The shafts have four stubs of 250 mm of length and 25 mm in diameter. As the gears were installed, the shafts were locked in a close loop mesh, which allowed torsional loading to be applied. A special coupling to apply torsion by twisting the stub on the driven shaft was introduced. The coupling consisted of two concentric flanges, in which one side of the coupling possessed a triangular platform where set screws forced the stubs to be twisted. This causes angular misalignment or commonly known as torsion, which in turn causes the gear to be loaded with tangential force. Accelerated wear is the aim for the construction of this type of test rig. The main shaft was fitted with a torque transducer via rigid couplings connected to the stubs, which measured the applied torsion for a precise loading. A 10 HP DC motor drove the main shaft with a variable speed of up to 2,900 rpm.

Figure 1: Power recirculating test rig.

Preliminary testing was conducted for a Hertzian contact stress of 551 and 957 MPa to identify the capacity of the test rig. The actual experiments were conducted under a loading of 1,231 MPa for 9 million cycles for both AISI 1018 carburised gear and a-C:H coated gear at a constant speed of 1,000 rpm and a lubricant starting temperature is at room temperature. Samples were taken for every 3.6×10^5 cycles at approximately 60 ml per sample through the sampling port of the rig.

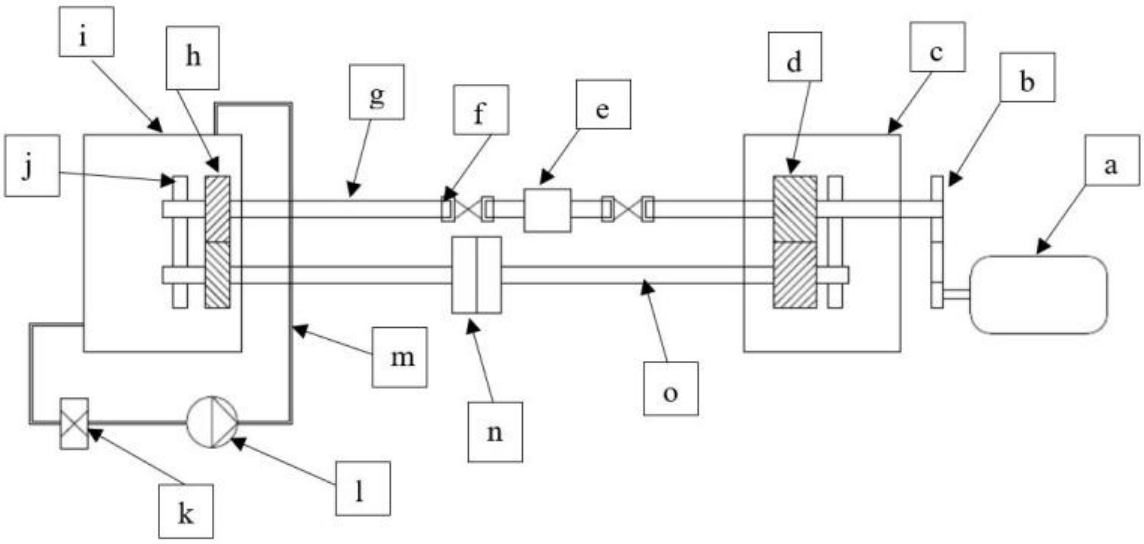

Figure 2: Schematic diagram of the gear test rig with lubricant path. The elements are: [a] AC motor, [b] tooth belt, [c] slave gear oil sump, [d] slave gear, [e] torque transducer, [f] flexible coupling, [g] drive shaft, [h] test gear, [i] test gear oil sump, [j] needle bearing casing, [k] 10 µm oil filter, [l] magnetic pump, [m] lubricant path, [n] torsional coupling, [o] driven shaft.

2.3 Wear Debris Analysis, Optical Imaging Analysis and Oil Analysis

The collected samples were analysed using a CSI Spectro 5200 trivector analyser for wear debris analysis and Q1000 Fluidscan for oil analysis using IR spectroscopy. Both equipment adhere to ASTM D7416 and ASTM D7889 respectively. A Dino-Lite AM4515 digital microscope was used to capture the surface conditions of both the uncoated and coated gears for the natural progression of pitting under accelerated loading conditions at the same interval as lubricant sampling. The results were then compared for both the uncoated and coated gears with progression of up to 9 million test cycles. At the end of the test cycles, as Axioskop 2 optical image analyser was utilised to capture the surface of isolated tooth at a 5x to 100x magnification for both gear surface conditions. The determination of the cumulative wear rate is given by:

$$Wear\ rate\ = \frac{Q\times M}{t_t - t_{t-1}} \tag{1}$$

where Q is the number of cumulative particles counted, M is the cumulative mass of the particles and t_t - t_{t-1} is the cycle of gear revolution for each test. The cumulative wear is used to determine the wear stages of both gear surface conditions through the quantitative analysis of particle counting.

3. RESULTS AND DISCUSSION

The overall wear performance in each test is assessed from the progression of micro-pitting damage, particle generation and lubricant condition. The results are limited to the formation of micro-pitting on the surface of the gear for both the uncoated and coated gear due to the test rig having a limitation of a low load output.

3.1 Particle Generation of Micro-Pitting Damage

The most significant factor in the particle generation is the ferrous index, which determines the ferrous composition of the particles dispersed in the lubricant. It is noted that the progressive nature of the micro-pitting on gear surfaces is a crucial feature for determining the wear performance of a gear under contact fatigue damage, thus provides useful information for predictive maintenance (Moorthy & Shaw, 2012).

Figures 3 to 5 present the particle generation for both the uncoated and coated gear. The particles are divided into three size categories, namely small diameter (SD), medium diameter (MD) and large diameter (LD). The details are listed in Table 3. The SD particles are associated but are not limited to various wear mechanisms comprising of rubbing wear, cutting wear, combined rolling and sliding wear as well as rolling fatigue, which involve pitting and spherical particles. However, SD particles are more prominent in the generation of spherical particles, which is generated through rolling fatigue wear and rubbing wear. These wear modes generally produce particles with sizes of 3 to 10 μm and 5 to 15 μm respectively.

Table 3: Particle size categories.

Particle Diameter	Size
Small Diameter (SD)	≤10 μm
Medium Diameter (MD)	≤28 μm
Large Diameter (LD)	≥32 μm

The MD particle generation categorised by its sizes are the result of various wear mechanisms faced by the gear during its operational life. The wear mechanism includes cutting wear, rolling fatigue generating spall and laminar particles, as well as combined rolling and sliding wear. However, MD particles is determined to be generated prominently via rolling fatigue generating laminar particles, and combined rolling and sliding wear, where both mechanisms produce particles of sizes 20 to 50 μm and 2 to 20 μm respectively. The combined rolling and sliding wear generate a complex fusion of particle morphology and thus, it is difficult to be categorised by size only. It is also worthy to note that severe sliding wear occurs only in MD particle sizes onwards. The wear modes resulting in the generation of the LD particles are determined to be of rubbing wear, cutting wear, rolling fatigue producing spall and laminar particles, and severe sliding wear (Anderson *et al*., 1991).

Ferrous index is sensitive to conductive, ferromagnetic particles that increase linearly with both particle size and concentration. The index measures recent, severe wear of oil-wetted steel and iron parts due to the surfaces of such particles that are likely to be conductive. Figure 3 shows the SD particle distribution. For the uncoated gear, the ferrous index was observed to increase significantly at the start of the test reaching a maximum ferrous index value and then decreased rapidly until the test reached 5.34 million test cycles. A small value of ferrous index is then observed at 6.54 million test cycles and between 7.26 and 7.62 million test cycles. The ferrous index measurements suggest that the particles generated at this specific point in the gear life cycle are of ferrous composition. As for the coated gear, the ferrous index remains at lower values observed throughout the gear cycles, which indicates that very little concentration of ferrous particles was removed from the coated gear gradually over the test cycle. Most of the particles are of non-ferrous composition.

The results in Figure 3 determines that the uncoated gear experienced wear mechanisms that are assumed to be rolling fatigue wear and rubbing wear. Uncoated gears produced larger particle sizes of 6 and 10 μm in the SD particle distribution as compared to those from the coated gear. Possible particle morphologies generated for these particle sizes include spherical particles and platelets (Anderson *et al*., 1991). Similar trends can also be observed for the case of MD and LD particles in

Figures 4 and 5 respectively. For the MD particles, the possible particle morphologies would be of laminar particles, striated particles, and a complex fusion of wear debris due to combined rolling and sliding wear. For the LD particles, the possible particle morphologies experienced are spherical, ribbons, chunks, platelets and striated particles, as shown in Figure 6.

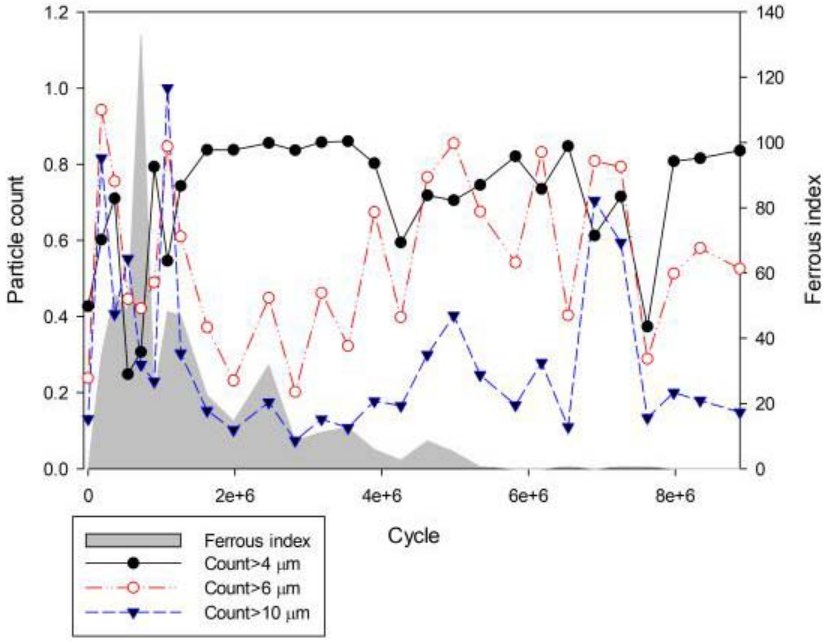

(a)

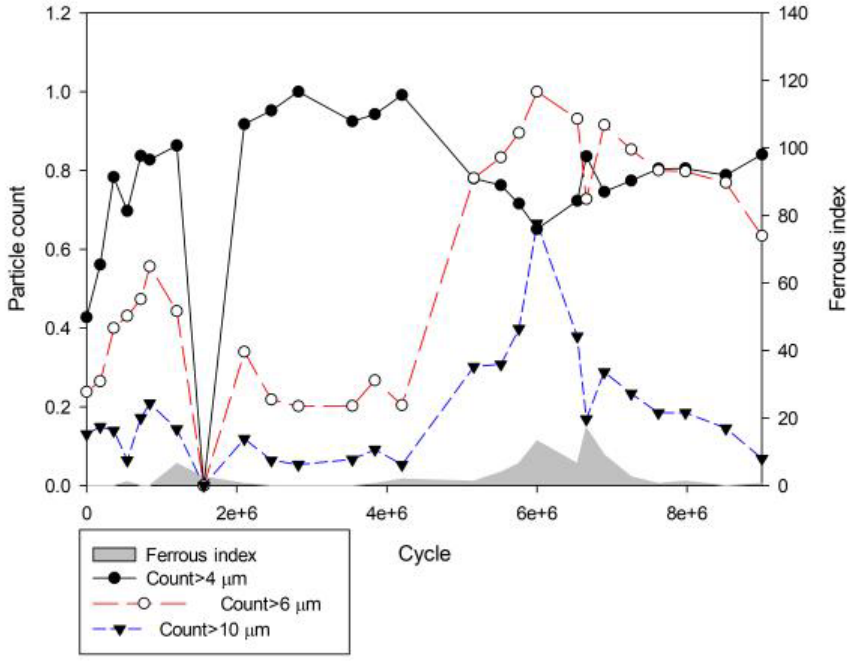

(b)

Figure 3: Small diameter (SD) particle generation progression: (a) AISI 1020 carburised and (b) a-C:H coated AISI 1020 carburised.

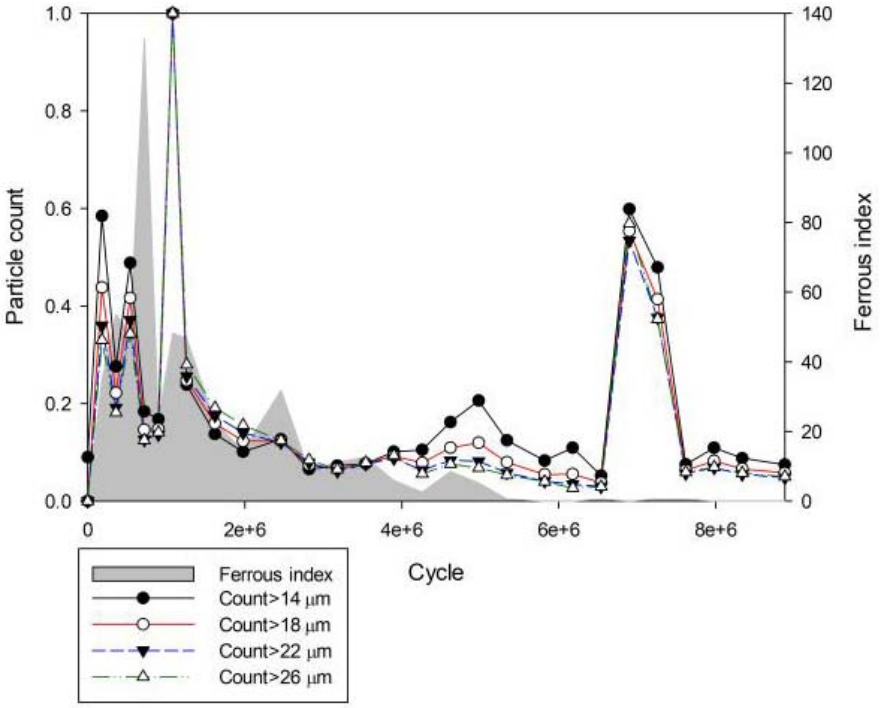

(a)

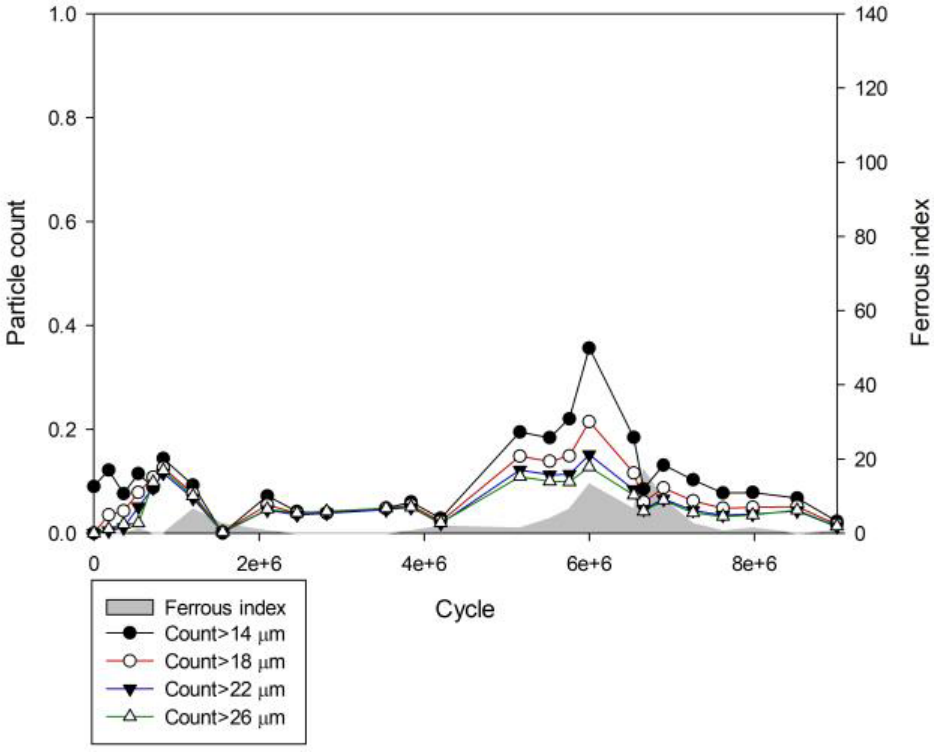

(b)

Figure 4: Medium diameter (MD) particle generation progression: (a) AISI 1020 carburised and (b) a-C:H coated AISI 1020 carburised.

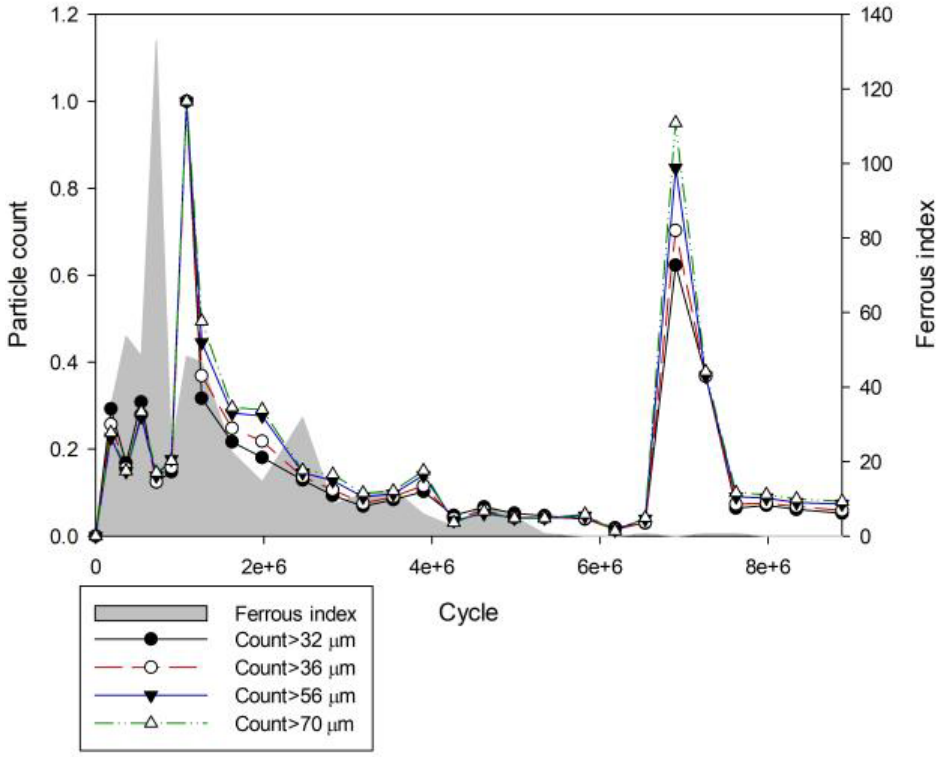

(a)

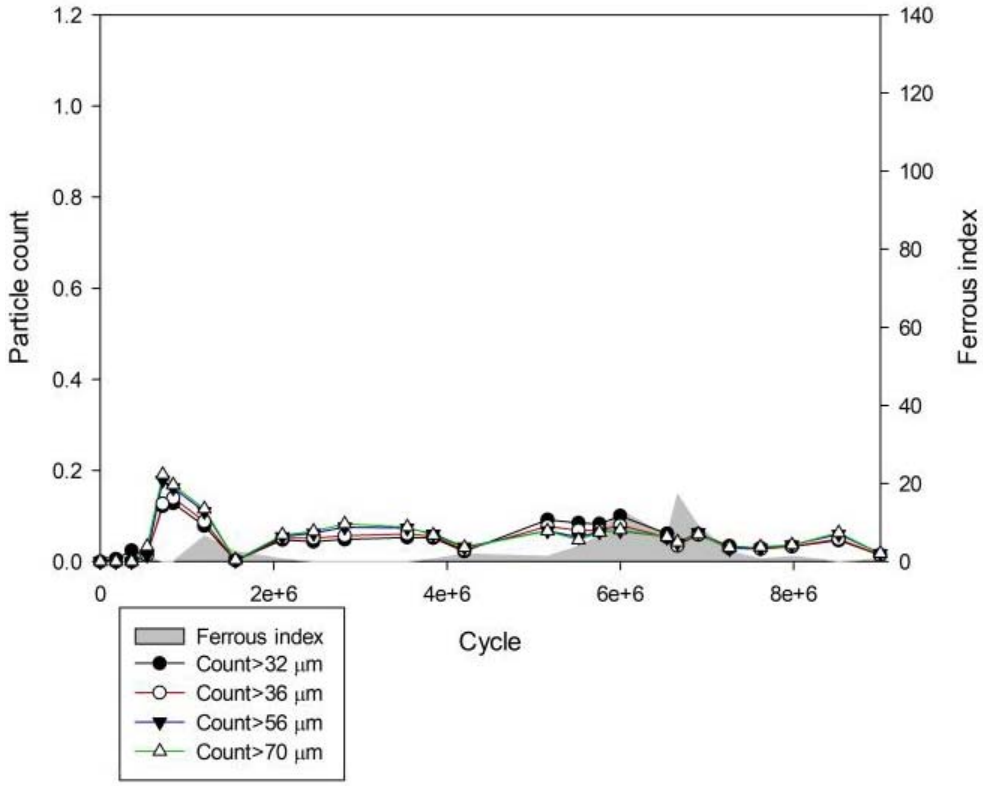

(b)

Figure 5: Large diameter (LD) particle generation progression: (a) AISI 1020 carburised and (b) a-C:H coated AISI 1020 carburised.

A cumulative wear rate of all the particle sizes are compared for the coated and uncoated gears as shown in Figure 7. From the trend, it can be clearly observed that the uncoated gear had three wear stages, which are run-in wear, steady-state wear and the initial failure zone, while the coated gear has an extended run-in wear that leads to a steady state wear. The run-in zone for the uncoated gear was determined to last for 1.62×10^6 gear revolutions, which then entered a steady state wear that lasted for 5.04×10^6 revolutions and subsequently entered an initial failure at 6.54×10^6 of gear revolution.

The coated gear showed an absolute divergence of wear debris generation behaviour as the run-in zone extended for 6.66×10^6 revolutions and then entered the steady state wear. This behaviour is consistent with the gear surface damage shown in Figures 9 and 10, which is discussed in more detail in Section 3.3. This finding determines the prolongation of the helical gear life by a factor of 3.11 through running-in quantification comparison.

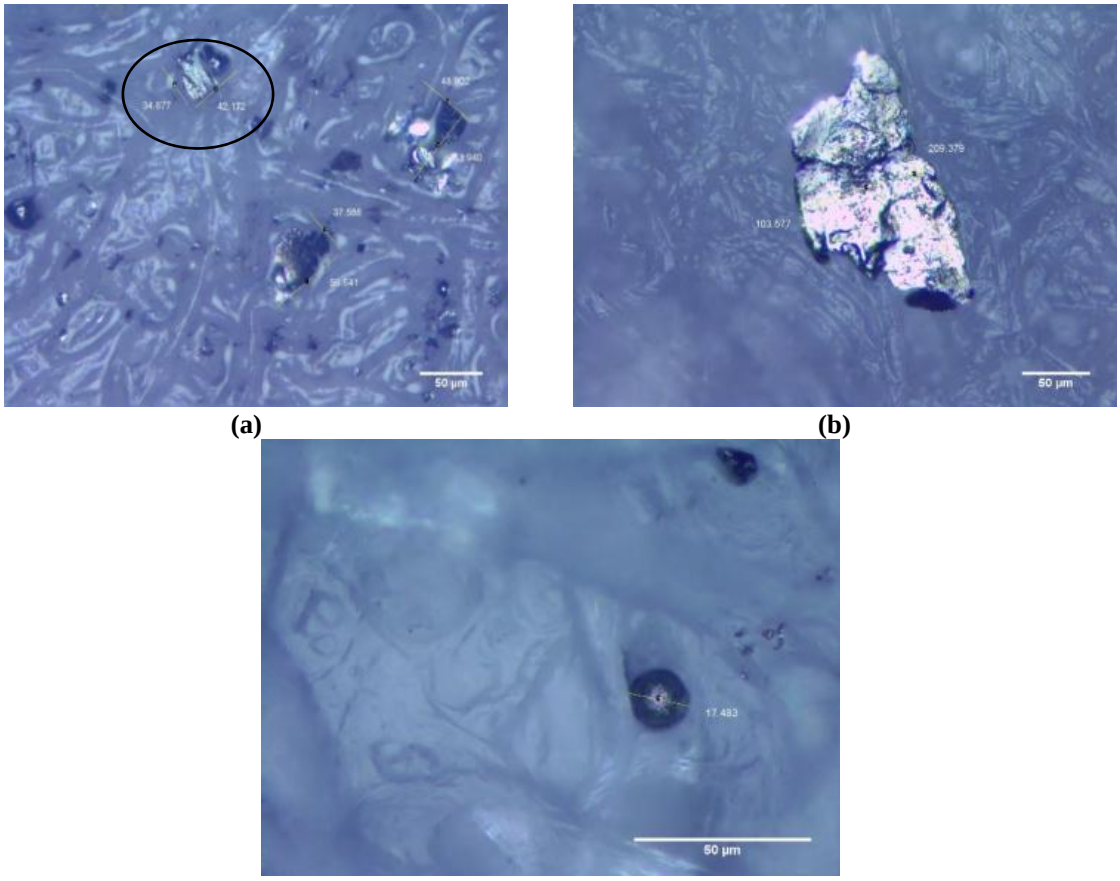

(a) **(b)**

(c)

Figure 6: Wear debris particles: (a) Platelets (annotation indicates platelets with striation marks) (b) Chunks (c) Spherical.

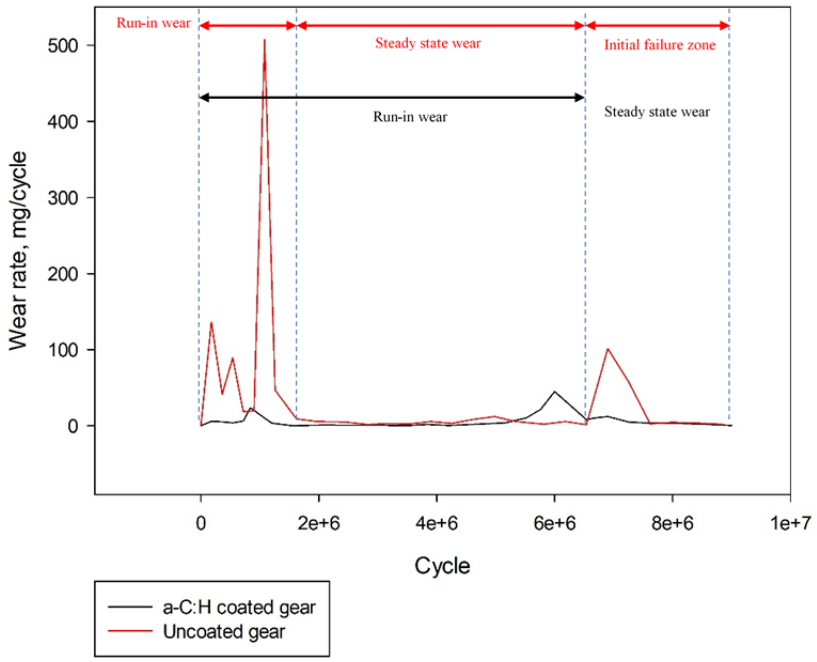

Figure 7: Cumulative wear rate of a-C:H coated gear vs uncoated gear.

3.2 Oil Analysis

The a-C:H coating has an insignificant impact on the condition of the lubricant, where the oxidation and viscosity has miniscule enhancement as compared to the uncoated gear lubricant through the progression of the test cycles, which can be observed in Figure 8. The uncoated gear has oxidation level ranges from 19.2 to 20.1 abs/0.1 m, while for the coated gear, it ranges from 19.3 to 19.9 abs/0.1 m. The degradation of oil due to oxidation or ageing is mainly caused by high temperatures of the lubricant, thus the behaviour shown in these experiments suggests that a high temperature during the experimentation did not occur.

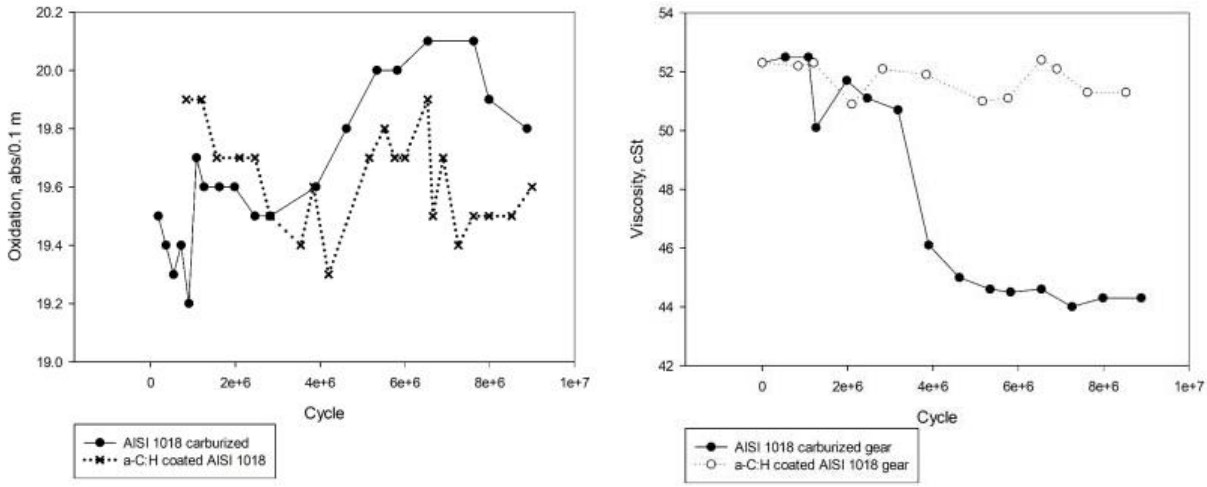

(**a**) (**b**)

Figure 8: Oil analysis of a-C:H coated gear vs uncoated gear: (a) Oxidation (b) Viscosity.

However, the viscosity of the lubricant differs from the influence of oxidation, where the uncoated gear debilitates over the course of the test cycle, while the viscosity of the coated gear remains constant towards the end of the experiment. As high temperature did not occur during the experiment, this result suggests that the uncoated gear lubricant may contain contamination.

3.3 Gear Tooth Image Analysis

Figures 9 and 10 present the gear surface image captured for the N^{th} test cycle. From the images, the wear mode can be identified with the formation of micro-pitting.

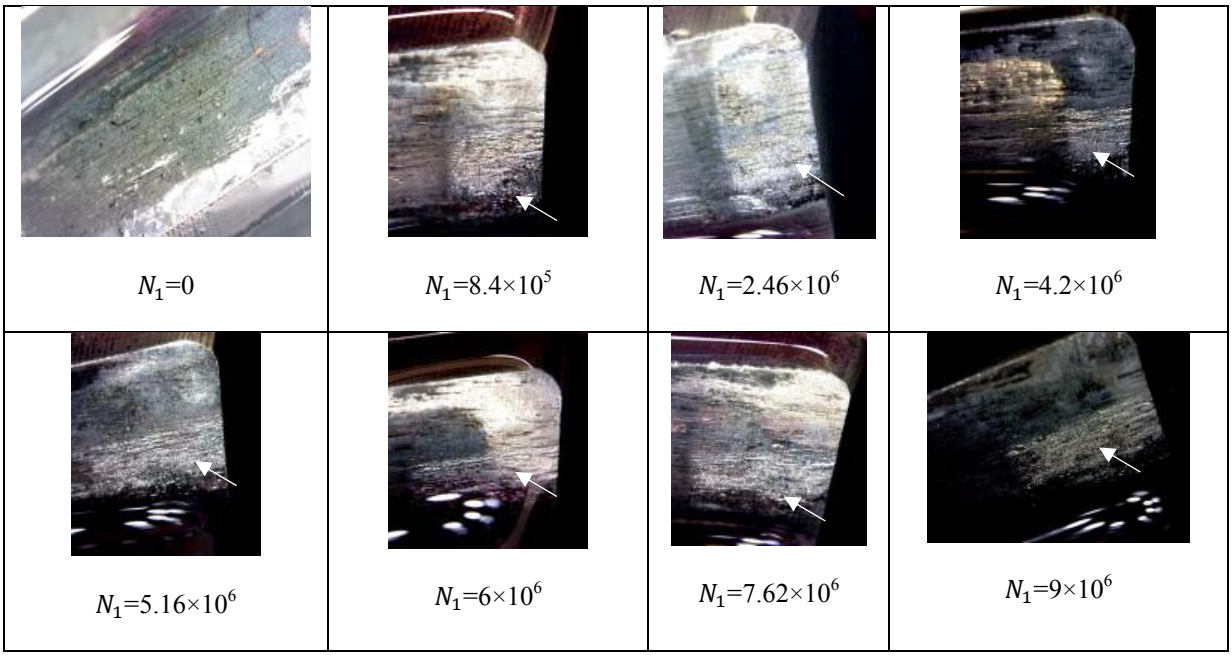

Figure 9: AISI 1020 carburised uncoated gear surface image (the arrows annotate the formation of micropitting).

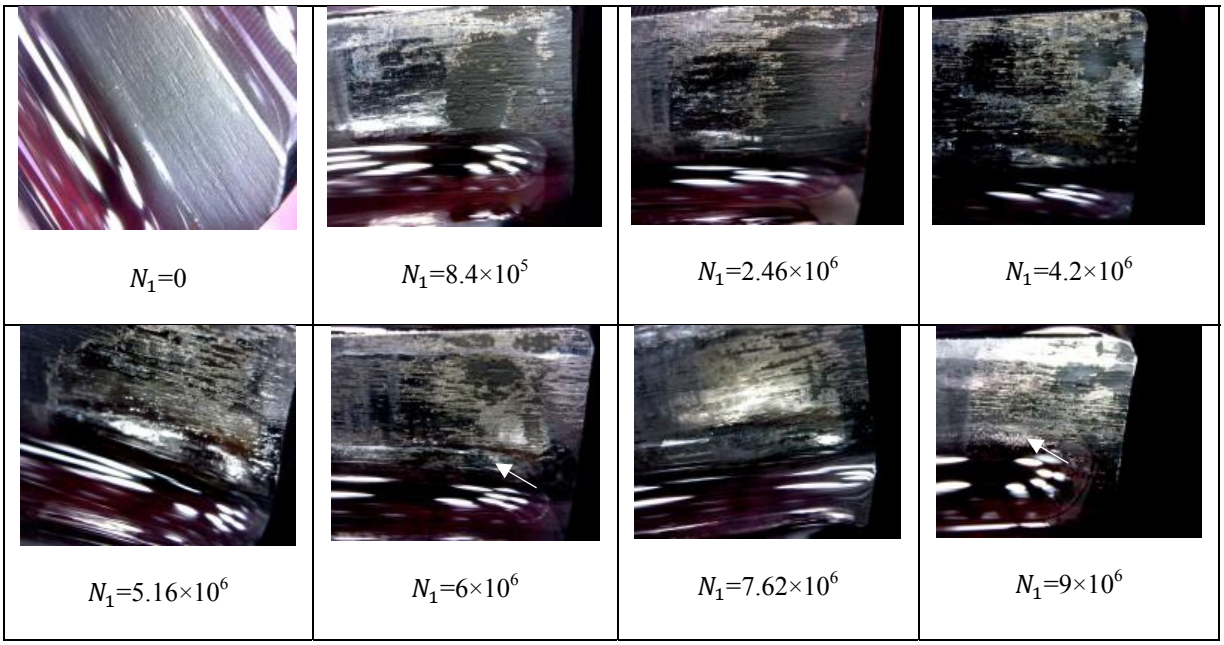

Figure 10: a-C:H coated AISI 1018 carburised gear surface image (the arrows annotate formation of micropitting).

A significant difference can be observed as the formation of micro-pitting occurred at an earlier cycle for the uncoated gear in Figure 9, while in Figure 10 the coated gear is shown to have experienced peeling at the earlier cycle and micro-pitting occurred only at 6×10^6 cycles onwards.

Through this observation, it is revealed that the a-C:H coating improves the scuffing and pitting resistance of the coated gear substantially in comparison with the uncoated gear where for the latter, prominent formation of micropits and scuff marks are scattered throughout the gear teeth. For the peak contact stress of 1,231 MPa in the experiment, it is found that for the uncoated gear, the generation of surface damage occurred frequently on the dedendum, indicating that the most severe mesh sliding condition prevail similar to the study demonstrated by Fernandes & McDuling (1997).

The uncoated gear showed progressive micropitting observed at the dedendum of the gear, which includes the gear tooth root and contact pitch line, as shown from optical imaging of the gear surface in Figures 11 (b) and (c). It can also be observed that scuffing mark occurrence is more prominent in the contact pitch line, lessens at the tooth root and is non-existent at the tooth tip. Microcracks are also observed solely at the tooth tip, which is also a sign of the initiation of micropits, as shown in Figure 11 (a).

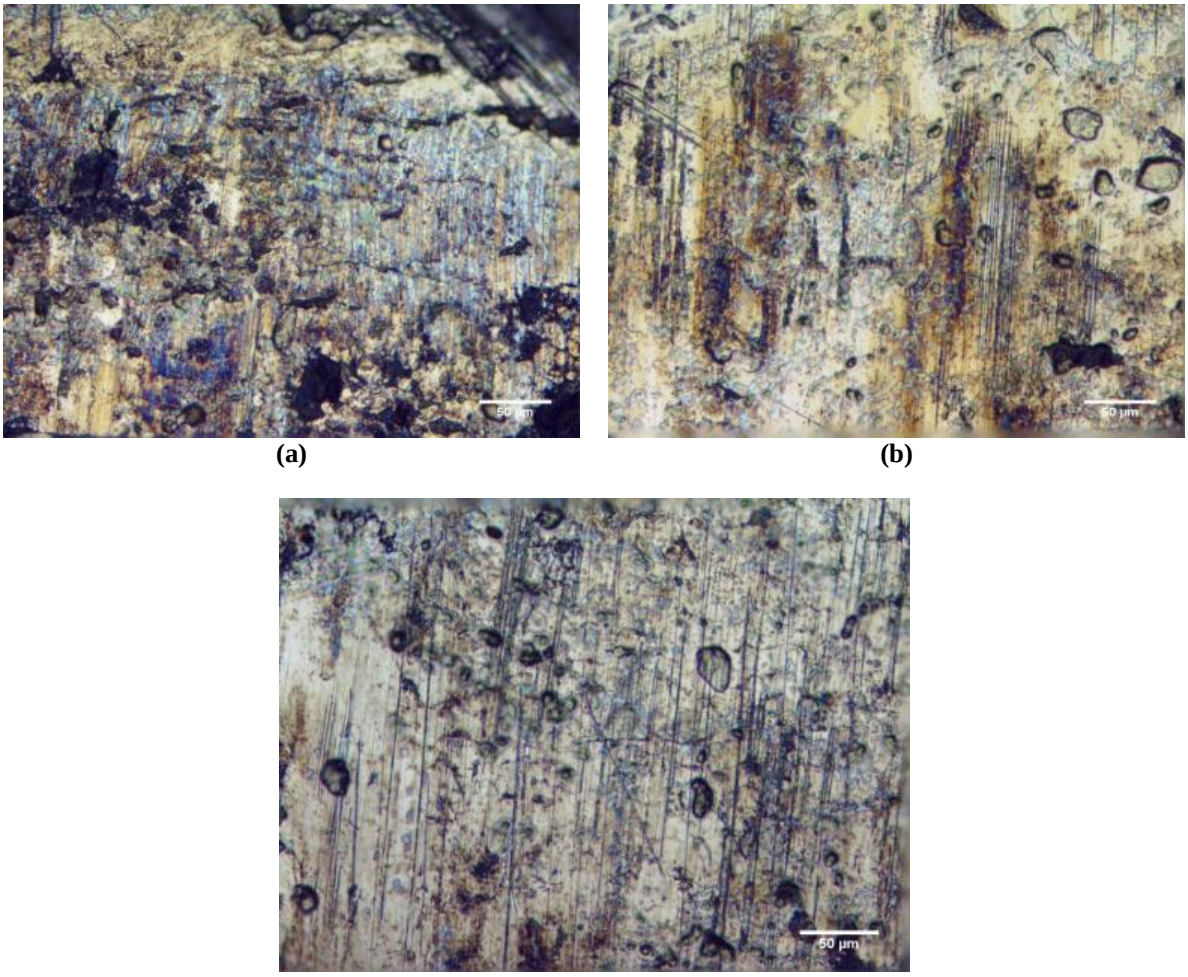

(a) **(b)**

(c)

Figure 11: Optical stereo images of uncoated gear surface at the end of the test with peak contact stress of 1,231 MPa: (a) Tooth tip (b) Tooth root (c) Contact pitch line.

The a-C:H coated gear exhibited completely different damage on its surface, where micropitting and scuffings are observed solely on the gear tooth tip, as shown in Figure 12 (a) albeit at a smaller scale and the coating partially remained intact. The tooth root suffered from large scale microcracks at the end of the test with partial peeling of the coating observed, as shown in Figure 12 (b). At the contact pitch line of the gear, no microcracks are observed.

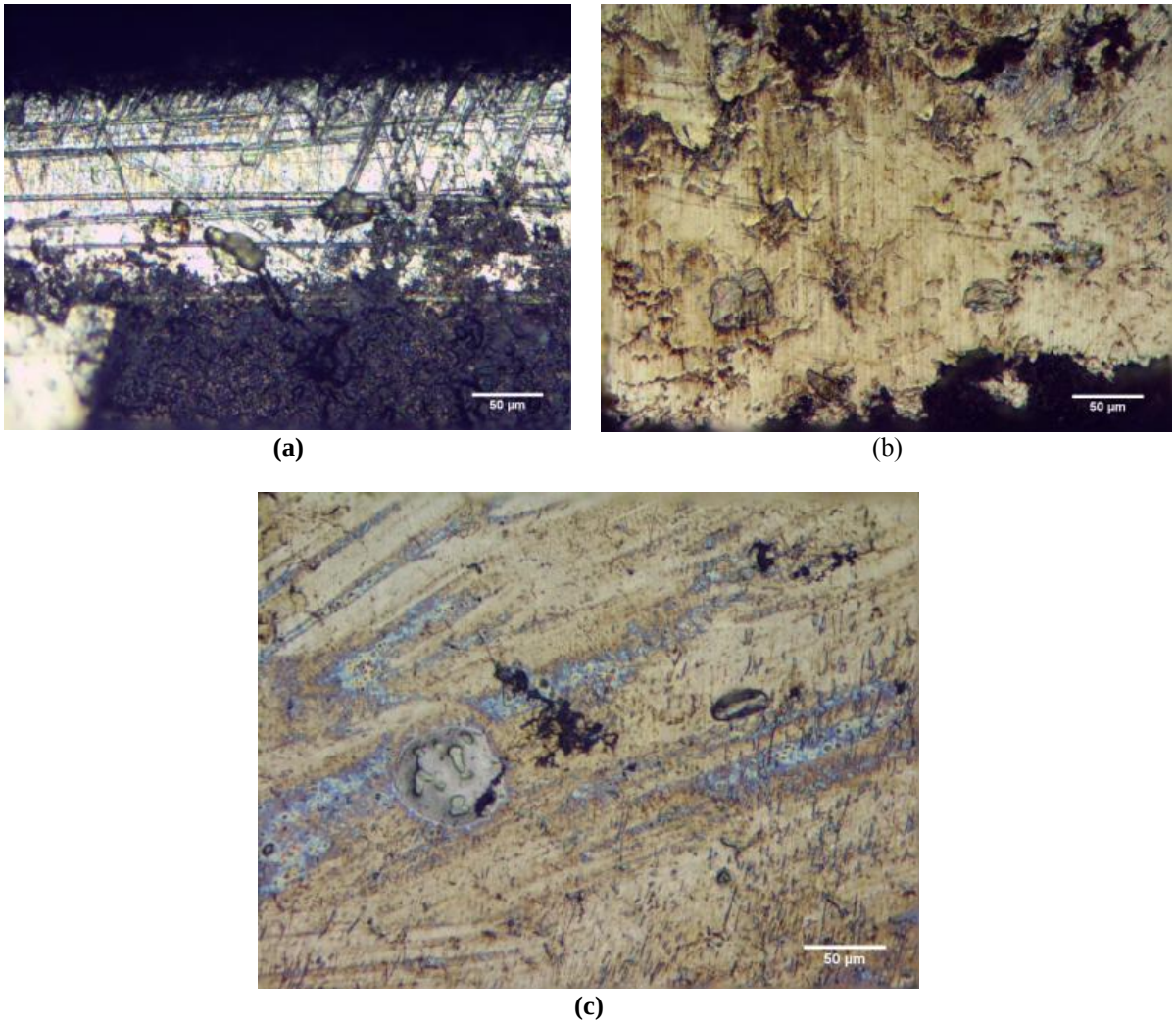

(a) (b)

(c)

Figure 12: Optical stereo images of coated gear surface at the end of the test with peak contact stress of 1,231 MPa: (a) Tooth tip (b) Tooth root (c) Contact pitch line.

The surface of the gear became smoother as a result of the interaction of the coating and gear surface after extended sliding and rolling mechanisms (Moorthy & Shaw, 2013). The surface coating is found to be completely removed as shown in Figure 12 (c). However, a polished surface would promote a decrease in material removal of the surface gear as no asperities or valleys are involved during the sliding and rolling mechanism of the gear.

4. CONCLUSION

The wear behaviour of a-C:H coated AISI 1018 carburised gear at peak Hertzian contact stress levels of 1,231 MPa in Pennzoil oil using power recirculating gear test rig was discussed in this manuscript. The results strongly suggest a significant improvement towards wear resistance of the carburised AISI 1018 gear. Through the particle generation analysis, it was concluded that the a-C:H coating influences the wear stages of the gear, where it was found that the running-in wear was experienced at

a relatively low wear rate with an extended cycle in comparison with the baseline testing. It was revealed that the a-C:H coating improved the life of the gear by a factor of 3.11 as compared to the uncoated gear. The a-C:H coating was observed to have no influence on the degradation of the gear lubricant. Peeling also occurred due to low adhesion between the deposited a-C:H and gear surface. The reduction of micro-pitting was significant for the a-C:H coated gear, which in our study occurred at 6×10^6 cycles. Thus, it can be concluded that a-C:H coating improved the material removal rate of the gear leading to a low wear debris generation due to its properties of high hardness and low coefficient of friction.

ACKNOWLEDGEMENT

This work was supported by the grant from the Ministry of Education of Malaysia (Grant RAGS/1/2014/TK01/FKM/B00070). The authors acknowledge the contributions from Universiti Teknikal Malaysia Melaka (UTeM) and the members of the Vibration and Structural Health Monitoring (ViBRO) research group.

REFERENCES

AGMA (American Gear Manufacturer Association) (2010). *ANSI/AGMA 1010-F14 Appearance of Gear Teeth-Terminology of Wear and Failure*. American Gear Manufacturer Association, Washington, D.C.

Anderson, D.P., Bowen, E.R. & Wescott, V. C. (1991). *Wear Particle Atlas*. Spectro Incorporated Industrial Tribology Systems, Chelmsford, Massachusetts.

Fernandes, P.J.L. & McDuling, C. (1997). Surface contact fatigue failures in gears. *Eng. Fail. Anal.*, **4**: 99–107.

Fujii, M., Ananth Kumar, M. & Yoshida, A. (2011). Influence of DLC coating thickness on tribological characteristics under sliding rolling contact condition. *Tribol. Int.*, **44:** 1289–1295.

Fujii, M., Seki, M. & Yoshida, A. (2010). Surface durability of WC/C-coated case-hardened steel gear. *J. Mech. Sci. Technol.*, **24**: 103–106.

Joachim, F., Kurz, N., & Glatthaar, B. (2002). Influence of coatings and surface improvements on the lifetime of gears. *VDI BERICHT*, ***2*:** 565–582.

Kalin, M., & Vižintin, J. (2005). The wear and temperature behaviour of DLC-coated gears lubricated with biodegradable oil. *VDI BERICHT*, **259:** 1005–1019.

Krantz, T., Cooper, C., Townsend, D., & Hansen, B. (2004). Increased Surface Fatigue Lives of Spur Gears by Application of a Coating. *J. Mech. Design*, **126:** 1047.

Kržan, B., Kalin, M. & Vižintin, J. (2006). The Lubrication of DLC Coated Gears with Environmentally Adapted Ester-Based Oil. *Int. Conf. Gears*, Düsseldorf, Germany, pp. 1345-1353.

Manier, C.A., Theiler, G., Spaltmann, D., Woydt, M. & Ziegele, H. (2010). Benchmark of thin film coatings for lubricated slip-rolling contacts. *Wear*, **268:** 1442–1454.

Michalczewski, R., Kalbarczyk, M., Michalak, M., Piekoszewski, W., Szczerek, M., Tuszynski, W., & Wulczynski, J. (2013a). New scuffing test methods for the determination of the scuffing resistance of coated gears. *Tribology–Fundamentals and Advancements, Intech, Croatia*, 187–215.

Michalczewski, R., Szczerek, M., Tuszy, W., & Antonov, M. (2013b). The effect of low-friction PVD coatings on scuffing and pitting resistance of spur gears. *Tribologia*, **5:** 8–11.

Moorthy, V., & Shaw, B. A. (2012). Contact fatigue performance of helical gears with surface coatings. *Wear*, **276:** 130–140.

Moorthy, V. & Shaw, B.A. (2013). An observation on the initiation of micro-pitting damage in as-ground and coated gears during contact fatigue. *Wear*, **297:** 878–884.

Tuszynski, W., Kalbarczyk, M., Michalak, M., Michalczewski, R., & Wieczorek, A. (2015). The effect of WC/C coating on the wear of bevel gears used in coal mines. *Mater Sci-Medzg*, **21:**

358–363.
Velmurugan, B., & Vijayakumar, S. (2017). Experimental Analysis of Hard Coating on Spur. *International Journal of Advances in Production and Mechanical Engineering*, **3:** 3–8.
Xiao, Y., Shi, W. & Li, L. (2014). Fatigue performance of cylindrical gearing with DLC coatings. *Int. Gear Conf. 2014*, Lyon, France, pp. 516–522.
Edwards, K. (2004). ASM handbook, volume 11: Failure analysis and prevention. *Mater. Design*, **25:** 735-736.